

1

Introduction

The discovery, understanding and mastery of materials and their properties have always been crucial to the technological advance of Humankind. The evolution of our society is so profoundly linked to our capability of mastering new materials that these have been used to refer to specific historical periods of the Human development. The Bronze and Iron Ages, for instance, are named after the metals which, harder and more durable than their stone and copper predecessors, allowed creation of improved tools, weapons and buildings. They are a testament that the search for “better” materials is pivotal in the tireless pursuit of Humans for scientific and technological progress.

1.1 Background and scope

Diamond is unique. Whether mechanical, thermal, electrical or optical, it possesses exceptional properties which are extremely difficult to be found combined in a single material. This, together with the fact that in the last fifty years the synthesis of artificial diamond has become a reality, makes it particularly attractive for engineering and technological purposes. The range of diamond-based applications is diverse and, among others, includes mechanical machining, high-power high-frequency electronics and high transmissivity optics.

Diamond is also host to a wide variety of crystallographic defects and colour centres. Appropriately controlled, they can be used to tune the characteristics of the material. Even more interestingly, they often possess properties on their own which can be exploited for

a completely different range of appealing technologies. Nitrogen-vacancy (NV) centres for instance, are diamond defects which have captured rising interest in the past few years. They possess unique room-temperature optical and spin properties and have therefore been proposed as a promising system to realise avant-garde applications spanning from quantum information technology to high resolution magnetometry, through biotechnology and nanomedicine.

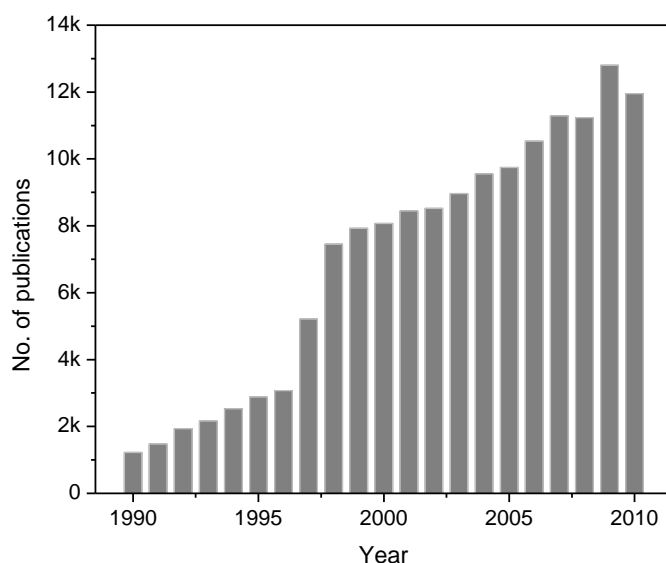


Figure 1.1. Number of diamond-related publications per year from 1990 to 2010. Source: ISI Web of KnowledgeSM (apps.isiknowledge.com).

Many of these NV centre-based technologies, however, have specific material requirements, such as the small size of the hosting diamond crystals or the optical stability of the defect. Up to now, some of these requirements could not or have not been tested. This led to a point where properties such as the photostability of the NV centre in nanodiamond (ND) have become almost implied assumptions. The capability of controlling the diamond material has rapidly improved in the last few years and specific production is now possible. NV centres can actually be created in synthesised diamond crystals only a few nanometres in size and the behaviour of the defect can finally be put under test.

In this thesis I focus on NV centres in nanodiamonds. I investigate the thermodynamical and optical stability of the centre as a function of a number of key parameters such as the size of the nanocrystals, the surface termination and the synthesis conditions of the

material. Based on these measurements, I try to build a framework for the feasibility and practical realisation of nanotechnologies based on NV centres in nanodiamonds.

1.2 Content

The main subject of this thesis is the nitrogen-vacancy (NV) centre and its properties in nanodiamond.

Chapter 2 contains an extensive *review* on diamond.

I present its physical properties: crystallographic, mechanical, thermal, electrical and optical, plus some of the relevant applications which exploit these. I then review the diamond lattice defects with the focus on nitrogen-related centres. I analyse in detail the nitrogen-vacancy (NV) centre and its general properties.

In the second part of the chapter, I review the main techniques that have been developed over the last fifty years to synthesise artificial diamond; the historical context is also considered. Finally, I show an overview of some of the promising technologies based on the use of NV centres in nanodiamond.

This chapter includes more than 160 references.

Chapter 3 contains the original *motivation* of this work.

I introduce the concept of magnetic microscopy and show potential benefits and drawbacks in comparison to classical microscopy. I present the idea of an NV centre-based magnetometer able to detect single spins. I show in detail its theoretical feasibility, but also the main experimental and practical challenges behind its realisation. This motivated our research towards a better understanding of the effects that parameters such as the size of the diamond nanoparticles, the proximity to the surface or the presence of surface functional groups have on the thermodynamical and optical stability of the NV centre in nanodiamonds.

Chapter 4 contains the description of the *experimental setup*.

I introduce the basic principles of confocal microscopy and atomic force microscopy. I describe in detail the components of the system we designed and used to fully characterise the NV centres in nanodiamonds. The setup consists of a lab-built confocal

microscope combined with an atomic force microscope (AFM). The size of the nanodiamonds was probed with the AFM, while the optical behaviour of the hosted NV centres was assessed with the confocal microscope which includes photodiodes in a Hanbury-Brown and Twiss interferometer configuration and a spectrometer.

Chapter 5 contains an analysis of the effects that *size* has on the *stability* of carbon structures and of NV centres in nanodiamonds.

The first part of the chapter is general, dealing with the various structures carbon can form at the nanoscale. I analyse how size is a critical parameter in determining the stability of the carbon phases and show that at the nanoscale certain carbon structures are unique and cannot exist at higher size ranges.

The second part of the chapter is more specifically focused on the thermodynamical stability of the NV centre in nanodiamond. I present an original and extensive collaborative study we conducted to address the probability of observing NV centres in nanodiamonds as a function of the particle size. The experimental data we obtained were compared with the theoretical predictions performed by our collaborator.

Chapter 6 contains an extensive analysis of the effects that *size* and *surface* have on the *optical properties* of NV centres in nanodiamonds.

I briefly review some of the techniques that have been recently proposed to fabricate ultrasmall nanodiamonds (size < 10 nm) containing fluorescent NV centres. In this context, I show our original contributions. First, I describe a technique we optimised to process detonation nanodiamonds (DNDs) and overcome the aggregation problem that this type of diamond material is subject to. I also present the first demonstration we reported on the stability of NV centres in isolated 5-nm detonation nanodiamonds. Second, I illustrate a method we perfected to tailor the size of selected nanodiamonds; the method is based on thermal oxidation of the diamond crystals in air.

With reference to these two studies I then focus attention specifically on the optical properties of NV centres when hosted in ultrasmall nanodiamonds. I present the very first report we made about the newly discovered fluorescence intermittency or blinking property of the centre in 5-nm nanodiamonds. I finally present a detailed and structured series of experiments we designed and realise to address the cause of the blinking

mechanism, investigating the effects of size of the nanodiamonds, surrounding media, functional groups and substrate. A proposed model explaining the blinking mechanism of NVs in nanodiamonds is also given.

Chapter 7 contains the *conclusions* of this work and some possible *future studies*.

2

Diamond and colour centres

The word diamond comes from Latin *adamantem* and this from the Greek *αδάμας* (*adamas*). It was initially used by Homer (ca VIII century B.C.) and Hesiod (VIII-VII century B.C.) to indicate both the “hard metal in arms”¹ and as a personal epithet meaning “invincible”². It was only Teophrastus (371-287 B.C.), Aristotle’s (384-322 B.C.) pupil, who firstly used the term composed by the alpha privativum *a-*, “not”, and by the word *damàc*, “to conquer, to tame”, to indicate the untameable crystal³.

Known for thousands of years, diamond has been used primarily as an engraving tool, but also as a prized gemstone. Its popularity rose in the 19th century due to improved techniques to shape and cut it. In the jewellery market it was only after the 1940s that diamond became the gemstone *par excellence* when in 1947 the copywriter F. Gerety working for the US advertising agency N. W. Ayer & Son coined the slogan “*A diamond is forever*” to advertise diamonds for De Beers, the South African mining firm that controls the majority of the world’s diamond supply. The De Beers’ marketing campaign was based on advertising the product rather than the brand and is acknowledged as one of the most successful and innovative campaigns in history which dramatically increased the demand for diamond gemstones and made diamond a true icon in the eyes of the public.

¹ Homer’s *Iliad*, b. XIII, vs. 35-39; Hesiod’s *Shield of Heracles*, vs. 135-138 and *Theogony* vs. 185-189.

² Homer’s *Odissey*, b. XXIII, vs. 176; Hesiod’s *Theogony* vs. 144-155.

³ Theophrastus’s *On Stones*, v. 19.

But diamond is not just a beautiful piece of jewellery. It has unique and remarkable mechanical, thermal, chemical, electronic and optical properties. It is therefore no surprise that the technological interest in this material has led, in the last fifty years, to the development of different techniques for synthesising artificial diamond. After the first successful attempt to synthesise diamond on December 16th 1954 by T. Hall from General Electric, today, many companies including, Element Six (De Beers), Gemesis, Diamond Innovations, Sumitomo Electric and Apollo Diamond, to cite only few of them, are investing great efforts to develop more reliable and more affordable processes to produce laboratory- and factory-grown synthetic diamonds.

2.1 Physical properties of diamond

Diamond has been known and utilised for a long time, but today, in addition to its traditional uses in machining and jewellery, it is also becoming the choice material of leading edge technologies.

Firstly, for almost any property –be it mechanical, thermal, electrical or optical– diamond exhibits the most extreme characteristics compared to any other material. Secondly, in the last fifty years man-made diamonds have become a reality. Natural diamonds can occur in quite a few different types and some of their properties can differ significantly from type to type. Until recently, this variability was enough to prevent diamond from being a suitable material for technological purposes on a commercial scale. Today however, material science has advanced sufficiently to enable production of dramatically improved diamond qualities. The more we study the material, the more intrigued we become by its extraordinary unicity. For instance, diamond is host to a wide variety of crystallographic defects, which are primarily responsible for all the colours and nuances diamond displays. Beyond the aesthetic of colour, what is really interesting is the fact that many of these defects, referred to as colour centres, are made of atomic inclusions that show interesting spin and optical properties. The study of these impurities constitutes by itself a vast field of investigation which may contribute to new technologies and farseeing applications.

Making a complete and exhaustive account of diamond as a material is almost impossible; the following sections of this chapter contain a review which summarises a large number of the unique properties diamond possesses.

2.1.1 Crystallographic properties

Diamond is an allotrope of carbon. The electronic configuration of carbon is $1s^2 2s^2 2p^2$ with four valence electrons spread over the $2s$ and $2p$ orbitals. In diamond, the s -orbital of carbon mixes with the three p -ones: they form sp^3 -hybrid orbitals with the four valence electrons equally distributed. For every carbon atom, each one of the four valence electrons forms a covalent bond with another carbon nearby. The result is a periodic structure where each atom forms strong covalent bonds with its four nearest neighbours arranged at the corners of a regular tetrahedron (Fig 2.1).

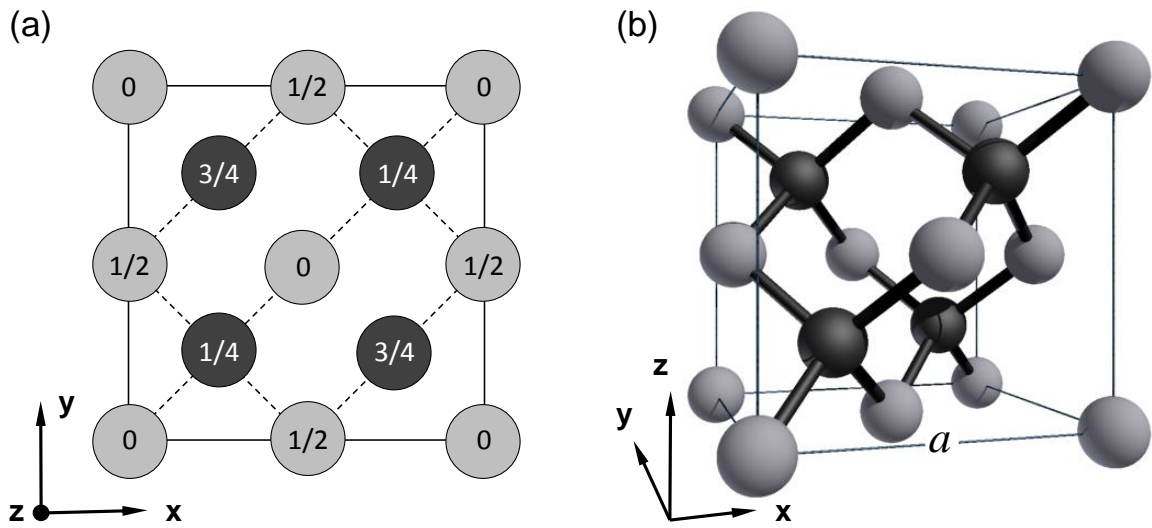


Figure 2.1. Conventional cubic cell of the diamond lattice. **a)** Position of the carbon atoms in the unit cell projected on a cube face: fractions denote the height above the base in units a of a cube edge. The difference in colour is used to indicate the two interpenetrating face-centered cubic (fcc) Bravais lattices: points 0 and $\frac{1}{2}$ (light grey) belong to the same fcc lattice, while points $\frac{1}{4}$ and $\frac{3}{4}$ (dark grey) are on a similar fcc lattice displaced from the first along the body diagonal by one fourth of its length a . **b)** Tridimensional view of the diamond unitary cubic cell; at room temperature, the unitary cubic side length a measures 0.356 nm, while the nearest-neighbour bonds (drawn as black sticks) measure 0.154 nm [1].

From a crystallography point of view, diamond belongs to the *isometric* crystal system; its space group is the number 227 (in the International Union of Crystallography notation) or equivalently the $Fd\bar{3}m$ (in the international short symbol notation).

The diamond lattice consists of two interpenetrating face-centered cubic (fcc) Bravais lattices, displaced along the body diagonal of the cubic cell by one quarter the length of the diagonal (Fig. 2.1). It can be regarded as a face-centered cubic lattice with the two point primitive basis $\mathbf{0}$ and $(a/4)(\hat{x} + \hat{y} + \hat{z})$, being a the length of the conventional cubic cell ($a = 0.356$ nm, at 293 K [1]). Each carbon atom has four nearest neighbours (coordination

number 4) and twelve next nearest neighbours. There are eight atoms in a unit cubic cell (the diamond density is 3.51 g/cm³ at 293 K [1]). The diamond lattice is not a Bravais lattice because the environment of any point differs in orientation from the environments of its nearest neighbours. In fact, only each half of the atoms lying on the same fcc lattice have identical environment.

The diamond lattice is relatively empty with an atomic packing factor (APF) of $(\pi/16)\sqrt{3}$. The atomic packing factor is defined as the fraction of volume of a unitary crystal cell which is occupied by atoms:

$$APF = \frac{NV_a}{V_c} \quad (2.1)$$

where N is the number of atoms per unitary cell, V_a is the volume of an atom and V_c is the volume of the unitary cell. Thus, in the diamond structure, the maximum proportion of the available volume which may be filled by the atoms is only 0.34, about 46% of the filling factor for a closed-packed structure.

Table 2.1 Summarises the crystallographic properties of diamond.

Table 2.1 – Crystallographic properties of diamond		
Property	Value	Reference(s)
Crystal system	Isometric	-
Space group	227 (International Union of Crystallography) F d -3 m (International Short Symbol)	-
Unitary cubic side length	0.356 nm (at 293 K)	[1]
Bond length	0.154 nm (at 293 K)	[1]
Coordinate number	4	-
Atoms per unitary cell	8	-
Density	3.51 g/cm ³ (at 293 K)	[1]
Atomic packing factor	$(\pi/16)\sqrt{3} = 0.34$	-

2.1.2 Mechanical properties

Due to its structure, with carbon atoms forming strong covalent bonds in the characteristic tetrahedral arrangement, diamond is the hardest-known natural material. Diamond extremely high hardness has made it, since its discovery, the ideal material for cutting, grinding and polishing. But hardness is just one aspect: unlike other hard materials, diamond has a high thermal conductivity which allows the removal of a high quantity of heat from the cutting tool and its coefficient of friction is quite low (when the

surface is terminated with hydrogen groups). These additional factors together with the hardness are what render diamond so effective for mechanical applications.

Scratch hardness (Mohs scale). On the traditional Mohs scale of mineral hardness, based on the ability of a harder material to scratch a softer material, diamond scores the top value, 10 [2]. It is four times harder than corundum (Al_2O_3) which occupies position 9 on the scale. Silicon (Si) and germanium (Ge) share the same crystalline structure of carbon in diamond, but score only 6-7 on the scale and are up to ten times softer to scratch than diamond. (Note: Mohs scale is not a linear scale).

Indentation hardness (Knoop scale). The Knoop indentation test determines the microhardness of materials [3]. In this test, a pyramid-shaped diamond indenter with a length to width ratio of 7 : 1 and face angles of 172° for the long edge and of 130° for the short edge, is pressed against the material with a known force and for a specified dwell time. The resulting indentation is measured using a microscope. The Knoop hardness HK is given by the following formula:

$$HK = \frac{P}{C_p L^2} \quad (2.2)$$

where P is the load, L is the indentation length along the long axis and C_p is the correction factor related to the shape of the indenter, ideally 0.070279. It must be noted that the measured hardness value is influenced by the normal load, the indenter shape, its crystallographic relationship with the indented surface and the temperature. The Knoop hardness for diamond can vary between 5700 kg/mm^2 and 10400 kg/mm^2 . On the (111) surface, for a load of 500 g applied along the $\langle 110 \rangle$ direction and at a temperature of 298 K the Knoop hardness of diamond has been measured to be 9000 kg/mm^2 [4]. (Note: there are other scales that can be used to measure the hardness of materials; the Knoop scale is considered the most accurate for crystalline solids).

Friction. In air, the coefficient of friction μ of diamond is about 0.1, but the value can vary according to load, geometry, polishing direction and orientation. On the (111) plane $\mu \sim 0.05$ and is approximately constant in all directions. On the (100) plane μ varies between ~ 0.05 along $\langle 011 \rangle$ and $\sim 0.1-0.15$ along $\langle 010 \rangle$ for surface polishing done along $\langle 100 \rangle$ [5].

Strength. The strength of a material is determined by the stress required to deform it. The ideal value for a hypothetical perfect diamond crystal can be above 90 GPa for all tensile, compression and shear stresses [6-12]. In comparison, the ideal strengths of silicon and germanium crystals are less than 25 GPa. The ideal strength value is calculated assuming a defect-free crystal and sets an upper limit for the strength of a real crystal. The strength of diamond is highly dependent on the crystallographic orientation. The experimental values of strength for real diamond crystals show wide variations. This is mainly due to the fact that the strength of individual crystals is affected by the amount and type of defects, inclusions and impurities they contain.

Elastic properties. The strength of a material is directly related to its elastic moduli: i) Young's modulus E , ii) Shear modulus G , iii) Poisson's ratio ν and iv) Bulk modulus K .

i) The Young's modulus E is related to the tensile strength and is defined as the ratio between the uniaxial stress and the uniaxial strain in the range of stress in which Hooke's law holds (i.e. in the linear-elastic range):

$$E = \frac{F / A_0}{\Delta L / L_0} \quad (2.3)$$

In equation (2.3), F is the force applied to the object, A_0 is the original cross sectional area through which the force is applied, ΔL is the amount by which the length of the object changes and L_0 is the original length of the object. The Young's modulus for diamond is very high (~ 1100 GPa), up to ten times that of silicon (~ 160 GPa) and germanium (~ 130 GPa) [10]. Such a high value of the Young's modulus reflects the high strength of diamond.

ii) The shear modulus G is relevant to the deformation of a solid when it experiences a force parallel to one of its surface while its opposite face experiences an opposing force. It is defined as the ratio between the shear stress and the shear strain:

$$G = \frac{F / A_0}{\Delta x / l} \quad (2.4)$$

In equation (2.4), F is the force applied to the object, A_0 is the original cross sectional area on which the force acts, Δx is the transverse displacement and l is the initial length. The Shear modulus of diamond is very high (~ 550 GPa), up to ten times that of silicon (~ 60 GPa) and germanium (~ 50 GPa) [10].

iii) The Poisson's ratio ν of a material refers to the deformation of a solid when it is stretched (or compressed) in one direction and it experiences a contraction (or expansion) in the other two. It is defined as the ratio between the transverse strain (perpendicular to the applied load) and the axial strain (in the direction of the applied load) when the sample object is stretched:

$$\nu = -\frac{\delta\epsilon_{trans}}{\delta\epsilon_{axial}} \quad (2.5)$$

In equation (2.5), assuming that the sample is stretched (or compressed) along the axial direction, $\delta\epsilon_{trans}$ is the transverse strain (< 0 for axial tension and > 0 for axial compression) while $\delta\epsilon_{axial}$ is the axial strain (> 0 for axial tension and < 0 for axial compression). The Poisson's ratio for diamond is very low (~ 0.07), which means that it is very hard to deform: it shows a very little lateral compression (or expansion) when stretched (or compressed). In comparison silicon and germanium have a Poisson's ratio almost three times higher (~ 0.2) [10].

iv) The Bulk modulus K of a material measures its resistance to uniform compression and is defined as:

$$K = -V \frac{\partial P}{\partial V} \quad (2.6)$$

In equation (2.6), P is the pressure applied, V is the volume of the sample material and $\partial P / \partial V$ is the partial derivative of pressure with respect to volume. Note that the inverse of the Bulk modulus of a material gives its compressibility. The Bulk modulus of diamond is very high (~ 440 GPa) which reflects its extremely high resistance to uniform compression; it is up to five times that of silicon (~ 100 GPa) and germanium (~ 80 GPa) [10].

Anisotropy. Anisotropy measures the degree at which the mechanical properties of a crystalline material vary with the different crystalline orientations. When the properties are the same in all directions the material is defined as isotropic. In crystalline materials, the linear relationships of stress σ_i and strain e_i can be expressed via the elastic constants C_{ij} :

$$\sigma_i = \sum_j C_{ij} e_j \quad (2.7)$$

where $i, j = 1-6$ (being $1 = xx, 2 = yy, 3 = zz, 4 = yz, 5 = xz, 6 = xy$). In cubic crystals like diamond, symmetry allows reducing the number of elastic constants to just three, C_{11} ($\equiv C_{22}, C_{33}$), C_{12} ($\equiv C_{13}, C_{23}$) and C_{44} ($\equiv C_{55}, C_{66}$). The condition for anisotropy A is given by:

$$A = \frac{2C_{44}}{C_{11} - C_{12}} \quad (2.8)$$

where $A = 1$ denotes perfect isotropy. For diamond $A = 1.21$ which means it is only weakly anisotropic; in comparison silicon ($A = 1.56$) and germanium ($A = 1.67$) show a higher degree of anisotropy [13].

Speed of Sound. The extreme elastic properties of diamond are also responsible for the very high velocity at which sound propagates through it. The acoustic velocity in a material is related to its change in pressure and density. Three acoustic waves can propagate in a material: one longitudinal wave with oscillation in the direction of propagation and two shear (transverse) waves with oscillations transverse to the propagation vector and orthogonal to each other. In general the acoustic velocity v in a material is given by the equation:

$$v = \sqrt{\frac{E}{\rho}} \quad (2.9)$$

where E is Young's modulus and ρ is the density of the medium. For a cubic crystal like diamond the longitudinal and shear wave velocities can be determined respectively as $v_L = \sqrt{C_{11}/\rho}$ and $v_T = \sqrt{C_{44}/\rho}$. In diamond, according to the different crystal orientations the longitudinal wave velocity can be ~ 18000 m/s, while the transverse ones can be in the range $\sim 10500-13000$ m/s [14].

Cleavage. Unlike hardness and strength, diamond toughness or tenacity, which measures the resistance to breakage, is no better than many other engineering materials. For instance, diamond can be fractured or cleaved along the (111) plane due to a minimum in the cohesion energy; cleavage can occur to a lesser extent also on different planes [6]. In a simplistic way, the cleavage surface energy density can be determined by calculating the number of bonds which cross the unit area of a chosen plane and multiplying this by the carbon-carbon bond strength. By using a value for the carbon-carbon energy of 5.8×10^{-19} J, the following values for the theoretical cleavage surface energy density can be obtained:

10.6 J/m² for the (111) plane, 13 J/m² for the (110) plane and 18.4 J/m² for the (100) plane. Experimental values may differ from the theoretical ones due to the presence of defects and inclusions. The cleavage velocity in diamond can be of the order of few thousand metres per second; velocities up to 7200 m/s have been recorded [12].

Plastic flow (Temperature of dislocation mobility). Plasticity describes the deformation of a material undergoing non-reversible changes in response to applied forces. Plastic bending due to dislocation mobility has been measured in diamond for temperatures above 1600 K [15].

Table 2.2 summarises the mechanical properties of diamond.

Table 2.2 – Mechanical properties of diamond		
Property	Value	Reference(s)
Scratch hardness (Mohs scale)	10	[2]
Indentation hardness (Knoop scale),	5700-10400 kg/mm ²	[3, 4]
Friction	0.05-0.15	[5]
Tensile strength (strain; stress; direction <xyz>)	~ 0.40 GPa; ~225 GPa; <100> ~ 0.24 GPa; ~130 GPa; <110> ~ 0.13 GPa; ~ 90 GPa; <111>	[6, 9, 11]
Compressive strength (strain; stress; direction <xyz>)	~ -0.28 GPa; ~ -220 GPa; <100> ~ -0.23 GPa; ~ -470 GPa; <110> ~ -0.23 GPa; ~ -470 GPa; <100>	[9]
Shear strength (strain; stress; plane (xyz); direction <xyz>)	~ 0.3 GPa; ~ 90 GPa; (111); <112> ~ 0.24 GPa; ~ 120 GPa; (111); <110>	[7, 12]
Young's modulus <i>E</i>	~1100 GPa	[10]
Shear modulus <i>G</i>	~ 550xGPa	[10]
Poisson's ratio <i>ν</i>	~ 0.07	[10]
Bulk modulus <i>K</i>	~ 440 GPa	[10]
Anisotropy	1.21	[13]
Acoustic velocity	~18000 m/s (longitudinal) ~ 10500-13000 m/s (transverse)	[14]
Cleavage surface energy density (on plane (xyz))	10.6 J/m ² ; (111) 13.0 J/m ² ; (110) 18.4 J/m ² ; (100)	[12]
Cleavage velocity	7200 m/s	[12]
Temperature of dislocation mobility	> 1600 K	[15]

2.1.3 Thermal properties

One of the most technologically relevant properties of diamond is its extremely high thermal conductivity. This property makes diamond ideal for mechanical purposes as well as an excellent candidate material for high-frequency, high-power, high-temperature, high-voltage electronics and high-efficiency heat sinks for electronic and optical devices.

In fact, diamond-based devices could bear high powers better than other materials, like for example silicon, whose lower thermal conductivity at room temperature requires large cooling systems and larger dimensions [16].

Thermal conductivity. The covalent bonding within carbons in diamond is responsible for its extremely high thermal conductivity. Natural single-crystal diamond is known to possess the highest thermal conductivity of all the bulk materials, up to 2200 W/m·K at room temperature [17]. Monocrystalline synthetic diamond enriched in ^{12}C isotope can feature even higher values, 3320 W/m·K, while electron-irradiated diamond shows a reduction in the thermal conductivity, mainly due to the presence of vacancies in the lattice. By comparison, aluminium and copper have thermal conductivities of 250 W/m·K and 400 W/m·K, respectively [18-20].

Thermal expansion (linear). The linear thermal expansion is the change in linear dimensions of a material due to a change in temperature:

$$\alpha_L = \frac{1}{L} \frac{dL}{dT} \quad (2.10)$$

In equation (2.10), α_L is the linear thermal expansion coefficient, L is the linear dimension and dL/dT is the rate of change of the linear dimension L per unit change in temperature T . Diamond has a small linear thermal expansion coefficient α_L : in the range 100-500 K the value of α_L in diamond goes from 0 K⁻¹ to 3×10^{-6} K⁻¹ (at 293 K, $\alpha_L \sim 1 \times 10^{-6}$ K⁻¹), while in the range 500-1700 K it goes from 3×10^{-6} K⁻¹ to 6×10^{-6} K⁻¹ [21].

Specific heat. The specific heat is the amount of heat per unit mass required to raise the temperature of a material by one degree Celsius. Diamond possesses a relatively low specific heat. At 300 K the specific heat of diamond both at constant pressure (C_p) and at constant volume (C_v), has been measured to be 6195 J/mol·K [12].

Debye Temperature. The Debye model treats the vibrations of the atomic lattice (heat) in a solid as phonons in a box, the box being the solid. The Debye temperature θ_D of a material is defined as the temperature above which all modes begin to be excited and below which modes begin to be “frozen out”. It separates the low-temperature region

where quantum statistics must be used from the high-temperature region where classical statistical mechanics is valid (i.e. where the Dulong-Petit law holds). Diamond possesses an extremely high Debye temperature $\theta_D = 1960$ K, up to three times that of silicon ($\theta_D = 668$ K) and to five times that of germanium ($\theta_D = 390$ K) [22]. Note that since the Debye temperature of diamond is so high, the heat capacity of diamond shows quantum nature even at room temperature.

Thermal shock parameter. Thermal shock is the cracking of a solid due to rapid temperature changes. It occurs when a thermal gradient causes different parts of a material to expand by different amounts: when the stress overcomes the strength of the material a crack forms causing the structure to fail. Due to its high thermal conductivity and its low (linear) thermal expansion coefficient, diamond possesses an extremely high thermal shock parameter, $\sim 30 \times 10^6$ W/m [23].

Melting Point. Diamond melts at ~ 4500 K. The graphite/diamond/liquid triple-point (cf. s. 2.3.1, Fig. 2.9) occurs at a pressure of ~ 11 MPa and at a temperature of ~ 4200 K [24].

Table 2.3 summarises the thermal properties of diamond.

Table 2.3 – Thermal properties of diamond		
Property	Value	Reference(s)
Thermal conductivity	~ 2200 W/m·K	[17]
Linear thermal expansion coefficient	$0-3 \times 10^{-6}$ K ⁻¹ (range 100-500 K) 3×10^{-6} K ⁻¹ - 6×10^{-6} K ⁻¹ (range 100-500 K)	[21]
Specific heat	6195 J/mol·K (at 300 K)	[12]
Debye temperature	1960 K	[22]
Thermal shock parameter	$\sim 30 \times 10^6$ W/m	[23]
Melting point	4500 K	[24]

2.1.4 Electrical properties

Diamond possesses excellent electronic and thermal properties whose combination makes it extremely attractive as an electronic device material especially for high-frequency and high-power applications. A crude comparison between diamond and any of the other competing semiconductors such as silicon (Si), silicon carbides (SiC) or gallium nitride (GaN) shows that diamond-based devices could deliver outstanding performances over the existing technologies. What has, so far, prevented diamond from finding its place in

the semiconductor market is most likely the fact that natural diamonds are too variable in their properties; the advent of processes to synthesize artificial diamonds, however, may enable access to increased volumes of high quality material [17].

Valence-conduction band gap. Electrically, diamond is an insulator or a wide-gap semiconductor. It has a direct valence-conduction band gap of ~ 7.5 eV and an indirect valence-conduction band gap of ~ 5.5 eV (deep ultraviolet 225 nm) at 300 K [25, 26].

Resistivity. The electrical resistivity of diamond can vary considerably, even several orders of magnitude according to the type of diamond (cf. s. 2.2.2, Fig. 2.4). Type IIb diamonds have resistivity in the range 0.1-100 $\Omega\cdot\text{m}$, while type I and most type IIa diamonds normally show resistivity greater than 10^{14} $\Omega\cdot\text{m}$ and up to 10^{18} $\Omega\cdot\text{m}$ [27, 28]. Doped with boron, diamond becomes a superconductor below the superconductive transition temperature $T_c = 4$ K [29].

Charge carrier mobility. At room temperature the charge carrier mobility in naturally occurring diamond is among the highest of any wide-bandgap semiconductor, ranging from 2000 $\text{cm}^2/\text{V}\cdot\text{s}$ to 2800 $\text{cm}^2/\text{V}\cdot\text{s}$ for electrons and from 1800 $\text{cm}^2/\text{V}\cdot\text{s}$ to 2100 $\text{cm}^2/\text{V}\cdot\text{s}$ for holes. Values even higher, 4500 $\text{cm}^2/\text{V}\cdot\text{s}$ for electrons and 3800 $\text{cm}^2/\text{V}\cdot\text{s}$ for holes, have been experimentally demonstrated in single crystal chemical vapour deposition (CVD) synthetic diamond [26]. In comparison, the mobility of electrons and holes in silicon are respectively 1450 $\text{cm}^2/\text{V}\cdot\text{s}$ and 500 $\text{cm}^2/\text{V}\cdot\text{s}$ [30]. It has been reported that the carrier mobility in diamond tends to drop with temperature. In the temperature range 300-380 K, where the phonon scattering mechanism starts to become a limiting factor, the carrier mobility drops with the temperature T as $\sim T^{-1.5}$. For temperatures higher than 400 K the mobility drops more rapidly with a dependence in the range $\sim T^{-2.5}$ - $T^{-3.7}$ and it seems to be controlled by optical phonons [31]. Even so, carrier mobility greater than 2000 $\text{cm}^2/\text{V}\cdot\text{s}$ at 400 K and greater than 1000 $\text{cm}^2/\text{V}\cdot\text{s}$ at 500 K have been measured making high temperature diamond based-devices feasible [17]. The presence of impurities and inclusions in diamond can cause a drop in the carrier mobility too; for instance a drop in the mobility from 1500 $\text{cm}^2/\text{V}\cdot\text{s}$ to 1000 $\text{cm}^2/\text{V}\cdot\text{s}$ has been measured in boron-doped CVD samples with concentration of boron in the range 5×10^{16} - 2×10^{18} cm^{-3} [32].

Saturation velocity. In the presence of an electric field, carriers acquire energy from the field and lose it to phonons by emitting more phonons than are absorbed. At moderate fields the most frequent scattering events involve the emission of acoustic phonons; the drift velocity of the carriers is proportional to the electric field and the mobility is constant. At sufficiently high fields the carrier velocity starts to deviate from being linearly dependent on the applied field and the carriers interact with optical phonons. At this point, the drift velocities of the carriers become less and less dependent on the applied field and the conductivity is not dominated anymore by the carrier mobility but by their saturation velocity v_s :

$$v_s = \sqrt{\frac{8E_p}{3\pi m_0}} \quad (2.11)$$

where E_p is the optical-phonon energy and m_0 is the effective mass of charge carriers [30]. High optical phonon energies give high saturation carrier velocities and diamond has the highest optical phonon energy ($E_p = 160$ MeV) of any semiconductor [33]. Experimentally measured values of v_s for diamond are of the order of 1.5×10^7 - 2.7×10^7 cm/s for electrons and 0.85×10^7 - 1.2×10^7 cm/s for holes [31]. Of the other wide-bandgap semiconductors, only silicon carbide (SiC) has values comparable to those of diamond. However, diamond has the advantage that its saturation velocity is reached in fields of ~ 10 kV/cm, roughly three orders of magnitude below its electrical breakdown, whereas for SiC, the velocity saturates at fields close to the material electrical breakdown strength, making its use in devices difficult [17].

Carrier Lifetime. Carrier lifetime is an important figure for some electronic devices. A high carrier lifetime generally indicates low impurities and defect concentrations. Even though in natural diamond carrier lifetimes less than 1 ns are typical, lifetimes of more than 2 μ s have been measured in single crystal CVD diamond [26].

Dielectric Breakdown Field. For high-power electronic devices a high value for the dielectric breakdown field is desirable. A high dielectric strength means that the material can withstand a high electric field before electrons get accelerated so much that they ignite an avalanche breakdown. The fact that a material can tolerate high fields also implies that a device built from it can be designed with smaller dimensions. Diamond has the highest

theoretically predicted breakdown field of any semiconductor, 5-10 MV/cm which is, for instance, up to twelve times that of silicon [16].

Static Relative Permittivity/Dielectric constant. Diamond dielectric constant is relatively low, 5.7 at 300 K, almost half of that of silicon [16]. A low dielectric constant is desirable for power electronics.

Table 2.4 summarises the electrical properties of diamond.

Table 2.4 – Electrical properties of diamond		
Property	Value	Reference(s)
Band gap	~ 7.5 eV (direct, at 300K) ~ 5.5 eV (indirect, at 300K)	[25, 26]
Resistivity	0.1-100 $\Omega\cdot\text{m}$ (type IIb diamonds) $\geq 10^{14}$ $\Omega\cdot\text{m}$ (type I and most IIa diamonds)	[27, 28]
Charge carrier mobility	~ 2000-4500 $\text{cm}^2/\text{V}\cdot\text{s}$ (for electrons at 300 K) ~ 1800-3800 $\text{cm}^2/\text{V}\cdot\text{s}$ (for holes at 300 K)	[26]
Saturation velocity	~ 1.5×10^7 - 2.7×10^7 cm/s (for electrons at 300 K) ~ 0.85×10^7 - 1.2×10^7 cm/s (for holes at 300 K)	[31]
Carrier lifetime	< 1 ns (natural diamond) > 2 μs (single-crystal CVD)	[26]
Dielectric breakdown field	~ 5-10 MV/cm	[16]
Static relative permittivity	~ 5.7 (at 300 K)	[16]

2.1.5 Optical Properties

Pure diamond is transparent. Transparency is one of the properties that give value to a diamond as a gem, but it also makes it appealing as a material for optical applications. Some of the traditional uses of diamond in optics include: windows for infrared instrumentation due to high transmissivity in this region of the light spectrum and fabrication of radiation detectors [23, 34]. Recently, a range of new applications are being revealed exploiting the fact that diamond is host to a wide variety of defects and colour centres. These impurities possess unique optical and spin properties which make them promising candidates for solid-state quantum technologies [35-38] and for biomedical applications [39, 40] (cf. s. 2.4).

Refraction, dispersion and critical angle. The refractive index n of diamond is relatively high and may vary according to the type of diamond. Below are some reference values of n measured at different wavelength λ for type IIa diamonds [41].

The properties of nitrogen-vacancy centres in nanodiamond

$$n = 2.715 \text{ for } \lambda = 226.5 \text{ nm}$$

$$n = 2.437 \text{ for } \lambda = 480.0 \text{ nm}$$

$$n = 2.424 \text{ for } \lambda = 535.8 \text{ nm}$$

$$n = 2.419 \text{ for } \lambda = 578.0 \text{ nm}$$

$$n = 2.410 \text{ for } \lambda = 656.0 \text{ nm}$$

$$n = 2.379 \text{ for } \lambda = 2500 \text{ nm}$$

$$n = 2.375 \text{ for } \lambda = 25000 \text{ nm}$$

Dispersion. Light dispersion in crystal, i.e. the dependence of the refractive index on the wavelength, is typically quite small in the visible region of the electromagnetic spectrum; diamond is an exception with relatively large dispersion. The coefficient of dispersion of a material is determined as the difference between the value of the refractive index in the blue-violet and of that in the red. Diamond has a coefficient of dispersion in the visible of 0.044; it is higher than that of some materials like quartz (0.013) or corundum (0.018), but smaller than that of other crystals like cassiterite (0.071) or rutile (0.330) [42].

Critical Angle. The critical angle is the limiting angle between refracted transmission and reflection of light. It depends on the difference of refractive index of the two materials the light passes through. For diamond in air the critical angle is 24.5° [42].

Reflectance. Reflectance is the amount of light reflected by a transparent material. It depends on the difference in refractive index between two materials and on the angle of observation. Diamond reflects 17% of the light hitting at an angle of 90° and 27% of light hitting at 30° . The two corresponding reflectance numbers for window glass are 4% and 17% [42].

Birefringence. Belonging to the holohedral cubic system diamond should not show birefringence; however the strain due to dislocations, lattice parameter variations, inclusions, fractures or plastic deformations can induce birefringence in diamond [43, 44]. With regard to its stress-birefringence behaviour, the diamond birefringence constant is $3 \times 10^{-13} \text{ Pa}$ [45].

Optical transparency and colour centres. Diamond has a wide band-gap of 5.5 eV corresponding to the deep ultraviolet wavelength of 225 nm. Its measured transmissivity is maximum, about 0.7 (< 1 due to Fresnel reflection losses at the high refractive index diamond-air interfaces), for wavelengths λ such that $225 \text{ nm} < \lambda < 2000 \text{ nm}$ and $\lambda > 6000 \text{ nm}$. The transmissivity drops instead in the window $2000 \text{ nm} < \lambda < 6000 \text{ nm}$ due to the infrared carbon-carbon absorption systems [46]. Moreover, even though diamond should be perfectly transparent, clear and colourless in the visible-light range, $390 \text{ nm} < \lambda < 750 \text{ nm}$, it normally shows different colourations: yellow, brown, blue, green, black, pink, orange, purple and red [42]. The different colours of diamond normally originate from inclusions of foreign atoms with characteristic optical absorptions, but in some cases, for example brown diamonds, the colouration is due to plastic deformations of the diamond crystal lattice [47]. The colour change is just aesthetic. Diamond impurities can significantly alter some of its properties. They can affect its hardness and fracture toughness or change its electrical conductivity as, for instance, for diamonds doped with boron (p-type) or phosphorous (n-type) atoms [16, 48]. Moreover, what is really interesting is the fact that many of these diamond colour centres, are made of atomic inclusions that show unique spin and optical characteristics as is for the case of the nitrogen-vacancy (NV) centre [49, 50], which is the main topic of this work.

Table 2.5 summarises the optical properties of diamond.

Table 2.5 – Optical properties of diamond		
Property	Value	Reference(s)
Refractive index	$n = 2.42\text{-}2.46$ (visible range: $\lambda = 390\text{-}750 \text{ nm}$)	[41]
Coefficient of dispersion	0.044 (visible range: $\lambda = 390\text{-}750 \text{ nm}$)	[42]
Critical angle	24.5°	[42]
Reflectance	17% (hitting light 90°), 27% (hitting light 30°)	[42]
Birefringence constant	$3 \times 10^{-13} \text{ Pa}$	[45]
Optical transmissivity	0.7 for $\lambda = 225\text{-}2000 \text{ nm}$, $\lambda > 6000 \text{ nm}$	[46]

2.2 Defects in diamond

A wide variety of crystallographic defects are known to be hosted in diamond. Recently, considerable efforts have been made to identify and characterize them. The reason for such an interest is that diamond defects disrupt the tetrahedral periodicity of the carbon atoms in the lattice and in some cases are responsible for significant changes in the

diamond properties. When considering the possible technological applications of diamond, these crystallographic imperfections have to be carefully considered because they can play an important role in determining the behaviour and response of the material.

Defects in diamond are generally classified as intrinsic or extrinsic, according to their nature and origin.

2.2.1 Intrinsic and extrinsic defects

Intrinsic defects, also known as lattice irregularities, are made of carbon atoms displaced from their nominal position in the periodic crystalline structure of diamond (Figs. 2.2a, b, c). They can be: i) interstitial carbon atoms or complexes where two or more carbon atoms share a single lattice site [51, 52], ii) vacancies or multi-vacancy complexes consisting of carbon atoms missing from crystallographic sites [47, 53-58], iii) dislocations with broken bonds between atoms of the same index (*shuffle set*) or between layers of atoms of different indexes (*glide set*) [59], iv) platelets of regular arrays of carbon interstitials [60-62], and v) voidities made of nanometre-sized carbon clusters [63, 64]. Intrinsic defects can be found in natural diamond; they can also be artificially produced or enhanced through irradiation with high-energy particles.

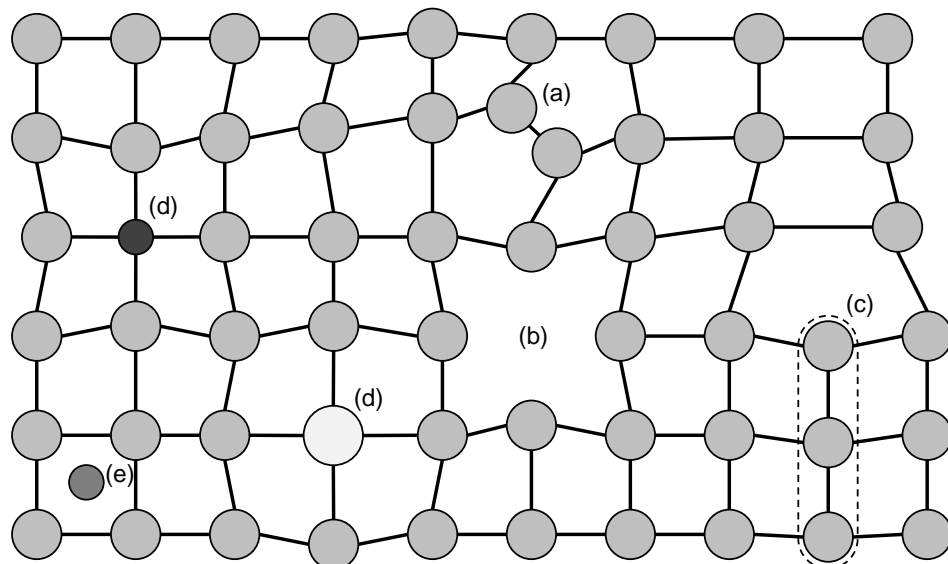


Figure 2.2. Two-dimension schematic of some point defects (a, b, d, e) and linear defects (c) in diamond. **a)** Self-interstitial carbon atom. **b)** Vacancy. **c)** Edge dislocation, with extra net plane. **d)** Foreign substitutional atoms, e.g. N, P, B. **e)** Foreign interstitial atom, e.g. Li.

Extrinsic defects are mostly made of substitutional and interstitial impurities of foreign elements embedded in the carbon matrix (Figs. 2.2d, e). They are present in diamond as isolated atoms or organized in small atomic clusters and as per the intrinsic ones they can be found naturally dispersed in diamond or artificially introduced in the structure, for example by ion-implantation or by addition during the diamond growth processes.

More than 150 vibrational and more than 500 electronic optical centres have been detected in diamond within the spectral range from 20 μm to 0.17 μm . Many impurities of foreign elements are known to form optically active defects in diamond including: H, He, Li, B, N, O, Ne, P, Si, As, Ti, Cr, Ni, Co, Zn, Zr, Ag, W, Xe and Tl [33, 65, 66].

2.2.2 Nitrogen-related defects

Over the hundreds of types of luminescent extrinsic impurities that can form in diamond, the nitrogen-related ones deserve special attention. The reason: nitrogen is the most common impurity to occur in diamond and is responsible for a large number of impurity-related centres which possess unique optical and spin properties interesting for technological applications.

Nitrogen as a diamond impurity was first identified in 1959 by W. Kaiser and W. L. Bond of Bell Telephone Laboratories [67]. A few years before, in 1934 R. Robertson et al. [68] reported striking differences in the optical and photoconductive properties of diamonds. They classified diamonds into type I and type II, according to their differences in ultraviolet and infrared transmission. The rarer type II crystals exhibit absorption bands between 3 μm and 6 μm and a strong absorption edge in the ultraviolet below 225 nm. Type I crystals show additional absorption bands between 6 μm and 13 μm and a tail on the absorption edge at 225 nm. The origin of the additional absorption in type I diamonds has been the subject of considerable speculation. Spectrographic and neutron activation techniques revealed concentrations $\sim 10^{18}$ impurity atoms per cm^3 of aluminium, calcium, silicon, and several other elements in diamond. They were firstly addressed as the main cause for the difference between types I and II crystals, but the fact that they could be found in both types of diamonds in similar quantities caused this hypothesis to be abandoned. Interstitial carbon atoms, carbon vacancies, or clusters of vacancies and cavities were also considered, but again the artificial creation of these structures by bombarding diamonds with fast electrons, neutrons, deuterons, and γ -rays did not reveal

a direct connection between these intrinsic defects and the infrared absorption between 6 μm and 13 μm characteristic of type I crystals. It was only in 1959 that W. Kaiser and W. L. Bond showed experimentally that the nitrogen content was responsible for the infrared absorption around 8 μm and for the ultraviolet absorption below 400 nm. They also observed that different concentrations of nitrogen could influence some diamond properties such as photoconductivity, thermal conductivity, and birefringence.

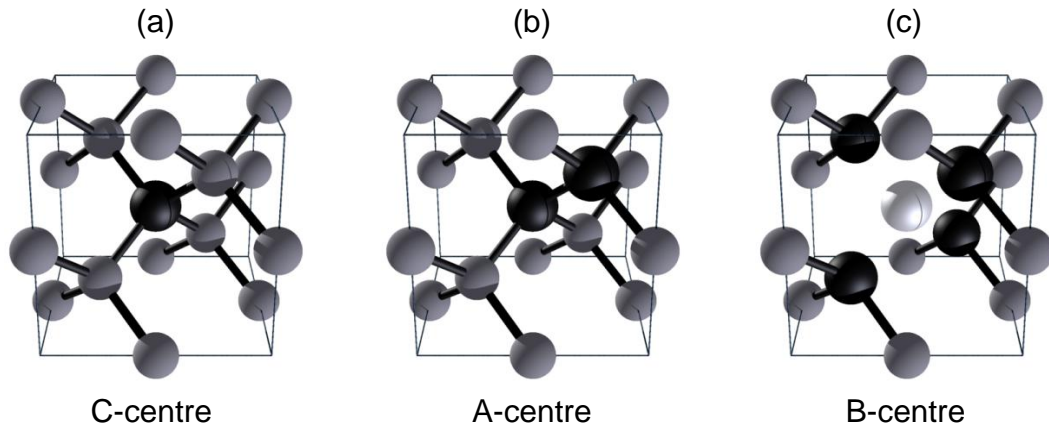


Figure 2.3. Structure of some nitrogen-related defects in diamond. **a)** C-centre. **b)** A-centre. **c)** B-centre. Nitrogen atoms are shown in black, carbon atoms in grey, and vacancies in white with no bonds (black sticks) indicated.

Nitrogen can form various complexes in diamond. It can exist as single substitutional impurities, called C-centres, or in aggregated structures, called A-centres and B-centres (Fig. 2.3). Nitrogen complexes can also coexist in combination with other defects like platelets and voidites. Apart from voidites, which can be observed via transmission electron microscopy (TEM) [63], all the other aggregates have characteristic optical spectroscopy signatures.

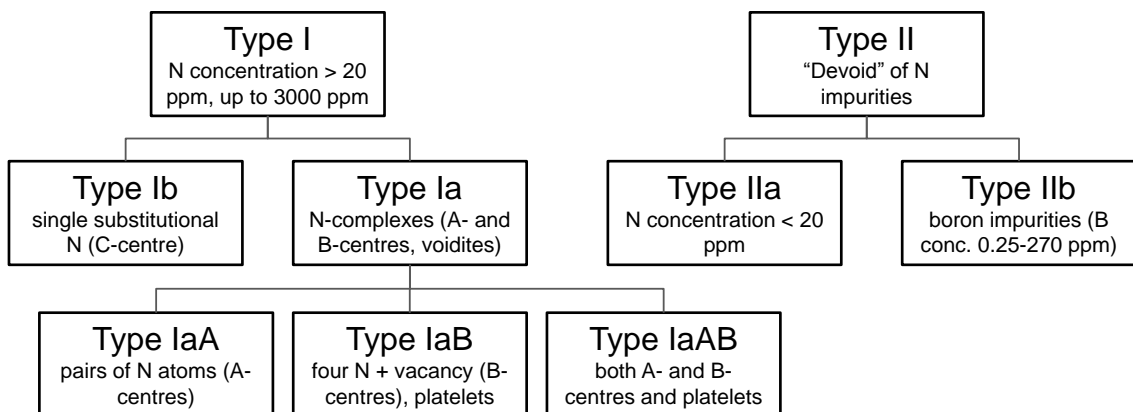


Figure 2.4. Schematic representation of the different types of diamond.

Diamonds containing mainly C-centre defects are classified as type Ib (N concentration up to 500 ppm, 0.05%), while diamonds containing mainly A-centres and B-centres are classified respectively as type IaA and type IaB (N concentration up to 3000 ppm, 0.3%). When A and B aggregates occur in similar concentrations, diamonds are generally identified as type IaAB. Type IIa diamonds are almost devoid of impurities (N concentration < 20 ppm, 0.002%). Type IIb diamonds are characterised by the presence of boron impurities (B concentration ~ 0.25 ppm, 0.000025%, in natural diamonds and up to 270 ppm, 0.027%, in doped synthetic diamonds) (Fig. 2.4).

C-centre. The C-centre defect consists of a single substitutional nitrogen atom, neutral or positively charged, in the diamond lattice (Figs. 2.3a and 2.5a, b). The nitrogen atom forming the C-centre alters the properties of diamond local to the centre.

- The neutral nitrogen defect does not possess the diamond tetrahedral (C_{3v}) symmetry. It undergoes a trigonal distortion with the nitrogen and one of the carbon atoms moving away from each other along the [111] direction (Fig. 2.5b). The estimated length of the nitrogen-carbon bond for the C-centre is about 1.92 Å, which is longer than the nearest-neighbour distance of 1.54 Å between carbon atoms in diamond [69].
- The centre has an identifiable infrared local mode of vibration at 1344 cm^{-1} [70].
- Because the nitrogen atom has five available electrons (one more than the carbon atom it replaces), it acts as a deep donor, forming a donor energy level within the diamond band gap, 1.7 eV below the conduction band edge [69].
- The C-centre shows an electron paramagnetic resonance (EPR) signal called P1 [71]. This signal identifies the C-centre to be an electron paramagnetic system with electron spin angular momentum $S = 1/2$ in the ground state [72].
- The C-centre is responsible for the yellow/brown colouration of diamonds [42].

A-centre. The A-centre defect consists of a nearest-neighbour pair of nitrogen atoms substituting for the carbon atoms (Figs. 2.3b and 2.5c, d).

- The nitrogen-nitrogen bond length is estimated to be 2.14 Å [73].
- The A-centre gives vibrational resonances at 1282, 1203, 1093, and 480 cm^{-1} [72].
- The A-centre does not cause discoloration on its own [74].

B-centre. The B-centre defect consists of four nitrogen atoms surrounding a vacancy (Fig. 2.3c).

- The nitrogen-carbon bond length in this structure is estimated to be 1.49 Å [73].
- The defect, sometimes indicated as VN_4 , gives vibrational bands at 1332, 1171, 1093, 1003 and 780 cm^{-1} [73].
- The B-centre defect does not cause discoloration on its own [74].

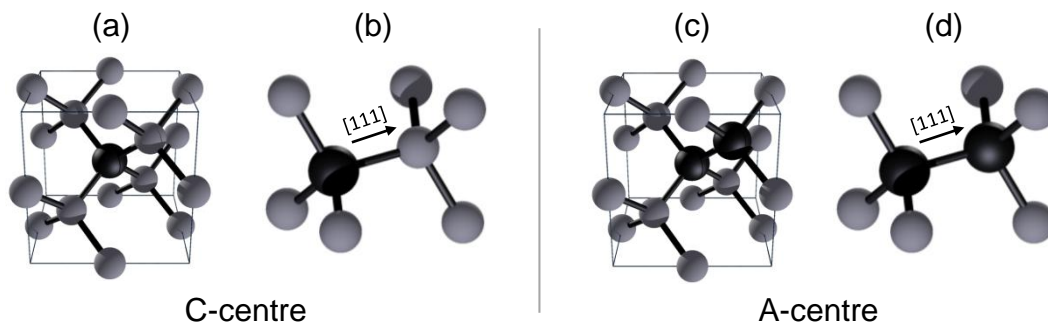


Figure 2.5. Structure of C-centre and A-centre in diamond. **a)** C-centre in the diamond lattice. **b)** Side view of the C-centre. **c)** A-centre in the diamond lattice. **d)** Side view of the A-centre. The crystallographic direction [111] is highlighted in (b) and (d). Nitrogen atoms are indicated in black and carbon atoms in grey. Local to the centre the diamond tetrahedral structure is lost, with the dilation of the nitrogen-carbon bond along the [111] direction, leading to a trigonal symmetry.

Platelets. Platelets are planar defects in the $\langle 100 \rangle$ lattice planes and can coexist with nitrogen complexes [61, 75, 76].

- Platelets generally possess a length scale of the order of 10-100 nm, but some can extend to the range 1-10 μm [75].
- They show a characteristic absorption peak at 328 cm^{-1} and an infrared absorption band with a maximum between 1358 cm^{-1} and 1373 cm^{-1} labelled B' [61, 73].
- Platelets do not affect diamond colour [74].

Other nitrogen-vacancy complexes. Other complexes made up of nitrogen and vacancies can be found in diamond. They are shown in figure 2.6.

- VN_2 or H3 centre. It has absorption with zero phonon line, i.e. pure electronic transition with no phonons involved, at 2.463 eV. It belongs to point group C_{2v} [33, 65, 77].
- V_2N_4 or H4 centre. It has absorption with zero phonon line at 2.498 eV. It belongs to point group C_{1h} [33, 65, 73, 77-79].

- VN₃ or N₃ centre. It has absorption with zero phonon line at 2.985 eV. It belongs to point group C_{3v} [33, 61, 65].
- VN₁ centre. It has absorption with zero phonon line at 1.945 eV. It belongs to point group C_{3v} [33, 65, 77].

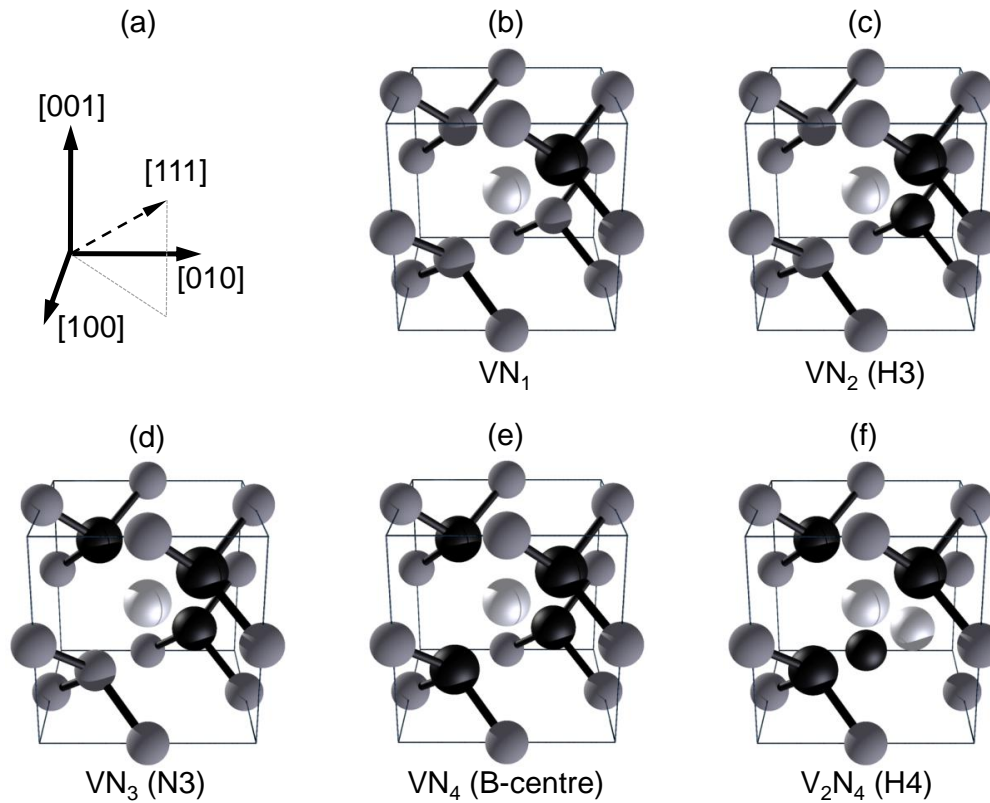


Figure 2.6. Schematic structure of nitrogen-vacancy complexes in diamond. **a)** Diamond unitary cell crystallographic axes. **b)** VN₁ defect. **c)** VN₂ (H3) defect. **d)** VN₃ (N3) defect. **e)** VN₄ (B-centre) defect. **f)** V₂N₄ (H4) defect. Nitrogen atoms are shown in black, carbon atoms in grey, and vacancies in white with no bonds (black sticks) indicated.

Table 2.6 summarises the most extensively studied peaks in the absorption spectrum of diamond due to defects, aggregates and impurity atoms.

Table 2.6 – Nomenclature for defect-related systems in diamond			
Designation	Significance	Range	Reference(s)
N	Natural diamond	N1 (1.50 eV) to N9 (5.26 eV)	[65]
GR	General radiation (induced in diamonds by irradiation)	GR1 (1.67 eV) to GR8 (3.00 eV)*	[65]
R	Radiation (masked in type Ia diamond by the secondary absorption edge)	R9 (3.04 eV) to R11 (3.99 eV) [†]	[65]
TR	Type II radiation (not observed in type I diamond)	TR12 (2.64 eV) to TR17 (2.83 eV)	[65]
H	Heat treatment (preceded by irradiation)	H1 (0.18 eV) to H18 (3.56 eV)	[65]

* = GR1 to GR8 is the most extensively studied system: these peaks are caused by neutral vacancies.

[†] = R10 is more frequently called ND1.

Table 2.7 is relevant to the vacancy-related and nitrogen-related defects. The peaks in the absorption spectrum are normally designated by letters.

Table 2.7 – Vacancy-related and nitrogen-related defects in diamond			
Designation	Type of defect	Zero phonon line (77K)	Reference(s)
GR1	Neutral vacancy (V^0)	741.1 nm / 1.673 eV	[33, 65, 77]
ND1 (R10)	Negative vacancy (V^-)	393.6 nm / 3.150 eV	[33, 65, 77]
H3	Vacancy and two nitrogens (VN_2)	503.2 nm / 2.463 eV	[33, 65, 77]
H4	Two vacancies and four nitrogens (V_2N_4)	496.2 nm / 2.498 eV	[33, 65, 77]
N3	Vacancy and three nitrogens (VN_3)	415.3 nm / 2.985 eV	[33, 61, 65]
NV	Vacancy plus single nitrogen (VN_1)	637.3 nm / 1.945 eV	[33, 65, 77]

2.2.3 Nitrogen-vacancy (NV) centre

Within all the structures that nitrogen can form in diamond, probably the most studied is the VN_1 structure (Fig. 2.6b). Generally addressed as the nitrogen-vacancy (NV) centre or simply NV, this diamond defect has been the subject of intense study in the recent past. The NV possesses unique room-temperature optical and spin properties which make it a fascinating object for practical applications in many fields of research. Promising possibilities include using the NV centre in quantum information technology and quantum cryptography, in nanomedicine and biotechnology and in high-resolution magnetometry (cf. ss. 2.4.1-3).

Structure. The nitrogen-vacancy (NV) centre is an extrinsic diamond crystallographic defect incorporated in the tetrahedral diamond structure of four carbon atoms where two adjacent sites are altered: one carbon atom replaced by a nitrogen atom and the other replaced by a vacant space (vacancy). The defect has a trigonal symmetry of point group C_{3v} where the C_3 principal axis is along the NV pair in the crystallographic [111] direction (Fig. 2.7a).

Being in group V of the periodic table, nitrogen has five valence electrons. In the NV complex, three of the nitrogen valence electrons are shared with the three nearest-neighbour carbon atoms, and the last two occupy the dangling bond in the direction of the vacancy. Looking at the vacancy, there are five unsatisfied active bonding electrons that belong to the dangling bonds of the atoms adjacent to the vacancy itself, two from the nitrogen and three from the surrounding carbons. Each of the three carbon atoms has

nominally four sp^3 symmetry bonds: one dangling bond near the vacancy and three back bonds pointing to the other carbons of the lattice. Similarly, the nitrogen atom has one dangling bond pointing to the vacancy and three back bonds pointing to other carbons of the lattice [80]. For the carbon, the sp^3 hybridisation is not complete: the orbital is 90% p -character and 10% s -character, against the general 75% p -character and 25% s -character of the fully hybridised tetrahedral sp^3 orbital. For nitrogen the ratio of p to s orbitals is almost the same ($p/s = 1.2$), while for carbon the p orbital dominates ($p/s = 9.8$). It has been estimated that in the NV complex $\sim 72\%$ of the charge density is at the three nearest-neighbour carbon atoms surrounding the vacancy, only $\sim 0.2\%$ is at the nitrogen and approximately $\sim 28\%$ is spread over the lattice [80, 81]. This means that, in a naïve view, the electrons spend most of their time in the dangling bonds on the three carbon atoms neighbouring the vacancy.

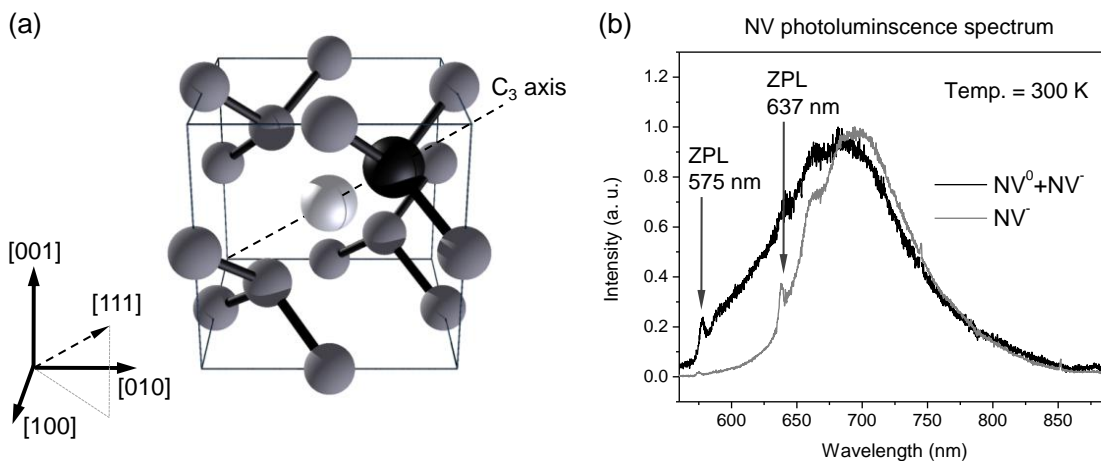


Figure 2.7. NV centre crystallographic structure and photoluminescence spectrum. **a)** The NV centre has a trigonal symmetry of point group C_{3v} , where the C_3 principal axis of symmetry is along the nitrogen-vacancy pair in the crystallographic [111] direction. The nitrogen atom is shown in black, carbon atoms are in grey, and the vacancy in white with no bonds (black sticks) indicated **b)** Photoluminescence spectra at room temperature of an NV^- centre (grey) and of $NV^0 + NV^-$ (black). The zero phonon lines (ZPL) at 575 nm (2156 eV) for the NV^0 and at 637 nm (1.945 eV) for the NV^- are indicated (arrows); they are accompanied by vibronic side bands at lower energies (longer wavelengths).

Charge state. The nitrogen-vacancy centre exists in diamond in two charge states. The charge state of the defect depends mainly on its local lattice environment: the presence of close surrounding impurities acting as electron acceptors or donors causes the NV to be either in its neutral state NV^0 or in its negatively charged state NV^- [82, 83]. In the case of the NV^- it is assumed that the neutral NV^0 defect, with five electrons occupying the

dangling bonds in the neighbourhood of the vacancy complex, acquires an additional sixth electron from elsewhere in the lattice, for instance from another nitrogen atom acting as a donor [82]:



The ground state of the neutrally charged NV^0 has an electron spin angular momentum $S = 1/2$, while electron paramagnetic resonance (EPR) measurements show that the negatively charged NV^- has a ground state with electron spin angular momentum $S = 1$ (triplet) [71]. This is compatible with having respectively an uneven (five for the NV^0) and even (six for the NV^-) number of electrons surrounding the vacancy in the NV complex.

Being the NV charge state a local effect depending on the presence of nearby electron donors or acceptors, NV^0 and NV^- can be found coexisting in the same diamond [83]. It has also been observed that the same NV defect can undergo photochromic switching between the two charge states. Two mechanisms can induce this photoconversion: directly, the ionisation of a negatively charged NV^- or, indirectly, the ionisation of the substitutional donors-nitrogen surrounding the NV centre in the crystal [84, 85]. The two charge states of the NV can be clearly identified spectrally due to their different and characteristic optical transition [33].

The NV^- has a strong optical transition with a zero phonon line (ZPL), i.e. the pure electronic transition, at 637 nm (1.945 eV) (Fig. 2.7b). Uniaxial strength measurements show that the zero phonon line is associated with an electric dipole transition between isolated states of spatial symmetry ${}^3\text{A}_2$ (ground state) and ${}^3\text{E}$ (excited state) at a site of trigonal symmetry [86, 87]. The transition is also accompanied by a vibronic side band to high energy in absorption and to low energy in emission. Absorption and emission do not show the same vibronic band: in absorption the first feature of the vibronic sideband gives a double peak, whereas in emission it gives only a single peak. This spectral difference has been early explained with the tunnelling of the nitrogen atom being able to interchange positions with the vacancy in the NV centre [86]. Recently, this idea has been disputed. Ab initio calculations show that the nitrogen strongly binds with the three neighbouring carbon atoms: the tunnelling of the nitrogen would require too much energy (> 4 eV) to make this mechanism likely. An alternative proposal considers the Jahn-Teller effect for the excited state of the NV centre [88]. The Jahn-Teller effect is a geometrical distortion

which occurs in non-linear molecules. It takes the form of the elongation or shortening of certain chemical bonds, since the removal of orbital and electronic degeneracies lowers the total energy of the complex, for instance by reducing the electrostatic repulsion amongst electrons [89]. In the case of the NV centre, the excited state would undergo a Jahn-Teller splitting: two local modes a_1 and e would couple in the vibration band of absorption giving rise to the observed double peak, whereas only the a_1 local mode would couple in the vibration band of emission with a corresponding single spectral peak [90].

The NV⁰ shows a zero phonon line (ZPL) at 575 nm (2.156 eV) corresponding to a transition between the ground state of spatial symmetry 2E and the excited state of symmetry 2A_1 (Fig. 2.7b) [91, 92].

Energy level scheme. Considerable efforts have been made to shed light on an intriguing aspect of the NV centre: its electronic structure. Here, we focus on the negatively charged state of the centre, since it turns out to be the more interesting in terms of spin, magnetic and optical properties.

A detailed description of the NV⁻ energy level scheme based both on experimental and theoretical considerations has recently been given [93-95]. The model assumes that the NV⁻ can be treated as a six-electron system with two unoccupied orbits (i.e. holes) to account for the fact that eight electrons would be required to form a closed shell. In this perspective, symmetry considerations enable assignment of specific level states for the NV⁻: ${}^3A_2(e^2)$, ${}^1A_1(e^2)$, ${}^1E(e^2)$, ${}^3E(a_1, e)$ and ${}^1E(a_1, e)$.

The dangling bonds surrounding the vacancy complex are formed from the sp^3 orbitals of the adjacent three carbons and by the orbital of the adjacent nitrogen pointing to the vacancy. If the vacancy was surrounded by four carbon atoms, the symmetry point group would be the tetrahedral T_d (instead of the C_{3v} which the NV centre belongs to) with a_1 and t_2 molecular orbitals of A_1 and T_2 symmetry respectively. From symmetry and charge overlap considerations the a_1 is considered to be lower in energy and the t_2 higher; therefore with six electrons, the lowest energy configuration would be the $a_1^2t_2^4$, with the holes in the configuration t_2^2 , meaning that the two electron-holes “occupy” the t_2 free orbitals. However, when one of the carbons surrounding the vacancy is substituted by a nitrogen atom, an NV centre is formed: the tetrahedral T_d symmetry is lowered to the

trigonal one and the t_2 orbitals are split to give, in C_{3v} notation, a_1 and e symmetry orbitals. This means that when a nitrogen substitutes a carbon around the vacancy the unoccupied-hole orbitals t_2^2 -system becomes a ea_1 -system, whose possible configurations for the electron-holes ordered by ascending energies are e^2 , ea_1 and a_1^2 . Figure 2.8 shows schematically the energy levels of the NV⁻ centre in C_{3v} symmetry.

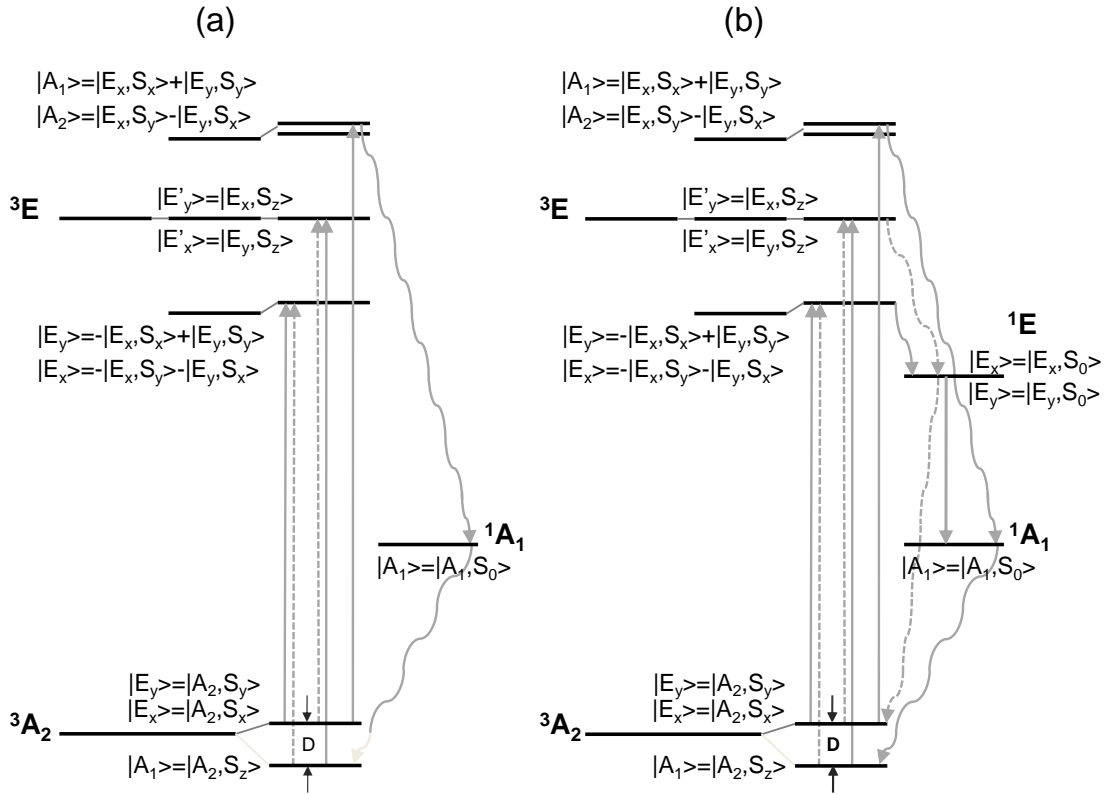


Figure 2.8. Energy level scheme for the NV⁻ centre (adapted from [94]). **a)** Model with one intermediate singlet level 1A_1 . **b)** Model with two singlet intermediate levels 1E and 1A_1 . For both models the 3E splitting is due to spin-orbit and spin-spin interactions; “D” is the zero field ground state splitting due to spin interaction. Irreducible representations of states are indicated as well as symmetric form of the wave-functions. Solid straight lines indicate spin-allowed optical transitions; solid wavy lines indicate intersystem crossing allowed by spin-orbit interaction; dashed lines indicate weak transitions which are allowed through the mixing of the $(^3E)E$ and $(^3E)E'$ states by transverse-non-axial spin-orbit interaction.

[Note about the notation. The capital letters, possibly with the subscript on the bottom right, “ A_1 ”, “ A_2 ” and “ E ” are the relevant symmetries for the C_{3v} point group, which the NV centre belongs to. Specifically, the symmetry elements of the C_{3v} point group are $(E, 2C_3, 3\sigma_v)$ for which $A_1 = (1, 1, 1)$, $A_2 = (1, 1, -1)$ and $E = (2, -1, 0)$, where within the parenthesis the character operations are specified. The singlet and the triplet nature of the states are respectively indicated by the superscript “1” and “3” on the top left of the capital letter. Finally, the small italic letters within the parenthesis, possibly followed by a

subscript, “ e ” and “ a_1 ” are the name of the molecular orbitals; their relevant superscripts indicate the electrons occupation].

The ground state of the centre is the ${}^3A_2(e^2)$, while the first optically excited state is the ${}^3E(a_1, e)$; they are both triplet and they are both manifold degenerate in energy [96-106]. The separation in energy between the ground and the first excited state is known, 1.945 eV, corresponding to the optical transition with the zero phonon line at 637 nm.

In the energy range between the triplet ground and excited states there are two singlet intermediate levels 1A_1 and 1E . This deserves special attention since it is an intense object of debate in the community.

The triplet ground 3A_2 state of the NV^- is virtually spin degenerate; however spin-spin interactions lift the degeneracy and split the ground state itself into a singlet $|A_1\rangle = |A_2, S_z\rangle$ with symmetry A_1 , and a doublet $|E_x\rangle = |A_2, S_x\rangle$, $|E_y\rangle = |A_2, S_y\rangle$ with symmetry E . Spin-orbit and spin-spin interactions do not give any mixing of the axial S_z and transverse S_x , S_y spin states meaning that the axial or transverse spin projection can be considered a good quantum number. The ground spin splitting between the singlet $|A_1\rangle = |A_2, S_z\rangle$ and the doublet $|E_x\rangle = |A_2, S_x\rangle$, $|E_y\rangle = |A_2, S_y\rangle$ is $D = 2.88$ GHz. It is generally called “zero field splitting”, because it exists without any applied external field. The two ground sublevels $|E_x\rangle = |A_2, S_x\rangle$ and $|E_y\rangle = |A_2, S_y\rangle$ are, in principle, degenerate in energy (parameter $E = 0$ MHz) because the trigonal symmetry of the centre along the nitrogen-vacancy z -axis makes any state with projection along the x and y directions spatially indistinguishable. However, it has been found that at room temperature or for ensembles of NV centres, the local axial symmetry could be lost and the degeneracy is lifted. Values for the E parameter have been measured to be: $E = (2 \pm 0.4)$ MHz for a single NV centre at 300 K, $E = 7.5$ MHz for ensembles of NV centres at 1.5 K and $E = (7 \pm 0.1)$ MHz for ensembles of NV centres at 300 K [36].

The 3E excited state of the NV^- is affected by both the spin-orbit and the spin-spin interactions. The spin-orbit interaction splits the 3E level into the three twofold degenerate states E , E' and (A_1, A_2) -pair. The twofold degenerate states for E are $|E_x\rangle = -|E_x, S_y\rangle - |E_y, S_x\rangle$ and $|E_y\rangle = -|E_x, S_x\rangle + |E_y, S_y\rangle$, the twofold degenerate states for E' are $|E'_x\rangle = |E_y, S_z\rangle$

and $|E'_y\rangle = |E_x, S_z\rangle$ and the twofold degenerate states for the pair (A_1 , A_2) are $|A_2\rangle = |E_x, S_y\rangle - |E_y, S_x\rangle$ and $|A_1\rangle = |E_x, S_x\rangle + |E_y, S_y\rangle$ (Fig. 2.8). The presence of the nitrogen substituting one carbon atom in the adamantane lattice lowers the symmetry of the system from tetrahedral to trigonal: in this last lowered symmetry the states with S_z spin projection are not mixed with the states with S_x and S_y spin projections. Recently, the fine structure of the NV^- excited state has been probed experimentally; pulsed optically detected magnetic resonance measurements revealed the occurrence of spin transitions in the emitting 3E excited state [107].

At intermediate energies between the ground (3A_2) and the excited (3E) state, the energy level structure of the NV^- centre is still object of debate since the theoretical, computational and experimental data do not always fully agree. Two singlet intermediate levels 1A_1 and 1E have been identified. Experimental data and symmetry considerations place 1E close in energy to the 3E excited state and 1A_1 close to the 3A_2 ground state [94, 108]. However computational calculations contradict this assignment: some of the performed local density calculations in fact, give a reverse position of the intermediate singlet level by putting the 1A_1 closer in energy to the 3E excited state and the 1E just above the 3A_2 ground state [109, 110].

The main disagreement surrounds a specific property shown by the NV^- centre: its optical polarisability, which consists in the fact that optical excitation preferentially populates the $|A_1\rangle = |A_2, S_z\rangle$ ground state of the centre. In other words, optical pumping causes a non-Boltzmann steady-state spin alignment of the NV^- centre in the ground state, consisting in a re-orientation of the ground state spins.

Optical transitions are spin conserving; therefore, transitions from the ground to the excited state via optical pumping and, vice versa, radiative decays from the excited to the ground states are expected to take place between sublevels with the same spin projection, i.e. $|S_{x,y}\rangle \rightarrow |S_{x,y}\rangle$ and $|S_z\rangle \rightarrow |S_z\rangle$, and with the same strength (Fig. 2.8, solid arrows). However, the fact that after few optical cycles the NV^- centre is found polarised in the ground S_z spin state suggests that there must be other non-spin conservative decay channels that account for system relaxation of the type $|S_{x,y}\rangle \rightarrow |S_z\rangle$. Throughout the literature the problem is commonly tackled using a simplified energy level scheme of the NV^- centre which assumes the presence of only one 1A_1 singlet level located between the

triplet ground and excited energy levels (cf. s. 3.3.1). This scheme is a simplification, but it is accurate enough to describe the dynamics of the system and its properties. The 1A_1 level opens a non-radiative path so that the system from the A_1 spin-orbit component of the 3E optically excited state can access the E component of the ground state level with S_z spin projection relaxing non-radiatively via 1A_1 (Fig. 2.8a). Such a non-radiative decay is not spin conserving and occurs between states sharing the same symmetry (i.e., using the C_{3v} point group notation, $A_1 \rightsquigarrow A_1$, $A_2 \rightsquigarrow A_2$ and $E \rightsquigarrow E$). This spin polarization, due to the optical excitation, together with the non-radiative decay has been demonstrated through electron paramagnetic resonant (EPR) spectroscopy measurements [71, 111, 112].

Once the system is spin polarized in the ground state $|A_1\rangle = |A_2, S_z\rangle$ with spin projection S_z , the optical emission of the NV^- is expected to increase. This happens because from the polarized ground state $|A_1\rangle = |A_2, S_z\rangle$ the system can only reach, through optical excitation (which is spin conserving), the E' two-manifold sublevels $|E'_x\rangle = |E_y, S_z\rangle$ and $|E'_y\rangle = |E_x, S_z\rangle$ having its same spin projection S_z , and from there decay radiatively (again, conserving the spin) towards the same ground state $|A_1\rangle = |A_2, S_z\rangle$. In the polarised NV centre, the non-radiative decay is symmetry forbidden, being the excited sublevels $|E'_x\rangle = |E_y, S_z\rangle$ and $|E'_y\rangle = |E_x, S_z\rangle$ of a different symmetry than the intermediate $|A_1\rangle = |A_1, S_0\rangle$. The increased emission for the polarized system has been observed and reported to be 14%, confirming the appropriateness of the model [93]. The proportion of increased fluorescence provides two interesting facts. First, before polarisation of the system, about 14% of the whole excited population decays non-radiatively. This value gives an estimation of the inter-system crossing rate for the excited states with spin projection $|S_x\rangle$ and $|S_y\rangle$. Note that 14% is very close to the proportion 1 : 6 and supports the model of the three twofold (i.e. six) degenerate levels scheme for the excited state 3E with the intersystem crossing involving mainly, for symmetry reasons, the $|A_1\rangle = |E_x, S_x\rangle + |E_y, S_y\rangle$ sublevel (Fig. 2.8a), consistently with the finding of N. Manson et al. [94]. Second, being 14% close to the proportion 1 : 6, it could be argued that for the excited state $|A_1\rangle = |E_x, S_x\rangle + |E_y, S_y\rangle$ the non-radiative triplet-singlet intersystem crossing decay through the intermediate singlet state $|A_1\rangle = |A_1, S_0\rangle$ is favoured over the allowed triplet-triplet direct radiative decay to the ground state; if the two decaying processes were equally probable in fact, the percentage would be approximately 7%, i.e. half of 14%.

Assuming that what is shown about the polarisation is correct, after the system is polarized all the population is expected to cycle radiatively between the ground state $|A_1\rangle = |A_2, S_z\rangle$ and the E' two manifold sublevels $|E'_x\rangle = |E_y, S_z\rangle$ and $|E'_y\rangle = |E_x, S_z\rangle$: the spin polarization of the system in the ground state $|A_1\rangle = |A_2, S_z\rangle$ would be 100% and there would not be any non-radiative decay. Electron paramagnetic resonant (EPR) spectroscopy measurements, however, reveal that the actual spin polarization is about 80% [111]. The reason for this is that the spin-orbit interaction causes a mixing of the states E and E': these states have different S_z and S_x, S_y spin projections and hence, the mixing gives rise to optical transitions that do not conserve the spin. These transitions have been observed in hole-burning spectra experiments and turn out to limit the degree of spin polarization [96-98, 113-116].

Carbon and nitrogen have low atomic number and a small spin-orbit coupling parameter of 28 cm^{-1} [94]. As a consequence, the intersystem crossing is expected to be weak, whereas in fact it is of the same order of the other spin radiative transitions (which, considering the sixfold degeneracy, are five each with probability 1 : 6, very close to 14% of the non-radiative one). To account for the high efficiency of the non-radiative singlet to triplet decay, the simplified NV⁻ energy level scheme needs to be refined. It can be considered that in addition to the intermediate 1A_1 level there is another singlet level 1E lying close in energy to the 3E state while 1A_1 is close to the ground 3A_2 state. Assuming that the energy between 3E and 1E and between 1A_1 and 3A_2 are close enough, a fast resonant transfer, perhaps involving a phonon mode is possible between each couple of levels, justifying the fast singlet to triplet non-radiative decay. However, this is where some of the incongruities in the literature become apparent. Non-radiative decay is allowed between states of same symmetry and this point is crucial to understand the relative energy position of the intermediate singlet 1E and 1A_1 levels. Looking at the intermediate 1E level, the only non-radiative symmetry allowed relaxation from the excited state is the one from the twofold degenerate sublevels E and E' towards the intermediate singlet 1E and then towards the (3A_2)E component of the ground state (i.e. towards $|E_x\rangle = |A_2, S_x\rangle$ and $|E_y\rangle = |A_2, S_y\rangle$). Instead, looking at the intermediate 1A_1 level, the only non-radiative symmetry allowed relaxation is the one from the $|A_1\rangle = |E_x, S_x\rangle + |E_y, S_y\rangle$ level of the pair (A_1, A_2) towards the intermediate singlet 1A_1 and then towards the (3A_2) A_1 component of the ground state (i.e. towards $|A_1\rangle = |A_2, S_z\rangle$). The problem is that

looking at the non-radiative path involving the intermediate singlet level 1E , the final sublevels of the ground state reached after a cycle have S_x and S_y spin projection which is in contrast with the experimentally observed optical polarisation in the ground state (3A_2) A_1 component whose spin projection is S_z ($|A_1\rangle = |A_2, S_z\rangle$ state). This suggests that the intermediate 1E level should be actually located at a higher energy than the 1A_1 , to account for the observed polarisation of the system. In fact, by locating 1E above 1A_1 it is possible to figure a radiative decay (independent from the symmetry of the states) from 1E to 1A_1 followed by the non-radiative relaxation from 1A_1 to the ground (3A_2) A_1 component with spin projection S_z . Experimental measurements of the radiative transition $^1E \rightarrow ^1A_1$ (1042 nm) have been reported: the nature of the states 1E and 1A_1 between which it occurs has been predicted from symmetry considerations [108]. Based on density functional theory (DFT) other authors calculate an inverted position for the singlet levels with the 1E located at a lower energy, 0.44 eV [109] or 0.48 eV [110] from the 3A_2 ground state, and the 1A_1 placed at a higher energy, 1.67 eV [109] or 2.03 eV [110] from the 3A_2 ground state. If that is the case, different mechanisms like coupling to non-symmetric phonons [86], strain or electron-phonon terms beyond the Born-Oppenheimer approximation, have to be considered to account for the experimentally observed polarisation of the NV⁻ centre.

2.3 Synthesis of diamond

You will not believe me even when I tell you, so it is fairly safe to tell you. And it will be a comfort to tell someone. I really have a big business in hand, a very big business. But there are troubles just now. The fact is... I make diamonds.

It was 1911 when these words appeared in the science fiction story “The Diamond Maker” by the English author H. G. Wells [117]. At that time, man-made diamonds were just that: science fiction.

Due to its astonishing properties (cf. ss. 2.1.1-5), it is no surprise that over the last two centuries many scientists and businessmen have pursued the dream of synthesising artificial diamond. Before that, however, it had to be discovered that diamond was composed entirely of carbon, while being uniquely different from the other common forms carbon can assume, such as graphite or charcoal. The very first documented study

of the composition of diamond appears to have been done by two Italian scientists, G. Averani and C. Targioni, at the Accademia del Cimento in Florence. In 1694, nineteen years after Sir I. Newton proposed the idea that diamond was combustible, the two Italian scientists succeeded in incinerating diamond, but could not trap or identify the product gases. Almost a hundred years later, in 1772, A. Lavoisier conducted an experiment to show that diamond and charcoal were chemically alike. He burnt about 150 mg of diamond in a sealed container and determined that the product gas was simply carbon dioxide (CO₂). He then measured that the very same amount of carbon dioxide was produced when 150 mg of amorphous carbon in the form of charcoal were burnt. Lavoisier was however reluctant to publicise such a striking and at first counterintuitive result. Only twenty-five years later, in 1797, the English chemist S. Tennant performed further combustion experiments and then concluded that diamond “*consists entirely of charcoal, differing from the usual state of that substance only by its crystallised form*” [118]. The significance of this discovery could be understood only by taking into account the context of the time. In fact, Lavoisier’s finding preceded J. Dalton’s atomistic theory stating that all matter consists of the same indivisible atoms, by almost thirty years and D. Mendeleev’s formulation of the periodic table by almost a hundred years.

The discovery that diamond is purely made of carbon fuelled the quest to artificially synthesize it. Over the following hundred and fifty years, at least thirty claims of success were proclaimed. The most famous were probably those reported by J. B. Hannay in 1879 [119] and by F. F. H. Moissan in 1893 [120].

In 1867 a deposit of natural diamonds of volcanic origin was found in South Africa. The volcanic origin suggested that natural diamonds are probably generated under geologic conditions of high pressure and high temperature and that reproducing such conditions would allow manufacturing artificial diamonds in a laboratory.

Moissan’s idea was to dissolve carbon in molten iron using an electric arc furnace capable of reaching temperatures around 3000 °C and to rapidly quench the iron in water. He believed that the solidification of the iron from the outside would exert high pressure on the still-liquid carbon trapped in the core causing this to crystallise in the form of diamond. Although few crystals were created during the process, further experiments

showed that Moissan was not actually able to synthesise diamond but silicon carbide (SiC) named, after him, moissanite.

More than ten years before, Hannay tried to synthesise diamond by heating a mixture of bone oil, paraffin and lithium in sealed iron tubes. The heating of the paraffin releases carbon, the raw matter to create diamond, and hydrogen, necessary to build up the pressure in the tube, as products. Hannay's experiments were particularly hazardous; in several occasions the iron tubes exploded and the furnace had to be rebuilt at least twice after it was completely demolished. With perseverance Hannay conducted more than eighty attempts claiming success in three. The so synthesised diamonds were then sent to Professor N. Story-Maskelyne of the British Museum mineralogical department for identification. After several tests Story-Maskelyne positively identified Hannay's samples as diamonds and announced the success in a letter to the Times (London) on February 20, 1880 [121]. The nine remaining specimens, each a few tenths of a millimetre across, are still held by the Natural History section of the British Museum. Many investigators through the years have since examined the crystals and have concluded that they are indeed diamonds; however, all the tests indicate that they are fragments of natural diamond. It is a matter of conjecture to know whether Hannay's equipment became contaminated, whether his claim was just fraudulent or whether one of his workmen tired of the continuous explosions planted the diamond hoping to put an end to the hazardous experiments.

None of these early attempts are believed to have been successful, but they must be given some credit. They have been the forerunners of what is today a reality: the synthesis of man-made diamonds. There are at least three main processes known and widely used today to synthesise artificial diamonds: high pressure high temperature (HPHT), chemical vapour deposition (CVD) and detonation. A fourth process called ultrasound cavitation, deserves a separate mention.

2.3.1 High pressure high temperature (HPHT)

The synthesis of artificial diamond by *high pressure and high temperature* (HPHT) processes has been historically the first to be developed and practically realised. The technique consists of subjecting carbon-containing material to high temperature (above 1500 °C) and

high pressure (above 5 GPa), inducing the phase transition of graphite to diamond. The method is inspired by, and is actually mimicking, the geological processes involved in the formation of natural diamond.

Recreate the right geological conditions in the laboratory and nothing should prevent the synthesis of man-made diamonds. This was at least what scientists, like the previously mentioned Hannay and Moissan, thought when they tried and failed (cf. s. 2.3). The problem is that the pressure and temperature conditions required are very extreme, so extreme that even in nature there are only two places on Earth where they can occur: in the lithospheric mantle at a depth about 200 km under the surface or at the site of a meteorite strike.

In 1938 F. Rossini and R. Jessup produced the first phase diagram for carbon [122]; this was then extended and completed in 1955 by R. Berman and Sir F. Simon [123].

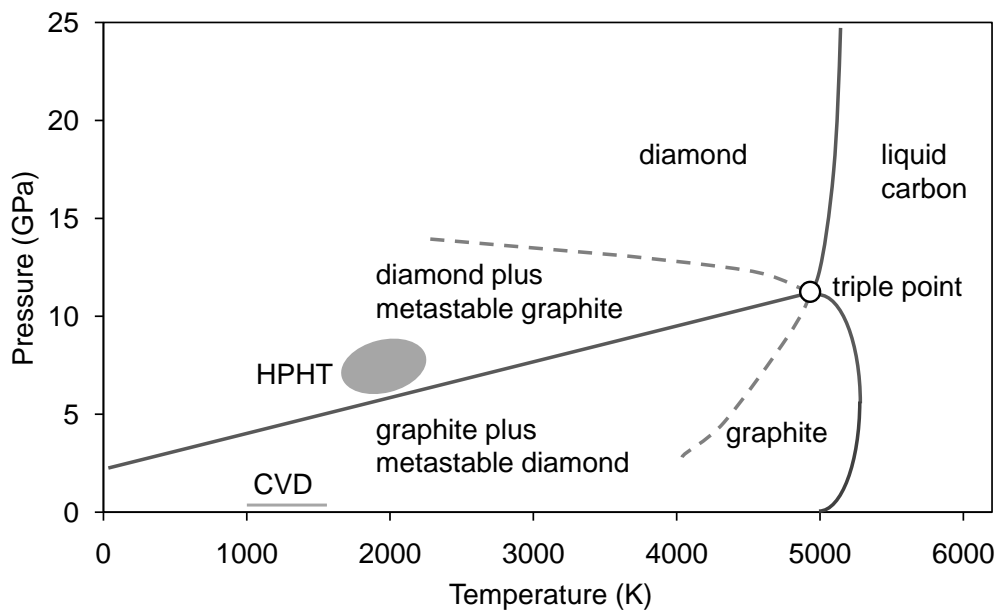


Figure 2.9. Sketch of the carbon phase diagram. Regions of metastability are bound (dashed lines) by extension of the melting curves of diamond and graphite. The approximate region for high pressure high temperature (HPHT) and chemical vapour deposition (CVD) synthesis of diamond are shown.

The phase diagram (Fig. 2.9) shows that the stable form of carbon at normal pressure and temperature is not diamond but graphite, even though the rate of transformation of diamond to graphite is negligible in ambient conditions. The phase diagram, even in its

early version, brought a new understanding and P. Bridgman, the father of high-pressure technology, started a series of experiments taking graphite to pressures and temperatures where diamond is stable. By using tungsten carbide anvils, he was able to bring graphite to pressures of 7 GPa and even 40 GPa at room temperature, but no diamond was formed in any of these room-temperature experiments. Higher temperatures were inaccessible because the strength of tungsten carbide decreases rapidly with increasing temperature. In some of his later experiments, Bridgman was able to subject graphite to pressures of 3 GPa and temperatures of 3000 °C, but again no diamond formation occurred. In 1947, after those continuous failures to synthesise diamond, Bridgman commented: “*Graphite is nature’s best spring*” [124]. The problem is that a large amount of energy has to be supplied in order to convert the graphite structure to diamond.

The problem was first solved in 1953 by a team of scientists from the Allmänna Svenska Elektriska Aktiebolaget (ASEA) laboratory in Stockholm, but the early success of the Swedish group was publicised only after the announcement, on February 15, 1955, that the U.S. General Electric (GE) team of F. Bundy, T. Hall, H. Strong and R. Wentorf had transformed graphite to diamond [125]. The General Electric team used a belt press system capable of producing pressure above 10 GPa and temperatures above 2000 °C. Graphite was dissolved in a pyrophyllite container within molten nickel, cobalt and iron which acted as solvent catalysts dissolving the carbon and accelerating its conversion to diamond.

This is how R. M. Hazen in “*The Diamond Makers*” describes the success of the method General Electric developed to synthesise diamond by high pressure high temperature [126]:

The first GE patent claimed that any substance rich in carbon, not just graphite, could be converted to diamond with the GE process. That was a tall claim, open to challenge by other companies unless a variety of carbonaceous materials could be shown to work. Bob Wentorf volunteered for the job, and began work on one of the most bizarre and amusing series of experiments in the history of high pressure.

Carbon-rich materials are everywhere: plastic, sugar, wood, paper, glue and all living things are loaded with the element carbon. Most scientists must have run diamond-making

experiments on fancy-sounding carbon-based chemicals like polyethylene or pentanedione, but Wentorf, true to his whimsical nature, turned to more familiar substances. In high-pressure runs of remarkable flamboyance he squeezed “Black Diamond Roofing Tar”, aged maple wood, moth flakes, and his favourite brand of crunchy peanut butter. The latter experiment was a consequence of Wentorf’s inclination as “an avid snacker”. He always kept a box of crackers and jar of peanut butter in his right-hand desk drawer. “The peanut butter turned into tiny green diamond crystals,” Bob laughs. “It was because of all the nitrogen.” The novel peanut butter experiments got Wentorf more press coverage than just about anything else the GE diamond makers did, but those runs also made a telling point. General Electric could turn just about any carbonaceous material into diamond.

After Wentorf repeated the famous peanut butter story for what must have been the thousandth time, Herb Strong gave the punch line: “The pity is you can’t turn diamonds into peanut butter.” It’s a well rehearsed line, but there is little doubt that, if given the chance to invent just one product in his life, Bob Wentorf would have been just as happy to have discovered peanut butter.

In the last fifty years several HPHT methods have been developed. The basic principle of achieving high pressure and high temperature has remained the same, but new press technologies have been introduced. The most common HPHT presses are: the belt system, the cubic system and the bars system [127].

Belt press. A belt press is a huge hydraulic press with a system of anvils and a ring shaped structure (Fig. 2.10). The modern versions are not much different from the original design firstly used in the 1950s by the General Electric team. The main improvement is that they are nowadays built on much larger scales. The upper and lower carbide anvils exert high pressure on the cylindrical inner cell, while a belt of steel bands confine the pressure radially. Pressure of 5-10 GPa can be achieved with such a system. A tubular graphite heater raises the temperature to over 1400 °C. In these conditions the solvent metal is melted and dissolves the high purity carbon source, which is then transported to the diamond seeds and precipitates.

Several manufacturers including De Beers and General Electric are still using belt press technologies to synthesise artificial diamonds.

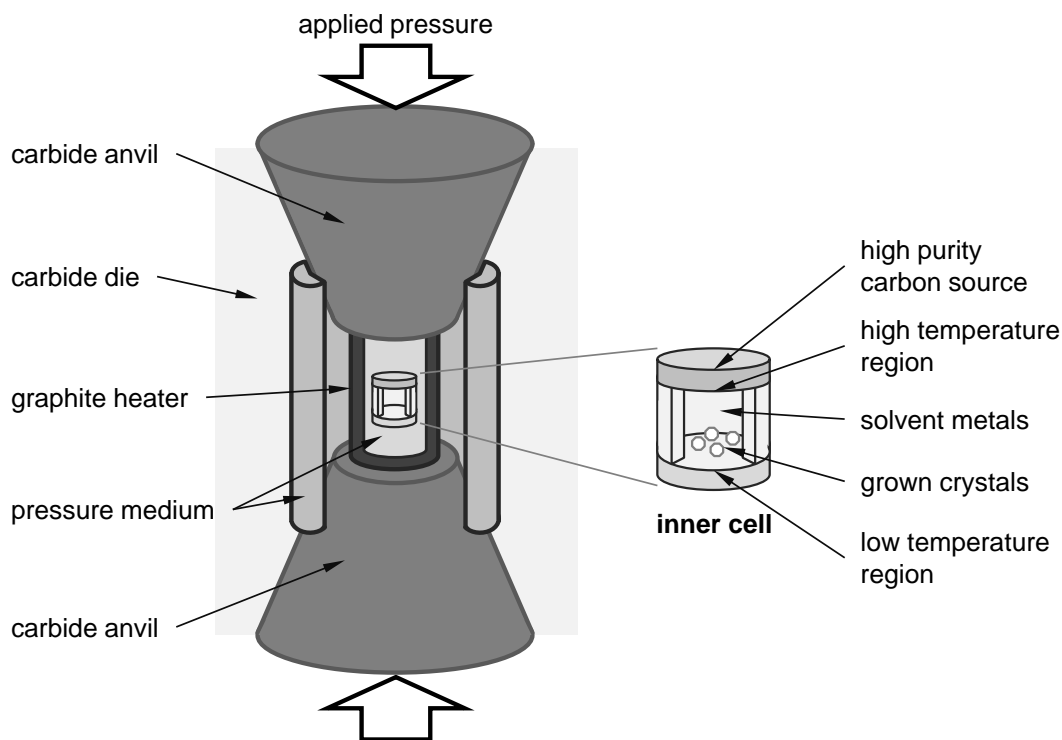


Figure 2.10. Schematic representation of a HPHT belt press. Diamond seeds are placed at the bottom of the inner cell, inside the press. Carbide anvils are used to apply high pressure on the chamber, while a belt of steel bands maintains the pressure radially. A graphite heater generates temperature above 1400 °C melting the solvent metal in the inner cell. The molten metal dissolves the high purity carbon source so that carbon atoms are transported to the seeds and precipitate forming diamond crystals.

Cubic press. A second type of press is the cubic system. It consists of six identical anvils compressing a cubic pressure medium along three opposite directions perpendicular to each other. The first multi-anvil press design was a tetrahedral press where four anvils were converging on a tetrahedron-shaped volume [128]. The cubic system was developed shortly thereafter to increase the volume to which the pressure could be applied. Cubic presses are generally smaller than belt presses and can more rapidly achieve the temperature and pressure required to synthesise diamond. However, unlike the belt presses, they cannot be easily scaled up to larger volumes since larger anvils and forces would be required to achieve the same pressure. With the cubic press, pressures up to 10 GPa over a volume of 1 cm³ can be achieved.

Bars Press. A third type of press is the bars system developed at the Russian Academy of Science in Novosibirsk [129]. The term “bars” is an acronym for “Bespressovye Apparaty tipa Razreznaya Sfera”, Russian for “Press-free, High Pressure Apparatus”. The system

comprises eight outer steel anvils which have a spherical outer shape and which close internally in the shape of an octahedron. A second set of six cemented carbide anvils fit inside the steel anvils, forming a second internal cavity of cubic shape where the inner ceramic cylindrical cell, called “synthesis capsule”, sits. The whole system is placed within a press and the pressure is transmitted uniformly from the two systems of anvils to the inner cell. The synthesis capsule is heated up by a graphite heater. The pressure applied to the cell can be of the order of 5.5-6.5 GPa, while the temperatures can be of the order of 1350-1700 °C. Bars presses are generally very compact, efficient and economical in comparison to other HPHT press technologies.

All HPHT press technologies use a core reaction cell. The cell contains a carbon source and some seed crystals so that when the extreme temperatures and pressures are reached diamonds grow. One of the most important elements in the process is the presence of a metal solvent or flux, which acts as a solvent and transport material for the carbon source to the seeds. This solvent is usually iron (Fe), nickel (Ni) or a mixture of the two. The flux makes it possible to synthesize diamond at much lower temperatures and pressures than necessary for direct conversion of graphite into diamond. The exact composition of the flux strongly influences the properties of the synthetic diamond. Only a few minutes are needed to convert graphite into powder-sized diamond, but it takes about three days under a well-controlled growth to obtain a rough gem-quality stone.

The HPHT method is relatively low cost and flexible since different technological solutions are available for creating the required temperature and pressure conditions. It is still one of the most widely used methods to synthesise artificial diamonds especially for industrial applications where mass-production is fundamental.

The HPHT diamonds synthesis has been dominating the scene of man-made diamonds for the last fifty years at least until recently when in 2005 the U.S. based company Apollo Diamonds Inc. announced a breakthrough: the growth of commercial mono-crystalline diamonds through chemical vapour deposition (CVD) technology [130].

2.3.2 Chemical vapour deposition (CVD)

Another method to synthesise artificial diamonds is by *chemical vapour deposition* (CVD). In this process diamonds are literally grown on a substrate from a hydrocarbon gas mixture, inside a chamber where temperature and pressure are controlled.

Research on the growth of artificial diamonds from the gas phase started in the 1950s. The first successful documented attempt to grow diamond at low pressure was by W. G. Eversole at the Union Carbide Corporation (USA) in 1952, making Eversole the very first “diamond-maker” in history [131]. But, at the very beginning the growth rates were very slow so the method ended up being eclipsed by the contemporary success of the high pressure high temperature diamond synthesis. A few years later the research on the growth of CVD diamond was boosted again. In 1968 the group led by B. Derjaguin at the Physical Chemistry Institute of Moscow described how to grow diamond filaments using a vapour-liquid-solid technique employing molten iron as a catalyst [132]. A significant step in the development of CVD diamond growth was then taken at the National Institute for Research in Inorganic Materials (NIRIM) in Tsukuba, Japan. There, a team led by N. Setaka started working on CVD diamond synthesis in 1974 and by 1981 they documented success in growing diamond at rates of up to 1 μm per hour using a hot-filament process to activate a methane-hydrogen gas mixture [133-136].

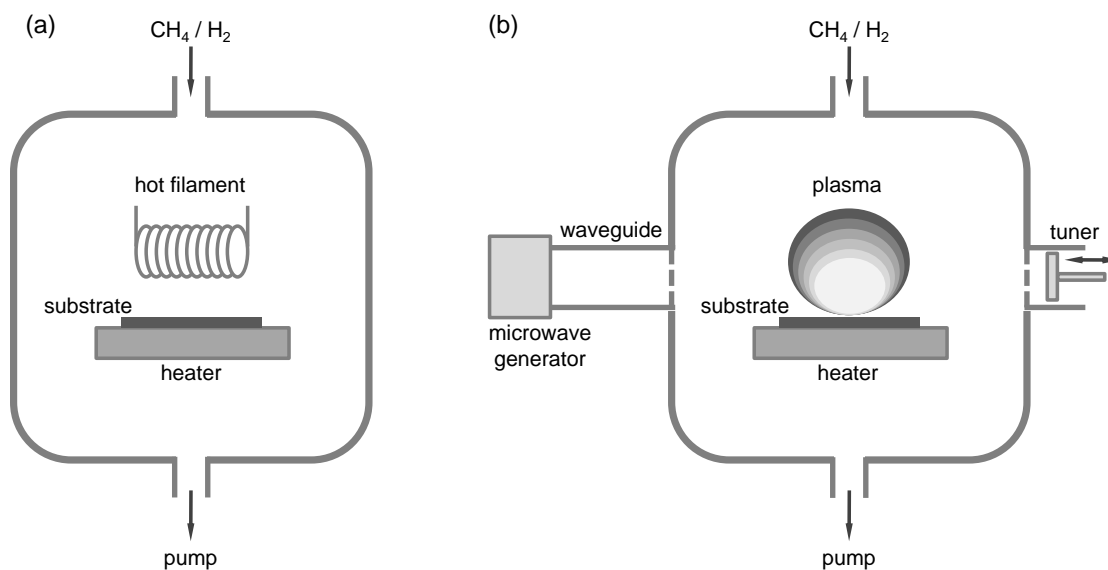


Figure 2.11. Schematic representation of two different types of CVD reactors for diamond growth. a) Hot filament. b) Microwave plasma-enhanced reactor.

The basic principle of CVD diamond growth is fairly straightforward (Fig. 2.11). A substrate, generally single crystal diamond, silicon, quartz, sapphire, or some type of metal, is chosen and placed inside the growth chamber where pressure and temperature are controlled. A mixture of hydrocarbon gas, typically methane (CH_4) and hydrogen (H_2), is then injected in the chamber. The mixture of gas is heated up by using a microwave beam, a hot filament, an arc discharge, a welding torch, a laser, an electron beam or other means. At temperatures above $800\text{ }^\circ\text{C}$ the mixture is ionised into chemically active radicals and a plasma forms. The radicals react and start forming diamond crystals around the substrate defects, which behave as trigger seeds for the diamond growth process. Typically, the substrate is seeded with nanodiamond powder. Initially, small diamond crystals can nucleate randomly and as the growth proceeds, those nuclei become larger and eventually coalesce to form a continuous polycrystalline film. In the process the methane serves as carbon source, while the hydrogen etches away the non-diamond carbon from the growing diamonds. In fact, atomic hydrogen is very reactive and dissolves everything which is not diamond; diamond is partially etched as well, but at a much slower rate than, for instance, graphite.

The main advantage of CVD diamond growth is its great flexibility. This method is particularly suitable for those applications, where the specificity of the outcome is more important than the high industrial throughput. The actual chemical process for diamond growth is still under study.

In 2005 Apollo Diamond Inc., Boston (MA, USA), developed and patented a method for growing extremely pure, gem-quality diamond by chemical vapour deposition [130]. The novelty consists in the fact that they discovered the “sweet spot” or, in other words, the right combination of pressure temperature and gas composition that results in the growth of a single diamond crystal as opposed to the polycrystalline fashion-like structure of the usual CVD diamond growth. Such CVD single diamond crystals are nearly 100% pure, almost flawless and therefore hard to be distinguished from natural diamonds.

The following is an extract from the article “*Diamonds on Demand*” written by U. Boser for the Smithsonian Magazine, June 2008 [137]:

Robert Linares has been at the forefront of crystal synthesis research since he started working at Bell Labs in Murray Hill, New Jersey, in 1958. He went on to start a semiconductor company, Spectrum Technologies, which he later sold, using the proceeds to bankroll further research on diamonds. In 1996, after nearly a decade working in the garage of his Boston home –no kidding, in the garage, where he'd set up equipment he declines to describe– he discovered the precise mixture of gases and temperatures that allowed him to create large single-crystal diamonds, the kind that are cut into gemstones. "It was quite a thrill," he says. "Like looking into a diamond mine." Seeking an unbiased assessment of the quality of these laboratory diamonds, I asked Bryant Linares to let me borrow an Apollo stone. The next day, I place the .38 carat, princess-cut stone in front of Virgil Ghita in Ghita's narrow jewelry store in downtown Boston. With a pair of tweezers, he brings the diamond up to his right eye and studies it with a jeweler's loupe, slowly turning the gem in the mote-filled afternoon sun. "Nice stone, excellent color. I don't see any imperfections," he says. "Where did you get it?" "It was grown in a lab about 20 miles from here," I reply. He lowers the loupe and looks at me for a moment. Then he studies the stone again, pursing his brow. He sighs. "There's no way to tell that it's lab-created.

2.3.3 Detonation

Another way to synthesise diamonds is by *detonation*. Diamond crystals nominally a few nanometres in size originate from the detonation of carbon-containing explosives in a metal chamber. These diamonds are commonly referred as detonation nanodiamonds (DNDs).

The detection of diamond in a preserved shock-compressed graphite sample was first observed in the USA by P. S. DeCarli and J. C. Jamieson in 1961 [138]. This discovery led a series of research groups on the other side of the globe to join in the so called "The diamond club". All based in the former Soviet Union, these groups conducted the first pioneering works on detonation nanodiamonds. Two years later, in July 1963, the synthesis of detonation diamond nanocrystals was actually realised by K. V. Volkov, V. V. Danilenkov and V. I. Elin, working at the USSR All Union Research Institute of Technical Physics (VNIITF) [139]. The team working at VNIITF, a research centre where nuclear weapons were developed, discovered that a popular military explosive made out of 40%

trinitrotoluene (TNT) and 60% hexogen (RDX) is oxygen deficient. Thus, upon detonation in an inert medium like argon or water, it produces up to 12% soot by incomplete combustion, which surprisingly contains up to 75% diamond carbon. In the following two years, between 1963 and 1965, the team conducted over a hundred experiments to analyse how the explosion conditions and the composition of the explosives were affecting the properties of the produced nanodiamonds.

At that time, in the former Soviet Union the information about the synthesis of detonation diamond was treated as highly classified and for security reasons the discovery was never circulated until twenty years later, in 1987, when part of the discovery reports were forwarded to the other institutions of "The diamond club". Ironically, during those twenty years due to lack of communication the process to synthesise detonation nanodiamonds was rediscovered independently several times by other groups, including: A. M. Staver, E. A. Petrov, and A. I. Lyamkin under the guidance of Academician V. M. Titov at the Institute of Hydrodynamics, Siberian Division, Academy of Sciences of the USSR (Novosibirsk) and G. I. Savvakina under the guidance of Academician V. I. Trefilov at the Institute of Problems of Materials Science, Ukraine Academy of Sciences (Kiev). In the USA, detonation nanodiamond synthesis was only discovered in 1988 [140].

The research on detonation nanodiamonds remained stagnant for almost forty years after its first discovery in 1963. Culture and politics played a big role in that since Soviet scientists, who mastered the diamond synthesis by detonation, were forced to concentrate their effort on the static high pressure high temperature method of diamond production which was gaining more and more attention after its first discovery by the US based General Electric in 1955 [125]. Only very recently, the striking interest raised around the new born nanotechnologies renewed the attention on detonation synthesis and from 2003 a few factories specialised in detonated nanodiamonds production started to spring up in different places including Russia, Ukraine, Belarus and China [141].

Detonation diamond crystals originate from the detonation of trinitrotoluene (TNT) and hexogen (RDX) inside a metal chamber (Fig. 2.12a). At the shock front of the explosion the right conditions of high pressure ($\sim 20\text{-}30$ GPa) and high temperature ($\sim 3000\text{-}4000$ K) for the thermodynamic stability of diamond in the phase diagram of carbon are achieved (Fig. 2.12b). In such conditions, the carbon atoms contained in the explosives themselves

assemble and form diamonds. The chamber needs to be rapidly cooled down (Fig. 2.12b-(i)) after the detonation to suppress the tendency of carbon to form graphite (Fig. 2.12b-(ii)). The time during which the pressure and temperature are suitable for carbon to form diamond is limited (fractions of microseconds). Detonation nanodiamonds are therefore very small (~ 5 nm) and tend to have an extremely narrow distribution in size (generally commercial detonation nanodiamond powders contain up to 98% diamond crystals in the range ~ 2-10 nm).

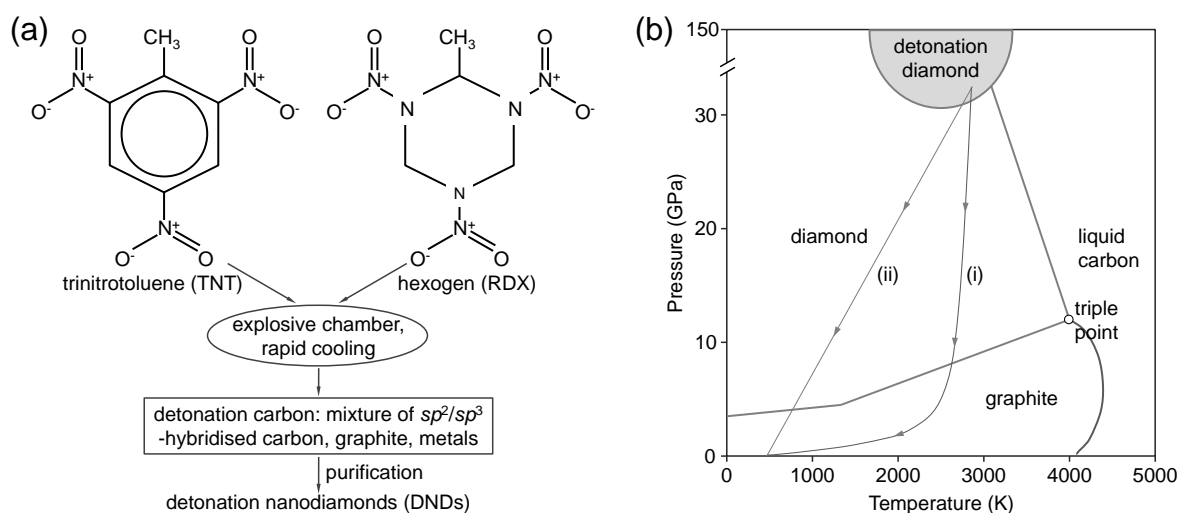


Figure 2.12. Scheme and carbon phase diagram of detonation diamond synthesis. **a)** Schematic representation of the detonation process. Trinitrotoluene (TNT) and hexogen (RDX) are detonated in a metal chamber and rapidly cooled off. The product: a mixture of sp^2/sp^3 -hybridised carbon, graphite and metals from which the detonated nanodiamonds are isolated after purification (mainly oxidation) and de-agglomeration [142]. **b)** Phase diagram for carbon showing the region of stability for detonation diamond synthesis (adapted from [141]). Rapid decrease in pressure at high temperatures facilitates the diamond-to-graphite transition (i). Rapid cooling ensures that diamond remains the most stable phase and results in higher yields of detonation nanodiamonds (ii). The conditions for diamond stability during the detonation process are only conserved for a very short time (sub-microsecond) before graphite becomes the more stable phase [143]. This is due to a fast decrease in pressure while the system is still at a high temperature favouring the diamond-to-graphite transformation. To obtain diamond, it is therefore important to control the rate at which the system cools: faster cooling at relatively high pressure results in a higher diamond yield.

Detonation nanodiamonds are complex objects. They possess a layered-structure where at least three zones can be distinguished (Fig. 2.13) [144]. The inner core is made of carbon sp^3 -hybridised atoms bound in a cubic crystal structure. It measures on average ~ 4-6 nm and can contain nitrogen as substitutional atoms. The core is surrounded by a second layer: an intermediate inhomogeneous sheath made of sp^2 -hybridised carbon. It measures ~ 0.4-1 nm and it possesses a porous structure containing defects and discontinuous regions of carbon formations. The third outer layer consists of carbon and a wide variety

of functional groups, mainly oxygen-containing groups such as hydroxyl, carboxyl, ketone, lactone, etc. The functional groups can constitute up to 10% of the total particle mass.

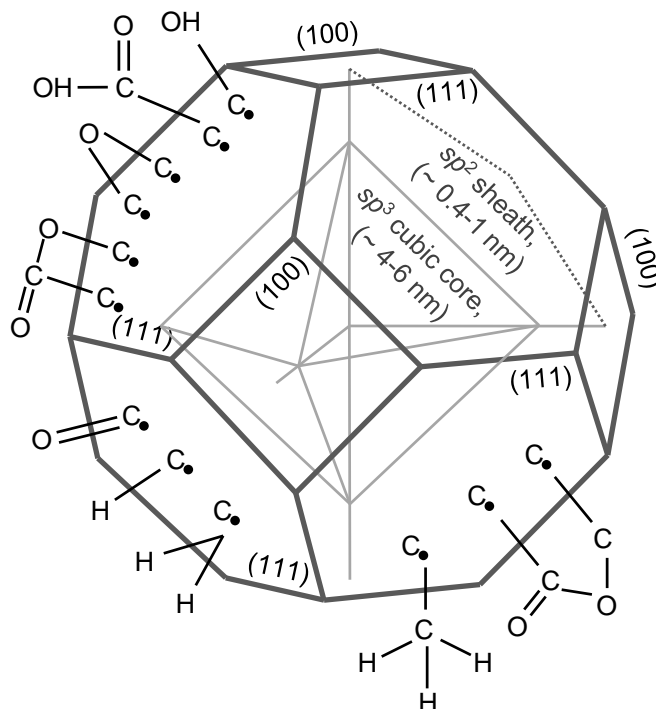


Figure 2.13. Schematic model of a detonation nanodiamond structure in the form of a truncated octahedron (adapted from [142]). Three layers can be identified. The inner core (thickness ~ 4-6 nm) is made of sp^3 -hybridised carbon bound in a cubic crystal structure. The intermediate layer is an inhomogeneous sheath of sp^2 -hybridised carbon (thickness ~ 0.4-1 nm), characterised by a porous structure and discontinuous region of carbon formations. The outer layer is constituted by various functional groups (hydroxyl, carboxyl, epoxy, cetone, anhydride, ester, methyl, methylene, methane, etc.).

Although its discovery was contemporaneous to that of HPHT and CVD methods, the synthesis of artificial diamonds by detonation has found a decisive upturn only in the past few years. The reason: on one side the extremely reduced size of detonation diamonds makes them less attractive than HPHT or CVD diamonds for generic industrial purposes or for the gem market, however on the other it makes them promising objects to look at for several applications in the rising field of nanotechnologies.

2.3.4 Ultrasound cavitation

Ultrasound cavitation is another possible technique to synthesise diamond. It is based on inducing the graphite-to-diamond transformation via the high pressure and high temperature briefly generated in an ad hoc flowing fluid by cavitation.

Using ultrasound cavitation to synthesise diamond is a relatively recent conception. In 1973 E. M. Galimov proposed the idea that the formation of diamond in nature could be explained by cavitation occurring in magma flowing in kimberlite pipes, which cross vertically the crust of the Earth from the mantle [145, 146]. Based on his theoretical study he and co-workers used a prototype ultrasonic reactor and successfully synthesise nanodiamonds by cavitation [147]. They proved that the concept was feasible, but due to the limitation in power and size of their apparatus the yield and efficiency of the process were too low for being of any commercial interest. One of the most significant works on the development of cavitation method for diamond synthesis is probably the US patent "Method and means for converting graphite to diamond" granted to H. G. Flynn in 1986 [148]. Recently, quite a few attempts to synthesise diamond by cavitation have been reported [149, 150]. In most cases however, only a low yield of nanosized diamond particles was obtained.

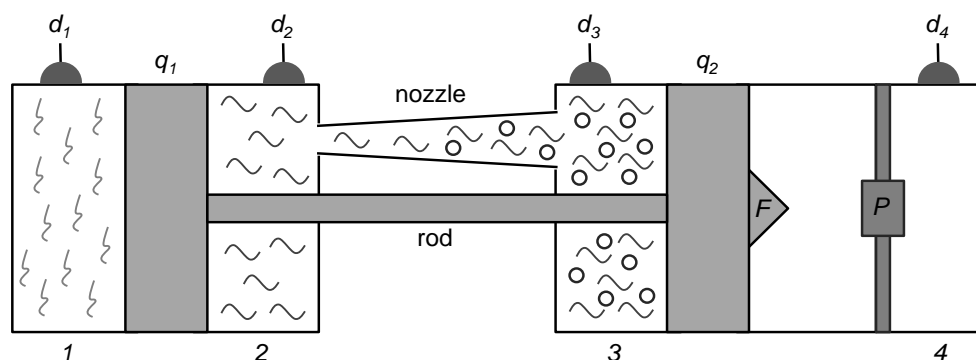


Figure 2.14. Schematic representation of a cavitation experimental setup (adapted from [147]). A powder charge in cavity 1 is ignited and the increased pressure induces the motion of the plunger q_1 towards the right side. As a result of the movement of the plunger q_1 , the working fluid is displaced from cavity 2 to cavity 3 through a nozzle shaped in the form of a Venturi tube. The tensile stress arising in the narrowest cross section of the nozzle induces the formation of vapour bubbles (first cavitation stage) which then enter cavity 3. When the plunger q_2 reaches the extreme right position, the firing pin (F) strikes the primer (P) and the powder charge in cavity 4 is ignited. Powder gases produced in cavity 4 displace the plunger q_2 in the opposite direction increasing the pressure in cavity 3 and providing the conditions for the fast collapse of vapour bubbles. During the process, the pressure is monitored in the cavities via four different transducers (d_1 - d_4).

The basic idea on which ultrasound cavitation is based is the following (Fig. 2.14). As an elastic wave like sound passes through a liquid, it produces alternating regions of reduced density (negative partial pressure) and increased density (positive partial pressure). If the sound wave is sufficiently intense, cavities or bubbles filled with the saturated vapour of

the liquid are formed in the regions of reduced density. Subsequently, when entering areas of positive pressures these bubbles collapse and the vapour within them experiences a rapid strong adiabatic compression. At the moment of collapse, the pressure and temperature inside the cavity may reach extremely high instantaneous values (pressure ~ 1-10 GPa and temperature ~ 1000 K). The simultaneous collapse of many cavities produces a cavitation zone in which the correct environment for the transformation of graphite into diamond is supplied, if a suitable working fluid is used (e.g. hydrocarbons like benzene, C₆H₆).

The synthesis of diamond by ultrasound cavitation offers costs comparable to those of HPHT methods and requires relatively simple equipment and procedures. These facts have driven, in the last ten years, consistent theoretical and experimental research into ultrasound cavitation in an attempt to better understand it and hence optimise the parameters of the process [151]. Although very promising, this method has not yet gained the same attention as the other processes of synthesising artificial diamonds.

2.3.5 Enhancement of colour centres concentration

The synthesis of artificial diamonds is only one aspect of tailoring the material for industrial and technological applications or even just for the gem-trade market. Defects and impurities can significantly alter the properties of diamond: its mechanical behaviour, its electrical and thermal conductivity and its colour, nuances and optical response (cf. ss. 2.1.2-5). Therefore, in parallel with the research of different synthesis methods, there has been a development of various techniques directed to enhance and control the formation of impurities and colour centres in diamond.

Different approaches have been perfected to ensure that colour centres are formed or included in diamond. All of them aim for highest possible control in terms of concentration, position, and isolation of colour centres; in fact, the quantity and quality of luminescent centres in diamond has to be accurately controlled to make certain technological applications feasible. Following is a list of some of these defect-enhancing techniques. We briefly analyse here specifically those relevant to the nitrogen-vacancy

(NV) centre, which is of main interest for this work. Some of these techniques however, can be applied to diamond defects of other kinds.

Irradiation. One of the most common approaches to induce the formation of NV centres in diamond is by *irradiation*. A focused beam of ions or electrons is used to irradiate the target diamond material. The incident particles penetrate the diamond lattice and create vacancies in the crystalline structure. The diamond is then put through a subsequent annealing process at temperatures of ~ 850 °C. The annealing enhances the migration of the vacancies, which become trapped by nitrogen atoms already present in the diamond lattice, forming stable NV centres [82]. This process works mainly because of two reasons. Firstly, the diffusion of vacancies in diamonds starts at about 650 °C, while diffusion of nitrogen atoms at about 1500 °C. This facilitates the migration of the vacancy towards fixed nitrogen atoms in their lattice positions and enhances the nitrogen-vacancy trapping mechanism [152]. Secondly the formation of nitrogen-vacancy pairs is guaranteed by the fact that they are energetically favoured over having nitrogens and vacant carbons separately and randomly dispersed in the diamond lattice. The irradiation technique is often used on nitrogen-rich type I diamond, since it naturally contains nitrogen in concentrations over 20 ppm (cf. s. 2.2.2, Fig. 2.4).

The number of NV centres created by irradiation depends on the energy and nature of the focused particles hitting the diamond. As a rule of thumb, higher energies and smaller incident ions result in deeper penetration with subsequent enhanced probability of creating vacancies. On the other hand, small penetration depths of the incident particles cause a significant fraction of vacancies to diffuse to the surface during annealing, where they annihilate without forming stable NV centres [153].

Ion implantation. NV defects can be directly created in nitrogen-free type IIa diamonds by *ion implantation*. The target diamond material is irradiated with N^+ ions and then annealed to enhance the migration of vacancies towards the implanted nitrogen atoms. Again, the annealing is performed at ~ 850 °C to mobilise the vacancies while keeping the nitrogen atoms fixed. This is desirable since it leads to stationary NV centres located at the positions where the N^+ ions have been initially implanted. The ability to localise the NV centre is one of the major strengths of this technique [154, 155]. This advantage is

unfortunately diminished by two effects. First, the stochastic nature of the ion beam obeying a Poissonian statistic causes some parts of the sample to contain more than one NV centre, while others contain none. Second, the straggle of the ions, i.e. the random spreading out of the incident ions once they penetrate into the sample, causes a reduction in the control of the ion beam spot size. The resolution can be increased by lowering the kinetic energy of the ions. In so doing, the lateral displacement is limited and the spot dimension is reduced; nevertheless the lower ion energy causes a reduction in the efficiency of NV centre formation during the subsequent annealing process [156]. The yield of NV creation as a function of the ion energy can be lower than 1% for energies < 5 keV and up to 45% for energies > 18 MeV [157].

Incorporation during CVD growth. When artificial diamonds are synthesised by chemical vapour deposition (CVD), the inclusion of NV centres in the diamond lattice occurs spontaneously during the growth of the crystals. This is due to the fact that nitrogen is abundant in the atmosphere (molecular nitrogen, N_2 , constitutes 78% of air) and that NV centres are energetically stable in diamond. Therefore, the incorporation of nitrogen and subsequently NV centres formation in CVD diamond growth is almost inevitable. However, using the right choice of gas mixture and process parameters in the CVD chamber a certain control over the concentration of NV centres can be exerted [158].

2.4 Applications of colour centres in diamond

Diamond has always been subject to extensive investigation. Besides its extreme material properties, diamond has recently attracted the interest of the scientific community for colour centres it is able to host. The reason is that colour centres in diamond possess unique room-temperature optical and spin properties that make them suitable candidates for a wide range of applications in the world of nanotechnology.

In this work the emphasis is on a particular diamond defect, the nitrogen-vacancy (NV) centre. Of the hundreds of defects that have been identified and characterised in diamond, the NV centre has turned out to be one of the most appealing for scientific purposes. There are at least three main research areas where diamond colour centres seem to offer appealing perspectives: quantum information technology, biomedicine, and high-resolution magnetometry.

2.4.1 Quantum information technology

Diamond colour centres are being studied as a promising candidate for the implementation of solid-state quantum technologies.

The NV centre for instance, may provide a feasible hardware system for the generation of addressable and easy to manipulate quantum states (qubits), even at room temperature [159]. The NV centre is a single-photon emitter which shows high oscillator strength for the dipole transition between the ground and the first optically excited state. Its spin state can be optically initialised, coherently manipulated and read-out with optical and microwave excitation and, additionally, it shows a desirable long spin coherence time [35, 49, 50, 160]. Simple logic gates have been demonstrated at room temperature using NV centres [161, 162]. Coherent coupling between electronic spins of the NV centre and the nuclear spin of proximal ^{13}C atom have been studied experimentally proving that selective addressing and manipulation of single isolated nuclear spins is possible [163]. The coupling of an NV centre to a neighbour single nitrogen defect [164] as well as to another NV centre [165] in diamond at room temperature have also been demonstrated, possibly opening the way towards a viable solid-state quantum device operating at ambient conditions.

NV centres have also been explored in quantum optics and in quantum cryptography as single photon sources to realise quantum cryptographic protocols [35, 166].

Although NV centres in diamond seem to be of great potential as building blocks for quantum devices, such devices are still far from implementation. For instance, the NV centre can produce a relatively high number of single-photon pulses, but its wavelength and bandwidth are not ideal for the eventual requirements of optical quantum information processing. For the NV centre, the overall linewidth is of the order of 200 nm, with the zero phonon line at 637 nm having itself a width of several nm at room temperature [158, 167]. In this context, studies have been conducted aiming to enhance both the emission rate and photon collection efficiency as well as manipulate the spectral shape of the NV centre. These include coupling the radiating NV to a localised mode of a high- Q resonator such as a microsphere [168, 169], a microdisc [170] or a photonic crystal cavity [171-174] or alternatively, using a solid immersion lens for the collection of the NV

emission [175, 176]. Different schemes have also been proposed, for instance, exploiting the coupling of the NV centre with localised surface plasmons to achieve an enhancement of the centre emission rate [177, 178].

Another problem is the technological challenge of positioning several single NV centres with enough control to guarantee the interaction of their spins with adjacent NV spins; regular arrays of single NV centres have been created, but the accuracy achieved is not sufficient for the realisation of actual applications [155, 156].

It is widely accepted that the potential for quantum technologies in diamond is real, but right now the main limitation is the materials science coping with the challenge of controlling and optimising the quality of the diamond material and of its defects.

2.4.2 Life science

In the life sciences, research towards exploiting colour centres in diamond for biological and medical purposes has become fairly active in the past few years.

Fluorescent nanodiamonds possess several attractive properties. They are biocompatible and non-cytotoxic, their surface can be functionalised and, when excited by a laser, defect centres within the nanodiamonds emit photons that are capable of penetrating tissues; the emission is generally stable being the diamond defects immune to photo-bleaching and photo-blinking [39, 179-182]. These characteristics are difficult to be found in combination, for example in biological probes. It is therefore conceivable to use fluorescent nanodiamonds as probes for bio-labelling and as drug-delivery vehicles [39, 183-185].

The main challenge right now is the material science since the majority of these biomedical applications require the synthesis of the smallest possible luminescent nanodiamonds (size ~ few nm).

2.4.3 High resolution magnetometry

Another intriguing area where single NV centres are the subject of active interest is that of high-resolution magnetometry.

Using NV centres to detect single spins and weak magnetic fields is a recent prospect. The key idea is that external fields acting on a single NV centre can measurably alter its fluorescence. The detection of the induced changes on the NV fluorescence can be used to probe and measure the surrounding fields, theoretically even the weak magnetic fields generated by single electron or nuclear spins. Promising applications have been identified both in the physical sciences for read-out of single spin-based magnetic memories [36] and in the life sciences for high-resolution imaging techniques [37, 38].

These applications have been proven to be feasible. The challenge now is to control and tailor the material.

3

Magnetometry at the nanoscale

The idea that sparked off this project three years ago was to develop a measuring system able to detect weak magnetic fields with nanoscale spatial resolution. The underlying concept is to use the room temperature magneto-optical properties of nitrogen-vacancy (NV) centres in diamond nanocrystals as a magnetic field sensor. This system would have high-resolution imaging capabilities at ambient conditions.

3.1 Classical optical microscopy

In the late 19th century Ernst Abbe and Lord Rayleigh established the foundation of modern light microscopy [186, 187]. Based on existing physics principles and experimentation, they demonstrated that image resolution in far field microscopy is limited by diffraction of light by the specimen and the objective lens. More than one century later, the development of microscopy systems remains an active field of research. The fundamental reason for this is the wealth of information in the nanoworld beyond the limit of conventional microscopy.

Resolution is defined as the minimum separation between two points that results in a certain level of contrast. The contrast for two objects of equal intensity is defined as the difference between the maximum and the minimum intensity occurring in the space between them. Contrast can be determined by many factors including: the number of photons collected from the specimen, the dynamic range of the signal, the optical aberrations of the system and, for those systems which employ digital elements, the

number of picture elements (pixels) per unit area in the final image. Often, the wider concept of visibility is used in place of those of resolution and contrast. Visibility is more loosely defined as the ability to recognize two closely spaced features as being separate. Resolution and contrast give a quantitative (but theoretical) value for the distinguishability of two objects, while visibility takes into account other factors such as specific experimental limitations or specific properties of the specimen and shows that imaging cannot, in general, be performed at the theoretical maximum resolution of the microscope.

The resolution of a microscope both in the image plane and in the axial direction is ultimately determined by a figure called the intensity point spread function (PSF). The intensity point spread function is the visible image of a point source formed in the microscope and recorded by the imaging system. For the lateral components x and y in the image focal plane the intensity distribution of the point spread function is given by the familiar rotationally symmetric Airy pattern (Fig. 3.1a), which is the result of Fraunhofer diffraction of light passing through a circular aperture (assuming cylindrical symmetry of the microscope lenses and components). This simply means that due to diffraction any point-like object or feature of the specimen is imaged by the system as an Airy disc. The characteristics of that Airy disc corresponding to a point-like source (i.e. the PSF of the system) define the resolution of the microscope. Qualitatively, giving two point-like objects and assuming that the image forming process is incoherent, i.e. there is no coherent interaction between the two objects in the image formation, the resulting image is just the sum of two Airy discs (Fig. 3.1b, c). If the two point-like objects are sufficiently separated, their Airy disc images do not or only slightly overlap and they are distinguishable and resolvable, but if they are not spatially separated enough the two Airy discs overlap, they are unresolvable and appear like a single larger or brighter point-like object (Fig. 3.1b). Quantitatively, the resolution is determined by the contrast. When two points are not sufficiently separated in space their point spread functions overlap and the dip in intensity between the two maxima, i.e. their contrast, is reduced. The distance at which two peak maxima are no longer discernible and their contrast becomes zero is referred as the contrast cut-off distance. From this, it follows that resolution can be defined as the separation distance at which two objects are imaged with a certain contrast value. Theoretically, the Sparrow criterion defines the resolution of an optical system as

being equivalent to the contrast cut-off distance. The Sparrow criterion is however quite impractical and it is more common to set a greater (arbitrary) contrast value to define the resolution of an optical system. The most common criterion is the Rayleigh criterion which states that two points are resolved when the first minimum of one Airy disc is aligned with the central maximum of the second Airy disc (Fig. 3.1c).

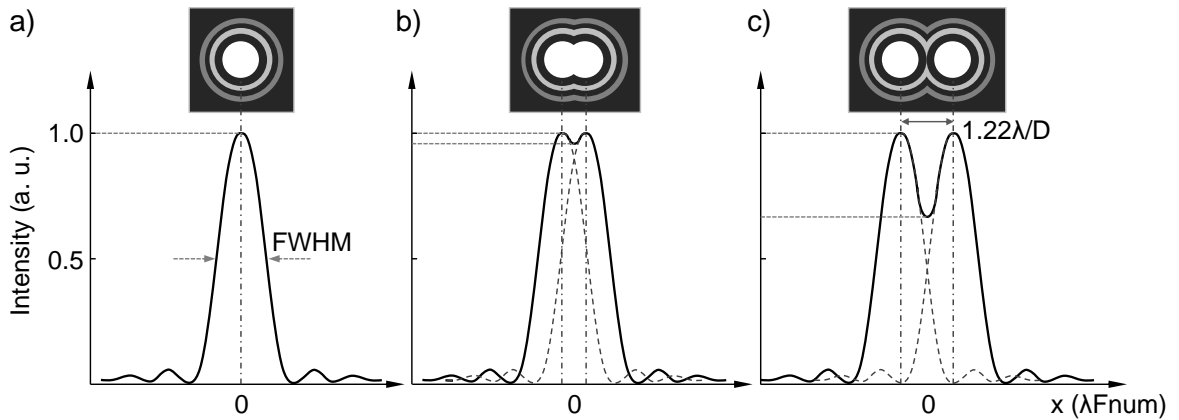


Figure 3.1. Schematic representation of the basic concepts of optical resolution. **a)** Intensity distribution of the point spread function (PSF) given by the rotationally symmetric Airy disc for a point-like object. The full width at half maximum (FWHM) is indicated. **b)** Example of unresolved objects: the Airy discs of the two point-like objects are overlapped and appear like a single larger object. **c)** Example of two resolved objects according to the Rayleigh criterion: the first minimum of one Airy disc is aligned with the central maximum of the second.

Mathematically the Rayleigh criterion separation distance corresponds to a contrast value of 26.4% and although any contrast value greater than zero can be used to define the resolution, the 26.4% contrast of the Rayleigh criterion is considered reasonable in typical fluorescence microscopy applications and is commonly used to define the lateral resolution R of an optical microscope:

$$R = \frac{1.22\lambda}{NA_c + NA_o} \quad (3.1)$$

In equation (3.1), the lateral resolution R is, according to the Rayleigh criterion, the point separation or distance between the central maximum and the first minimum in the Airy disc, λ is the emitted light wavelength, NA_c is the numerical aperture of the condenser and NA_o is the numerical aperture of the objective. The numerical aperture is the product of the sine of the half-angle θ of the cone of light either acceptable by the objective lens (NA_o) or emerging from the condenser lens (NA_c) and the refracting indexes n of the medium between the specimen and the objective or condenser lens ($NA = n\sin(\theta)$). If the

condenser and the objective have the same numerical aperture NA , equation (3.1) becomes simply:

$$R = \frac{0.61\lambda}{NA} \quad (3.2)$$

Small values of the wavelength λ and large values for the numerical aperture NA give smaller lateral resolution, i.e. better capability of distinguishing two close point-like sources. Typical values of NA can range from 0.95 for air objectives to 1.45 for oil immersion objectives. This means that even with perfect lenses, optimal alignment and large numerical apertures, the optical resolution of light microscopy is limited to approximately half of the wavelength of the light used. In practical terms, conventional light microscopy is able to resolve only objects that are at least 200-350 nm in size, making it incapable of reaching the molecular scale desirable in biological and physical sciences.

In the recent past, several light microscopy technologies have been developed to overcome the theoretical resolution limit [188]. In this work a different approach is taken: the feasibility of a detector which is magneto-optical is studied. It would use an NV centre-based scanning probe to perform high resolution measurements at room temperature of magnetic fields. Such a sensor would, in principle, be able to reach the nanoscale world overcoming the diffraction resolution limit of common optical systems.

3.2 Magnetic microscopy

Magnetic microscopy exploits the physical phenomenon of magnetism to detect structures by measuring their interaction with a quantified magnetic field or magnetic probes.

3.2.1 Magnetic resonance imaging (MRI)

The idea of using magnetic resonance imaging to overcome the wavelength diffraction limit of conventional optical microscopy is not new. It was 1938 when I. I. Rabi and his group first introduced nuclear magnetic resonance (NMR) measurements to detect nuclear or other magnetic moments via known magnetic fields [189, 190]. In 1973 P. C. Lauterbur developed the concept of using NMR as an imaging technique. He proposed to exploit the coupling interaction that an object generates between a static radio frequency field and a gradient magnetic field to create an image of the object itself [191]. Lauterbur

called this new imaging technique “Zeugmatography” from the Greek word ζευγμα, “that which is used for joining”, to indicate the coupling interaction of the two fields with the object. The name “Zeugmatography” was not adopted and the technique became known with different denominations: magnetic resonance imaging (MRI), nuclear magnetic resonance imaging (NMRI) or, especially in the medical field, magnetic resonant tomography (MRT). Magnetic resonance imaging has been in use as a whole-body imaging technique for thirty years after the first study on a human was performed on July 3, 1977. In 1986, J. B. Aguayo-Martel and co-workers obtained the first NMR images of a single cell announcing the advent of NMR microscopy: the resolution of their NMR microscope was of the order of 10 μm in plane [192]. Better in plane and three-dimensional resolutions were obtained in 1988 and 1990 by Z. H. Cho et al. [193, 194] and in 2001 by S. C. Lee et al. [195]. In 2002 L. Ciobanu and co-workers performed a three-dimensional magnetic resonance microscopy image with resolution 3.7 μm \times 3.3 μm \times 3.3 μm [196].

The resolution of the NMR microscopy is, however, intrinsically restricted to few micrometres and cannot be improved beyond this due to the theoretical limits that affect parameters such as signal to noise ratio, molecular diffusion, transverse relaxation and susceptibility [194]. Therefore, although NMR microscopy is a non-invasive, high-contrast three dimensional imaging technique relevant both for physical and for life science, it is incapable of reaching the nanoscale range.

3.2.2 Magnetic resonance force microscopy (MRFM)

Higher resolutions can be obtained with magnetic resonance force microscopy (MRFM). MRFM is an imaging technique that can reach the nanometre scale by combining together the ideas of magnetic resonance imaging (MRI) and of atomic force microscopy (AFM). The basic principles of MRFM imaging were first described by J. A. Sidles in 1991 [197]. He suggested that the presence of a particle laying on a substrate could be detected by measuring non-inductively the nuclear magnetic resonance between the particle nuclear spin and the motion of a mechanical oscillator carrying a magnetic source. The gradient magnetic field of the source attached to the oscillator would couple with the magnetic moment of the particle and produce a force between them that would cause a detectable

change in the resonance of the scanning oscillator. Therefore, while conventional MRI uses an inductive coil to sense nuclear or electronic spins in a magnetic field gradient, MRFM uses a cantilever tipped with a ferromagnetic particle to directly detect a modulated spin gradient force between the sample spins and the tip itself. The first MRFM image was obtained in 1993 by O. Züger and D. Rugar at the IBM Almaden Research Centre [198]. In their experiment, they obtained a magnetic resonance force map of a sample of dyphenylpicrylhydrazil micrometre-size particles, by detecting the angstrom-scale vibrations induced by a magnetic tip on a cantilever holding the sample. The real-space spin density information, arising from the coupling between the magnetic tip and the resonantly excited spins in the sample, was recovered by using an image reconstruction technique. With their experimental apparatus Züger and Rugar achieved a lateral resolution of 5 μm and an axial resolution of 1 μm . The nanometric scale for the MRFM technique was reached only in 2004 when Rugar and co-workers obtained a 25 nm spatial resolution in one dimension for an unpaired spin in silicon dioxide [199]. In 2007 H. J. Mamin et al. performed a two dimensional nuclear magnetic resonance image with 90 nm spatial resolution [200]. They characterized a CaF_2 sample estimating that the detected signal came from a 90 nm \times 90 nm \times 80 nm volume containing an ensemble of roughly 30 million nuclear spins. This result turned out to be a considerable improvement over previous MRFM-based nuclear spin imaging achievements [201] and it established new frontiers for the MRFM technique, showing that it was capable of measuring signal coming from volumes 6×10^4 times smaller than those detectable through conventional MRI microscopy [196]. This result was a promising outcome especially considering that even with tip field gradients in the gauss per nanometre range, the force from an electron spin is only a few attonewtons, which is roughly a million times smaller than the force typically detected by an atomic force microscope (AFM).

The main limitation of the MRFM technique is that it requires cryogenic temperatures for the sample to be scanned. To obtain a 25 nm spatial resolution in one dimension Rugar's group had to maintain the vitreous silica sample at a temperature of 1.6 K in a small vacuum chamber [199], while to obtain a two dimensional 90 nm resolution Mamin and collaborators had to perform the measurement on their CaF_2 sample in vacuum and at 0.6 K [200]. The requirement of maintaining the sample at cryogenic temperatures limits most of the potential biological and medical applications for MRFM techniques [202].

3.3 An NV centre-based magnetometer

What originally motivated this work was determining whether it was possible to develop an imaging technique capable of detecting single spins or small spin ensembles in a target sample.

We looked at the nitrogen-vacancy (NV) centre in diamond in search for a positive answer, knowing that this particular diamond defect possesses unique magneto-optical properties that could be used for the purpose.

The idea is to use a nitrogen-vacancy (NV) centre hosted in a diamond nanocrystal as a probe. This probe would sense very weak magnetic fields, theoretically even those generated by electron and nuclear spins, allowing the development of an imaging technique with extremely high resolution. To detect single spins in the target sample, these have to be “frozen”. The sample would most likely have to be kept at cryogenic temperatures as per standard MRFM techniques, but the advantage of using an NV centre as the sensing probe is that it could operate at room temperature.

The basic concepts are the following. The nitrogen-vacancy centre in diamond is a unique solid state system whose electronic spin can be polarized by optical pumping and measured through state-selective fluorescence.

Excitation of the NV⁻ centre with a resonant microwave field and with an external magnetic field alters respectively its steady state population and its spin sublevel splitting, causing detectable changes in the fluorescence of the centre.

Using a single NV⁻ as a scanning probe, nanometre-sized magnetic structures present on a sample surface could be profiled by measuring the detectable changes they cause in the NV⁻ fluorescence.

3.3.1 The simplified energy level scheme of the NV⁻ centre

To present the spin and optical properties of the diamond NV⁻ centre, and to show how they can be used in quantum information technologies and in magnetometry, a simplified energy level scheme of the centre is considered (Fig. 3.2).

The NV⁻ centre is treated as a three-level system, with a ground triplet state ³A, a first optically excited triplet state ³E and an intermediate singlet state ¹A. The separation in energy between the triplet ³A ground and the optically excited ³E state is 1.945 eV (zero phonon line at 637 nm). They are both manifold in energy, showing a zero-field splitting between the spin sublevels of the electronic spin quantum number $m_s = 0$ and $m_s = \pm 1$. For the ground state the zero-field splitting has been measured to be $D_{gs} = 2.88$ GHz, which means that this transition is accessible via microwave excitation. The two ground sublevels $m_s = +1$ and $m_s = -1$ are degenerate in energy for symmetry reasons. A local change in the symmetry due to lattice irregularities, strain or external fields can lift the degeneracy making the sublevels distinguishable.

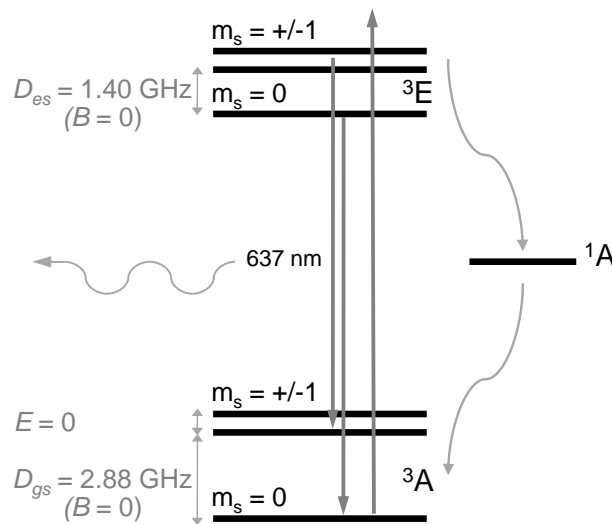


Figure 3.2. Simplified electronic-level scheme of the NV⁻ centre. The ground ³A and the excited ³E states are triplets and their separation in energy is 1.945 eV (ZPL at 637 nm). They both show a zero-field splitting between spin sublevels of electronic spin quantum number $m_s = 0$ and $m_s = \pm 1$; the ground-state zero-field splitting is $D_{gs} = 2.88$ GHz. The ground sublevels $m_s = +1$ and $m_s = -1$ are degenerate in energy for symmetry reasons, but a local change in the symmetry can lift the degeneracy making them distinguishable. The intermediate energy level ¹A is a singlet. The straight arrows indicate the optical excitation and the subsequent radiative decay, while the curved arrows indicate the non-radiative decay via the metastable singlet state ¹A (cf. c. 2, s. 2.2.3).

This simplified energy level scheme is the same presented in section 2.2.3, figure 2.8a, apart from a difference in the notation: here, the splitting of the levels is indicated by specifying the spin quantum number m_s instead of using the irreducible representations of states and the symmetric form of the wave-functions.

3.3.2 Optical and spin properties of the NV⁻ centre in diamond

The simplified energy level scheme of the NV⁻ is the working scheme we consider to describe the dynamic of the system and its properties.

Polarisation. The first interesting property of the NV⁻ centre is its optical polarisability (cf. c. 2, s. 2.2.3). This property is crucial for using the NV⁻ centre both as a spin quantum bit (qubit) and as a probe for high-resolution magnetometry.

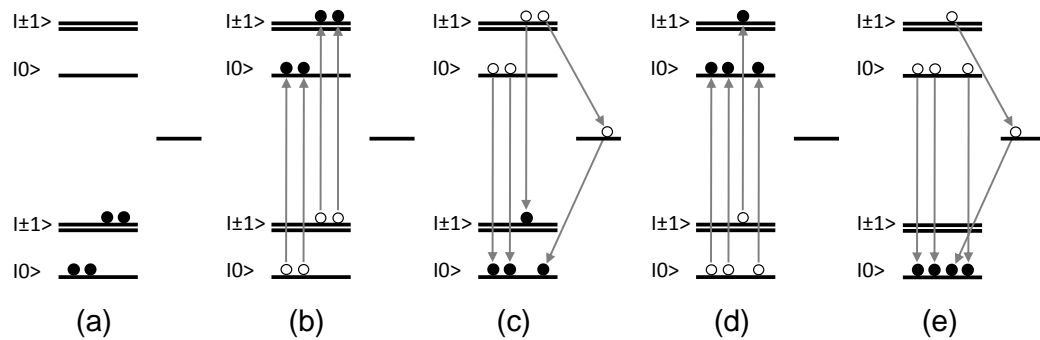


Figure 3.3. Schematic representation of the NV⁻ polarisation mechanism*. **a)** Initially the NV⁻ population is evenly distributed between the ground spin sublevels $m_s = 0$ and $m_s = \pm 1$ (indicated, respectively, as $|0\rangle$ and $|\pm 1\rangle$). **b)** The green laser excitation drives the optical transition (which is spin-conserving, i.e. $\Delta m_s = 0$) towards the excited state. **c)** The system relaxes, mainly radiatively (again $\Delta m_s = 0$), by emitting photons at 637 nm, but some part of the population from the excited spin sublevel $m_s = \pm 1$ relaxes non-radiatively, via the intermediate singlet level, towards the ground sublevel $m_s = 0$ (in this case the relaxation mechanism is not spin-conserving). **d)** At the following cycle, the green laser excitation drives again the optical transition (which is spin-conserving, $\Delta m_s = 0$) towards the excited state. **e)** As per step (c) part of the population from the excited spin sublevel $m_s = \pm 1$ relaxes non-radiatively towards the ground sublevel $m_s = 0$. After a few optical cycles, all the population ends up in the ground spin sublevel $m_s = 0$ and the NV spin state is therefore initialised. Note the clear difference between the unpolarised system in (a) and the polarised in (e).

Polarisation preferentially populates a certain state. In the case of the NV⁻, optical excitation preferentially populates the $m_s = 0$ ground spin state of the centre. Optical pumping causes a non-Boltzmann steady-state spin alignment of the NV⁻ in the ground state consisting of a re-orientation of the ground state spins. The direct implication of this is that the initial state of the system can be easily and reliably “set”.

* An isolated NV⁻ centre is a single photon source. This schematic representation is therefore only indicative and applies rigorously to an ensemble of NV⁻ centres. An alternative way of interpreting this is to consider the population of the states as that of a single NV⁻ centre, but at different instants of time shown simultaneously.

The polarisation mechanism is explained in figure 3.3*. Initially the NV⁻ is unpolarised (Fig. 3.3a) and the ground spin sublevels $m_s = 0$ and $m_s = \pm 1$ are equally populated. In reality the occupation probability of the two sublevels obeys the Boltzmann steady-state distribution, but in this example it is assumed for simplicity (without losing generality) that the two sublevels are equally populated (the concept can be easily extended to the case with the actual Boltzmann steady-state distribution for the system). By pumping the NV⁻ centre with an exciting laser (e.g. 514 nm or 532 nm), the population is optically excited from the ground spin sublevels $m_s = 0$ and $m_s = \pm 1$ to the corresponding optically excited spin levels (Fig. 3.3b). The optical transition is spin-conserving, meaning that the quantum spin number m_s is conserved ($\Delta m_s = 0$). From the optically excited electron state, the system can decay radiatively, directly towards the ground state with emission of photons ($\lambda = 637$ nm), or non-radiatively, towards the ground state through the singlet intermediate spin level (Fig. 3.3c). The radiative optical transition is again spin-conserving ($\Delta m_s = 0$). The non-radiative decay is allowed by symmetry and it is not necessarily spin-conserving. Although it can involve both the excited sublevels with spin numbers $m_s = 0$ and $m_s = \pm 1$, it turns out, from symmetry considerations (i.e. the involved levels/orbitals must share the same symmetry), that the most probable non-radiative path is the one from the excited state with $m_s = \pm 1$, through the intermediate singlet level, and eventually to the ground state with $m_s = 0$ (Fig. 3.3c). After a few optical cycles, the NV⁻ ends up polarised in the ground-state sublevel with the quantum number $m_s = 0$ (Figs. 3.3d, e). More precisely, such an excitation and decay cycle causes a non-Boltzmann steady-state spin alignment of the NV⁻ centre in the ground state, consisting of a re-orientation of the ground-state spins. Note the clear difference in the population distribution between the unpolarised system in the schematic representation of figure 3.3a and the polarised system of figure 3.3e after a few optical polarising cycles. For the sake of completeness and as already pointed out (cf. c. 2, s. 2.2.3) the NV⁻ spin polarisation is actually not complete (~ 70-80%), due to a slight mixing of the spin sublevels.

The key point to remember about the polarisation of the NV⁻ centre is that, starting from a random spin population density, the NV⁻ can be initialised (polarised) into a specific spin state. This is necessary to prepare the system for further manipulations.

Control. Considering an NV⁻ centre initialised (polarised) in its ground state with $m_s = 0$, manipulation of the NV⁻ spin state would enable driving the ground-state spin sublevel transition from $m_s = 0$ to $m_s = \pm 1$ (Fig. 3.4).

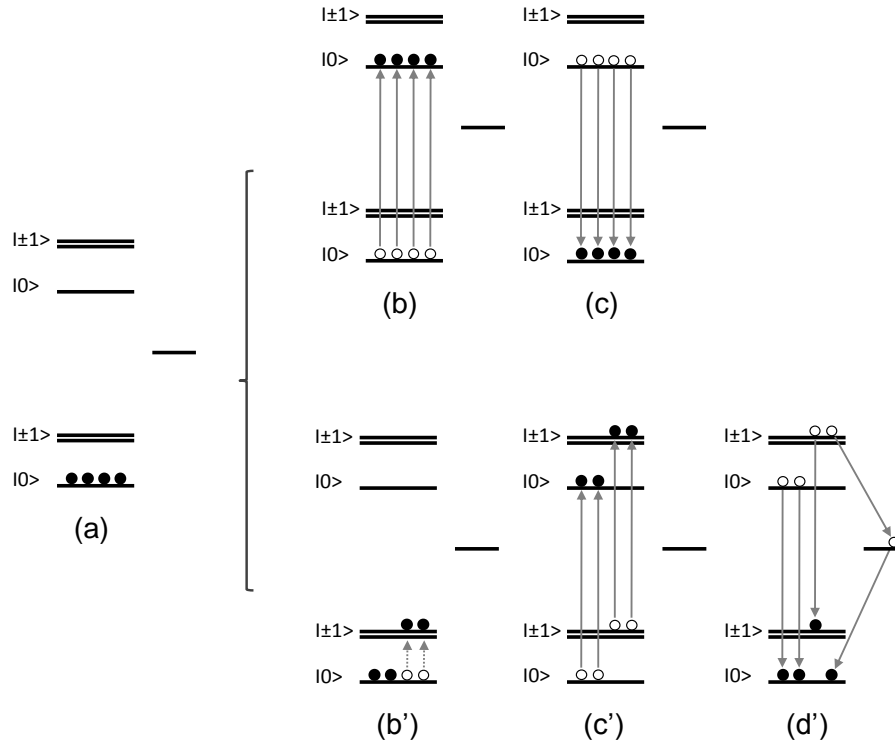


Figure 3.4. Schematic representation of the NV⁻ spin manipulation and read-out mechanisms*. **a)** Initially the NV⁻ centre is polarised by optical excitation. **b, c)** With no microwave field applied all the population cycle radiatively emitting photons (ZPL at 637 nm) with a maximum in the corresponding detected fluorescence. **b')** A resonant (2.88 GHz) microwave field (dashed lines) is used to raise part of the population from the ground spin sublevel $m_s = 0$ to the ground-state spin sublevel $m_s = \pm 1$ (indicated, respectively, as $|0\rangle$ and $|\pm 1\rangle$). **c', d')** This fraction of raised population can relax to the ground state non-radiatively through the intermediate singlet level: the non-radiative relaxation mechanism causes a detectable drop ($\sim 30\%$) in the fluorescence of the NV⁻ centre. Note the difference between (c), where all the population cycles radiatively and (d'), where only a fraction of it cycles radiatively.

The controlled ground-state spin transition is achieved by applying a resonant microwave field (~ 2.88 GHz at zero magnetic field) with the transition to access (Fig. 3.4b'). Averaging in time, the electron spin nutates between the $m_s = 0$ and $m_s = \pm 1$ ground spin

* An isolated NV⁻ centre is a single photon source. This schematic representation is therefore only indicative and applies rigorously to an ensemble of NV⁻ centres. An alternative way of interpreting this is to consider the population of the states as that of a single NV⁻ centre, but at different instants of time and shown together.

states due to the coherent interaction of the spin with the microwave field. The spin nutation can be described as [161, 203]:

$$r_3(t) = r_3(0)(1/\varpi^2)(\Delta\omega^2 + \omega_1^2 \cos\varpi t) \quad (3.3)$$

where $r_3(t)$ is the difference between the probability to find the system in the $m_s = 0$ and $m_s = \pm 1$ sublevel, $\Delta\omega$ is the detuning between the microwave frequency and the actual transition frequency, ω_1 is the microwave Rabi frequency and $\varpi = \sqrt{\Delta\omega^2 + \omega_1^2}$.

Measurement. Considering an NV⁻ centre that has been initialised (polarised) in its ground-state spin sublevel $m_s = 0$ (Fig. 3.4a), applying a resonant microwave field causes an increase in the population of the $m_s = \pm 1$ spin sublevels (Fig. 3.4b') which leads to an overall decrease in the fluorescence because of the non-radiative decay via the intermediate metastable state (Figs. 3.4c', d'). The fluorescence intensity carries the information about the spin state of the NV⁻ centre (optically detected electron spin resonance (ESR) spectrum). In figure 3.4, note the difference between (c) where there is no microwave field applied and all the population cycle radiatively and (d') where only a fraction of it cycles radiatively.

In magnetometry applications, measuring the decrease in fluorescence when the transition $m_s = 0 \rightarrow m_s = \pm 1$ is driven by the resonant microwave field is indispensable for observing optically detected magnetic resonance (ODMR) based on a change in the resonant frequency as a function of magnetic field (cf. s. 3.3.3).

Relaxation time. The control and measurement of the NV⁻ centre spin-state requires taking into account the spin relaxation time. This refers to the time over which the spin stays in a certain state before it starts randomly losing its phase or is involved in a spin-flip event due to coupling to the environment (i.e. interaction with another electron or a nuclear spin). More specifically, placed in a coherent superposition of spin-up and spin-down states, the spin of an isolated NV⁻ centre undergoes, in time, energy and phase relaxation processes. These relaxation processes occur on different and characteristic time scales, generally indicated with T_1 , T_2 and T_2^* .

T_1 is known as spin-lattice or longitudinal (spin-flip) relaxation time. It involves the interaction of a single spin with the surrounding lattice field. The lattice field is the complex overall magnetic field caused by the nuclei in the crystal lattice structure undergoing vibrational and rotational thermal motion around their equilibrium positions. The spin-lattice relaxation mechanism refers to the process in which a spin, brought to a higher energy spin-state for instance by a radio-frequency (RF) pulse, gives the extra-energy it obtained back to the surrounding lattice (i.e. the lattice excitation modes carry away energy quanta on the scale of the spin Larmor frequency), thereby restoring its equilibrium state (spin-flip).

T_1 is affected by the mobility of the lattice. In general, higher lattice mobility, with associated higher vibrational and rotational frequencies of the nuclei, are more likely to induce the transition (relaxation) from high to low spin states. On the other hand, the relaxation probability decreases for extremely high lattice mobility since the extremely high vibrational and rotational frequencies become too far off-resonance to induce the transition between the spin-states. In other words, only lattice vibrations with frequency matching the Larmor frequency of the spin can induce a spin-flip with a rate [204, 205]:

$$\frac{1}{T_1} = \left(\frac{54\pi\nu^2}{\hbar\rho\nu_0^5} \right) \left(\frac{\mu_B^2}{r_0^3} \right)^2 kT \quad (3.4)$$

where ρ is the mass density, ν is the oscillator frequency, ν_0 is the velocity of sound, r_0 is the lattice separation of neighbours, μ_B is the Bohr magneton, k is the Boltzmann's constant and T is the temperature. Due to the strong covalent bonds between the low-mass carbon atoms, which results in low lattice mobility, diamond shows relatively long phonon-limited spin-lattice relaxation times $T_1 \sim 10^4$ s (at $T = 300$ K).

The electron spin-flip process can also be induced by inelastic scattering of a higher frequency lattice phonon. In this case (Raman process) the relaxation rate is [204, 205]:

$$\frac{1}{T_1} = \left(\frac{163\pi^2 6!}{\rho^2\nu_0^{10}} \right) \left(\frac{\mu_B^2}{r_0^3} \right)^2 \left(\frac{kT}{h} \right) \quad (3.5)$$

and the corresponding relaxation time is $T_1 \sim 10^2$ s (at $T = 300$ K).

Another spin-lattice relaxation mechanism involves the interaction with optical phonons (Orbach process [206]). In diamond this process is not efficient since optical phonons are not excited under ambient conditions.

The spin-lattice relaxation time T_1 can be measured by using pulsed electron paramagnetic resonance (EPR) spectroscopy and performing echo-detected inversion recovery or saturation recovery sequence experiments [207].

T_2 is known as spin-spin or transverse dephasing relaxation time. It is also commonly referred to as coherence time, although the two terms are not strictly interchangeable [208]. It involves the dipolar interaction of a single spin with the “spin bath” formed by the surrounding spins. The bath spins undergo spin-flips events and produce a fluctuating local field so that the dipolar coupling induces energy conserving spin flip-flop processes in the NV⁻ single spin; this results in a loss of the NV⁻ spin memory phase.

In diamond, the spin bath can vary from sample to sample. In general the spin bath is dominated by the electron spins of residual nitrogen atoms: they constitute the most significant source of dephasing for the NV⁻ centre and shorten its T_2 [161, 209]. Temperature plays a key role too: the lower the temperature the lower the spin bath flip rate is and therefore the longer the NV⁻ coherence time T_2 is. The spin-spin relaxation time T_2 of the NV⁻ centre increases when the concentration of nitrogen impurities in the sample is reduced; for very low nitrogen concentration (e.g. 5×10^{-2} ppb) the main source of electron spin decoherence becomes the nuclear spin bath constituted by ¹³C atoms and the corresponding spin-spin relaxation time T_2 can rise up to ~ 0.5 -2 ms [204, 207, 210].

The spin-spin relaxation time T_2 can be measured by using pulsed electron paramagnetic resonance (EPR) spectroscopy and performing Hahn echo sequence experiments [211].

Nutation experiments show that initialising, manipulating, and reading out an NV⁻ centre spin state is feasible. The NV⁻ centre is initialised with a green laser, then the laser is switched off and a microwave pulse of certain duration is applied and the intensity of the fluorescence is monitored. A transient nutation (periodic modulation) in the fluorescence intensity is observed according to the duration of the microwave pulse applied. Upon increasing the microwave pulse length, more of the population is inverted (from the $m_s = 0$ ground state to the $m_s = \pm 1$ ground state), until the full population inversion is reached (for a pulse, indicated as a π -pulse, of specific duration) and therefore the minimum fluorescence is observed [50, 161]. Usually, in a nutation experiment the harmonic oscillation pattern of the fluorescence appears to be modulated by an exponentially decaying function: the decay envelope represents the decoherence or dephasing time T_2^*

of the NV⁻ centre. A long coherence time is a technologically desirable characteristic for a quantum spin system. It means that once the spin state is initially set, there is a window of time long enough to actually manipulate and read-out the state before the information is lost due to interactions with the environment. The NV⁻ has a long coherence time T_2 , up to 1.8 ms [204] This is a few orders of magnitude larger than the duration of a π -pulse (as fast as a few ns, depending on power and resonant frequency of the microwave field applied) required to induce the NV⁻ spin-state inversion, and which sets the time basis for performing single quantum operations. In comparison, the spin coherence times T_2 of, for instance, semiconductor quantum dots are much shorter, in the range of $\sim 1 \mu\text{s}$ [212], while those of single molecules are of the order of $\sim 1\text{-}10 \text{ ns}$ [213, 214].

For the coherence time T_2 , a distinction is generally made between the spin-spin relaxation times T_2 and T_2^* . T_2 refers rigorously to the homogeneous relaxation time for a single quantum system, while T_2^* to the inhomogeneous decay time averaged over an ensemble of quantum systems. The inhomogeneous coherence time T_2^* is also used for single quantum systems in place of T_2 to account for variation of the system over time, under the hypothesis of ergodicity (i.e. the average of the variations of T_2 for a single system in time coincides with the average of the variations over an ensemble of systems in space).

In general, the following relationships hold between the relaxation times T_1 , T_2 and T_2^* :

$$\begin{cases} T_2 \leq 2T_1 \\ T_2^* \leq T_2 \end{cases} \quad (3.6)$$

The bounds in (3.6) show that the ultimate limit for the coherence time is given by the spin-lattice relaxation process (T_1), which is expected to occur in the timescale of seconds, and that local field inhomogeneities result in a T_2^* relaxation time shorter than T_2 .

3.3.3 Continuous wave optically detected magnetic resonance (cwODMR)

The energy-level structure of the NV⁻ centre in diamond is unique. The described capability of preparing, manipulating, and reading-out its electron spin state together with the fact that it is possible to detect optically the response of the centre to external fields makes it theoretically feasible to consider an NV⁻ centre-based high resolution magnetometer at room temperature.

In presenting the read-out of the NV⁻ spin state (cf. s. 3.3.2), it has been shown that a microwave field resonant with the transition between the $m_s = 0$ and the $m_s = \pm 1$ ground-state spin sublevels causes a decrease in the fluorescence signal. The fraction of population that is driven by the microwave radiation to the $m_s = \pm 1$ ground spin state, once optically pumped to the electronic excited state, can decay non-radiatively again to the ground state via the intermediate singlet level, without emitting a photon. This results in a decrease in fluorescence intensity from the NV⁻ centre. Practically, if an experiment is performed in which an NV⁻ centre is optically pumped and its emission is measured while a microwave field, sweeping in frequency, is applied, the fluorescence intensity will decrease when the microwave frequency is exactly resonant with the transition between the $m_s = 0$ and the $m_s = \pm 1$ ground-state spin sublevels. This measurement is known as continuous wave optically detected magnetic resonance (cwODMR) and the presence of the above said negative peak in the fluorescence (Fig. 3.5) proves the magnetic resonance in the triplet ground state of the NV⁻ centre [100, 215].

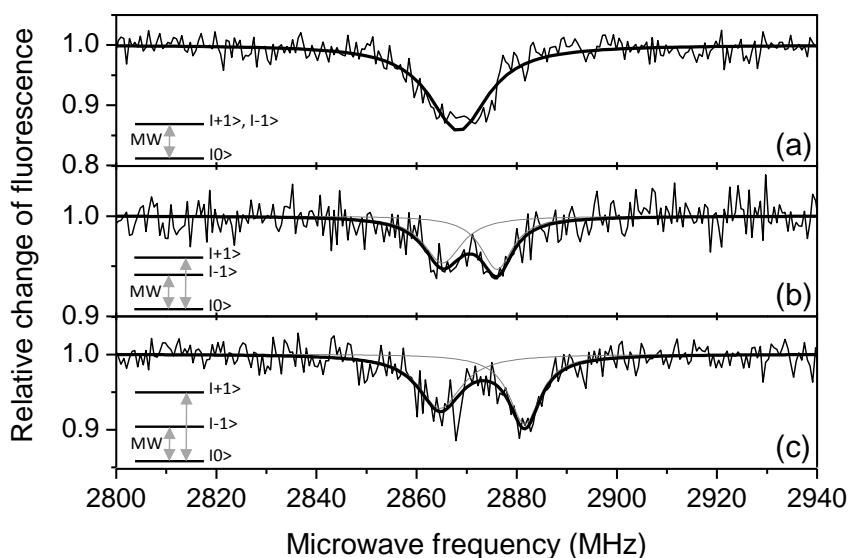


Figure 3.5. Continuous wave optically detected magnetic resonance (cwODMR) spectrum measured for different NV⁻ centres. The relative change in fluorescence for three different centres, while a microwave field was sweeping in the range 2800-2940 MHz, was recorded. The smooth curves superimposed on the data are Lorentzian fits. The insets show the spin sublevels in the ³A ground state of the centre with the arrows indicating the microwave (MW) frequency. **a)** The ground-state sublevels $m_s = +1$ and $m_s = -1$ are degenerate and only one negative peak in the fluorescence can be resolved. **b, c)** The ground state sublevels $m_s = +1$ and $m_s = -1$ are distinguishable in energy and two distinct negative peaks can be detected in fluorescence.

Ideally, the two ground-state sublevels $m_s = +1$ and $m_s = -1$ are degenerate and hence indistinguishable in energy. The degeneracy is a consequence of the trigonal symmetry of the NV⁻ centre. In this symmetry, assuming the z-axis lying along the nitrogen and the vacancy as the major axis, the states with S_z spin projection, $|A_1\rangle = |A_2, S_z\rangle$ (or equivalently with $m_s = 0$), are distinguished in energy from those with S_x and S_y spin projections, $|E_x\rangle = |A_2, S_x\rangle$ and $|E_y\rangle = |A_2, S_y\rangle$ (i.e. $m_s = \pm 1$). The states with S_x and S_y spin projection, respectively $|E_x\rangle = |A_2, S_x\rangle$ and $|E_y\rangle = |A_2, S_y\rangle$ ($m_s = -1$ and $m_s = +1$), are degenerate in energy because spatially the x- and the y-axes are symmetry-indistinguishable. However, the splitting in energy of these sublevels is possible (Fig. 3.5b, c). As already described (cf. c. 2, s. 2.2.3), ensembles of NV⁻ centres or even single NV⁻ centres located on sites under strain are subject to a distortion in the ideal trigonal symmetry and have the degeneracy between the sublevels with $m_s = -1$ and $m_s = +1$ removed. But, more interestingly, the splitting can be induced by the presence of an external magnetic field B .

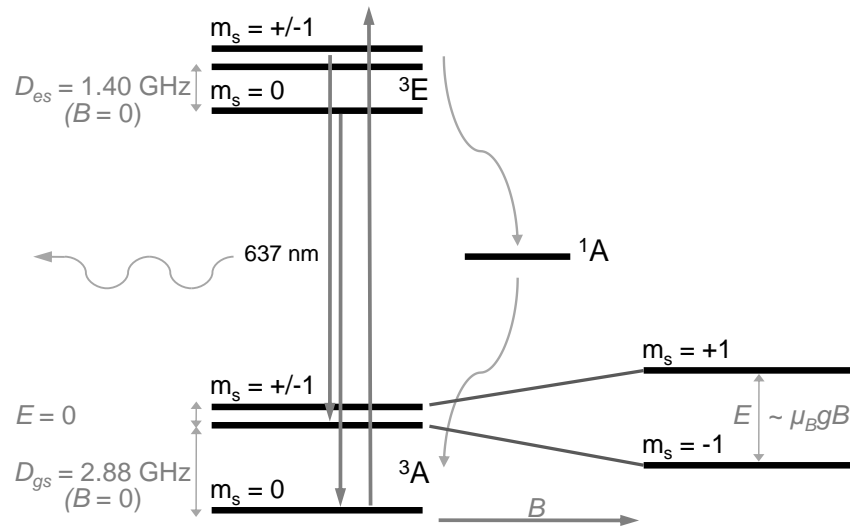


Figure 3.6. Effect of an external magnetic field B applied to an NV⁻ centre along the z-axis coinciding with the centre principal C_3 axis of symmetry. According to the Zeeman effect the field interacts differently with electrons having different spin projections and modifies their energies. For B parallel to z , the doublet ground-state sublevel with the quantum spin number $m_s = \pm 1$ is split and the two sublevels with $m_s = -1$ and $m_s = +1$ are no longer degenerate. The energy separation is proportional to $g\mu_B B$ where μ_B is the Bohr magneton, $g = 2$ is the g -factor, and B is the intensity of the external magnetic field. A similar splitting, although of a different type, would be observed in the absence of an external magnetic field for an NV⁻ centre site whose symmetry is reduced by strain or by the effect of other NV⁻ centres close to it.

Specifically, when a static magnetic field is applied to an NV⁻ centre along the [111] direction, coinciding with the principal C_3 axis lying along the nitrogen and the vacancy,

the degeneracy between the ground-state doublet spin levels is lifted by the Zeeman effect and the two sublevels become distinguishable in energy (Fig. 3.6).

The effects of an applied magnetic field and lowered symmetry in the NV⁻ site are similar. In fact, even if the nature of the two phenomena is different, they both separate the degenerate doublet ground-state spin levels in energy. In more detail, the spin Hamiltonian H of the NV⁻ defect (neglecting the electron-nuclear spin coupling) can be written as the sum of the zero field and the Zeeman terms [37]:

$$H = D[S_z^2 - S(S+1)/3] + E(S_x^2 - S_y^2) + g\mu_B \mathbf{B} \cdot \mathbf{S} \quad (3.7)$$

where D and E are the zero-field splitting parameters, $S = 1$ is the spin number, $g = 2$ is the electron g -factor, μ_B is the Bohr magneton, and \mathbf{B} is the applied magnetic field. The sublevels $m_s = 0$ and $m_s = \pm 1$ are separated even at zero external magnetic field ($D = 2.88$ GHz), and for symmetry reasons, the sublevel $m_s = \pm 1$ of the NV⁻ defect is nominally degenerate ($E = 0$).

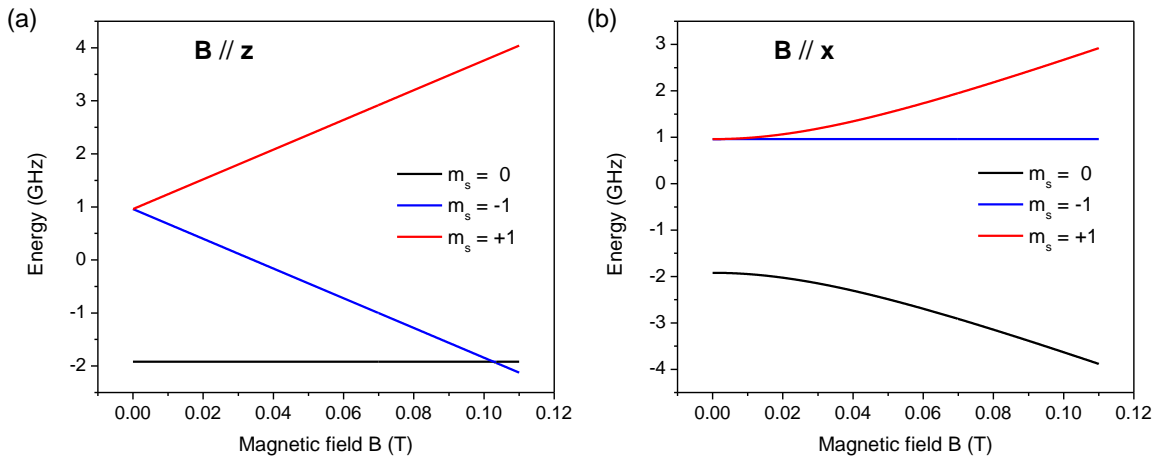


Figure 3.7. Energy shift for the NV⁻ ground state sublevels $m_s = 0$, $m_s = +1$ and $m_s = -1$, calculated using the Hamiltonian described in equation (3.7) for magnetic field \mathbf{B} parallel to the nitrogen-vacancy z -axis (a) and parallel to the x -axis (b).

The energy splitting of the doublet ground-state sublevel can hence be the result of two different effects that can also be combined:

- A lowered symmetry of the NV⁻ site (term proportional to E in the Hamiltonian H).
- The Zeeman effect induced by the external magnetic field (term proportional to \mathbf{B} in the Hamiltonian H). In this case, the field interacts differently with electrons having

different spin projections and quantum numbers $m_s = 0$, $m_s = +1$ and $m_s = -1$, modifying their energies with regard to the orientation of the magnetic field B .

In the case of the Zeeman effect, the splitting is obviously proportional to the intensity of the magnetic field. As the intensity increases, the separation in energy between the spin sublevels increases. At a value for the magnetic field B parallel to z of about 0.1 T, the ground spin sublevel with $m_s = -1$ reaches the ground-state spin sublevel with $m_s = 0$ and “level anticrossing” occurs (Fig. 3.7) [216, 217].

3.3.4 Towards a practical implementation

In 1993, the detection of single-molecule spin by optically detected magnetic resonance (ODMR) was demonstrated for a pentacene molecule in a host crystal of p-terphenyl [218, 219]. These experiments showed that ODMR measurements could overcome the sensitivity of conventional magnetic resonance spectroscopy, limited to the detection of 10^{10} electron spins or 10^{16} nuclear spins, and fuelled the idea of a spin microscope based on optically detected magnetic resonance. Such a microscope, or magnetometer, would use a photoluminescence nanoprobe mounted on a scanning tip and exhibiting ODMR to map the target sample with single spin sensitivity [220].

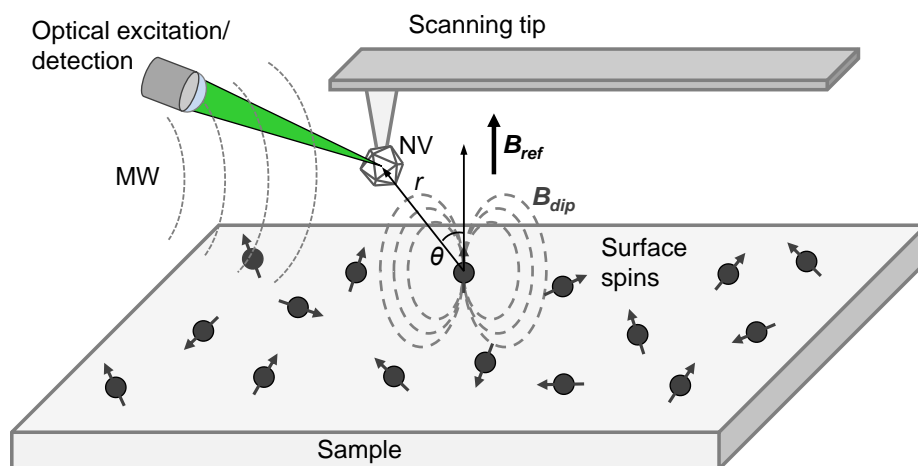


Figure 3.8. Schematic representation of a possible setup for an NV⁻ centre-based magnetometer. A single NV⁻ centre hosted in a nanometre scale diamond crystal is attached to a scanning tip. The centre is constantly excited optically and its fluorescence intensity is measured. A resonant microwave (MW) field and a reference magnetic field B_{ref} are applied and ODMR is observed, which initialises the magnetometer. The scanning tip can then be moved over the sample and any additional magnetic field, theoretically even that of surface spins B_{dip} , is detected as a frequency shift in the ODMR spectrum.

The negatively charged nitrogen-vacancy (NV^-) centre in diamond possesses the capability for spin-state initialisation, manipulation and optical read-out; it also exhibits ODMR. These features make it a perfect candidate probe for a spin magnetometer.

Figure 3.8 shows a possible design for such a magnetometer [37, 220]. In this case an NV^- centre in a diamond nanocrystal is attached to the end of an atomic force microscope (AFM) scanning tip and is used as a photoluminescence nanoprobe.

Here, the simplest operational scheme of the magnetometer is presented to illustrate the principle; variations of this scheme are possible. The NV^- centre is constantly excited optically while a microwave (MW) field is swept in frequency (resonantly with the NV^- transition between the $m_s = 0$ and $m_s = \pm 1$ spin ground states) and a reference magnetic field B_{ref} is applied.

The microwave field disrupts the optically pumped polarisation of the NV^- centre inducing the transition from the spin state $m_s = 0$ to the $m_s = \pm 1$. Since the “brighter” spin state $m_s = 0$ scatters $\sim 30\%$ more photons than the “darker” $m_s = \pm 1$, the effect of the MW field is to produce a negative peak in the trace of the NV^- fluorescence against the MW frequency. At the same time, the applied reference magnetic field B_{ref} splits the single negative peak in two distinctive peaks by lifting the degeneracy in energy between the two sublevels with quantum numbers $m_s = +1$ and $m_s = -1$ with respect to the relative orientation of the field to the nitrogen-vacancy principal axis. The positions of the ESR resonances allow for calculation of the intensity of a certain external magnetic field acting on the NV^- probe. The initial frequency separation between the two peaks is fixed by the reference magnetic field B_{ref} . Whenever the scanning NV^- probe is affected by an additional magnetic field B_{dip} , that field induces an extra shift in frequency separation in the ODMR trace.

Frequency shifts in the ODMR spectrum of the probing NV^- centre could therefore be used to locally map the distribution of magnetic domains over a target sample.

3.3.5 Experimental and practical challenges

High-resolution magnetometry using the NV^- centre in diamond as a probe is theoretically feasible. Nevertheless the actual realisation of an NV^- centre-based

magnetometer like the one proposed in figure 3.8 requires overcoming several practical issues.

Nanodiamond-to-AFM tip attachment. One of the first challenges is to attach a nanodiamond of only few nanometres in size containing an NV⁻ centre to the end of an atomic force microscope (AFM) tip.

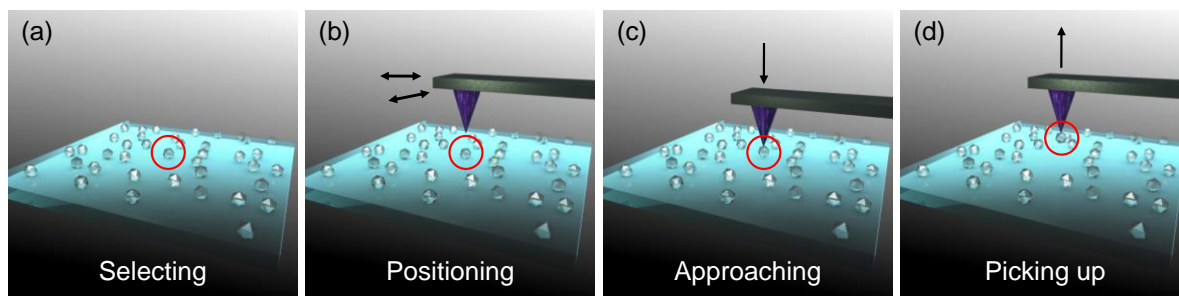


Figure 3.9. Step-by-step procedure illustrating the attachment of a fluorescent nanodiamond to the apex of an atomic force microscope (AFM) tip. **a)** Isolated diamond nanocrystals are prepared on a cover slip; a nanodiamond containing an NV⁻ centre is selected (red circle). **b)** The AFM tip is positioned carefully on top of the identified nanodiamond. **c)** The AFM tip is lowered; it approaches and reaches the crystal. **d)** The AFM tip is lifted and the nanodiamond, now attached to the tip, is picked up.

The method we employ is conceptually straightforward and shown schematically in figure 3.9. A cover slip is prepared to have several diamond nanocrystals lying on the surface. An atomic force microscope (AFM) scan and a corresponding confocal scan (cf. c. 4, s. 4.5) are performed to select a nanodiamond containing a fluorescent NV⁻ centre [221, 222]. Once the candidate nanodiamond has been identified, the AFM tip is lowered down to the cover slip and the nanodiamond is picked up. The AFM tips we use have radius of curvature in the range 6-10 nm (Silicon tip NSG01; NT-MDT), while the fluorescent diamond nanoparticles can have diameters of any size greater than ~ 5 nm.

To guarantee that the nanodiamond stays attached to the AFM tip we use a UV-cure glue (Adhesive NOA61; Thorlabs) which cures under UV-light illumination. Before being positioned on top of the nanodiamond, the AFM tip is dipped in a drop of glue located nearby on the sample. The tip is then positioned on top of the candidate nanodiamond and lowered to reach it. UV light (or alternatively suitable laser light) is shone on the apex of the tip for a few minutes and the glue is cured. The tip with the nanodiamond firmly attached to it can then be lifted and moved around using the AFM controls.

Figure 3.10 shows two fluorescence images we have taken of the same AFM tip before (a) and after (b) attaching a nanodiamond containing an NV⁻ centre (arrow) to the end of the tip.

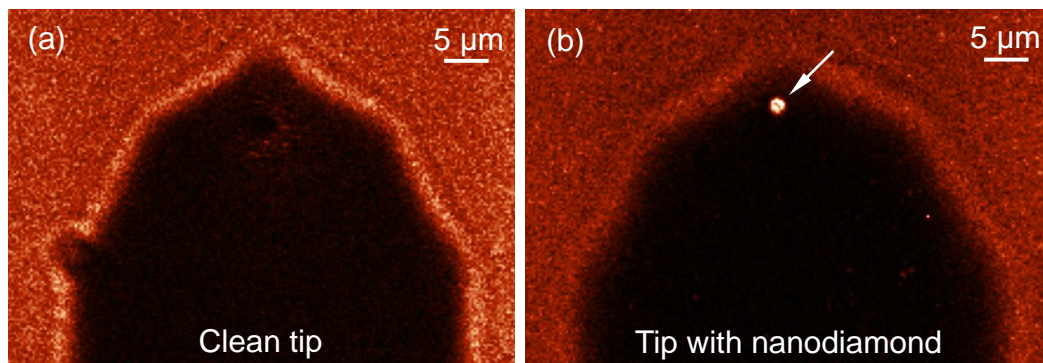


Figure 3.10. Fluorescence images from the same AFM tip. **a)** Clean tip. **b)** The same tip after we attached a nanodiamond containing an NV⁻ centre to the apex of the tip (arrow).

The method we use to attach a diamond nanoparticle to the end of an AFM tip presents few additional technical challenges. For instance, we use a specific procedure to limit the amount of glue on the cantilever to a volume below cubic microns. After the tip is dipped into the glue, it is moved to a clear area and tapped several times on the cover slip to allow some of the glue to drop off. Another aspect to consider is that the glue can be hygroscopic and, in time, absorb moisture from the air; this can obscure the fluorescence signal of the NV⁻ centre hosted in the diamond probe and can reduce its total life span.

Our approach and others [223] build on previous work. The attachment of particles to AFM cantilevers was first demonstrated in 1991, but at that time the particles were several microns in size [224]. We are now trying to push the limit and functionalise AFM cantilevers with particles at the nanoscale.

The manipulation of nanoparticles is nowadays becoming more and more feasible thanks, for instance, to the integration of near-field scanning optical microscopy (NSOM) systems with AFM technologies [177, 225, 226].

Another possibility to be considered is the direct fabrication of a diamond AFM scanning tip with an NV⁻ centre located at its apex. Diamond has already been used both to coat silicon AFM tips [227] and to make full diamond tips [228-230]. Generating an NV⁻ centre,

for instance via electron-irradiation or ion-implantation at the end of a high-purity diamond AFM tip, is feasible and would overcome many of the technical challenges our technique faces. However, the main drawback of such an approach is controlling the position of the NV⁻ centre in the diamond relative to the surface. As described below, this is crucial for the resolution of the magnetometer.

Sensitivity. The magnetometer exploits the frequency shift in the ODMR spectrum of the probing NV⁻ due to the Zeeman effect to detect and measure magnetic fields (cf. s. 3.3.3). This phenomenon can clearly be measured and proves the feasibility of a magnetometer that uses an NV⁻ centre in diamond as a sensing probe.

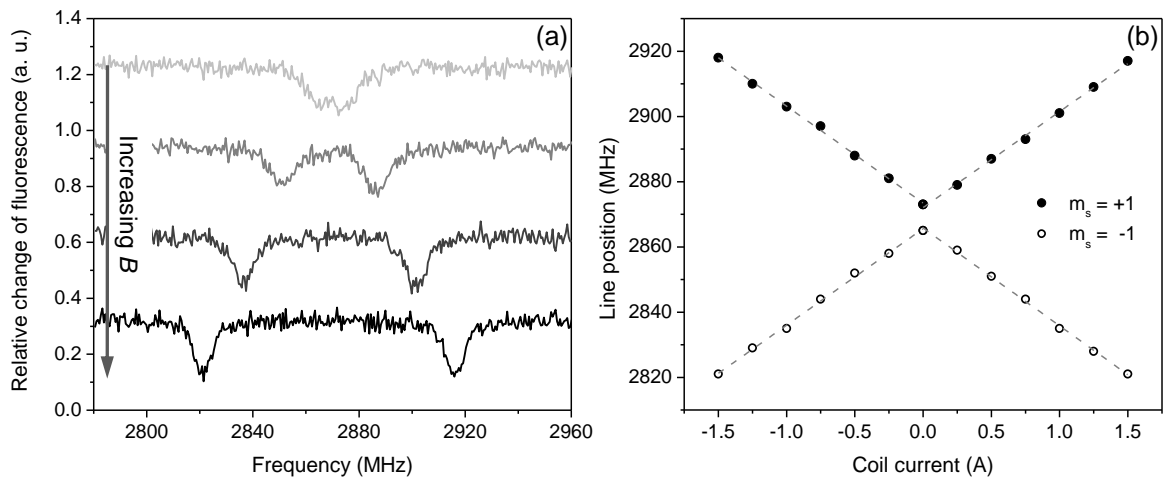


Figure 3.11. Effect of an external magnetic field B on the continuous wave optically detected magnetic resonance (cwODMR) spectrum of a single NV⁻ centre. **a)** CwODMR spectra of the NV⁻ centre measured experimentally with different magnitudes of the field B applied. In each trace the two negative fluorescence peaks are due to the depolarisation (ground state spin level transition $m_s = 0 \rightarrow m_s = \pm 1$) induced by the resonant microwave field constantly sweeping in the range 2780-2960 MHz. **b)** Line position in frequency for the pairs ($m_s = +1$, $m_s = -1$) of fluorescence negative peaks plotted against the coil current generating the magnetic field B : experimental data-points (circles) and corresponding linear fits (dashed lines) are represented. In (a) and (b) the separation in frequency (energy) between the peaks is proportional to the intensity of the magnetic field B (Zeeman effect). As the magnetic field intensity increases the negative fluorescence peaks separate in frequency. Note the strong direct proportionality (dashed lines in b) between the frequency shift and the magnetic field applied.

Figure 3.11 shows a cwODMR experiment conducted on a single NV⁻ centre isolated in a diamond nanocrystal. We recorded the relative change in fluorescence for the same single centre while a microwave field was constantly sweeping in the range 2780-2960 MHz and an external magnetic field B was applied. As we increased the intensity of the field B , the

separation in frequency (energy) between the negative fluorescence peaks increased proportionally (Fig. 3.11b, dashed lines).

Theoretically the detection of single electron and nuclear spins with this method is possible. In 2008, G. Balasubramanian and collaborators firstly demonstrated the feasibility of an NV centre-based magnetometer [37]. They attached a nanocrystal containing a single NV centre to the tip of an AFM cantilever and used it to profile the magnetic field produced by a nanometre-sized magnetic structure. The magnetic field resolution of such a system was 0.5 mT.

Referring to the setup presented in figure 3.8, the intensity of the magnetic field B_{dip} created by a single spin and located at a distance r from the nitrogen-vacancy nanoprobe can be expressed as [37]:

$$B = \frac{\mu_0 \mu}{4\pi} \frac{\sqrt{3 \cos^2 \theta + 1}}{r^3} \quad (3.8)$$

where μ is the single spin magnetic moment and θ is the angle between the vector connecting the two spins (the NV⁻ probe spin and the single spin to be detected) and the vector of the external magnetic field. Given $\mu = -(1/2)g_e \mu_B \approx 10^{-23} \text{ JT}^{-1}$ and $\mu_0/4\pi \approx 10^{-7} \text{ NA}^{-2}$, a field of 10^{-5} T can be obtained for a distance between the electron and the nitrogen-vacancy spin of 5 nm. For the nitrogen-vacancy centre this gives up to 0.3 MHz of electron spin resonance (ESR) frequency shift which is within the detectable limits. Nuclear spins are harder to detect as they produce lower magnetic fields $\sim 10^{-8} \text{ T}$ with a corresponding kHz shift in the ESR spectrum of the probe NV⁻ centre.

The resolution of such a magnetometer based on the cwODMR signal of an NV⁻ centre would be determined by the ESR linewidth. The narrower the linewidth, the better the capability of resolving the separation between the two negative fluorescence peaks is. From a practical point of view, the linewidth is mainly limited by two factors: the oscillation of the nanodiamond attached to the AFM scanning cantilever and the decoherence time T_2 of the probing NV⁻ centre. The first effect can be countered by phase locking the detection to the oscillatory motion of the cantilever and by using echo-based techniques with an echo period matched to a single oscillation period of the cantilever. The second effect can be reduced by using ultrapure diamond with long decoherence time T_2 ($\sim \text{ms}$) for the hosted NV⁻ centre. The use of echo-based techniques and ultrapure

diamond ESR linewidths $\sim 10^2$ Hz are achievable and even single nuclear spins at few nanometres distance from the NV^- probe could in principle be detected under ambient conditions [38, 160].

CwODMR demonstrates the basic principles of an NV^- centre-based magnetometer. Different operating regimes have been developed to increase the sensitivity of such a magnetometer beyond the ESR linewidth. These schemes use single [37, 38, 204] and multiple [231-233] spin-echo pulsed sequences. The NV^- is polarised via laser pulse excitation in its $m_s = 0$ spin-state and then prepared in a superposition of spin-states $m_s = 0$ and $m_s = \pm 1$ via a microwave $\pi/2$ pulse tuned to this transition (“initialising” stage). After the initialisation, the NV^- spin-state is let to evolve; the Zeeman shift due to the magnetic field produces a phase difference proportional to the field (“sensing” stage). Finally, the phase shift is detected as a population difference upon the application of a suitable control pulse (“read-out” stage). In 2008 the group of J. R. Maze, quickly followed by others, started conducting proof-of-principles experiments using the NV^- centre and spin-echo schemes to show the capability of detecting oscillating magnetic fields at room temperature with sensitivities approaching the shot-noise-limit, i.e. \sim few nT $\text{Hz}^{-1/2}$ [38, 231-233].

Single NV^- centre probe. For the type of magnetometer proposed here, a desirable feature would be to have the magnetic sensing nanodiamond hosting only a single NV^- centre. The reason is that several NV^- centres with randomly orientated dipoles in the same nanodiamond would make it much harder to identify and distinguish the frequency shift of the negative fluorescence peaks in the ESR spectrum. This is however possible, providing that the number and relative orientations of the NV^- centres in the nanodiamond probe are thoroughly characterised in advance.

The requirement of selecting a nanodiamond hosting a single NV^- centre is not very difficult to achieve. Autocorrelation measurements (cf. c. 4, s. 4.5.3) reveal the presence of a single quantum emitter based on the fact that it cannot simultaneously emit two photons. This allows advanced selection of the “right” fluorescing nanodiamond candidate containing a single NV^- centre to be picked up by the AFM tip and used as a magnetic field probe.

However, if this is not a problem when the method of picking up a selected nanodiamond with the AFM tip is used, it might become a challenging task in the mentioned case of AFM diamond tips with directly implanted NV⁻ centres. NV⁻ centres can be created in ultrapure nitrogen-free diamond either by irradiation or by N⁺ ion-implantation followed by an annealing step (cf. c. 2, s. 2.3.5). The limitations of these techniques, apart from the technological problem of producing such ultrapure diamond AFM tips, include the low control over the location and number of NV⁻ centres created inside the diamond and make the realisation of an AFM diamond tip with a single NV⁻ centre at its apex a difficult task.

Size of the diamond crystal hosting the NV⁻. Theoretical calculations and preliminary experimental results show that high resolution magnetometry at the nanoscale can be achieved by exploiting the unique properties of NV⁻ centres in diamond. However there is a practical limit: the *size* of the diamond crystal hosting the NV⁻ centres.

Equation (3.8) shows that the spin of the probing NV⁻ centre and the spin to be detected have to be only *few nanometres* apart for the ESR frequency shift to be measured. If the hosting nanodiamond is too large, even only tens of nanometres, the NV⁻ centre would not be able to be sufficiently close to detect and resolve the weak magnetic field generated by the surface spins.

This problem is crucial and turns out to be relevant not only for high resolution magnetometry, but also for life science applications where the interest is centred on having the smallest possible nanodiamonds, still able to contain luminescent colour centres.

The significance and multidisciplinary nature of fabricating and characterising diamond crystals only a few nanometres in size and containing NV⁻ centres became therefore a central focus of my work.

4

Experimental setup

In the past few years, it has been clearly recognised that the feasibility of NV centre-based technologies depends upon specific diamond material requirements. For instance, diamonds must be of ultra high purity for quantum science technologies where the spin coherence time is critical, while for high-resolution magnetometry and biomedical imaging the small size of the diamond nanocrystals and the optical stability of the hosted NV centres is crucial (cf. c. 2, ss. 2.4.1-3).

At present, one of the biggest challenges is, thus, to develop a more complete understanding and eventually control over the properties of this unique defect and the hosting diamond.

In this work, I focus the attention specifically on NV centres in diamond crystals which are only a few nanometres in size (nanodiamonds, NDs). They are potentially a key element in diamond-based spin-imaging and bio-labelling applications.

My aim is to investigate what happens to the nitrogen-vacancy centre in truly nanoscale diamond particles. This poses a series of experimental challenges. For instance, we need to be able to spatially isolate the diamond nanocrystals and address separately the individual grains. We also need to be able to characterise the fluorescent NV centres and look for possible correlations between their optical behaviour and the physical and chemical properties of the hosting nanodiamonds and of the surrounding environment.

In this chapter, I present the experimental procedures and technological solutions we have developed to tackle these challenges and to address some of the fundamental questions about NV centres in nanodiamond.

4.1 Lab-built combined confocal and atomic force microscope

One of the main aspects of this study consists of measuring the fluorescence of nitrogen-vacancy centres and the size of the hosting diamond nanocrystals. We look for correlations between the optical behaviour of NV centres and the size of the nanodiamonds.

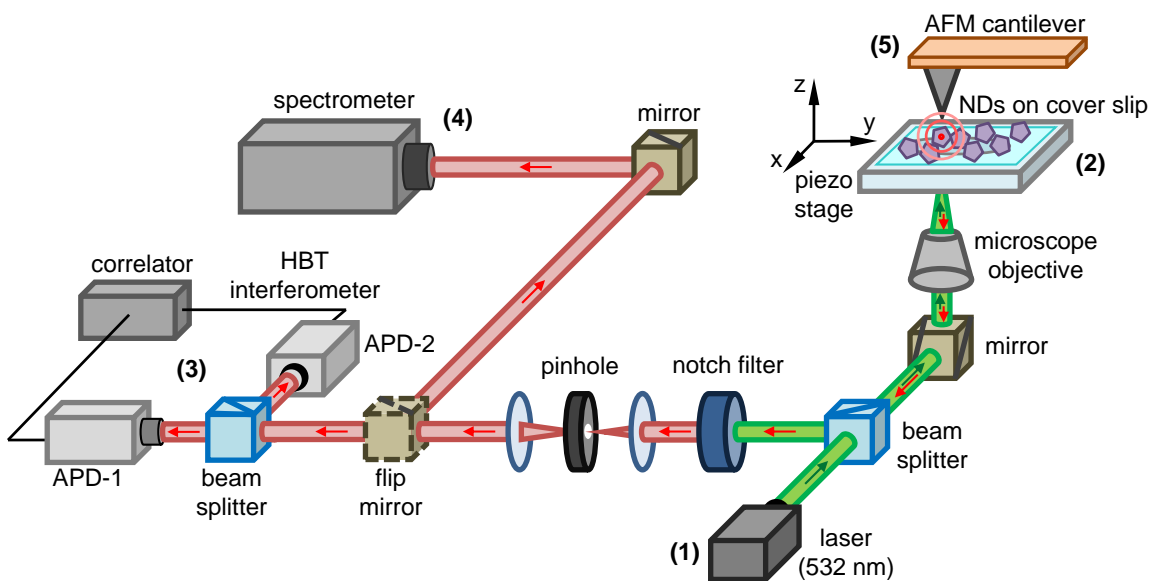


Figure 4.1. Schematic representation of the combined confocal and atomic force microscope (AFM) setup. **1)** A green laser beam (wavelength 532 nm) is focused through the confocal setup on the sample. **2)** The sample consists of fluorescent diamond nanocrystals placed on a transparent cover slip mounted on a piezoelectric stage. **3)** The fluorescence from the nanodiamonds is collected by the microscope objective, filtered (a notch filter is used to cut out the excitation green laser light) and directed to a Hanbury-Brown and Twiss (HBT) interferometer, where two avalanche photodiodes (APDs) work in coincidence to evaluate the second-order correlation function $g^{(2)}(t)$ revealing when required the presence of a single NV centre (cf. s. 4.5.3). **4)** By switching a flippable mirror, the fluorescence is also collected by a spectrometer to identify the NV centres. The coloured arrows indicate the path followed by the light. **5)** The AFM scans the sample, measuring the size of the diamond nanocrystals.

To enable this, we have built a measuring system that combines a room-temperature scanning confocal microscope and an atomic force microscope (AFM). The setup is shown schematically in figure 4.1 [221, 222]. The key feature of this lab-built system is its ability to acquire the luminescence and the corresponding topographic image of the target sample simultaneously. This is made possible by having the laser of the confocal system

(Fig. 4.1(1)) exciting the nanodiamonds directly from below through a transparent substrate, while the atomic force microscope scanning tip is perfectly aligned with the laser from above (Fig. 4.1(2, 5)). The detection path of the confocal microscope comprises both a system of two avalanche photodiodes in a Hanbury-Brown and Twiss (HBT) interferometer configuration (Fig. 4.1(3)) and a spectrometer (Fig. 4.1(4)). Simultaneously, the AFM (Fig. 4.1(5)) provides the information about the size of the diamond nanoparticles and is used to map their profile over the substrate.

The next two sections of this chapter present the basic principles of confocal and of atomic force microscopy.

4.2 Confocal microscopy: basic principles

A confocal microscope creates sharp images of a specimen using single point-by-point illumination and detection that reject most of the out-of-focus light.

Confocal microscopy was pioneered by M. Minsky in 1955, while he was a Junior Fellow at Harvard University, and then patented in 1961 [234, 235]. Figure 4.2 shows the schematic design and principle of a reflection confocal microscope as Minsky first devised it.

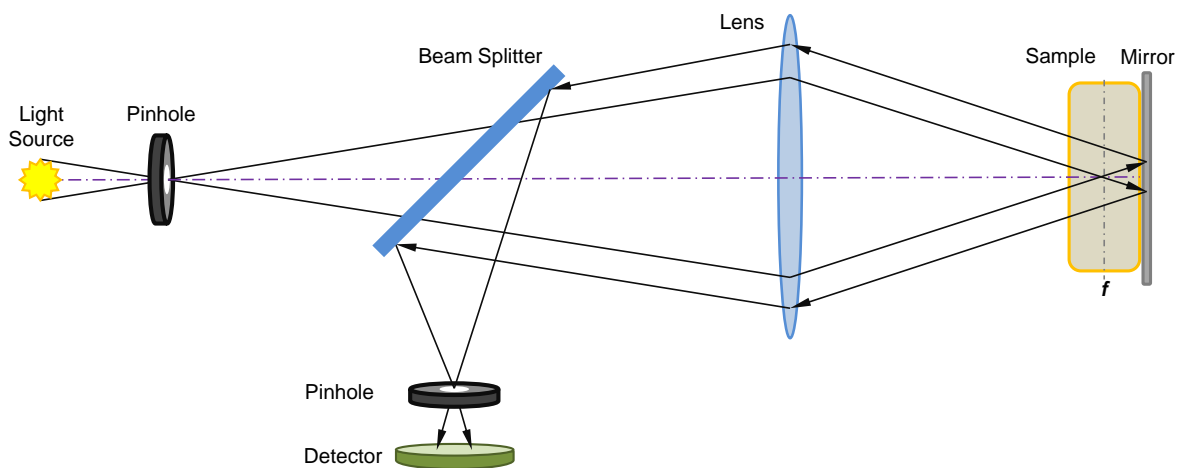


Figure 4.2. Schematic design and principle of a reflection confocal microscope. The light from the source is directed through a pinhole and a beam splitter; a lens is then used to focus the light on the sample. In this particular configuration, the sample is mounted on a mirror that reflects the light back to the beam splitter and through a second pinhole towards the detector. The apparatus strongly favours collection of fluorescence from the in-focus plane (f) and cuts off, via the second pinhole, all the back-reflected light from the out-of-plane points.

In a conventional wide-field fluorescence microscope, the light source illuminates the sample entirely and the observed fluorescence carries information indistinctively from the whole specimen. In contrast, in a confocal microscope only a single point at a time is illuminated and most of the light which is scattered outside of the focal plane is rejected. This yields a sharp image of a “slice” through the sample corresponding to the focal plane. The spatial resolution, especially in the axial direction, is higher and there is a significant reduction of the background signal typical of conventional fluorescence images, where the light comes from any point of the specimen. In other words, the single point illumination and detection of a confocal microscope increase its resolution at the expenses of the field of view [236]. The field of view is increased by doing a raster scan, one point at a time, of the in-focus plane of the sample. The relatively long acquisition time required to build a full image of the specimen is probably the biggest drawback of a confocal microscope. Moreover, the number of photons that can be collected from a single point can be very low and long integration times are required. To overcome this last problem high intensity light sources are used. Minsky originally used a zirconium arc lamp, but the common modern choice is a laser source which has the benefit of high intensity and of being available in a wide range of wavelengths. A confocal microscope acquires only two-dimensional sections of the specimen, however, three-dimensional renditions can easily be achieved by joining together scans taken at short and regular intervals along the optical axis.

There are quite a few possible variations of confocal microscope setups. Despite minor technical differences they all maintain the basic principle of single-point illumination and detection. The majority of confocal microscopes image the specimen either by light reflection, as per the original Minsky’s design (Fig. 4.2), or by stimulating fluorescence from dyes or luminescent centres in the sample. Setups that involve transmission of light through the specimen are also possible [237, 238].

In this work, we use a fluorescence type of confocal microscope which is slightly different from Minsky’s reflection type. Our setup has no mirror mounted on the back of the specimen and the incident light excites luminescent NV centres in the diamond. The fluorescence is then collected back by an objective and directed to a detector.

The ray optics of figure 4.3 clearly shows schematically how a fluorescence confocal microscope like ours works. The first pinhole is placed in front of the light source and provides point-wise illumination (alternatively, and nowadays more commonly, a laser source is used). The second pinhole is placed in front of the detector on a plane conjugate to the focal plane of the focusing lens. Ideally, only the light coming from the exact focal plane f of the sample can pass through the second pinhole. The light coming from any other plane above (f') or below (f'') is out of focus and is mostly blocked by the pinhole.

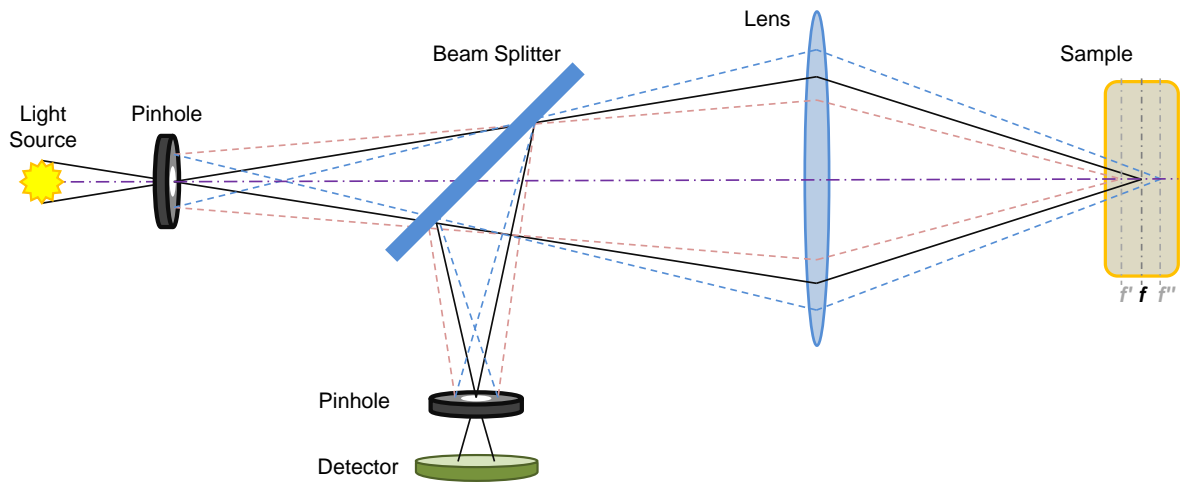


Figure 4.3. Basic principle of a fluorescence confocal microscope. The light from the source is directed through a first pinhole and focused on the sample. The second pinhole is placed in front of the detector on a plane conjugate to the focal plane f of the focusing lens. Only the light (black-continuous rays) coming from the focal plane f of the sample can pass through the second pinhole. The light (dashed-red and dashed-blue rays) coming from any plane above f' or below f'' the focal plane f is out of focus, cannot pass through the pinhole and therefore does not contribute to the image formation.

As per any other optical microscope, the resolution of a confocal microscope is limited by diffraction (cf. c. 3, s. 3.1). However, both the lateral and the axial resolution, respectively in the focal plane and along the optical axis, of a confocal microscope are generally better than those of a traditional wide-field microscope [239]. The reason is that in confocal microscopy due to the point-wise illumination and detection only the point-like objects in the shared volume of the illumination and detection point spread functions (PSFs) are detected. The resulting overall intensity PSF is the product of the independent point-like illumination and detection intensity PSFs, convoluted with the finite pinhole aperture. Consequently, in a confocal microscope the separation of two point-like objects required to produce acceptable contrast is smaller than that of a traditional microscope. Applying

the Rayleigh criterion of having 26.4% contrast dip between adjacent peaks, we obtain a lateral resolution R (assuming the condenser and the objective lenses having the same numerical aperture, $NA_c = NA_o$):

$$R = \frac{0.44\lambda}{NA} \quad (4.1)$$

which is about 30% smaller than the lateral resolution of a traditional wide-field microscope (cf. c. 3, s. 3.1 eq. (3.2), $R = 0.61\lambda/NA$).

The axial resolution along the optical axis of a microscope is proportional to the wavelength and refractive index of the specimen medium and inversely proportional to the square of the numerical aperture. The axial resolution R_a of a confocal microscope is relatively better (smaller value of R_a) than that of a common wide-field microscope because of the pinhole dramatically suppressing the intensity of out-of-focus scatterers:

$$R_a = \frac{1.5\lambda n}{NA^2} \quad (4.2)$$

where n is the index of refraction of the specimen and λ is the wavelength of the emitted light.

Another element that plays an important role in defining the capabilities of a confocal microscope is the pinhole. The size of the pinhole in fact, defines the optical sectioning capability of the confocal microscope and affects inevitably its resolution and contrast. It would seem desirable to have the pinhole size as small as possible to increase the rejection of the out-of-focus light rays. However, as the pinhole size is reduced the number of photons that arrives at the detector decreases as does the signal-to-noise ratio. The choice of the pinhole size may vary from case to case, but in general it does not have to be smaller than a single resel, which is defined as the radius of the first dark fringe in the diffraction pattern or half the diameter of the Airy disk in a lens. With this regard is worth reminding that the magnification of the objective lens reduces accordingly the pinhole size at the object plane. For instance, for a pinhole that is physically 1 mm across, a 100× magnification objective lens reduces its effective size to 10 μm at the object plane [239].

4.3 Atomic force microscopy: basic principles

The atomic force microscope (AFM) was invented by G. Binnig, C. F. Quate, and C. Gerber in 1986 as a tool to investigate the surface of a target sample on an atomic scale

[240]. It was developed after the invention in 1982 of the scanning tunnelling microscope (STM) also by G. Binnig with H. Rohrer [241] which earned them the Nobel prize in physics in 1986. While the STM is able to resolve the atomic structure only of conductive materials, the AFM can do the same for any material including insulators, and with extremely high resolution. In its first iteration it was able to achieve lateral resolutions of 30 Å and vertical resolutions less than 1 Å [240]. Since then, the AFM has been and still is today one of the foremost tools for surface topographic imaging and manipulation at the nanoscale.

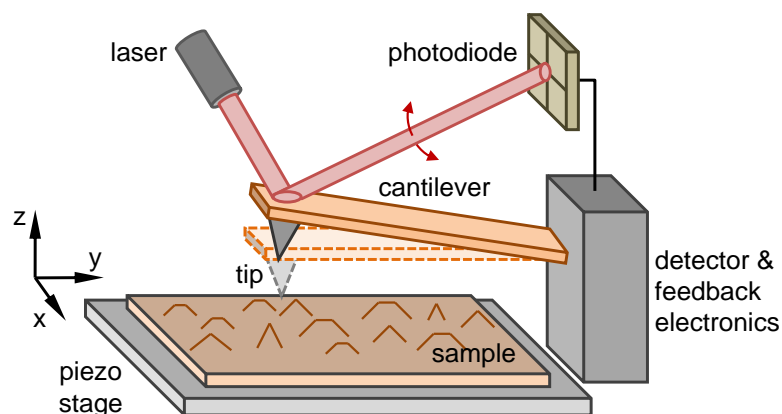


Figure 4.4. Block diagram of an atomic force microscope (AFM). The sample is mounted on a piezoelectric stage and scanned under the AFM tip sitting at the apex of the cantilever. Every feature on the sample surface produces a force (as small as 10^{-18} N) on the tip and deflects the cantilever. A laser beam is incident on the back-reflective surface of the cantilever while this is scanning and the reflected light is directed onto a photodiode. The detector measures the deflection of the beam corresponding to the cantilever position producing an image of the surface topology. Alternative operative modes are possible. The stage can be kept fixed while the tip moves over the sample. Plus, instead of having the tip pushed up and pulled down according to the profile, the feedback electronics can use the photodiode signal to maintain the height of the tip constant over the contour preventing the tip from crashing on the sample.

The AFM provides high resolution images of a sample by scanning the surface with a sharp tip placed at the end of a moving cantilever (Fig. 4.4). The tip can have a radius of curvature as small as a few nanometres, be made of a range of materials and be coated or functionalised for different applications. Controlled by piezoelectric elements and closed-loop feedback mechanisms, the tip is lowered down to the sample surface to a point where inter-atomic forces as small as 10^{-18} N [240] between the tip and the surface cause a deflection of the cantilever. The cantilever deflection is measured while the tip moves relative to the sample surface and the topographic structure is derived accordingly. The cantilever movement is measured via a position sensitive detector consisting most simply

of two closely, vertically-spaced photodiodes (Fig. 4.5). A laser beam hits the cantilever and is reflected back against the photodiodes so that the cantilever angular position can be determined by measuring the difference between the outputs of the two photodiodes.

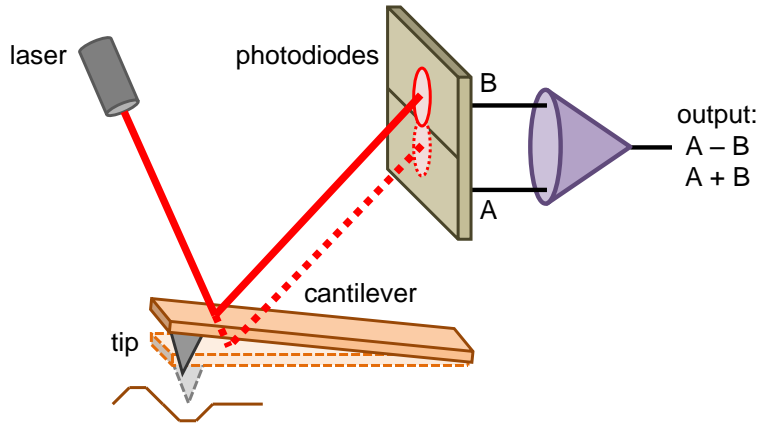


Figure 4.5. Schematic representation of the position sensitive detector used to measure the AFM cantilever deflection. In the simplest version, a laser beam reflects off the cantilever towards two vertically-placed photodiodes. The intensity signal measured by the two photodiodes is used to quantify the cantilever deflection.

The interaction forces acting between the tip and the surface can be of different kinds (e.g. van der Waals, capillary, chemical bonding, electrostatic, magnetic, etc.) and therefore different arrangements, different scanning modes, and even different tip materials can give a considerable variety of information about the surface structure and composition (e.g. topographic, magnetic, chemical, etc.).

According to the application, the AFM can generally operate in different modes (Fig. 4.6), mainly: static or contact mode, dynamic or non-contact mode and tapping mode [242].

Static or contact mode. In the static or contact mode, the static tip deflection is used either as the direct measuring signal or as the feedback control. The tip in fact experiences increasing repulsive forces when it gets closer to the surface due to the fact that at inter-atomic distances the electron clouds in the atoms of the tip and of the sample repel each other electrostatically. The varying deflection signal is used to reconstruct the topographic image of the surface. This can be done either by operating in constant height mode or in constant force mode. In the constant height mode the piezoelectric elements move the AFM tip over the surface at a fixed height and the cantilever deflection signal caused by

the sample contour is used to estimate the profile. In the constant force mode the deflection signal is used by the feedback electronics to maintain constant the force between the surface and the tip thus yielding in real time the surface contour. The constant force mode is generally preferred to the constant height mode since by following the profile in real time it is less likely to damage the tip against surface irregularities during the scanning process.

Low stiffness cantilevers are generally used in the static or contact mode to maximise the deflection signal and increase the sensitivity. The main drawback of this operating mode is that the shear forces exerted by the tip on the sample during the scanning process tend to damage both the sample and the tip. It is therefore unsuitable for examining soft biological or polymer surfaces.

Dynamic or non-contact mode. In the dynamic or non-contact mode, the cantilever is oscillated at a specific frequency, generally just above its resonance, with oscillation amplitude typically in the nanometre range. It is suspended about 10 nm above the sample and is subjected to van der Waals forces between the tip and the sample that generally dominate in this distance range. The changes in amplitude, phase or frequency of the oscillating cantilever due to the tip-surface interactions are used either as the measuring signal or as the feedback control. In general the signal is used by the feedback electronics to adjust the average tip-to-sample distance and to maintain a constant oscillation as the position of the tip over the sample changes. The adjustment is recorded to reconstruct the topography of the sample.

The main advantage of the non-contact mode is that it does not lead to tip or sample degradation as the contact mode does. However, there are drawbacks. Often a few layers of adsorbed fluid may coat the sample surface, which leads to a degradation in resolution in comparison to a corresponding contact mode image. The oscillating tip can become trapped in the fluid and image a sort of average overall combination of the sample-fluid surface.

Stiff cantilevers are generally used in the dynamic or non-contact mode to provide stability when near the surface. This mode is ideal for scanning soft polymers and biological materials; it is also often chosen to image a wider range of materials including metals and semiconductors. In the case of semiconductors for instance, it is advantageous

because it allows contamination-free characterisation of the surface of silicon wafers for technological purposes, which avoids the potential impact on device performance.

Tapping mode. In tapping mode, the cantilever is oscillated at or near its resonance frequency with oscillations typically less than 100 nm in amplitude. During scanning, the tip alternatively touches the sample surface. The vibration amplitude changes according to the surface topography as the energy losses caused by the intermittent contacting are different depending on the proximity of the tip to the surface. The amplitude change is used by the feedback electronics to adjust the height of the tip over the sample so that the height itself and the interaction force stay constant; the signal is a measure of the surface irregularities and is used to reconstruct the topography of the sample. The tapping mode is ideal for soft samples that are subject to damage that may occur in contact mode.

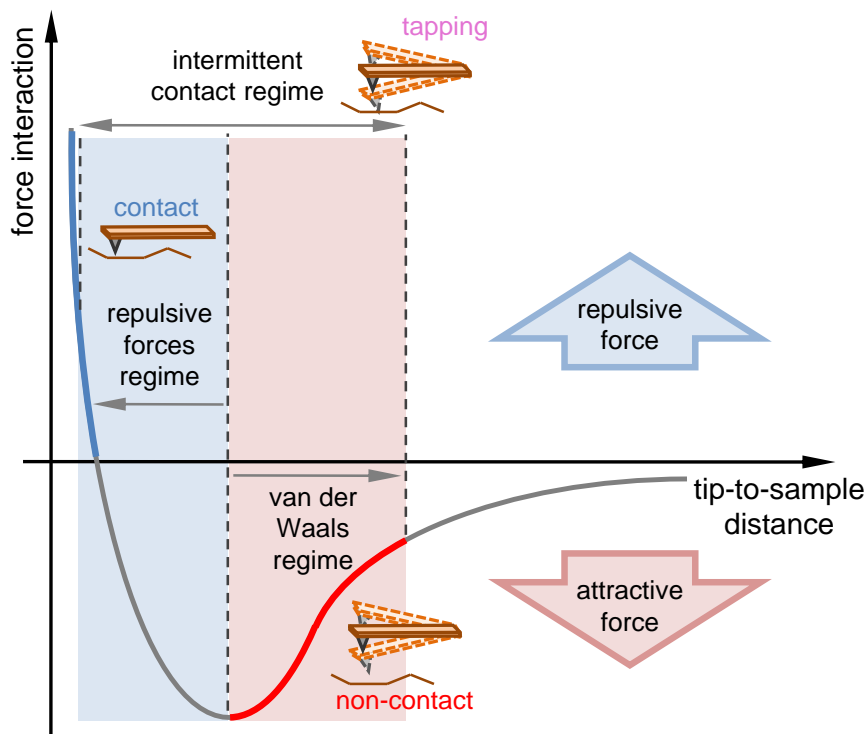


Figure 4.6. Scheme of the possible AFM operating modes. The operating regimes are shown with respect to the inter-atomic force variation as a function of the tip-to-sample distance. In contact mode, the tip is brought to a position relative to the sample where the repulsive electrostatic forces between the electron clouds in the atoms of the tip and of the sample are dominant. In non-contact mode the cantilever is oscillated above the surface at a distance where the dominant interactions are the attractive van der Waals forces between the tip and the sample. Tapping mode combines the contact and non-contact regimes whereby the cantilever is oscillated over the sample with the tip alternatively touching the surface.

The atomic force microscope is a very versatile instrument. It finds a variety of applications far beyond the mere topographic imaging of surfaces [242]. It is used, for instance, to visualise nanoscale variations in surface hardness of certain materials or to perform plastic nanoindentation, scratch and wear mechanical tests. Another extension of AFM imaging is force modulation microscopy (FMM) where the cantilever scans the surface in contact mode while a periodic signal is applied. The cantilever amplitude modulation that results from this applied signal varies according to the local elastic properties of the sample, which can therefore be measured simultaneously with the topographic information. The AFM can also be used to perform lateral force microscopy (LFM). In this technique, the tip is scanned sideways on a fast axis and also forward and backward on a slow axis; a quadrant photodiode detector measures the torsion of the cantilever which depends on the frictional characteristics of the surface and is used to determine varying surface compositions. Other AFM techniques include electric force microscopy (EFM) and surface potential (SP) imaging which are used to characterise the electrical properties of a material. In these techniques, a conductive AFM tip interacts with the sample through long-range Coulomb forces which change the oscillation amplitude and phase of the AFM cantilever providing information about the electric domains distribution and the potential variations on the sample surface. Other applications include electrical failure analysis, detecting trapped charges, quantifying contact potential difference (CPD) between metals and/or semi-conductors, mapping relative strength and direction of electric polarisation, testing electrical continuity and performing electrical read and write operations. Remarkably, the AFM is becoming a powerful tool not only to characterise, but far more interestingly to manipulate objects and even fabricate structures with nanoscale precision.

A field where AFM has been quite successful is that of biological applications. For instance, cell movement and cell-surface interactions are interesting dynamic events that can occur on a time scale of minutes in living species and the AFM is a suitable instrument to image and examine such events. Time-lapse AFM scans can be used to follow biological processes in solution, while real-time scans can qualitatively be used to correlate structural conformations and functional states of individual biomolecular assemblies. In force microscopy, the AFM can be used to measure the interactions between single molecules, antigen and antibody pairs, proteins and ligands, proteins and

membranes and proteins and cells. Other applications include the characterization of the properties of protein-protein and protein-nucleic acid complexes or even of the conformation of DNA-protein assemblies. Pushed by the interest in biological applications, several techniques have been developed to improve the AFM scanning capabilities and resolution. These include: cryo-AFM imaging at cryogenic temperatures, using better and sharper probes (e.g. carbon nanotubes) and even new operating mechanisms such as magnetic (MAC) and photothermal (PMOD) modes, where respectively magnetism and thermal expansion are used instead of piezoelectric transduction to directly vibrate the cantilever.

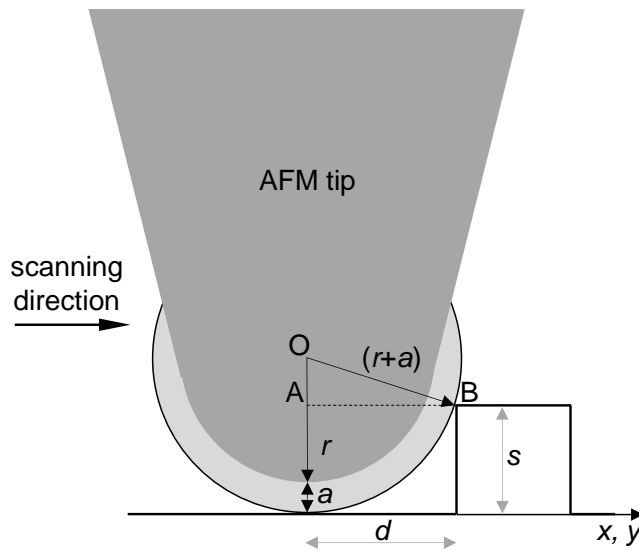


Figure 4.7. Geometrical parameters of an AFM tip. The tip has a radius of curvature r ; a is the distance at which the tip-surface interaction is considered to start; s is the height of the surface step to be measured; d is the corresponding lateral resolution.

The vertical resolution of an AFM can be as small as fractions of a nanometre. The physical dimensions of the probing tip however, limit its lateral resolution to a few tens of nanometres. With reference to figure 4.7, we can use geometrical considerations to estimate the value of the lateral resolution d of an AFM tip. In the figure, r is the radius of curvature of the tip, a is the physical distance between the tip and the surface at which we can assume the tip-surface interaction starts and s is the height of a certain surface step to be measured. If we apply the Pythagorean theorem to the triangle AOB we obtain:

$$OA^2 + AB^2 = OB^2, \text{ i.e. } (r + a - s)^2 + d^2 = (r + a)^2 \quad (4.3)$$

from which:

$$(r + a)^2 + s^2 - 2(r + a)s + d^2 = (r + a)^2 \quad (4.4)$$

where simplifying $(r + a)^2$ we get:

$$d = \sqrt{2(r + a)s - s^2} \quad (4.5)$$

Assuming reasonably $r \gg a$, equation (4.5) becomes:

$$d \cong \sqrt{2rs - s^2} \quad (4.6)$$

The tip radius r is in general ~ 10 nm, which means that, for instance, for a step $s \sim 10$ nm the corresponding AFM lateral resolution is ~ 10 nm.

4.4 Sample preparation

Before going into the details of the experimental apparatus, I briefly present here how the nanodiamond sample is prepared for characterisation. This description is very general. The aim of this section is to give an idea of the kind of samples we are dealing with. More details will be given in the following chapters wherever the specificity of the experiments requires it.

In chapter 2, sections 2.3.1-5 we have presented some of the different techniques used to synthesise diamonds including HPHT, CVD, detonation and ultrasound cavitation. We have also shown that there are specific procedures like irradiation or ion-implantation followed by annealing to enhance the presence and the quantity of NV centres in diamond. Regardless of the synthesis methods utilised, we generally work with nanodiamonds less than 100 nm in size. They come in the form of powder and are commercially available. They either naturally contain NV centres, or they are treated to include them.

To prepare a sample for our setup, the diamond powder is first diluted in deionised water (Milli-Q®) to the desired concentration. A few drops of the obtained solution are then put on a glass cover slip (dimensions $\geq 18 \times 18$ mm² and thickness ~ 0.13 - 0.17 mm; Menzel-Glaser), which is spin-coated or simply allowed to dry so that the diamond crystals remain dispersed on the surface. This procedure can be modified with regard to particular experimental requirements [221, 222]. The cover slips, for instance, can be of different materials (e.g. quartz, sapphire, mica, etc.) or can be specifically treated (e.g. chemically-etched, plasma-etched, etc.). Also, the solvent used to dilute the diamond powder can vary from deionised water. For example, polymers can be added to the water-diamond

solution to provide an embedding matrix for the diamond crystals (a very common polymer often used in such cases is polyvinyl alcohol, PVA). Finally, some sort of chemical or physical treatments may be carried out (e.g. acid cleaning, ultrasonication, etc.).

In any of these cases, the final outcome is a sample where a layer of diamond nanocrystals lays on a cover slip which is then mounted on a scanning piezoelectric stage. The nanodiamonds on top of the cover slip are accessible both by the laser from the bottom for the optical analysis of the colour centres and by the AFM scanning tip from the top for the size investigation (Fig. 4.1(2, 5)).

4.5 Our experimental setup

The system we have designed and built to characterise NV centres in diamond nanocrystals, combines in a single setup both a confocal and an atomic force microscope (AFM).

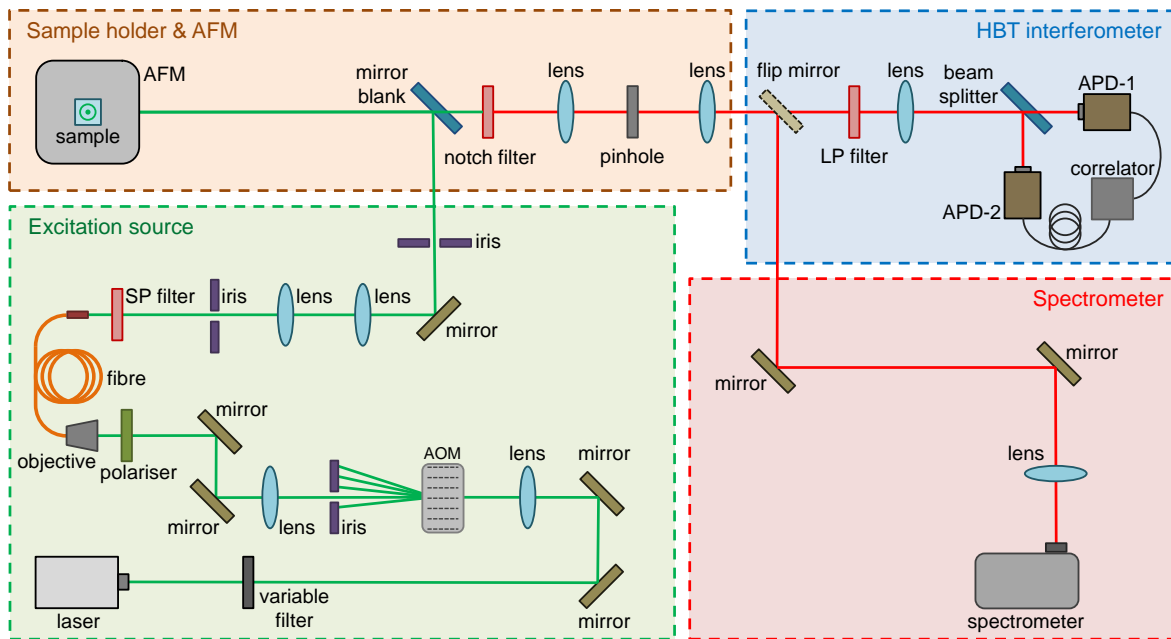


Figure 4.8. Schematic detailed top-view of our lab-built combined confocal and atomic force microscope (AFM) setup. For clarity of presentation, four main parts have been highlighted: i) the excitation source, ii) the sample holder and the atomic force microscope (AFM), iii) the Hanbury-Brown and Twiss (HBT) interferometer and iv) the spectrometer.

Figure 4.8 shows a schematic and detailed top-view of it where, for clarity of presentation, four main parts have been highlighted:

- the excitation source
- the sample holder and the atomic force microscope (AFM)
- the Hanbury-Brown and Twiss (HBT) interferometer
- the spectrometer

They are analysed in details in the following sections.

4.5.1 Excitation source

The illumination source of our confocal setup is a continuous-wave 532-nm diode-pumped solid-state laser from Coherent, model Compass 315M-100 (Table 4.1). The setup is designed to investigate nitrogen-vacancy centres which have zero phonon lines (ZPLs) at 637 nm for the negatively charged state NV⁻ and at 575 nm for the neutral charge state NV⁰. The choice of the laser is optimised to guarantee that the excitation wavelength is shorter than the NV centres ZPLs. Note however that according to the nature of the study different light sources can be used. They can in some cases even operate in parallel in the setup. Currently, the sources we use include: a 531 nm pulsed laser (LDH-P-FA-530; PicoQuant), a 733 nm pulsed laser (LDH-P-C-730; PicoQuant) and a 467-472 nm pulsed laser (LDH-D-C-470; PicoQuant).

Table 4.1 – Compass 315M specifications	
Wavelength	532 nm
Maximum output power	100 mW
Spatial mode	TEM ₀₀
Circularity of beam	> 95%
Beam diameter at 1/e ²	0.32 mm
Beam divergence	< 2.2 mrad
Pointing stability	< 6 μrad/°C
Noise (10 HZ to 1 GHz)	< 0.25% rms
Long term power stability (> 8h)	< ±2%
Warm up time	< 10 min
Polarisation ratio	100:1, vertical

The laser is firstly directed through a circular, continuously variable metallic neutral density filter (NDC-25C-2M; Thorlabs). The filter is coated with Inconel film of very hard metallic alloy whose optical density varies linearly. By rotating the filter, the laser source power can be adjusted linearly.

Mirrors (BB1-EO2; Thorlabs) redirect then the laser through a converging lens that focuses the beam into an acousto-optic modulator (OD-8813A; NEC). The acousto-optic modulator (AOM) diffracts the light of the incoming beam whenever a driving electric signal is sent to the piezoelectric transducer of the device. The transducer oscillates upon the driving signal and creates sound waves in the glass. They form moving periodic planes of expansion and compression that change the index of refraction, so that the incoming light scatters (Brillouin scattering) off the periodic index modulation and interference occurs (similarly to Bragg diffraction). An iris (ID25; Thorlabs) placed after the AOM blocks every diffraction order but the first, so that the laser beam can be stopped or can be let pass through on demand with electronic speed (minimum switch time 50 ns) (Fig. 4.9). This is required in some kinds of measurements, for instance in Rabi nutation experiments (cf. c. 3, s. 3.3.2) where specific time sequencing of the excitation laser and the microwave fields requires the starting point and the duration to be precisely controlled, generally in the microseconds range.

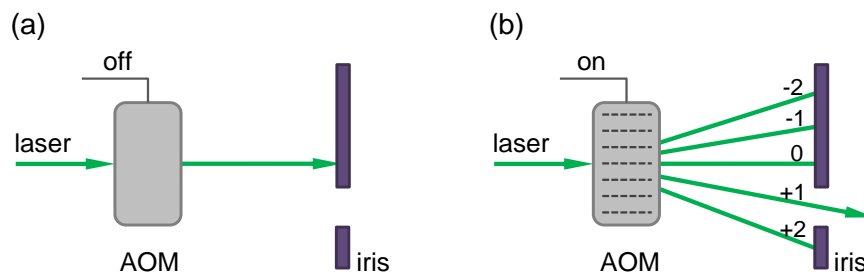


Figure 4.9. Schematic representation of the acousto-optic modulator (AOM) in our setup. **a)** When the electric driving signal is “off” the incoming laser is not scattered and the iris placed behind the AOM blocks the light. **b)** When the electric driving signal is “on” periodic index modulation occurs in the glass medium of the AOM, light is scattered and the iris placed behind the AOM lets the first diffraction order light to get through.

The diverging beam coming out of the acousto-optic modulator is then made parallel by a lens placed after it (Fig. 4.10).

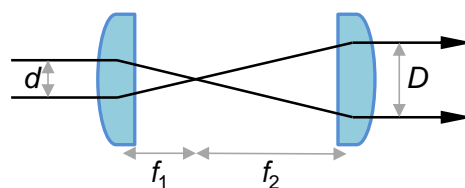


Figure 4.10. Schematic of a Keplerian beam expander. The incoming beam of diameter d is diverged by the first lens of focal length f_1 and then re-collimated with a larger waist D and smaller divergence by the second lens of focal length f_2 .

The beam is firstly diverged by the first short focal length lens and then re-collimated with a larger beam waist and smaller divergence by the second lens. The resulting magnification m is expressed as:

$$m = \frac{f_2}{f_1} = \frac{D}{d} \quad (4.7)$$

where d and D are the diameters respectively of the entering and exiting beam, while f_1 and f_2 are the focal lengths of the first and second lens. The expanded beam is then redirected with mirrors through a polariser (LPVISA; Thorlabs) and focused by an objective (Plan N, 10× / N. A. 0.25 / W. D. 10.6 mm / F. N. 22; Olympus) into an optical fibre (PM-S460-HP; Thorlabs). The fibre holder is mounted on a three-axis stage (MBT616; Thorlabs) for the optimal alignment of the beam into the fibre. The fibre decouples the excitation source from the other parts of the measuring system and provides an additional degree of flexibility. This design allows for a quick change of the excitation laser simply by coupling a different source into the fibre without having to re-set all the optics in the detection path, since these are aligned with respect only to the fibre output.

The beam coming out from the fibre passes through a 550 nm short pass filter (FES0550; Thorlabs) which cuts the longer wavelength components of the light. It goes then through an iris and another system of two lenses working as a beam expander. It is finally redirected via a mirror towards the atomic force microscope where the sample is placed.

4.5.2 Sample holder and atomic force microscope (AFM)

The excitation beam is directed to a mirror blank working as a beam splitter (PF20-03; Thorlabs) angled at 45° towards the AFM stage where the sample is placed.

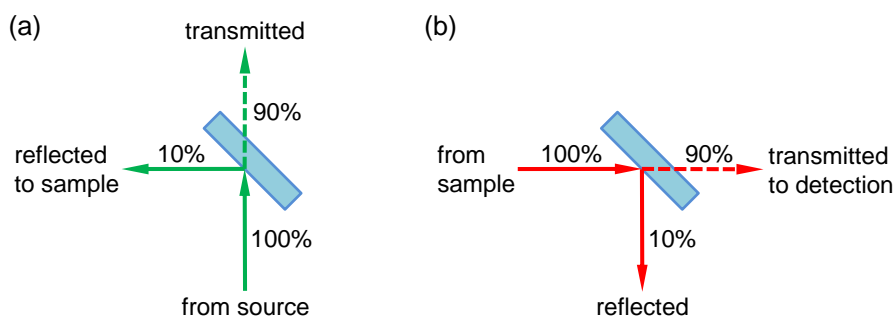


Figure 4.11. Schematic representation of the mirror blank working as a beam splitter for the excitation of the sample and the detection of the emitted light. **a)** 10% of the incoming laser light from the source is reflected towards the sample for the excitation while the other 90% is transmitted and blocked by a screen. **b)** When the light is emitted back from the excited specimen, 90% of the light from the sample is now transmitted to the detection path and only 10% is reflected.

The mirror transmits 90% of the incoming light and reflects 10% of it towards the sample (Fig. 4.11a). This assures that 90% of the light that comes back from the sample, which is of interest for the characterisation, is transmitted while only 10% is reflected (Fig. 4.11b).

The laser light reflected by the beam splitter is then directed towards a mirror angled upwards at 45° (Fig. 4.12). The light passes through an oil objective (UPlanFL N, $100\times$ / N. A. 1.3 / W. D. 0.2 mm / F. N. 26.5; Olympus) which focuses it through the transparent cover slip, onto the nanodiamonds (NDs) placed over the top surface. The specimen in fact is sitting horizontally on the AFM piezoelectric stage which can move along all the three dimensions of space: vertically, $10\ \mu\text{m}$ along the z -axis, and horizontally, over a $50 \times 50\ \mu\text{m}^2$ area along the xy -plane.

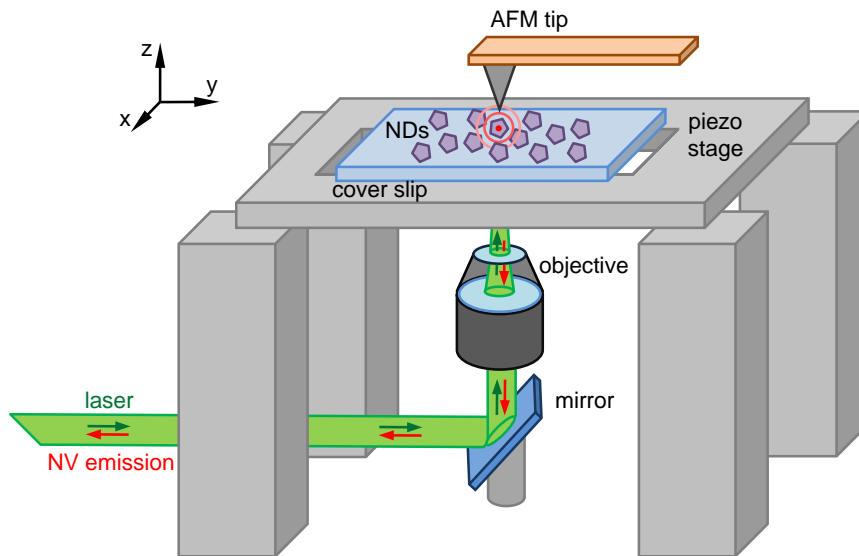


Figure 4.12. Schematic representation of the arrangement designed to characterise the sample. The sample is sitting over a piezoelectric stage which can move in all the three dimensions of space. The laser light is directed upwards by a mirror angled at 45° and focused onto the nanodiamonds (NDs) through an oil objective (green arrows). The fluorescent crystals, excited by the laser beam, emit light that is collected back by the objective and is directed to the detection path (red arrows). Simultaneously, the atomic force microscope (AFM) tip, from above, measures the size of the nanodiamonds.

The NV centres contained in the nanodiamonds are excited by the laser beam and fluoresce. The light emitted by the centres is recollected back by the oil objective (Fig. 4.12) and redirected towards the mirror blank that transmits 90% of it towards the detection path (Fig. 4.11b). A notch filter (NF-533-17; Thorlabs) or a long pass filter (FEL0550; Thorlabs) is placed just after the beam splitter to cut out the undesired green laser light (wavelength 532 nm) used for the excitation of the centres, so that only the fluorescence

light is collected for characterisation (the zero phonon lines of the NV^0 and NV^- are respectively at 575 nm and 637 nm and the vibronic side bands follow at longer wavelengths).

After the filter, the light passes through a set of two expansion lenses. In the focal plane between the lenses, a 50- μm pinhole (P50S; Thorlabs), the central element of a confocal microscope, is placed just before the detection path. The detection path contains two avalanche photodiodes arranged in a Hanbury-Brown and Twiss (HBT) interferometer configuration and a spectrometer.

In our system, the sample is mounted on the piezoelectric stage of the atomic force microscope (AFM) for characterisation. The AFM is a commercial model (SMENA; NT-MDT). The AFM head is mounted, as shown in figure 4.12, on top of the sample so that the probing tip is aligned with the laser beam of the confocal setup coming from underneath the sample. This enables simultaneous characterisation of the size and the optical properties of the nanodiamonds. Figure 4.13 shows paired images produced simultaneously by the aligned AFM tip and laser beam for straightforward correlation. The commercial AFM we are using guarantees a vertical resolution of 0.7 nm.

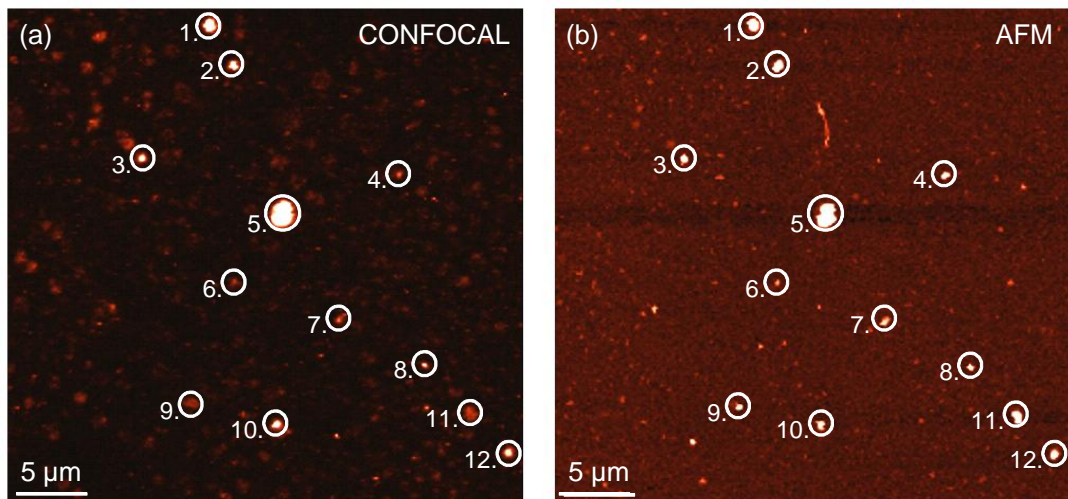


Figure 4.13. Confocal and AFM images of fluorescent nanodiamonds acquired simultaneously with our experimental setup. **a)** Confocal system image: bright fluorescing spots indicate emission from NV centres in nanodiamond crystals. **b)** Corresponding AFM image of nanocrystalline diamonds deposited on the substrate: the brightness of the spots is directly proportional to the height of the crystals. Data refers to an HPHT monocrystalline diamond powder from Microdiamant (MSY 0-0.1 μm).

The atomic force microscope in our setup is quite flexible. The objective focusing the laser beam and the piezoelectric stage can be moved independently along the vertical z-axis. The objective can be mechanically moved via a micrometric screw for several mm while the piezoelectric stage has a range of movement of 10 μm . The sample can be scanned either by stage or by tip. In the scan by stage the sample is scanned by moving the piezoelectric stage; this has a range of movement of $50 \times 50 \mu\text{m}^2$ (minimum scanning step 0.006 nm) and both the confocal and the AFM images can be acquired simultaneously. In the scan by tip, the sample is scanned by hovering the probing tip above while the specimen is kept fixed; the scanning range in this case is $100 \times 100 \mu\text{m}^2$ (minimum scanning step 0.012 nm) but only the topography of the sample is measured. The AFM can scan the sample both in contact and non-contact mode. In addition, the contact mode can be used to pick up, manipulate or move selected nanodiamonds.

4.5.3 Hanbury-Brown and Twiss (HBT) interferometer

The Hanbury-Brown and Twiss effect is any manifestation of correlation and anti-correlation between intensity fluctuations measured by two detectors from a beam of particles. Historically, the HBT interferometer was invented by, and named after, R. Hanbury Brown and R. Q. Twiss who designed it to measure the angular diameter of radio stars [243-246]. In an HBT interferometer the signal coming from a certain source is detected independently by two detectors and the correlation in the intensity fluctuation is recorded. The information about their relative phases instead is lost. The absence of knowledge about the relative phase is what makes this interferometer radically different from the more familiar Michelson's one where the signal is firstly split in two beams that follow different paths and are then recombined before detection, so that their relative phase is preserved [247, 248].

In our setup, two avalanche photodiode detectors (SPCM-AQR-14; Perkin Elmer) are arranged in a HBT interferometer configuration to identify single quantum emitters or, in our specific case, single NV centres. In general, when a light source emits photons, these tend to distribute in time following different statistics according to the characteristics of the source (Fig. 4.14a). For instance, when the emission from the source is random, the statistics of the photons in time follows a Poissonian distribution according to which the probability $P(k, n)$ of measuring k occurrences in a certain interval of time is:

$$P(k, n) = \frac{n^k e^{-n}}{k!} \quad (4.8)$$

where n is a real positive number equal to the expected number of occurrences during a given interval of time. A laser far above threshold is an example of a source that emits photons in time with Poissonian statistics. However, there are cases where the source emits photons in “non-random patterns”. For instance, photons can be almost equally spaced in time and follow a so called sub-Poissonian distribution giving rise to what is called photon antibunching. Single quantum systems like single atoms or single NV centres are typical examples of sub-Poissonian emitters. Oppositely, photons can be emitted in bunches in super-Poissonian statistics causing what is called photon bunching. Thermal light fields fall into this category.

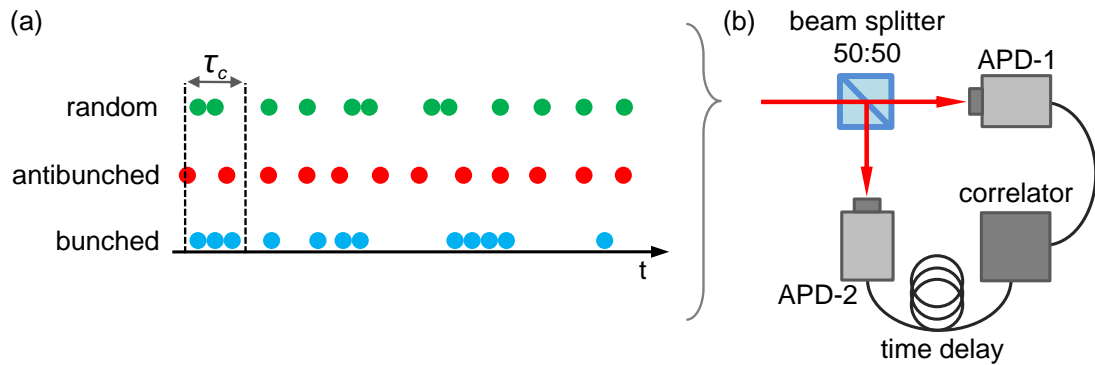


Figure 4.14. Schematic representation of photon distribution in time for three different types of source and scheme of our Hanbury-Brown and Twiss (HBT) interferometer. **a)** Representation of how photons would be detected in time for: a random source (uncorrelated, Poissonian statistics), an antibunched source (anti-correlated, sub-Poissonian statistics) and a bunched source (positively correlated, super-Poissonian statistics); τ_c is the coherence time, the time scale of photon or intensity fluctuations. **b)** In the HBT interferometer the signal is separated by a 50 : 50 beam splitter and sent to two avalanche photodiode detectors; a correlator measures the time delay between two consecutive photons (start and stop photons) detected by the two photodiodes and builds a histogram of the number of events per time bin, showing, if occurring, possible correlations.

The two avalanche photodiodes in our setup have precisely the purpose of addressing the nature of the source and whether the photon emission is uncorrelated (random), anti-correlated (antibunched) or positively correlated (bunched). The photodiodes are placed at an angle of 90° , with a 50 : 50 beam splitter (BSW10; Thorlabs) placed in front (Fig. 4.14b), and a long pass filter (FEL0650; Thorlabs) placed just before the splitter. The photodetectors work in coincidence with a correlator (PicoHarp 300, TCSPC System,

channel width 4 ps, with digital and analog units PH 300; PicoQuant) to measure the delay time between subsequent photons emitted by a selected fluorescent nanodiamond. The HBT interferometer measures a parameter called the second-order correlation function $g^{(2)}(\tau)$, which is defined as:

$$g^{(2)}(\tau) = \left\langle \frac{I(t)I(t+\tau)}{I(t)^2} \right\rangle \quad (4.9)$$

The correlation function $g^{(2)}(0)$ is the probability of detecting two simultaneous (delay time $\tau = 0$) photons normalised by the probability of detecting two photons at once for a random photon source. What we are interested in, is measuring an “antibunching” dip in the function $g^{(2)}(0)$ because it would indicate sub-Poissonian statistics of the emitted photons and it would reveal the presence of a single quantum emitter that cannot emit two photons simultaneously. Figure 4.15 shows autocorrelation measurements performed on three different luminescent diamond crystals (size < 100 nm) hosting NV centres.

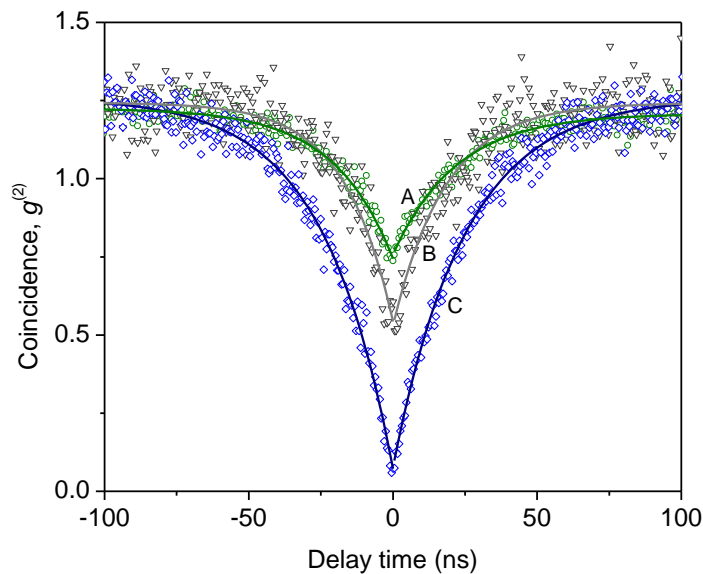


Figure 4.15 Autocorrelation function $g^{(2)}(\tau)$ measured for three different diamond nanocrystals hosting NV centre(s). The contrast in $g^{(2)}$ scales as $1/N$, where N is the number of emitters. The contrast in the curves A and B indicates multiple NV emitters, and curve C shows a single emitter. Data refers to an HPHT monocrystalline diamond powder from Microdiamant (MSY 0-0.1 μm).

The naïve way of interpreting the antibunching dip in the autocorrelation function for a single NV centre is by considering that there is a physical intrinsic delay ($\tau \neq 0$) between the emission of two consecutive single photons due to the time required by the system to be excited, emit, be excited again and emit a second photon. This means that if the source

is a single quantum emitter, as in the case of a single NV centre, it is impossible that the two photodiodes in the HBT interferometer would detect two photons at the exact same time. Based on $g^{(2)}$ it is possible to quantify, to some extent, the actual number of emitters: precisely, the contrast in the function $g^{(2)}$ scales as $1/N$, where N is the number of emitters [249, 250]. Therefore by measuring the contrast in $g^{(2)}(0)$ of a fluorescent nanodiamond we can conclude whether the fluorescence is actually due to a single or to multiple NV centres.

The avalanche photodiodes can also be used to measure a series of other quantities of interest for NV centres in nanodiamonds: fluorescence time trace, optically detected magnetic resonance (ODMR) and lifetime.

The ODMR of NV⁻ centres (cf. c. 3, ss. 3.3.2-3) is measured with a single avalanche photodiode. In our setup, the 2.88 GHz microwave radiation, which raises the population from the $m_s = 0$ to the $m_s = \pm 1$ NV⁻ electron spin ground state and induces a decrease in the NV⁻ fluorescence, is produced by a signal generator (SMIQ 06B, 300 kHz to 6.4 GHz; Rohde & Schwarz). The probing signal (0.2-0.6 mW) is transmitted along a 20 μm -diameter copper wire situated on the sample surface in sub-millimetre proximity to the probed NV⁻ centre (Fig. 4.16). The magnetic field that lifts the $m_s = \pm 1$ degeneracy and causes two distinct features is generated through a simple coil and a variable current source placed close to the sample.

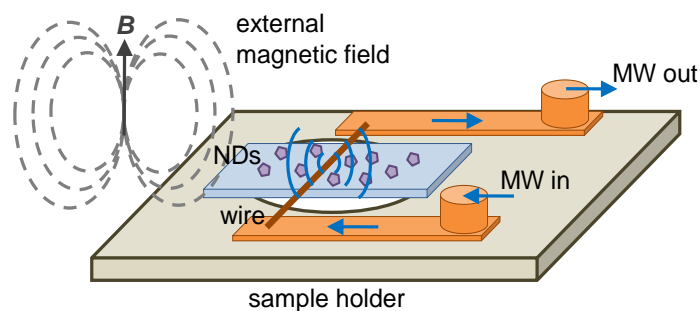


Figure 4.16. Schematic representation of the sample arrangement for ODMR measurement of NV-centres. The sample, the nanodiamonds (NDs) dispersed on a cover slip, is sitting on a holder of insulating material. Two metal contacts are adjacent, while a copper wire 20 μm in diameter crosses in close proximity to the NDs. The microwave field is driven by the generator through the metal contacts and radiates from the wire. An external magnetic field can be applied by using permanent magnet or coils with flowing electric current.

The excited-state lifetime of an NV centre is measured using the photodiodes in the detection path of the confocal setup. The NV centre under study is excited by a 531 nm pulsed laser (LDH-P-FA-530; PicoQuant) which triggers simultaneously with the counting card of the correlator. The correlator measures the time delay between the start signal given by the laser trigger and the subsequent stop signal given by the detection of the photon emitted by the NV centre. The histogram corresponding to the number of events measured per time-bin can be fitted with an exponential decay whose time constant gives the mean lifetime of the excited state of the observed NV centre. Figure 4.17 shows a lifetime graph measured on an NV⁻ centre hosted in an 80 nm diamond nanocrystal. The lifetime information is particularly interesting for our purposes since it gives hints about how the environment and the boundary conditions can affect the dynamics of an NV.

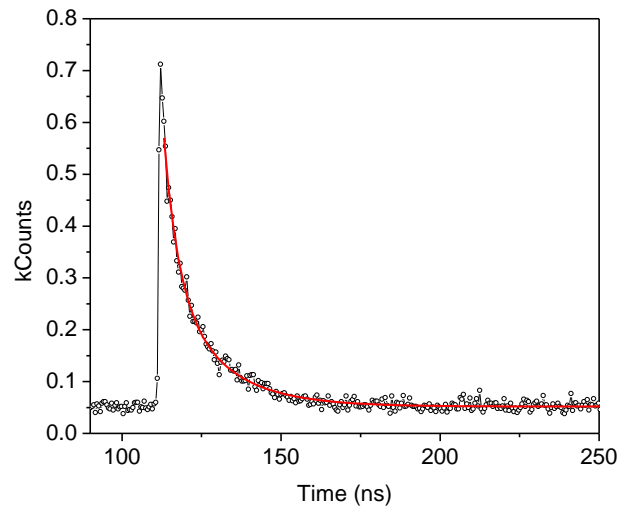


Figure 4.17 Lifetime measurement for a single NV⁻ centre in a diamond nanocrystal 80 nm in size: experimental data (points) and exponential fit (solid line) are shown. The estimated lifetime of this centre is 16.2 ns. Data refers to an HPHT monocrystalline diamond powder from Microdiamant (MSY 0-0.1 μm).

For example, in bulk diamond the accepted mean lifetime of the NV⁻ excited state is 11.6 ns [251], while for a centre in an isolated diamond nanocrystal it can go be as high as roughly 25 ns [250]. In the literature, such difference in the fluorescence lifetime of the NV⁻ centre is explained simply by considering the difference in the effective refractive index experienced by the centre embedded in a nanodiamond or in the bulk [250, 252]. In the weak coupling regime, the spontaneous emission rate Γ_n of a dipole embedded in a homogeneous medium is proportional to the refractive index n as a result of a n^3 proportionality (the mode density is proportional to the elementary volume in the wave-

vector space, from which arises the cubic exponent of n) outweighing a reduction in the electric field intensity of n^2 ($\epsilon_r = n^2$, ϵ_r being the relative susceptibility) [253]:

$$\Gamma_n(n) = n\Gamma_0 \quad (4.10)$$

where Γ_0 is the emission rate of the dipole in free space. In previously accepted reports [250, 252], the emission of NV⁻ centres has been characterised as follows. While in the bulk the NV⁻ dipole emits in the surrounding diamond matrix (refractive index $n_d \cong 2.4$), in a diamond nanocrystal deposited on a substrate, the centre is considered to effectively emit in two half-spaces, the air (refractive index $n_a = 1$) and the substrate (refractive index $n_s \cong 1.5$, for glass). The resulting emission rate Γ_{ND} for NV⁻ centres in nanodiamonds would therefore turn out to be an average value given by:

$$\Gamma_{ND} = \frac{1}{f_s} \left[\frac{n_a}{n_d \tau_b} + \frac{n_s}{n_d \tau_b} \right] \quad (4.11)$$

where f_s is the volume fraction of the substrate (generally it is assumed $f_s = 1/2$) and $\tau_b = 11.6$ ns is the accepted spontaneous emission lifetime for an NV⁻ centre in bulk diamond. Equation (4.11) predicts a value of the NV lifetime in nanodiamonds of $\tau_{ND} = (\Gamma_{ND})^{-1} \cong 23$ ns, which is in good agreement with the measured value.

Recently, we challenged this model observing that while the argument leading to equation (4.11) is reasonable for an isolated dipole (e.g. a dye molecule) close to the surface, it may not be appropriate for a dipole trapped inside a high-index sub-wavelength particle, such as an NV⁻ centre in a nanodiamond less than 100 nm in size [253]. The study showed that the environment surrounding the NV⁻ centre and the hosting nanodiamond play an important role in determining the optical properties of the centre. This last aspect is one of the main focuses of this thesis (cf. cs. 5 and 6).

4.5.4 Spectrometer

The detection channel also comprises a commercial spectrometer (SpectraPro Monochromator Acton SP2500, provided with a Pixis Camera model 7515-0001; Princeton Instruments) (Table 4.2). The light is diverted from the HBT interferometer by a motorised flippable mirror (8892-K; New Focus) and redirected by another two mirrors to a lens that focuses it on the aperture of the spectrometer. The system has three gratings mounted on a motorised rotation turret and with different groove density and blazing: a 1200

groves/mm blazed at 750 nm a 300 groves/mm blazed at 750 nm and a 300 groves/mm blazed at 500 nm.

Table 4.2 – SpectraPRO Monochromator SP2500 specifications	
Focal length	500 mm
Aperture ratio	f/6.5
Scan range (1200 g/mm grating)	0-1400 nm, mechanical range
Linear dispersion (1200 g/mm rating at 435.833 nm)	1.52 nm/mm
CCD resolution (1200 g/mm rating at 435.833 nm, 20 µm slit width and 20 µm pixel)	0.09 nm
PMT resolution (1200 g/mm rating at 435.833 nm, 10 µm slit width and 4 mm slit height)	0.05 nm
Wavelength coverage (across 26.8 mm CCD)	41 nm
Grating size	68 × 68 mm ² Mounted on a motorised triple grating turret
Focal plane size (front exit port)	27 mm wide × 14 mm high
Astigmatism (at focal plane edges)	250-300 µm
Manual slits (micrometre adjustable)	10 µm to 3 mm (manual)
Wavelength accuracy	± 0.2 nm
Repeatability	± 0.05 nm
Drive step size	0.005 nm

The spectrometer collects the fluorescent light emitted by the defects in the diamond sample. By recognising the spectral features, mainly the zero phonon line and the vibronic side bands at longer wavelengths, it enables identifying whether the fluorescence comes from NV centres or has different origin.

System resolution and collection efficiency. The lateral resolution of our lab-built confocal setup is ≤ 200 nm for a 532-nm wavelength excitation laser (cf. s. 4.2).

The collection efficiency of the system is $\eta \sim 1\text{-}2\%$. This results from combining the efficiency of each component along the detection path. The oil immersion objective (UPlanFL N, 100× / N. A. 1.3 / W. D. 0.2 mm / F. N. 26.5; Olympus) collecting the light of the fluorescent NV centres is the main limiting factor. In fact, the solid angle it subtends covers only a small fraction of the sphere in which the photons are emitted, isotropically,

by the luminescent NV centres. The objective collection efficiency is $\eta_{obj} \sim 25\%$ ($\eta_{obj} = [1 - \sqrt{1 - (NA/n)^2}]/2$, being NA the numerical aperture of the objective and n the refractive index of the medium). The additional losses are due to the optical components of the system (cf. Fig. 4.8): mirror blank (90 : 10, PF20-03; Thorlabs), optical filters (NF-533-17, FEL0550 and FEL0650; Thorlabs), 50- μm pinhole (P50S; Thorlabs), beam splitter (50 : 50, PF20-03; Thorlabs), avalanche photodiode (SPCM-AQR-14; Perkin Elmer), other optical components such as lenses and mirrors.

5

Size-dependency of carbon structures and properties of NV centres at the nanoscale

Applications based on nitrogen-vacancy (NV) centres in diamond are incredibly promising (cf. c. 2, ss. 2.4.1-3 and c. 3, ss. 3.3.1-5). In the past few years the interest has been shifted to the more practical issues of material science. Each NV centre-based technology requires the defects to be thermodynamically and optically stable and available at suitable concentrations.

In this chapter, I focus on one parameter in particular: the size of the carbon particles. We are interested in determining whether and how the properties of the NV centre are affected by the size of the nanodiamond hosts, since certain applications such as for instance high-resolution magnetometry and biomedical imaging rely on the optical stability of the NV within the smallest possible diamond nanocrystals. This is, however, just one aspect that motivates our interest in the size of the nanodiamonds. Size in fact, has an influence on a more general level and determines the actual behaviour of carbon at different scales. It affects for instance the stability, and therefore the existence, of certain carbon structures, and influences the thermodynamic equilibrium of the carbon phases themselves.

Here, I consider all these aspects. The goal is to frame the role played by size with regard to the actual realisation of diamond-based technologies and, more specifically for the

purposes of this work, with regard to applications based on NV centres in nanodiamonds (NDs).

5.1 Carbon at the nanoscale

At different scales, matter looks and behaves differently. Carbon for instance, can form unique nanostructures which have no equivalent at the macroscopic scale and even its phase transitions and thermodynamic equilibrium points are different.

Understanding the effects that size has on the stability and properties of carbon is mandatory if we want to exploit and possibly tailor diamond as a material for specific technological purposes.

5.1.1 Carbon structures

In the range 1-10³ nm carbon can exist in several very specific forms that are stable only in this particular range and cannot exist at higher scales. The variety of structures is so diverse, that numerous and often conflicting schemes, have been proposed to classify them.

Classification schemes can for instance be based on the dimensionalities of the structures [254, 255]. Within this scheme, carbon structures are regarded as zero-dimensional (fullerene, diamond clusters), one-dimensional (nanotubes), two-dimensional (graphene) and three-dimensional (nanocrystalline diamond, fullerite).

In different approaches, the carbon structures are classified on the basis of their characteristic sizes, shapes and spatial arrangements of the structural carbon units. In this scheme, the classification can be based, for instance, on the different distributions of penta- or hexa-rings within the carbon structures, on the different types of cage structures carbon can form or on its various and more complicated hierarchical assemblies such as carbon fibres or carbon polyhedral particles [256].

Other classification schemes are based instead on the type of chemical bonds carbon can form [257]. Elemental carbon exists in three bonding states: sp^3 , sp^2 and sp hybridisation of

the atomic orbitals. To these three bonding states correspond three different carbon allotropes: diamond, graphite and carbyne. They are used for classification. In this scheme, all the other carbon structures constitute a fourth group of so called “transitional forms” that are generally divided into two subgroups. The first subgroup comprises forms of arranged carbon atoms of different hybridisation states. They include: diamond-like carbon, vitreous carbon, soot, carbon-blacks, etc. The second subgroup includes intermediate carbon forms with a non-integer degree n of carbon bond hybridisation, sp^n . The forms with $1 < n < 2$ include various monocyclic carbon structures, while the forms with $2 < n < 3$ comprise closed-shell carbon structures as fullerenes, carbon onions and nanotubes.

More general schemes adopt a wider classification approach in which both the type of carbon atom hybridisation and the characteristic sizes of the nanostructures are considered [258]. The basic idea is that the different nature of the sp^n bond, n being either integer ($n = 1, 2, 3$) or non-integer ($1 < n < 2$ and $2 < n < 3$), is responsible for the existence of various carbon forms. For different scales, number of carbon atoms and ways in which the carbon atoms arrange in networks, different corresponding carbon structures are identified (Fig. 5.1).

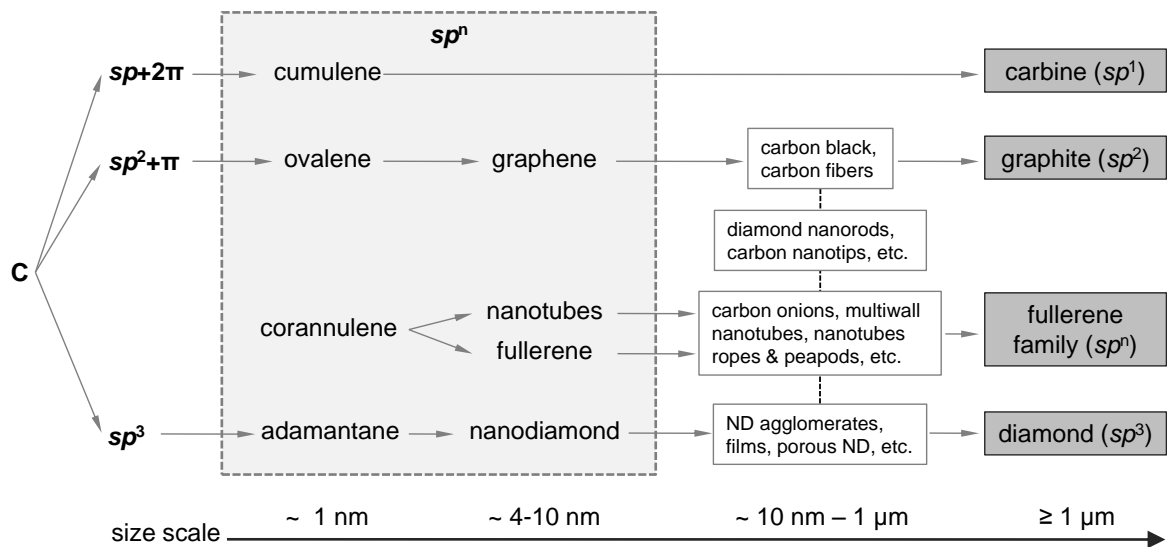


Figure 5.1. Classification of carbon structures. The mark “ sp^n ” indicates intermediate carbon forms with non-integer degree n of carbon bond hybridisation. The size scale helps identifying the hierarchy of the carbon materials.

Figure 5.1 shows the hierarchy of various carbon structures based on the classification scheme where both the type of carbon atom hybridisation and the characteristic sizes of the structures are considered. First, we encounter the very small entities of the nanoworld (size range ~ 1 nm) which include: cumulene, ovalene, corannulene, adamantane etc. Then, we find the basic structural carbon units (range ~ 4 -10 nm): fullerenes, nanotubes, graphene, nanodiamond clusters, etc. Assemblies of structural units follow (range ~ 0.01 -1 μm): carbon black, carbon fibres, carbon onions, multiwall nanotubes, nanotube ropes and peapods, nanodiamond agglomerates, nanocrystalline films, etc. Finally the forms of carbons at the upper micro/macroscale come (range ≥ 1 μm): carbide, graphite, fullerene and diamond.

From this section, it should be clear that the family of carbon nanostructures is quite vast. Nanodiamond finds its place in it, but in the literature the term “nanodiamond” is often used, broadly, to address a variety of materials ranging from single diamond particles, whose size is limited to only few nanometres (~ 2 -10 nm), to bulk monocrystalline films, whose size can go up to the micrometre scale (~ 0.01 -1 μm).

In this work I will use the term “nanodiamond” in its more rigorous acceptance, indicating diamond nanoparticles whose size is limited to be less than 100 nm.

5.1.2 Carbon phase diagram at the nanoscale

In recent years, improved theoretical and experimental techniques have expanded the understanding of the pressure-temperature phase and transformation diagram for carbon. In addition to the four main thermodynamically stable forms of carbon, i.e. graphite, diamond, liquid and vapour, other metastable and hybrid forms have been synthesised under specific temperature and pressure conditions and have been included in the phase diagram (Fig. 5.2) [259]. The diagram includes regions for the solid phase transformation of diamond to graphite, graphite to diamond, hexagonal graphite to hexagonal diamond, the shock compression of graphite to hexagonal or cubic diamond and other experimentally observed phase transitions.

Once again, size is a key factor. The dimension of carbon clusters in fact influences the stability of the diamond and graphite phases [260] and to be complete, a carbon phase

diagram must include the thermodynamical properties of nanoscale carbon particles as a function of size. Different approaches have been proposed to consider this aspect.

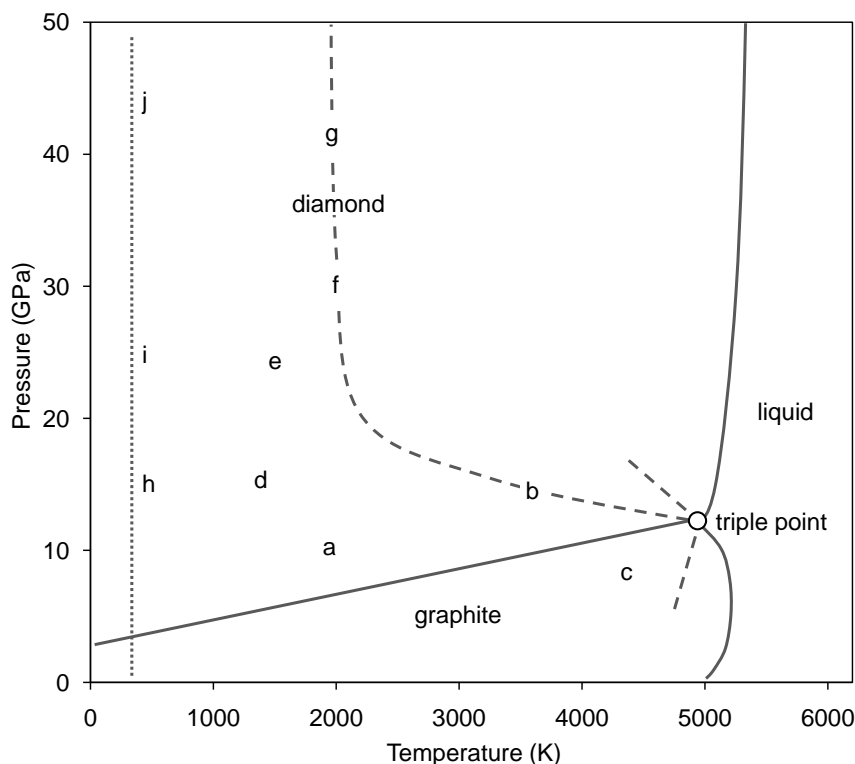


Figure 5.2. Pressure-temperature phase and transition diagram for carbon up to 50 GPa and 6000 K (adapted from [259]). Solid lines represent equilibrium phase boundaries. Other phase transitions are indicated by the letters. Commercial synthesis of diamond from graphite by catalysis (a). Pressure-temperature threshold of very fast (less than 1 ms) solid-solid transformation of graphite to diamond (b). Pressure-temperature threshold of very fast transformation of diamond to graphite (c). Single crystal hexagonal graphite transformation to retrievable hexagonal-type diamond (d). Upper ends of shock compression/quench cycles that convert hexagonal graphite particles to hexagonal diamond (e). Upper ends of shock compression/quench cycles that convert hexagonal graphite to cubic diamond (f). Threshold of fast pressure-temperature cycles, however generated, that convert either type of graphite or hexagonal diamond into cubic diamond (b, f, g). Path along which a single crystal hexagonal graphite compressed in the *c*-direction at room temperature loses some graphite characteristics and acquires properties consistent with a diamond-like polytype, but reverses to graphite upon release of pressure (h, i, j).

One possibility is to determine the thermodynamical stability of the particles by using equations of state that account for the coexistence of several gas, liquid and solid phases in chemical equilibrium [261].

In a different approach, the total Gibbs free energy for the carbon nanoparticles is considered. The carbon clusters, of either the graphite- or the diamond-type, are assumed to have a total Gibbs free energy given by the sum of two contributions. These are the

contribution from the bulk, of either the graphite- or the diamond-type, and the contribution from the surface, which is proportional to the cluster outer area:

$$G_i(P, T, n) = \hat{G}_i(T, P) + dE_i n^{-1/3} \quad (5.1)$$

In equation (5.1), G_i is the total Gibbs free energy, \hat{G}_i is the bulk Gibbs free energy which depends only on pressure (P) and temperature (T), dE_i is the n -atom cluster surface energy of the i -th phase (dE_i is assumed constant and equal to 70kcal/mol, 40kcal/mol and 1kcal/mol for i being diamond, graphite and liquid carbon phase respectively) and n is the number of atoms the cluster is made of. The exponent of n accounts for the fact that in a cluster of n atoms, its surface to mass ratio is proportional to $n^{-1/3}$, assuming the cluster spherical [262]. At given temperature and pressure, a cluster is regarded as being of diamond type if its diamond Gibbs free energy is less than its graphite Gibbs free energy, i.e. if $G_{\text{graphite}}(P, T, n) > G_{\text{diamond}}(P, T, n)$, and vice versa for the graphite type. The phase equilibrium lines for the n -atom clusters can be determined by equating the Gibbs free energies of the corresponding phases [258, 261, 263]. Figure 5.3 shows the carbon phase diagram including the displacement of the phase equilibrium lines for carbon nanoparticles containing $\sim 10^3$ atoms [262, 264].

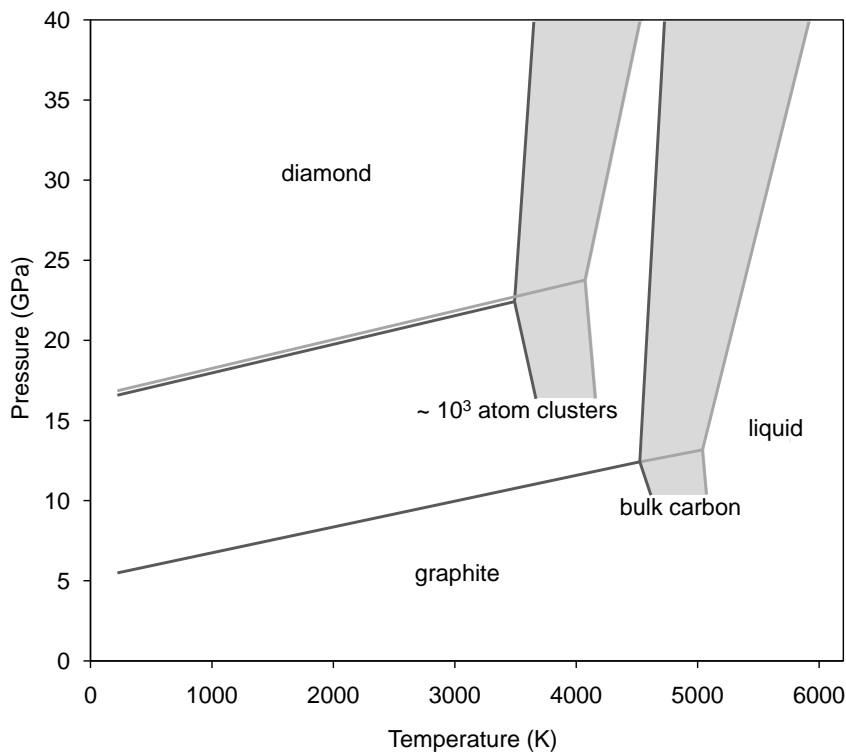


Figure 5.3. Estimate phase diagram for $\sim 10^3$ atom clusters. Shaded regions correspond to uncertainties in location of equilibrium lines derived from experimental data. (Graph adapted from [264]).

Three-dimensional phase diagrams (Fig. 5.4) where size is accounted as an additional parameter emphasise even more the importance of the cluster dimensionality in determining the thermodynamical equilibrium of carbon phases [265].

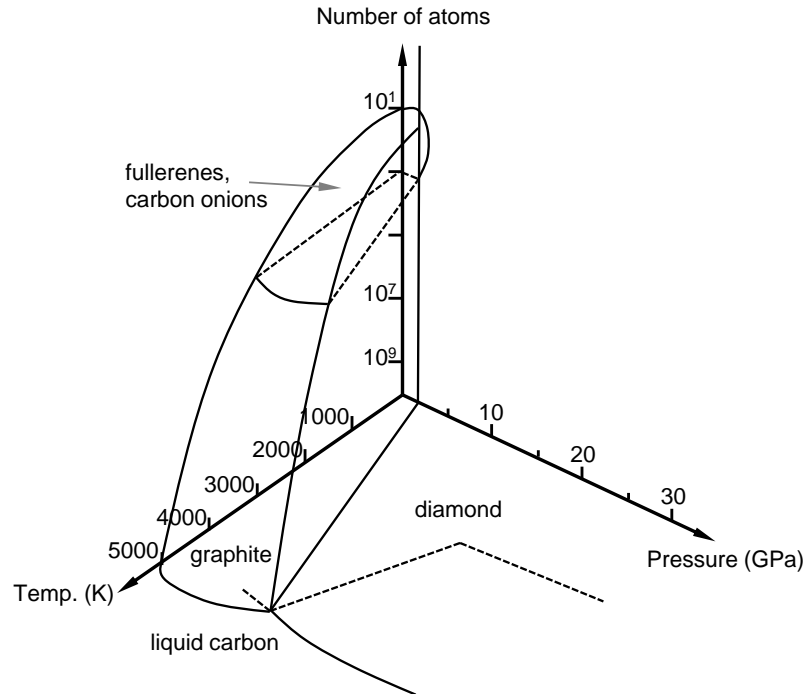


Figure 5.4. Schematic three-dimensional phase diagram for carbon including fullerene and onion-like carbon for a number of atoms n ranging from 10 to 10^3 (adapted from [266]).

In such diagrams, the lower horizontal plane corresponds to the phase diagram for carbon bulk phases, while the vertical axis provides the size dependence. Nanodiamond appears to be the most stable phase at particle size below 3 nm. The diamond phase though, diminishes at sizes below 1.8 nm; this is the minimum particle size observed experimentally. The particle dimensionality also influences the position of the triple point of carbon, but the literature in this case is not always consistent reporting that for smaller particles the triple point shifts towards higher pressures [264] or, oppositely, towards lower pressures [265]. Another variant of the three-dimensional phase diagram proposes tentatively a change of the slope of the diamond-graphite equilibrium line as the particle size decreases [258]. This results in a higher stability of nanodiamond over nanographite at ambient conditions. Another aspect to consider is the fact that at sizes below 1.8 nm, other carbon forms, such as fullerenes and onion-like carbon, are abundant and they have to be taken into account. As a consequence, a corresponding region of the carbon phase

diagram has been assigned to closed-shell sp^2 -bonded nanocarbons for a number n of atoms from 10 to 10^3 (Fig. 5.4) [266-269].

The carbon family at the nanoscale comprises several other low-dimensional carbon systems (Fig. 5.1). Their inclusion in the carbon-phase diagram is a necessary but still-to-come step towards the construction of a complete P - T - n phase diagram of carbon.

5.1.3 Theoretical studies on the stability of carbon at the nanoscale

The stability of the carbon phases at the nanoscale has been addressed in several theoretical studies based on ab initio, semi-empirical and first principles calculations [258, 270]. These methods determine the stability of specific carbon structures based on energy minimisation criteria, once the conditions for the theoretical models are set. In principle, they can account for any parameter involved in the occurrence of certain carbon forms under specific conditions, as long as each parameter is of course identified and opportunely modelled in the theoretical computation. Temperature, pressure, cluster size, but also number of atoms in the clusters, surface to volume ratio, number of dangling bonds, surface chemistry etc. are all factors that these methods can include and help investigating.

The earliest theoretical computational studies on the stability of carbon phases date back to 1987 when J. Amlöf and H. P. Lüthi conducted the first ab initio restricted Hartree-Fock calculations on the phase stability of several planar graphene sheet structures and cubic diamond clusters [271]. They aimed to computationally determine the cohesive energy of carbon clusters where these clusters were either considered with their surface dangling bonds left unsaturated or terminated with hydrogen. Respectively, clusters C_n and C_nH_m , n being the number of carbon atoms in the cluster and m the number of hydrogen atoms at the surface. Neglecting the contribution from the cluster zero-point energy, they determined the cohesive energy of the cluster as the difference between the total energy per carbon atom in the cluster and the energy per corresponding free carbon atom. The cohesive energies they calculated for the considered graphite and diamond structures however (n and m in the range ~ 10 - 10^2), turned out to be higher than the corresponding experimental values [272]. The inaccuracy can be attributed to the fact that the ab initio

restricted Hartree-Fock method omits crucial parameters in the calculation, such as electron correlation and vibrational zero-point corrections. Results in better agreement with the experimental values are obtained by using semi-empirical Hartree-Fock methods which can account for these parameters [273].

Shortly after Amlöf and Lüthi's study, M. S. Shaw and J. D. Johnson proposed a diffusion-limited model which highlighted the importance of surface atoms in determining the stability of carbon clusters [263]. Their model estimates the difference in energy ΔE between carbon clusters and macroscopic bulk diamond assuming ΔE proportional to $n^{1/3}$, where n is the total number of carbon atoms and its exponent accounts for the surface to mass ratio of the (assumed) spherical cluster.

The important role played by the surface in determining the phase stability of carbon nanoparticles was later reinvigorated by a study conducted by P. Badziag and collaborators [274]. They calculated the binding energies of a set of relatively simple tetrahedral and hexagonal carbon clusters and they correlated such energies with the effects of terminating the surface bonds of the structures with hydrogen atoms. The calculations of the binding energies as a function of the hydrogen to carbon ratio showed that for comparable hydrogen to carbon ratios, diamond-like clusters smaller than ~ 3 nm tend to be more stable than graphite structures. They quantified the graphite-diamond transitions and observed that these, depending on the type of cluster considered, occur at hydrogen/carbon ratios between 0.5 (corresponding to an octahedral nanodiamond of ~ 300 atoms, diameter ~ 1.4 nm) and 0.12 (corresponding to an octahedral nanodiamond of ~ 21000 atoms, diameter ~ 6 nm). A similar result was obtained more recently by D. W. Brenner and co-workers for relaxed hydrogenated graphitic and diamond-like structures using bond-order inter-atomic potential functions [275].

M. Y. Gamarnik investigated the stability regions of graphite and diamond nanoparticles at low pressure and different temperatures by using a semi-empirical model of inter-atomic interactions [276]. To determine the energy difference between the phases, the model includes the contribution of the Helmholtz free energy $dF = T(S_{\text{graphite}} - S_{\text{diamond}})$, where T is the temperature and $(S_{\text{graphite}} - S_{\text{diamond}})$ is the difference in entropy of graphite and

diamond. The model also accounts for the kinetic energies of the graphite and diamond bond electron charges. They differ in the fact that in diamond the charge of a bond electron is equally distributed along the four axis of a tetrahedron (due to the sp^3 hybridisation), while in graphite it is distributed along three directions only, in a planar fashion (due to the sp^2 hybridisation). The computational results showed that the energy per atom is again dependent on the size of the nanoparticles as well as on the temperature T . For instance, the model predicts that diamond nanocrystals are stable below 10.2 nm at room temperature; they are stable below 6.1 nm at 545 °C, below 4.8 nm at 800 °C and below 4.3 nm at 1100 °C.

N. M. Hwang et al. analysed the low pressure synthesis of nanodiamond via a model that considers the chemical potential and the surface energies of carbon clusters [277]. The method has the advantage of being applicable to non-equilibrium conditions. They were able, for instance, to predict the precipitation of graphite and diamond from the gas phase: assuming spherical particles, the crossover from the gas phase was estimated (at temperature $T = 1200$ K) to be 104 atoms for graphitic clusters and 177-584 atoms for diamond clusters. The method was also used to examine the nucleation of carbon clusters on a substrate during chemical vapour deposition (CVD) growth. They also tried to analyse the effect of the charge on the stability of the diamond and graphite clusters [278]. The idea is that in the conductive graphite the charge is distributed uniformly over the bulk and the interface while in diamond it is localised at the interface. This is likely to reduce the surface energy of diamond in comparison to that of graphite [279].

F. H. Ree, N. Winter and collaborators considered the heats of formation for graphene sheets and diamond clusters as a function of size to predict the relative stability of carbon phase nanoparticles [260, 273]. The dependence of the total energy on the number of carbon atoms is obtained by fitting the calculated cluster energies to the equation [273]:

$$E = N_c E_c + N_{db} E_{db} \quad (5.2)$$

Where E is the total energy, N_c is the number of carbon atoms, N_{db} is the number of dangling bonds and E_c and E_{db} are the energies per carbon atom and per dangling bond, respectively. Equation (5.2) shows that the surface energy contribution due to the dangling bonds is relevant for small clusters, but becomes less important for larger

clusters for which $N_C \gg N_{db}$. For large clusters, the surface contribution is negligible and the cohesive energy tends to the bulk cohesive energy $N_C E_C$.

The same scheme can be applied to cluster surfaces terminated with hydrogen atoms instead of uncapped dangling bonds. In this case equation (5.2) is naturally modified as:

$$E = E_C N_C + N_H E_H \quad (5.3)$$

Where E , E_C and N_C are the same as in equation (5.2), while N_H and E_H replace respectively N_{db} and E_{db} , being in equation (5.3), N_H the number of hydrogen atoms which saturate the dangling bonds and E_H the carbon-hydrogen (C-H) energy contribution. Several different computational methods have been applied to this general scheme to calculate the graphene and diamond cluster cohesive energies of different carbon particulates. They show good agreement with experimental values [273].

These results can be extended to take into account the effect of the heat of formation on the cluster size. In graphite, each carbon atom forms three intra-layer sp^2 bonds and experiences a weak inter-layer interaction with the atoms of the nearest neighbour graphite sheets. In diamond, each carbon atom forms identical sp^3 bonds with the other nearest neighbour carbons. By considering the carbon-carbon (C-C) bond energies and the carbon-hydrogen (C-H) surface bond energies for the two different carbon phases, it is possible to express the heats of formation for sp^2 and sp^3 carbon clusters as follows [273]:

$$\begin{aligned} \Delta H_f^0(sp^2) = & (1/2)(3N_C - N_H)E_{CC}^{sp^2} + N_H E_{CH}^{sp^2} + \\ & + N_C \Delta H_f^0(C) + N_H \Delta H_f^0(H) + (1/2)N_C E_{CC}^{disp} \end{aligned} \quad (5.4)$$

$$\begin{aligned} \Delta H_f^0(sp^3) = & (1/2)(4N_C - N_H)E_{CC}^{sp^3} + N_H E_{CH}^{sp^3} + \\ & + N_C \Delta H_f^0(C) + N_H \Delta H_f^0(H) \end{aligned} \quad (5.5)$$

where, N_C and N_H are the numbers of carbon and hydrogen atoms, E_{CC} is the energy of the carbon-carbon bond, E_{CH} is the energy of the carbon-hydrogen surface bond and E_{CC}^{disp} is the carbon-carbon pair energy due to the inter-layer dispersion within the graphite sheets. Equations (5.4) and (5.5) can be used to estimate the C-C bond energies both for the sp^2 and sp^3 phases simply by using the experimental values for the corresponding cohesive energies of graphite and diamond. More interestingly, they can as well be used to predict the stability of (hydrogenated) nanographite and nanodiamond as a function of size. This is done by determining the intercept between the calculated heats of formation as a function of the number of carbon atoms for the two phases. Calculations show that

(hydrogen-capped) diamond clusters smaller than 30000-70000 atoms ($\sim 7-9$ nm particle size) are more stable than three-dimensional graphite clusters of the same size, but become less stable for clusters made of a larger number of carbon atoms [273].

Q. Jiang and co-authors investigated another specific aspect: the contribution of the size-dependent internal pressure of the carbon nanoparticles on their phase stability [280]. Including this variable, the model shows that the transition size of nanodiamond decreases from ~ 8 nm at temperature $T = 0$ K, to ~ 3 nm at $T = 1500$ K. The model was later extended by D. Zhao and co-authors to include as well the effects of surface stress on the internal pressure of the nanoparticles [281]. It was found that the transition size of nanodiamond decreases from ~ 11 nm at temperature $T = 0$ K, to ~ 4 nm at $T = 1500$ K. This 1-3 nm difference between the results of the two groups in the transition size of nanodiamond with and without including the surface stress shows once more how important is the role played by surface in determining the phase stability of nanocarbon.

All these studies address the phase stability of carbon for clusters $\sim 5-6$ nm in size. Smaller particles (< 2.5 nm), with the inclusion of fullerenes, have also been investigated for instance by A. S. Barnard and collaborators [282]. Their method, based on enthalpy of formation as a function of size, takes into account several parameters including bond energies of diamond-like and fullerene clusters, energies of dangling bonds, number of surface dangling bonds, number of carbon atoms and heat of formation of carbon at ambient temperature. For the analysis of fullerenes, since they can be regarded as homogeneous and isotropic elastic spheres made of single bent carbon sheets, it is nonsense to define an effective surface to volume ratio; the model instead, considers an additional contribution derived from the stretching and bending of the carbon sheets. The enthalpy of formation for relaxed dehydrogenated (stable) nanodiamond crystals and fullerenes was determined and the cross-over point was reported to be ~ 1100 atoms, corresponding approximately to a cubic nanodiamond crystal of 1.9 nm in diameter [282].

A few studies have also been conducted on the stability of carbon structures even smaller than fullerenes, below ~ 1.5 nm in size [283-286]. There are also studies on the relative stability of fullerenes and carbon nanotubes [287] and on multishell carbon nanoparticles

[288]. In this last case, the results showed that the sp^2 -bonded onion-like carbon and fullerene clusters are energetically almost indistinguishable below ~ 2000 atoms and that the enthalpy of formation of bucky-diamond is closer to onion-like carbons than to nanodiamonds. It was also found that within ~ 500 and ~ 1850 atoms there is a region of thermodynamic coexistence of several nanocarbon structures. More specifically: from ~ 500 to ~ 900 atoms (~ 1.4 - 1.7 nm) the enthalpy of formation of bucky-diamond appears to be indistinguishable from that of fullerenes, from ~ 900 to ~ 1350 atoms (~ 1.7 - 2.0 nm) bucky-diamond and onion-like carbon coexist and finally from ~ 1350 to 1850 atoms (~ 2.0 - 2.2 nm) bucky-diamond is found to coexist with nanodiamond. However, the intersection of the bucky-diamond and onion-like carbon stability is very close to the intersection for nanodiamonds and fullerenes at ~ 1100 atoms. This suggests that at ~ 1100 atoms a sp^3 -bonded core becomes more favourable than a sp^2 -bonded core, in spite of the surface structure.

To complete this review, it must be said that there are several studies which investigate other aspects relevant to the phase transitions of carbon. Here, I reference only a few of them. There are studies related to the effect of the crystal morphology of the cluster [289], the effect of the charge [290], studies on the phase transition between nanodiamond and onion-like carbon structures [281, 291] or between graphene and nanotubes [292] and studies investigating the relative phase stability of carbon via kinetic theories as oppose to thermodynamic approaches [293].

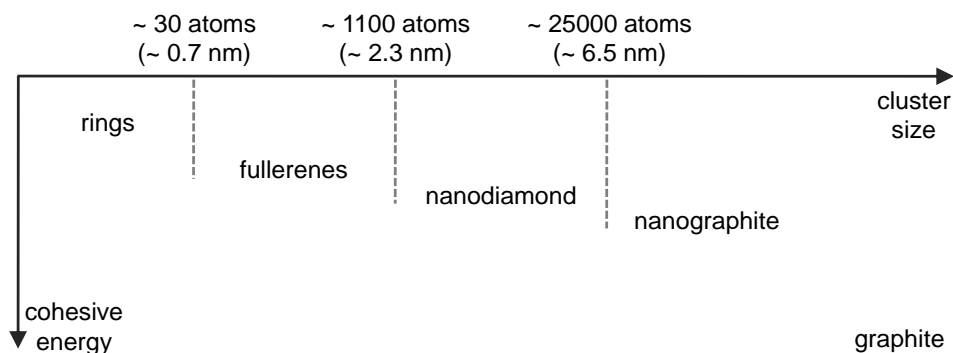


Figure 5.5. Scheme of the most stable phases of carbon as a function of the cluster size/number of atoms.

From this section it should be clear that theoretical-computational methods can be used in conjunction with experimental observation to better investigate the phase transitions of carbon at the nanoscale. At this scale, both theory and experiments suggest that the size of the carbon clusters is crucial in determining the relative stability between the sp^2 - and sp^3 -bonding characters of the particles. The evidences show that macroscopically, or even just above the strict nanoscale, graphite rather than diamond is the more stable form of carbon. But, when the nanoscale is accessed this does not hold anymore and the carbon phase stability experiences a cross over. For particles ~ 5 -10 nm in diameter, nanodiamond becomes energetically more favourable than nanographite and similarly, for smaller particles ~ 1.5 -2 nm in diameter, fullerenic structures are expected to be more stable than nanodiamond (Fig. 5.5). These studies also show that at the nanoscale the phase transitions of carbon are not solely driven by thermodynamic. On top of pressure and temperature other factors such as size, surface chemistry, surface stress, surface charge and kinesis of the processes may play a relevant role in inducing a phase change.

In conclusion, size does affect the phase stability of carbon clusters. This has to be carefully considered especially in the perspective of tailoring and utilising nanodiamond as a technological material. However, as a last note, I want to make clear that even though nanodiamond is stable only in a certain size range (~ 5 -10 nm), diamond nanoparticles can be found (metastable with respect to the other phases) in the whole nanoscale (i.e. ~ 1 -100 nm) with characteristics and properties often determined by the processes utilised to synthesise them.

5.1.4 Structural properties of diamond nanoclusters

In this section, I briefly discuss the relationship between the number of atoms in a nanodiamond and its size, the number of surface atoms and finally the shape of the clusters.

Number of atoms. From a crystallographic point of view (cf. c. 2 sec. 2.2.1), in diamond the conventional unitary cubic cell has a length $a = 0.356$ nm (at temperature $T = 293$ K) and contains eight atoms (the diamond density is 3.51 g/cm³ at $T = 293$ K) [1]. Thus, the effective atomic volume V_c of a single carbon atom can be calculated as $V_c = a^3/8$, which

results in a value of 0.00564 nm^3 . Considering a spherical cluster of radius R and a total volume $V = (4\pi R^3)/3$, the total number N_{tot} of carbon atoms can be simply obtained as V/V_c or, explicitly:

$$N_{tot} = (4\pi R^3) / 3V_c \quad (5.6)$$

According to equation (5.6), the smallest diamond nanoparticle observed experimentally (diameter $\sim 1.8 \text{ nm}$) is made of ~ 550 atoms while nanodiamonds 5-nm and 10-nm in diameter are made of ~ 11500 and ~ 93000 atoms respectively.

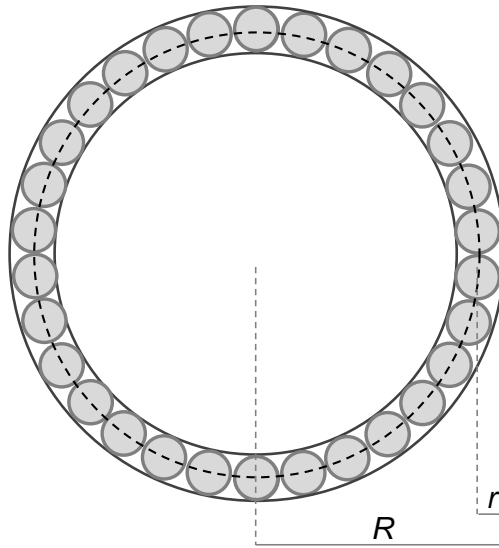


Figure 5.6. Cross section of spherical atoms (radius r) packed on the surface of a spherical particle (radius R): schematic representation.

Number of surface atoms. A very simple way of estimating the number of surface atoms is the following. Figure 5.6 shows the cross section of a hypothetical particle (radius R) where a single layer of closely packed carbon atoms (radius r) covers the surface. From the figure, it can be seen that the cross sectional area $A = \pi r^2$ of an atom, multiplied by the number N_{surf} of atoms on the surface, is approximately equal to the surface area of the sphere $S_{tot} = 4\pi R^2$, i.e.:

$$4\pi R^2 \cong N_{surf} (\pi r^2) \quad (5.7)$$

Putting together equations (5.6) and (5.7), we can thus calculate the ratio between the number N_{surf} of surface atoms and the total number N_{tot} of atoms in the cluster as:

$$N_{surf} / N_{tot} \cong 4r / R \quad (5.8)$$

which clearly shows that the fraction of surface atoms is inversely proportional to the particle size.

In another approach, in figure 5.6 the volume of the outer shell made by the surface atoms is simply the difference between the volume of the particle of radius R and that of the inner sphere with radius $(R-2r)$, i.e.: $(4/3)\pi[R^3-(R-2r)^3]$. The ratio between the surface atoms and the total number of atoms is then roughly equal to the ratio between the volume of the outer shell and that of the whole particle:

$$N_{surf} / N_{tot} \cong [R^3 - (R - 2r)^3] / R^3 \quad (5.9)$$

According to equations (5.8) and (5.9), in a nanodiamond with a diameter of ~ 1.8 nm, ~ 40 - 49% of the atoms are on the surface, while in nanodiamonds 5-nm and 10-nm in diameter the percentages are ~ 15 - 20% and ~ 7 - 11% respectively (the uncertainty on each percentage value depends on the equation used in the calculation).

As an alternative to equations (5.8) and (5.9), the following analytical expression is often used [258]:

$$N_{surf} / N_{tot} = 3 / (4Rn_{bulk}^{1/3}) \quad (5.10)$$

where n_{bulk} is the bulk atomic density; it is related to the surface atomic density n_{surf} by the relationship $n_{surf} = (n_{bulk})^{2/3}$.

Before concluding this subsection, I would like to point out that the values obtained for the ratio N_{surf}/N_{tot} depend on which equation is used. Plus, a more rigorous analysis should include the different surface morphologies that the diamond structure allows for nanoclusters. In fact, considering the nanodiamonds as spheres is a simplification: the fraction of surface atoms could differ quite significantly according to whether the cluster is considered spherical or faceted [294].

Shape of nanodiamonds. High resolution transmission electron microscopy (HRTEM) shows that while in some cases nanodiamonds resemble spherical forms [295], in others they display polyhedral shapes where faceted surfaces are clearly visible [136]. The latter case can be observed, for instance, in CVD-grown nanodiamond often appearing as cubic, octahedral, cubo-octahedral, twinned, etc. (Fig. 5.7), according mainly to the deposition conditions [136, 296-298]. The former case of quasi-spherical particles instead, is thought to be a result of buckification, a process which predominantly involves the (111) planes of

the diamond surface and causes the outer carbon atoms of the particle to “separate” from the inner core and form a carbon onion-like structure [289].

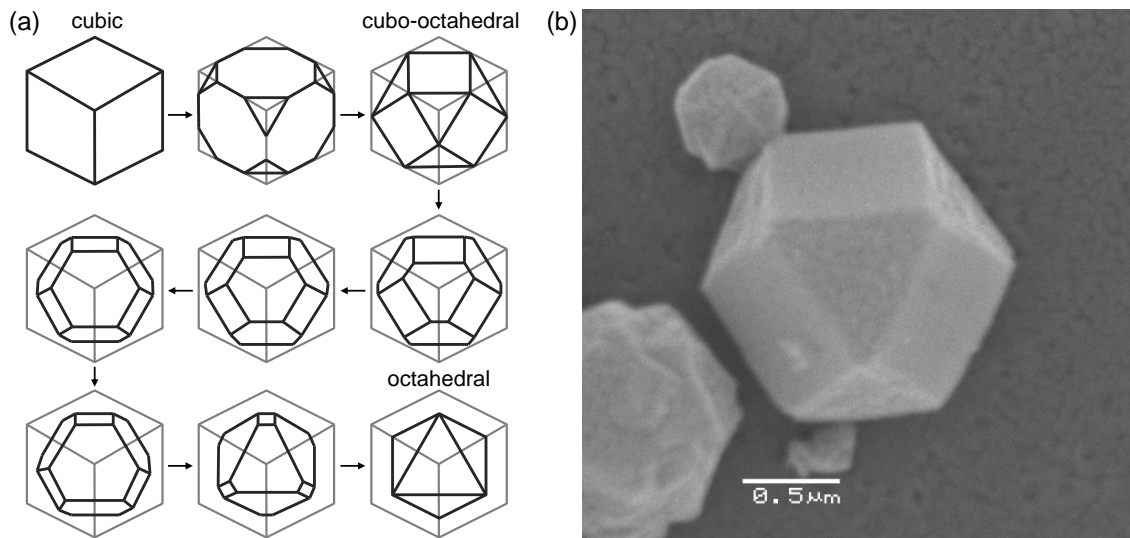


Figure 5.7. Diamonds polyhedral shapes and surface facets. **a)** Examples of some morphologies nanodiamond crystals can display. **b)** Scanning electron microscopy (SEM) image of a CVD-grown diamond in the μm range; the particle is a cubo-octahedron, its faceted surfaces are defined and well distinguishable.

In general, the shape of diamond nanoclusters is determined by energy stability considerations. In this sense, the state of the surface atoms and the fact that their bonds are either dangling or saturated with hydrogen atoms or other active groups plays a relevant role. The differences in binding energies of the various morphologies can be very small, of the order of $\sim 0.01\text{-}0.02$ eV per atom [258]. However, the hydrogenated octahedron and slightly truncated octahedron seem to be the most favourable morphologies. They have the maximum number of surface carbon atoms forming, each, three bonds with the three nearest neighbour carbons and a fourth bond with a hydrogen atom: this configuration in fact, turns out to be the most energetically favourable for a carbon atom at the surface of a cluster. The quasi-spherical nanodiamonds can still be observed. They are the product of the surface buckification process which seems to be favoured in the case of non-hydrogenated clusters, mainly on the (111) surface undergoing a transition from the sp^3 bonding structure of octahedron- or cubic-like diamond to the sp^2 bonding structure of graphite and fullerene [289].

5.2 Thermodynamical stability of NV centres in nanodiamond

Size does affect the stability of carbon at the nanoscale. Different carbon phases, morphologies and structures can be favoured, possible or highly improbable due to the size of the nanoparticles. In this section, I discuss this further by analysing the effect that size has on the stability of the nitrogen-vacancy (NV) centre in nanodiamond.

In the very recent past, several studies have been conducted on NV centres in diamond nanoparticles, motivated by the possibility of implementing new technologies (cf. c. 2, ss. 2.4.2-3). Studies were conducted to determine the intrinsic limit of the smallest diamond nanoparticle capable of hosting stable NV centres and, in parallel, other studies were performed trying to optimise processes and procedures to achieve that. Here, I briefly report chronologically some of the work on this subject.

In 2007, J. R. Rabeau and collaborators investigated the incorporation of NV centres in CVD-grown isolated nanodiamonds [158]. They synthesised diamond nanocrystals on quartz cover slips, using a microwave plasma chemical vapour deposition reactor which had a small background level of molecular nitrogen (N_2). They characterised the nanodiamonds using an AFM-confocal system similar to the one described in chapter 4 section 4.5 and they found that there was a limit. Under the condition employed, NV centres were not observed in particles smaller than ~ 40 nm.

In 2008, Y. -R. Chang and co-authors reported the production of large quantities of fluorescent nanodiamonds for biological applications [185]. They irradiated synthetic diamond crystallites with helium ions to enhance the formation of NV colour centres and found that the photo-physical characteristics of the luminescent nanodiamonds remained stable for particles as small as 25 nm.

In 2009, B. R. Smith and collaborators showed NV centre emission from aggregates of 5-nm detonation nanodiamond which were proton irradiated and annealed [299]. Their study helped to clarify some of the concerns that NV centres could perhaps not form in such small nanodiamonds due to physical barriers such as the proximity to surface traps and reduced stability of defects [300]. The question of photoluminescent defects in single isolated nanodiamonds as small as 5 nm remained however unsolved.

In 2009, J. Tisler and co-authors shed light on this last issue reporting on stable NV centre emission from isolated nanodiamonds only 8 nm in size [301]. In this study, commercially available diamond nanocrystals (average size 10 nm) were used. They were nitrogen rich nanodiamonds, which were electron irradiated (energy 8 MeV, corresponding to a dose of 10^{20} electrons/cm²) and then annealed (temperature above 700 °C). Interestingly, about 35% of the so obtained nanocrystals contained an NV centre. This proved on one hand that NV centres can be energetically stable in 8-nm diamond nanocrystals and on the other, that the production yield of NVs in nanodiamonds is comparable to that of bulk material.

In 2010, in our group we demonstrated the stability of NV centres in 5-nm sized detonation nanodiamonds [222].

I will discuss some of these results in more detail later (cf. s. 5.2.3). Here, I have given this brief overview mainly to show how this topic has experienced a significant boost in recent years, probably fuelled by the realisation that some of the technologies based on NV centres in nanodiamonds might soon be possible.

5.2.1 NV centre stability: a computational theoretical study

Control over the diamond material is a key to achieving NV centre-based nanotechnologies. We focused on using the NV centre for high resolution magnetometry and soon realised that the first step would have to be a thorough investigation of the conditions under which the NV centre is stable in nanodiamond. In fact, an NV-based magnetometer requires the centre to be stable inside a nanodiamond as small as possible (ideally only a few nanometres) to optimise the detection resolution ($\sim 1/r^3$, being r the distance between the single spin to detect and the probing NV centre; cf. c. 3, s 3.3.5, equation (3.8)).

We thus concentrated our efforts on examining the effect of size on the stability of the NV centre in diamond crystals. Studying this problem was, for our purposes, the natural and complementary follow up to the more general study on the stability of carbon clusters as a function of size that was presented in sections 5.1.1-4.

To investigate the stability of the NV centre, we conducted a study in partnership with Dr. Amanda S. Barnard [221]. The idea was to combine the data from the experiment we designed, with a computational model our collaborator developed to interpret our findings. The computational model can simulate diamond clusters with defect inclusions like NVs, so that the correlations between the characteristic of the hosting diamond particle and the stability properties of the hosted centre can be studied. In the model, the location of the NV centres within the particles can be chosen as well; this allows probing different geometric sites or lattice directions for the defects and investigating computationally the stability of the various configurations.

I report here the details of the computational method. The stability of a certain simulated configuration is determined via energy minimisation criteria, once the conditions for the diamond cluster including the NV are set.

The calculations are performed using the density functional based tight-binding method with self consistent charges (SCC-DFTB) which is a two-centres approach to density functional theory (DFT), where the Kohn-Sham density functional is expanded to second order around a reference electron density [302, 303]. This method falls into the well populated list of methods developed in the field of computational materials science to undertake the study of condensed many-body systems or even of more complex crystalline and amorphous cluster-assembled matter and solids. In general, there are two main types of approach used to determine, through computational simulation, equilibrium geometries, total energies and vibrational modes of atoms and molecules in a many-body system: empirical methods and ab initio methods.

Empirical methods, also known as classical methods, are based on the construction of derived-empirical potentials (derived from experimental data or, in turn, from other ab initio calculations) to simulate the interactions and the forces exerted by each atom of the solid on the others and which determine their equilibrium positions and energies. This method is computationally inexpensive and fast, but has the main limit of being reliable only for those systems whose structures are well understood and where electronic and spin information is not required. This comes from the fact that the empirical potentials are derived from “standard” systems normally considered at equilibrium, but for structures which differ from the usual cases due for example to the presence of defects or other

specific chemistry or physics conditions, it can produce incorrect or only rough predictions.

Ab initio methods on the other hand, are very accurate because they rely on a proper evaluation of many-particles wavefunctions and on the explicit inclusion, in the simulation, of electronic exchange and correlation interactions between the electronic clouds of each atom. The main limitation of ab initio methods consists in a high computational demand which makes them not suitable for the simulation of large or for long time frames systems and complex solids.

For the purpose of our study neither a full empirical method nor a full ab initio one is applicable. The many-body systems we are interested in, contain both hundreds of carbon atoms and a large number of individual simulations, which make it impossible to be treated using a full ab initio method. Each structure contains point (NV) defects and surfaces that can be functionalised with other chemical species like hydrogen or oxygen atoms, resulting in chemical and electronic complexity that make a full empirical approach inappropriate as well. The limitations in the transferability of empirical potential and in the use of time consuming ab initio methods lead us towards the SCC-DFTB semi-empirical approach which allows simulating and handling relatively large (hundreds of atoms) systems numerous times, with adequate accuracy and flexibility.

In general, there are other methods that fit the same criteria, such as traditional semi-empirical (SE) methods in quantum chemistry like the popular Hartree–Fock (HF) based MNDO, AM1 and PM3 methods. Unlike these methods however, SCC-DFTB is not an entirely semi-empirical, since its parameterisation procedure is completely based on DFT and is self consistent at the level of Mulliken charges (which form part of the energy functional). The essential chemical information are provided by parameterised Slater–Koster files, which contain information about the on-site energies, Hubbard U's, the tabulated radial parts of the Hamiltonian and the overlap matrix, the repulsive potential, either in spline form or as polynomial coefficients and the basis functions used in the calculation of the matrix elements. SCC-DFTB is also a non-orthogonal method, which is important for transferability (the ability of a parameterised method to perform sufficiently well also for chemical environments not included in the parameterisation procedure). As a result, SCC-DFTB often displays DFT-like characteristics, such as the size of the Kohn–Sham energy gap or the tendency to underestimate reaction barriers. In other words,

although SCC-DFTB results are closer to DFT than its counterparts, it also inherits some of DFT flaws. Having said that, this method has been successfully applied to carbon-based materials and clusters and to diamond nanoparticles in their pure state or in the presence of substitutional defects (like N, B, Si, SiV and NV centres) and with the passivated or functionalised surface (including monolayers of hydrogen or oxygen atoms).

This computational method can be used to “build” diamond nanoparticles with unpassivated and passivated surfaces and hosting NV substitutional inclusions. In this study, we specifically considered two reference nanodiamonds made both of 837 carbon atoms (~ 2.2 nm in diameter): a dehydrogenated C_{837} cluster and a fully hydrogenated $C_{837}H_{252}$ cluster with each undercoordinated surface atom terminated with hydrogen atoms.

The choice of the C_{837} and $C_{837}H_{252}$ particles is a compromise between several factors. Firstly, such systems are in the right size range for being stable nanodiamonds. They fall in fact, in the window between the range of smaller sizes where the fullerene carbon structures are more stable and that of the larger sizes where the graphitic-like carbon structures are more favourable than diamond (cf. ss. 5.1.1-4). Secondly, the number of atoms composing such clusters is large enough to be physically appropriate for our purposes, but at the same time not too large to make unfeasible the computation of the minimum equilibrium energies. Finally, studying both the unpassivated C_{837} and the hydrogen passivated $C_{837}H_{252}$ version of the same representative particle allows investigating whether the chemical passivation of the surface plays any role in determining the stability of NV centres in small nanodiamonds. On this last point, it could be argued that in reality nanodiamonds surface can react with several chemical groups other than hydrogen and that the hydrogen passivation is only one very specific case. That is true, but here we are interested in determining the generic effect of the surface passivation rather than the effects of specific chemical functionalisations and hydrogen termination is considered suitable and is traditionally used in literature for such purpose.

The stability of both the unpassivated C_{837} and the hydrogen passivated $C_{837}H_{252}$ particles is calculated. The convergence criterion in the energy minimisation computation for a

stationary point is set at 10^{-4} au ≈ 5 meV/Å for the forces. Both particles relax in truncated octahedral nanodiamonds, displaying six (100) facets and eight (111) facets (Fig. 5.8). Upon relaxation, the C_{837} nanoparticle exhibits delamination of the (111) surfaces and (111)/(111) edges, forming a truncated octahedral bucky-diamond with a sp^3 -bonded diamond-like core encapsulated by a sp^2 -bonded fullerenic/graphitic outer shell. The outer shell at the surface remains attached to the core along the (111)/(100) edges and the (100) surfaces undergo the (2×1) reconstruction. The $C_{837}H_{252}$ nanoparticle instead, maintains the sp^3 -bonded diamond structure upon relaxation, with again the (100) surfaces relaxing to form the (2×1) reconstruction [304].

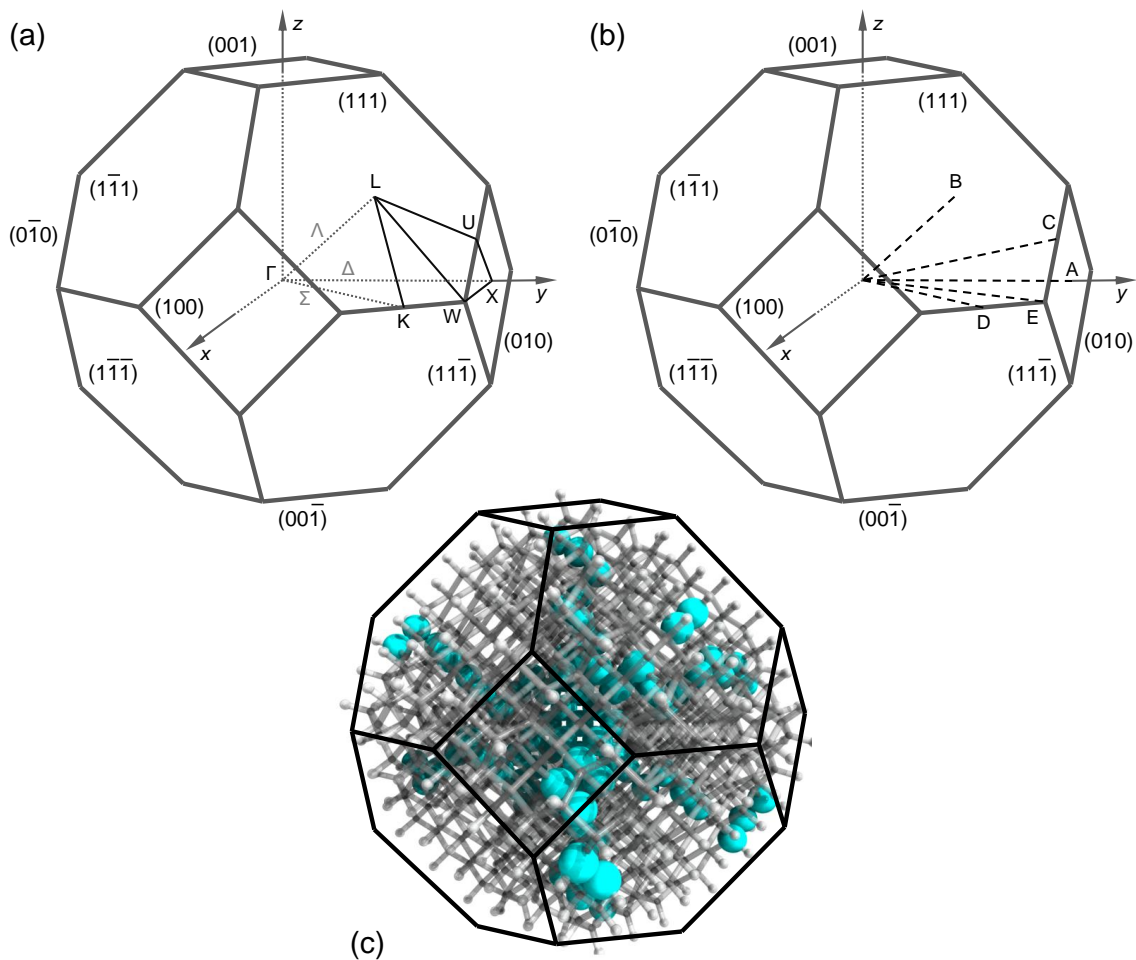


Figure 5.8. Truncated octahedral structure relevant to the simulated nanoparticles (C_{837} and $C_{837}H_{252}$). **a)** Diamond Brillouin zone with high symmetry points (Γ , X, L, U, K and W) and lines (Δ , Λ and Σ) indicated. **b)** Diamond Brillouin zone with the substitution paths (A, B, C, D and E) indicated. The substitution paths extend from the centrosymmetric lattice site, out to the terminal sites located: in the direction of the (100) facets (path A), in the direction of the (111) facets (path B), at the edges between the (100) and the (111) facets (path C), at the edges between the (111) and the (111) facets (path D) and at the corners formed by the (111), (111) and (100) facets (path E). **c)** Structural representation of a few NV substitution sites along the different paths within the C_{837} truncated octahedral bucky-diamond particle.

In these computationally simulated clusters, the NV centres are introduced. The defect is considered both in its neutral (NV^0) and negatively charged (NV^-) state. The NVs are introduced within the particle individually, along “substitution paths”. Over 50 different sites were probed with the NVs sitting along all the four different lattice directions. This allows sampling the whole configuration space of the crystallographic and geometrical lattice sites. More precisely, the NV centres are individually substituted for carbon atoms located within the lattice along the specific albeit zigzagged paths A, B, C, D and E (Fig. 5.8) [300]. The paths A, B, C, D and E extend from the centrosymmetric lattice site, out to the terminal site along directions analogous, respectively, to the directions X, L, U, K and W in the diamond Brillouin zone. In the calculations performed by A. S. Barnard, the simulated particles are pre-relaxed and the NV centres are introduced in the structure only subsequently. In other words, the energy of the “unperturbed” particle without any NV is minimised and the equilibrium positions of the carbon atoms are obtained, then the NV centre is introduced and the new equilibrium positions for the atoms in the particle hosting the NV are recalculated from the pre-relaxed computation. The convergence criterion used for the relaxation of the particles including the NV centre is the same used for the “unperturbed” C_{837} and $C_{837}H_{252}$ particles (force convergence criterion for a stationary point set at 10^{-4} au ≈ 5 meV/Å).

5.2.2 Favoured location of NV centres in diamond nanoparticles

By using the computational model just described it is possible to investigate where, within a diamond nanoparticle, the NV centre is most likely to be located. Whether, based on energy minimisation criteria, NV centres along the substitutional paths A, B, C, D, and E are stable at the core or at the surface of the simulated C_{837} and $C_{837}H_{252}$ nanoparticles. The role that surface passivation plays can also be addressed. The results on the calculated stability of NV centres in nanoparticles are shown in figure 5.9. In the graph the x -axis represents the scaled, dimensionless radius of the particle. This is defined as the ratio r/R , where r is the distance between the centre of the particle and the NV defect and R is the distance between the centre and the outer surface, i.e the actual radius of the particle. According to this definition, $r/R = 0$ corresponds to the defect sitting in the centre of the particle, while $r/R = 1$ corresponds to the defect being on the surface, on an edge or on a corner of the truncated-octahedral cluster. Similarly the y -axis represents the relative

energy of the system. This is defined as $(E_r - E_0)$, where E_r is the energy of the system with the NV defect sitting at a distance r from the centre of the particle and E_0 is the energy when the defect is in the middle of it. We use the scaled radius r/R and the relative energy $(E_r - E_0)$ so that the results are normalised and can be extended to nanoparticles of different sizes.

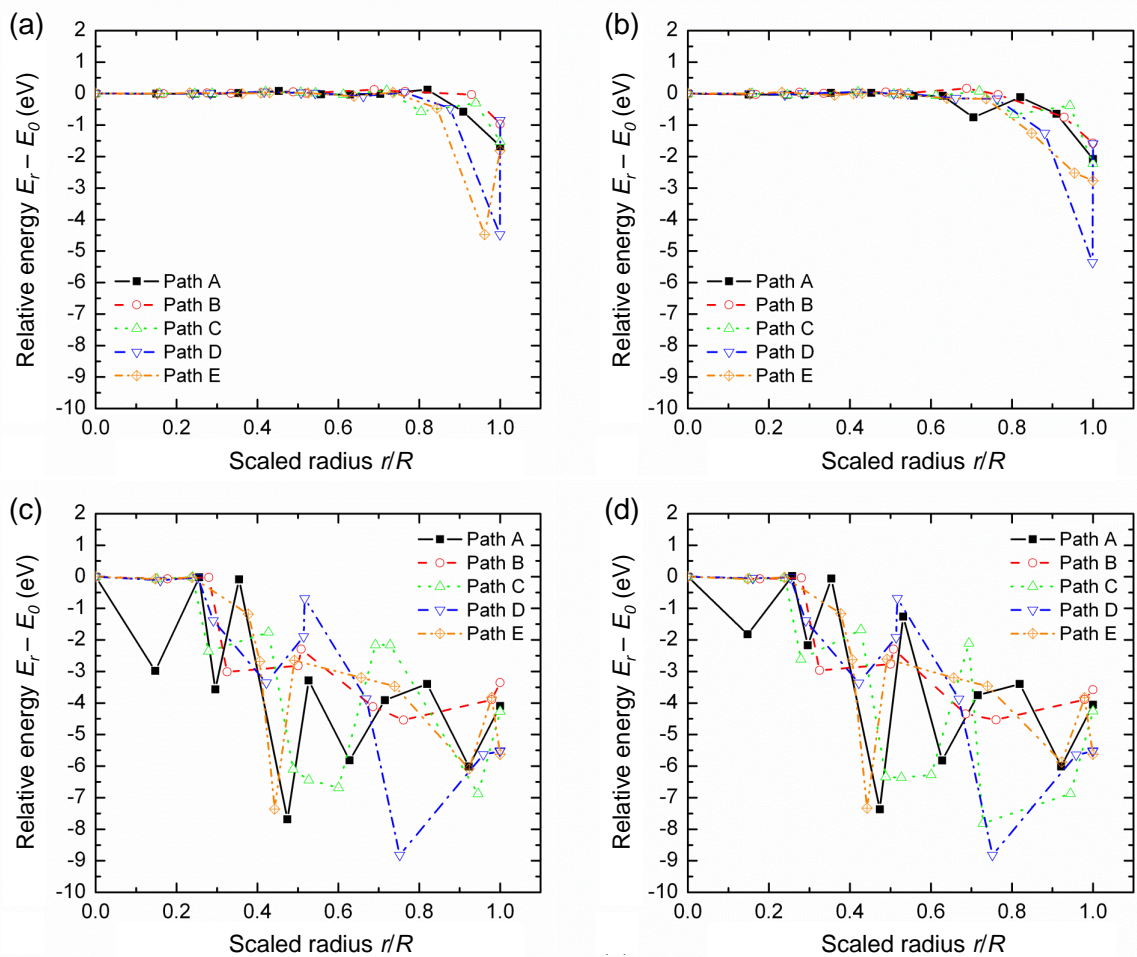


Figure 5.9. Calculated stability of the NV centre in nanodiamonds. **a)** NV⁰ in C₈₃₇H₂₅₂. **b)** NV⁻ in C₈₃₇H₂₅₂. **c)** NV⁰ in C₈₃₇. **d)** NV⁻ in C₈₃₇. The relative energy for the NV within the particle has been calculated at lattice sites located along the substitutional paths A, B, C, D and E (see text). In each graph the x -axis represents the scaled, dimensionless radius of the particle r/R obtained by dividing the distance from the centre of the particle to the NV substitutional site by the total distance from the centre to the extremum of each path. The y -axis represents the relative energy of the system $(E_r - E_0)$, where E_r is the energy of the system with the NV defect sitting at a distance r from the centre of the particle and E_0 is the energy when the defect is in the middle of it.

Figure 5.9 shows that the calculations of the relative energies as a function of the scaled radius are significantly different for the passivated C₈₃₇H₂₅₂ and the unpassivated C₈₃₇ clusters (respectively, Figs. 5.9a and b versus Figs. 5.9c and d).

$C_{837}H_{252}$. In the passivated particle $C_{837}H_{252}$, for values of the scaled radius $r/R < 0.6$, there is almost no fluctuation in energy for the different NV substitutional sites. In other words, all the different positions the NV centre could occupy within the inner sphere of scaled radius $r/R < 0.6$ are energetically indistinguishable. It seems reasonable to say that this inner region resembles a bulk-like behaviour and an NV centre located there would probably not be involved in surface-related effects and would appear isolated from the influence of the external environment. On the contrary, the outer region ($r/R > 0.6$) shows a rapid change in the equilibrium energies (in general towards lower values), suggesting that the bulk-like aspect of the inner region of the particle is lost quickly as the NV is located closer and closer to the surface. An NV centre located in this outer region would be affected by the boundaries and would certainly be more exposed to phenomena occurring at the surface; it could also undergo structural distortions with subsequent loss of its symmetry and optical properties. A more detailed analysis of these considerations is reported below.

At $r/R < 0.6$, despite the mentioned energy indistinguishability of where the NV sits, very small energy fluctuations can be detected. They are attributed to the redistribution of the excess charge from the donor electron. The differences in energy depend on the defect site being within or not the Bohr excitonic radius of the particle extremes. This effect has been previously reported and analysed by A. S. Barnard and M. Sternberg [300]. They studied the effects of nitrogen substitution within a C_{837} truncated-octahedral bucky-diamond along the same substitutional paths considered here. They calculated a gradual increase in the relative energy ($E_r - E_0$) of the particle for values of the ratio r/R going from ~ 0.2 to ~ 0.75 and explained this increase with the donor electron of the substitutional nitrogen atom gradually "seeing" more and more the nanoparticle extremum or the inner surfaces of the outer buckified-diamond shell. They used these results to estimate the Bohr radius of the electron to be ~ 0.6 nm (~ 7 atomic layers).

At $r/R > 0.8$, there is a general trend for the relative energy of the particle towards lower values, indicating that in a passivated nanodiamond it is energetically favourable for the NV defect to be located near the surface. At the surface, however, structural changes and symmetry rearrangement of the structure could occur affecting the NV centre stability and its properties, and making it no longer optically active.

In the region $r/R < 0.6$ the nitrogen atom is sp^3 -hybridised, and although thermodynamically unfavourable, the energetic barrier for a transformation to a lower energy configuration is too high. At $r/R > 0.7$ there is a ~ 1.5 - 4.5 eV thermodynamic driving force for diffusion which increases the closer the vacancy is to the surface, an edge or a corner of the nanodiamond [300].

This distinction showed between the inner and the outer regions of a nanodiamond at $r/R = \sim 0.6$ has to be considered carefully. Although reasonable, it is probably consistent only for particles in the size range ~ 2 - 10 nm. In fact, particles smaller in size tend to be more fullerenic-like and as the size becomes smaller it makes less sense to define a proper particle core which extends with continuity from the centre towards the outer surface. Instead, particles larger in size have possibly the inner core bulk-like region extending even further, to values of the ratio r/R bigger than 0.6. This is because the ratio of the number of atoms at the surface to the total number of atoms in the cluster gets small very quickly as the particle size increase, making the surface effects less pronounced and restricting them to the very few atomic layers at the surface (cf. s. 5.1.4).

C_{837} . Different from the hydrogen passivated $C_{837}H_{252}$ particle, in the unpassivated C_{837} there are no specific trends in the relative energy of the nanodiamond hosting an NV centre as a function of the scaled radius. In the C_{837} bucky-diamond cluster, the outer layers form a sp^2 -bonded fullerenic/graphitic outer shell; the lattice parameter is different from the value in the bulk and because of the hybridisation discontinuity between the inner (sp^3 -bonded) and outer (sp^2 -bonded) regions, a considerable amount of strain is accumulated throughout the nanodiamond. Because of that, the energy barrier for the possible distortion of the NV defect is lowered and, locally, the region surrounding the NV defect can change to reduce the total stress and the overall energy of the particle. The variability Barnard et al. observed between the calculated relative energies of the different substitutional paths (Fig. 5.9c and d) suggests that the local change for stress reduction highly depends on the position the NV occupies within the C_{837} nanodiamond. These structural changes generally manifest as subsurface graphitisation, since the energy of the NV centre is lower in the sp^2 -bonded regions. The local minima in figures 5.9c and d show that in an unpassivated particle these transformations take place with the NV sitting almost anywhere within the whole particle, even very close to the centre of it. These

structural changes in the unpassivated C_{837} cluster are “beneficial” for the nanodiamond in terms of overall system energy minimisation, but can lead to a distortion of the NV centre and possibly to a configuration of the defect that could make it no longer optically active.

From this analysis it can be concluded that the NV centre, either in its neutral (NV^0) or negatively charged (NV^-) state, is stable when it sits in the *core* of the nanodiamonds, where it is prevented from undergoing structural distortions. In the case of an unpassivated nanoparticle, the NV stability relies on the nanoparticle itself being large enough to have an extended and predominantly bulk-diamond-like core that would maintain the sp^3 character and preserve the undistorted NV trigonal symmetry. In the case of a passivated nanoparticle the NV stability requirements are less stringent since, as shown, the surface passivation tends to stabilise the nanodiamond extending the bulk-diamond-like core region up to 75-80% of the total particle radius and reducing consequently the probability of NV distortion.

This conclusion finds an experimental confirmation in previous studies of electron energy loss spectroscopy (EELS) measurements in detonated nanodiamonds [305]. Such measurements indicate that the nitrogen impurities in detonated nanodiamonds are embedded within the nanoparticle core with the sp^3 tetrahedral coordination and are not positioned close to the surface or within the graphitic shell.

5.2.3 Probability of observing NV centres in nanodiamonds

The theoretical-computational model established that the NV centre is more likely to be stable in the core of a nanodiamond rather than at the surface. We tested experimentally the probability of observing optically active NV centres in high pressure high temperature (HPHT) nanodiamonds and compared our findings with the predictions of the theoretical model A. S. Barnard developed [221].

The theoretical model predicts the probability of observing NV centres in nanodiamond based on the kinetic barriers. I briefly describe it below for completeness to set up the context for the comparison with the experimental measurements we performed. Intuitively, it is assumed that the probability P_{obs} of observing an NV centre in a diamond nanoparticle is given by the difference between the probability P_{form} that an NV is initially

created during the synthesis and the probability P_{esc} that, once created, the defect could diffuse to the surface and escape:

$$P_{obs}(R, E_K) = P_{form}(R)[1 - P_{esc}(R, E_K)] \quad (5.11)$$

In equation (5.11), is shown explicitly that the observation probability P_{obs} is function of the radius R of the nanodiamond and the kinetic energy during probing E_K (E_K coincides, for instance, with the energy of the pumping laser in case of optical excitation of the NV centre). The radius R plays a key role, since both the probability of formation P_{form} and escape P_{esc} depend on it. In fact, the larger is the radius of the particle the higher is the probability P_{form} that an NV could form in it, simply because there is a higher number of possible, stable sites where the defect could be hosted. At the same time, the larger is the radius the lower is the probability P_{esc} that the NV could diffuse towards the surface and annihilate, because of the average higher number of lattice sites it would have to diffuse through. The probability P_{esc} of escaping is of course dependent as well on the kinetic energy during probing E_K . The probe energy E_K is deposited into the diamond lattice and may have different effects. It can excite electronic states and generate photons. The extra energy can be used as work and since the NV defects are high-energy sites they are ideal places where such work can be used. Hence, if the total available energy, including E_K , is greater than the kinetic energy barrier the NV defect could diffuse: this is a form of energy dissipation. The defect barrier is always dominated by the carbon-nitrogen (C-N) exchange energy, but the transition state also involves strain in the neighbouring atoms, so some work is also used in distorting the lattice in the vicinity of the defect to accommodate the atomic exchange [306].

Explicitly, the probability of formation P_{form} of an NV centre is function of the concentration C of nitrogen present during the synthesis (independently from the synthesis process utilised), of the kinetic energy during growth $E_{K,growth}$ and of the characteristic energy of the defect E_d at a position r from the centre of the particle. Using the approximation of a Boltzmann function, the probability P_{form} can be defined as:

$$P_{form}(R) = C \sum_{r=0}^R P(r) e^{-\frac{E_d(r)}{E_{K,growth}}} \quad (5.12)$$

where $P(r)$ is the probability of the defect to be at any of the discrete number of possible lattice sites, located at a distance r from the centre of the particle of total radius R . According to what has been said in the previous section, there are two possible different

sets of values for the probability $P(r)$ and the characteristic energy $E_d(r)$, depending on where the NV is located within the particle. In fact, the centre may either be in the sp^3 -bonded environment of the bulk-like core region or in the sp^2 -bonded environment, in proximity of the buckyified outer shell or of the localised defect-induced subsurface graphitisation region (cf. s. 5.2.2). Equation (5.12) can thus be simplified to:

$$P_{form}(R) = C \left[P_{core}(R_{core}) e^{-\frac{E_{d,core}}{E_{K,growth}}} + P_{shell}(R - R_{core}) e^{-\frac{E_{d,shell}}{E_{K,growth}}} \right] \quad (5.13)$$

where $E_{d,core}$ and $E_{d,shell}$ are the characteristic energies of the defects respectively in the sp^3 -bonded core region and in the sp^2 -bonded shell region; R_{core} is the radius of the particle core and P_{core} and P_{shell} are the probabilities of the defect to be located in the core or in the shell, respectively. Explicitly, we can calculate such probabilities as $P_{core} = N_{core}/N$ and $P_{shell} = 1 - N_{core}/N$, where N_{core} is the number of atom in the core and N the total number of atoms in the nanodiamond. In the case of a cubo-octahedral diamond particle with n atoms along the (111)/(111) edge N is given by:

$$\begin{cases} (1/12)n(2n+1)(5n+2) & \forall n \in (2, 4, 6, 8, \dots) \\ (1/12)(10n^3 + 9n^2 + 2n - 9) & \forall n \in (1, 3, 5, 7, \dots) \end{cases} \quad (5.14)$$

and N_{core} can be determined using equations (5.14), once the size of the core has been estimated (for instance, from the energy calculations of figure 5.9 it can be estimated that the core extends up to four atomic layers from the surface of the hydrogen terminated $C_{837}H_{252}$ particle and to eight atomic layers of the unpassivated C_{837} one).

Similarly to equation (5.13), an expression for the probability P_{esc} of escape can be derived considering the contributions from the core and the shell regions. The probabilities $P_{esc,core}$ and $P_{esc,shell}$ of escape for the core and the shell are function of the escape energies $E_{esc,core}$ and $E_{esc,shell}$; these depends in turn on the input kinetic energy E_K combining the probe and the environment. Intuitively, if the kinetic energy E_K of the probe is significantly lower than the escape energy for each region, i.e. $E_K \ll E_{esc}(E_K)$, then $P_{esc}(E_K)$ is negligible, whereas if E_K is comparable with the escape energy of a certain region, i.e. $E_K \approx E_{esc}(E_K)$, then the probability for diffusion approaches unity in that same region. The expression for the total probability P_{esc} of escape can be written as:

$$P_{esc}(R, E_K) = [P_{core}(R)P_{esc,core}(E_K) + P_{shell}(R)]P_{esc,shell}(E_K) \quad (5.15)$$

which, by using the Boltzmann function for the escape energies and by using the expression $P_{core} = N_{core}/N$ and $P_{shell} = 1 - N_{core}/N$ for the probabilities of the defect being located in the core or in the shell, becomes:

$$P_{esc}(R, E_K) = \left[\frac{N_{core}}{N} e^{-\frac{E_{esc,core}}{E_K}} + \frac{N - N_{core}}{N} \right] e^{-\frac{E_{esc,shell}}{E_K}} \quad (5.16)$$

In equation (5.16), $E_{esc,core} = |E_{diff,core} - E_{d,core}|$ and $E_{esc,shell} = |E_{diff,shell} - E_{d,shell}|$ are the differences in the kinetic barrier to diffusion E_{diff} and the energy of the static defect E_d in the core and in the shell, respectively.

From equations (5.11-16), it derives that the only quantities actually required to calculate P_{obs} are the concentration C of nitrogen during the synthesis and the energies $E_{d,core}$, $E_{d,shell}$, $E_{diff,core}$ and $E_{diff,shell}$. From the calculations it results: $E_{d,core} = (5.17 \pm 0.2)$ eV and $E_{d,shell} = (0.60 \pm 0.2)$ eV in the C_{837} bucky-diamond and $E_{d,shell} = (3.81 \pm 0.2)$ eV in the $C_{837}H_{252}$ hydrogen-terminated nanodiamond. These values are obtained from the data of figure 5.9, where $E_{d,core}$ has been subtracted to obtain the relative particle energies in each case. The diffusion barrier for a neutral NV centre in the sp^3 -bonded bulk-like core are calculated to be $E_{diff,core} = (6.68 \pm 0.2)$ eV, which is in agreement with values reported in other studies [78, 307]. Similarly, for the sp^2 -bonded graphitic-like shell the (c -axis) diffusion barrier for a neutral NV centre is calculated to be $E_{diff,shell} = (13.30 \pm 0.2)$ eV.

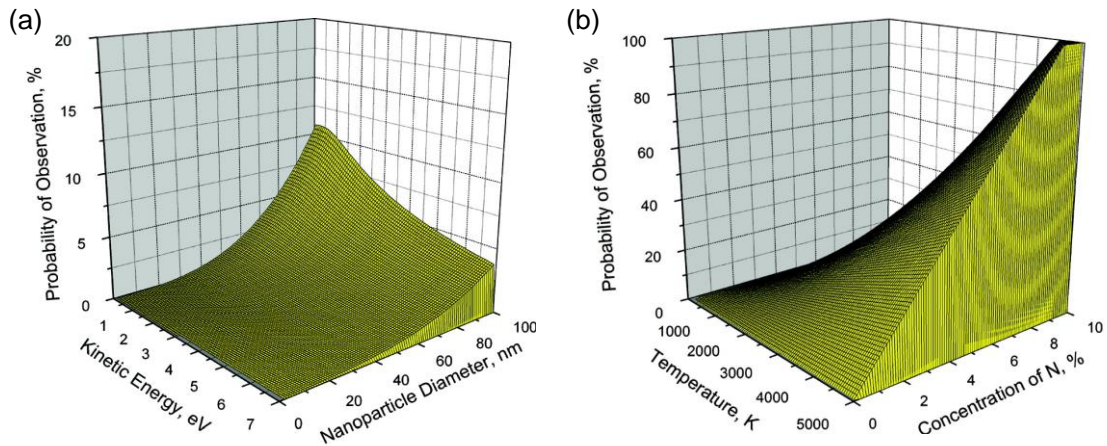


Figure 5.10. Probability of observation of stable NV centres in diamond nanoparticles. **a)** Probability calculated as a function of particle diameter and kinetic energy during probing; the calculation is run using CVD growth conditions temperature $T_{growth} = 800$ °C and nitrogen concentration $C = 0.1\%$. **b)** Probability calculated for 30-nm particles as a function of synthesis temperatures and nitrogen concentration in the precursor materials.

This model is quite general and can be used as a powerful tool to predict the probability of observing NV centres in diamond nanoparticles synthesised under different conditions.

Figure 5.10a for instance, shows the probability of observing an NV centre in hydrogen-terminated nanodiamond calculated with $T_{growth} = 800 \text{ }^\circ\text{C}$ and $C = 0.1\%$; these are the experimental values J. R. Rabeau and collaborators used to grow CVD diamond containing optically active NV centres [158] (cf. s. 5.2). In good agreement with their experimental results, A. S. Barnard calculation shows that with such values for T_{growth} and C the probability that nanodiamonds would contain a stable NV centre is less than 1% when their diameter is smaller than $\sim 20 \text{ nm}$, even under ambient conditions, and between 2% and 3% when the particle diameter is between 60 nm and 70 nm.

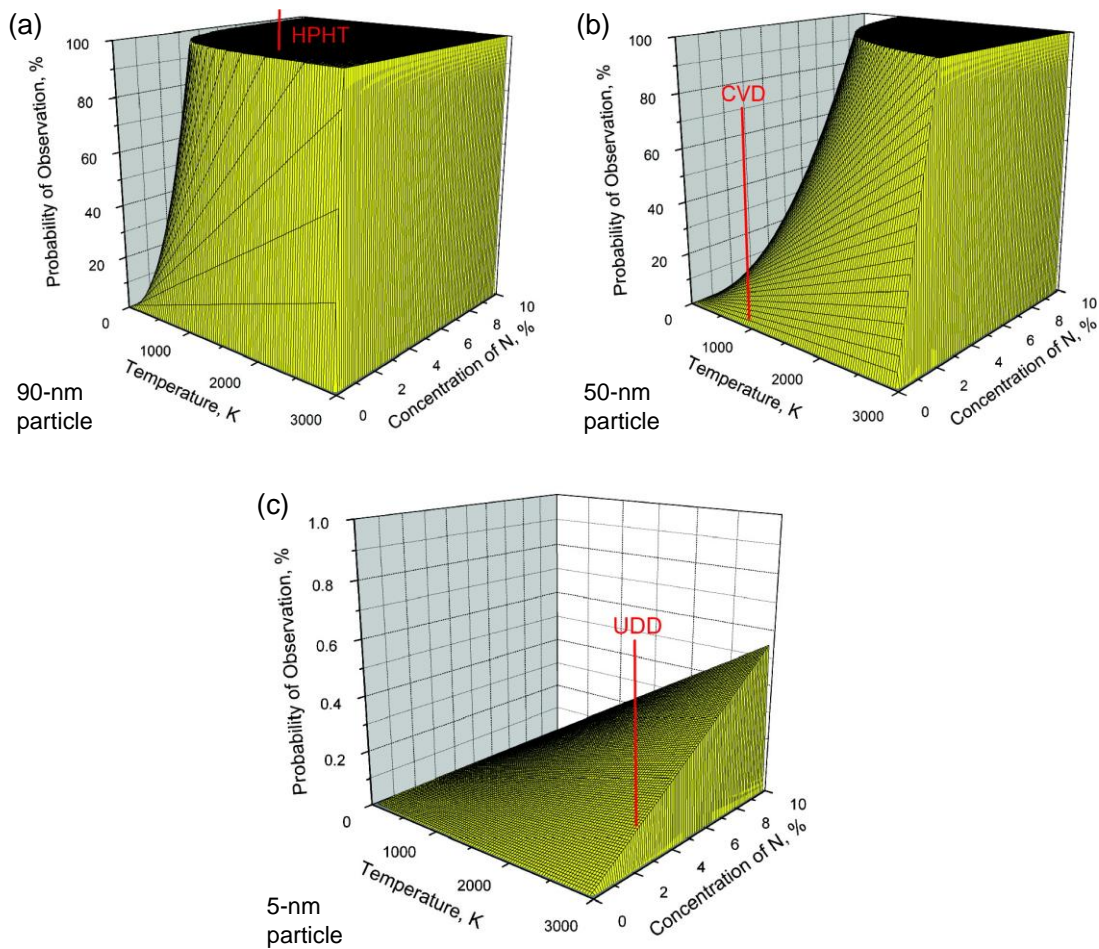


Figure 5.11. Probability of observation of NV centres in diamond nanoparticles. **a)** Data for nanoparticles 90 nm in size. **b)** Data for nanoparticles 50 nm in size. **c)** Data for nanoparticles 5 nm in size. The synthesis parameters of temperature T_{growth} and nitrogen concentration C corresponding to high pressure high temperature (HPHT), chemical vapour deposition (CVD) and detonation ultradispersed (UDD) particles are marked.

Figure 5.10b is a complementary plot representing the dependence on the formation conditions: it shows the probability of observation of NV centres in nanodiamond as a function of the synthesis temperature and of the nitrogen concentration in the precursor

materials. As the synthesis temperature and quantity of nitrogen in the precursors increase, the probability that NV centres would be present in the lattice increases accordingly. It should be noted that all these estimations are made assuming that diffusion occurs on the same time scale observed in bulk diamond and graphite.

The theoretical-computational model offers a predictive framework where several parameters including size of the nanodiamonds, kinetic energies, temperatures and concentration of nitrogen during the diamond synthesis can be taken into account to estimate the probability of observing NV centres in nanodiamond or their effective concentration. This is hardly achievable, for instance, via mere experimental techniques without undertaking and combining together a very large number of separated investigations of statistical significance. On this note, figure 5.11 presents the calculated probability of observing NV centres in nanodiamonds as a function of temperature and nitrogen concentration, for the three most common diamond synthesis techniques: high pressure high temperature (HPHT), chemical vapour deposition (CVD) and detonation (cf. c. 2, ss. 2.3.1-3).

As per the CVD nanodiamonds, the model predictions were compared with the available experimental data for detonation nanodiamonds [299] (cf. s. 5.2). The computational results of figure 5.9 and the data for the diffusions barriers for graphitised bucky-diamond particles in equations (5.13) and (5.16) were used to predict the probability of finding stable NV centres in detonation nanodiamonds at room temperature and with a nitrogen concentration during synthesis of 300 ppm. Under these conditions, the probability of observation of NV centres is 0.0017% and 0.00004% in 5-nm and in 3-nm detonation nanodiamonds, respectively. These values are in reasonable agreement with the estimation done by B. R. Smith and collaborators who measured an NV centre with a probability of 10% in 55-nm detonation nanoparticles and, based on fluorescent measurements, estimated that a 5-nm particle should host an NV with a probability ~ 65000 times smaller (i.e. $\sim 0.00015\%$), being its volume ~ 1300 times smaller than that of a 55-nm particle [299]. It has to be noted that variations between the experimentally estimated and the theoretically calculated probabilities are possible and due to several factors including: the use in the experiments of non-mono-disperse samples or even small

differences in the temperature or in the nitrogen concentration during synthesis. On this particular aspect, one of the advantages of the model is its capability to pin down such parametrical differences and address where the uncertainties associated to the real samples might come from. Therefore, despite not being a substitute for experimental characterisations, the model can be used complementarily to them, for instance as a predictor to choose which parameters need to be controlled to have a certain expected probability of observing NV centres in specifically synthesised nanodiamonds.

To test the theoretical model, we conducted an experimental and statistically robust analysis on the probability of observing NV centres in a sample of high pressure high temperature (HPHT) nanodiamonds [221]. The aim was to use the experimental results to improve our understanding of the rules that govern the stability of NV centres in diamonds crystal at the nanoscale, which is one of the main goals of this thesis. Finally we wanted to compare the experimental results with the probabilities predicted by the theoretical model of A. S. Barnard.

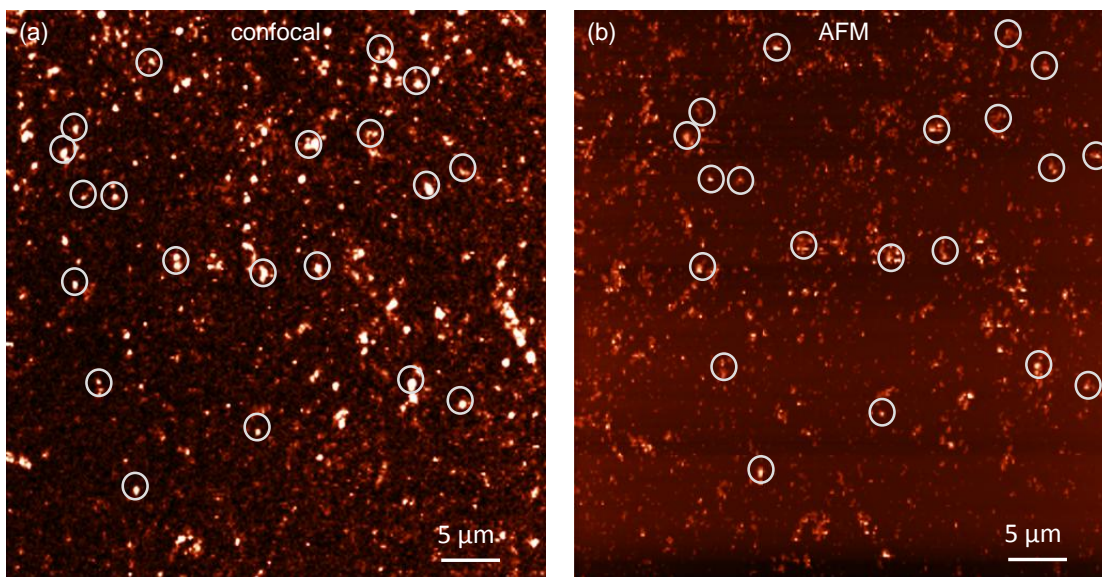


Figure 5.12. Corresponding confocal and atomic force microscope (AFM) images of diamond nanocrystals dispersed on a cover slip. **a)** Confocal image: bright fluorescing spots indicate emission from NV centre(s). **b)** Corresponding atomic force microscope (AFM) image: the brightness of the spots is directly proportional to the height of the diamond nanocrystals. Data refers to HPHT monocrystalline diamond powder from Microdiamant (MSY 0-0.1 μm).

The sample we studied consisted of monocrystalline diamond powder (Microdiamant, MSY 0-0.1 μm) formed by high pressure high temperature (HPHT) synthesis. According to the specifications, the powder is made of nanodiamonds of 50 nm average size with a

tolerance of 40-60 nm and upper limit 150 nm. We analysed the nanodiamonds “as received”, i.e. without performing any further NV enhancing treatment. We prepared the sample as described in details in chapter 4, section 4.4. Briefly, the diamond powder was first suspended in deionised water (Milli-Q®) in a suitable concentration and a few drops of the obtained solution were put on a glass cover slip (dimensions $\geq 18 \times 18 \text{ mm}^2$ and thickness $\sim 0.13\text{-}0.17 \text{ mm}$; Menzel-Glaser) and allowed to dry so that the diamond crystals remained dispersed on the surface. We characterised thoroughly a $50 \times 50 \mu\text{m}^2$ area of the sample with the combined confocal-AFM setup described in chapter 4, section 4.5. We obtained for the area both the optical map of the fluorescing nanodiamonds containing NV centres and the corresponding topographical map with the information of the size of all the nanodiamonds (Fig. 5.12).

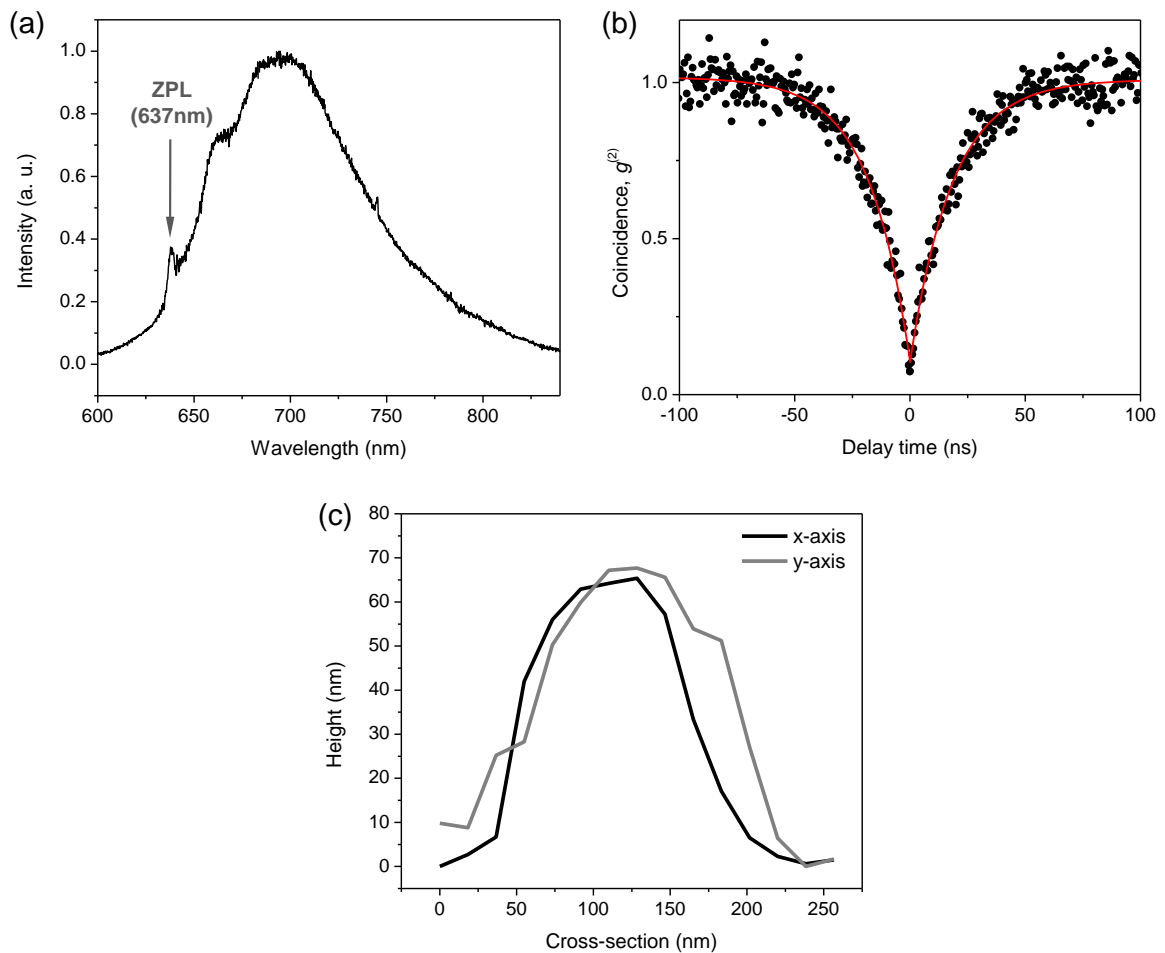


Figure 5.13. Dataset for a representative fluorescent nanodiamond. **a)** Emission spectrum: the characteristic features, the zero phonon line (ZPL) at 637 nm in primis, reveals the emission from NV centre(s). **b)** Autocorrelation function $g^{(2)}(\tau)$: the contrast in the autocorrelation function with the “antibunching” dip for $g^{(2)}(\tau = 0)$ shows that the emitter is a single NV centre. **c)** Height (along the x - and y -axis) of the selected nanodiamond hosting the NV centre, measured with the atomic force microscope (AFM). Data refers to a HPHT monocrystalline diamond powder from Microdiamant (MSY 0-0.1 μm).

The $50 \times 50 \mu\text{m}^2$ area contains in total 3690 diamond nanocrystals, which corresponds to a distribution of ~ 1.5 crystals per μm^2 . Of all the 3690 nanodiamonds, 94 ($\sim 2.5\%$) exhibited fluorescence due to hosted nitrogen vacancy (NV) centre(s). For each fluorescent nanodiamond we collected the set of information including: NV photoemission spectrum, NV autocorrelation function $g^{(2)}(\tau)$ and crystal size (Fig. 5.13).

We analysed each of the 94 fluorescing nanodiamonds and built the histogram of the probability of finding NV centre(s) in diamond nanocrystals as a function of the crystal size. These results are reported in figure 5.14a, where we distinguished explicitly between the probabilities of observing a single NV centre from that of observing multiple NV centres. The histogram clearly shows that, in the HPHT nanodiamond sample we studied, the probability of finding any NV centre is negligible for particles with a diameter less than 30-35 nm. The probability of finding a single NV centre incorporated in a diamond nanocrystal becomes significant for particles ~ 35 nm in diameter, while that of finding more than one NV centre becomes significant only for particles ~ 55 nm in diameter. Finally, the probability of hosting a single centre saturates when the diameter of the particle reaches $\sim 65-70$ nm, while that of hosting multiple NV centres keeps increasing, non-linearly, as the size increases. These results are indicative only of the sample we investigated. Different diamond samples synthesised and treated differently will yield different results. Beyond the specific values, the general conclusion is that there is a cut-off value for the size under which the stability of the NV centre is not guaranteed. This is because the stability of the centre depends on several parameters which are all size-dependent, such as the number and the availability of lattice sites where the NV could sit stably or the proximity to the surface that makes the defect more or less likely to diffuse and annihilate at the interface. But, even more interestingly, the set of data we analysed is statistically large enough to quantitatively address the problem. We can extract from the experimental data trends and dependencies of the NV stability as a function of the size of the nanodiamonds and, also, compare them with the predictions of the theoretical model to conclude about its validity.

Regarding this last point, the experimental results can be used to support the assumptions that have been made to build the theoretical model. In equation (5.11), it is assumed that the probability $P_{obs}(R, E_K)$ of observing a stable NV centre in a nanodiamond is the outcome

of two main processes which are both dependent on the size of the nanoparticle: the probability $P_{form}(R)$ of having the centre initially formed in the particle and the probability $P_{esc}(R, E_K)$ that the NV centre, or the associated vacancy, would diffuse to the surface and annihilates. The experimental data shows that a minimum value for the size (the radius R) is actually required for the particles to host NV centres. In our sample, NV centres can in fact only be observed for particles whose diameter is bigger than ~ 30 -35 nm. This corresponds, assuming for simplicity a spherical host nanodiamond with the NV centre sitting in the middle, to a value for the minimum radius R of ~ 15 nm. Such a value for R can be interpreted in the model as the critical particle size at which, even though an NV centre could hypothetically form in the nanodiamond (i.e. $P_{form}(R) > 0$), the associated vacancy would very likely diffuse and annihilate at the surface (i.e. for $R < 15$ nm $\rightarrow P_{esc}(R, E_K) = 1$, which means in equation (5.11) $P_{obs}(R, E_K) = 0$). The appropriateness of the model is further supported by observing that the experimentally measured probability of finding NV centres in nanodiamonds increases non-linearly with the crystal size and the data matches the prediction of the theoretical calculation (Fig. 5.10a). The experimental measurements and the theoretical predictions calculated for our sample are directly compared in figure 5.14b and are in good agreement for the diamond nanoparticles over the entire nanoscale (0-100 nm) [221].

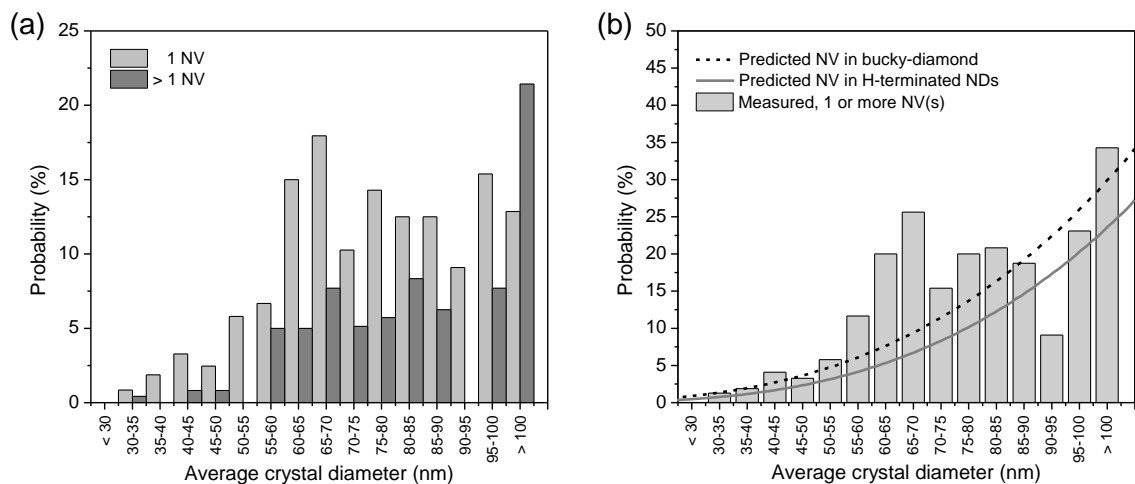


Figure 5.14. Probability of observation of NV centre(s) in diamond nanoparticles over the entire nanoscale (0-100 nm). **a)** Experimental measurements of the probability of finding a single NV centre (light grey) and of the probability of finding more than one NV centre (dark grey). Data refers to a HPHT monocrystalline diamond powder from Microdiamant (MSY 0-0.1 μm). **b)** Total probability for a given crystal size range to contain one or more NV centre(s) at room temperature. Histogram: experimental measurements combining the probability of finding one NV defect and the probability of finding more than one NV in HPHT diamond nanoparticles. Lines: corresponding theoretically predicted probability of finding NV defects in diamond nanoparticles for bucky-diamonds (dashed) and for hydrogen-terminated nanodiamonds (solid).

With reference to figure 5.14b, it has to be said that the surface of the nanodiamonds in our sample was oxygen-terminated, while the theoretical prediction refers to hydrogen-terminated crystals. Recent studies have clearly shown that the chemistry of the nanodiamonds at the surface is crucial in determining the optical behaviour of the NV centres [308-310]. I will discuss this in detail in the next chapter. Here, I just want to highlight the fact that in the characterisation we made, the surface chemistry does not play a major role since it becomes relevant only for NV centres very close to the surface (\sim only very few nm) which, according to the nanodiamonds we investigated (minimum $R \sim 15$ nm), is not the case.

Both the direct experimental analysis and the theoretical computational results of figure 5.14a and b show that there is a correlation between the probability of observing NV centre(s) and the size of the host diamond particles. More specifically, they show a non-linear increasing probability as the dimensions of the crystal increase. The increasing trend varies depending on the synthesis method, via the values of the temperature, the nitrogen concentration during synthesis and the surface termination of the nanodiamonds. In general we found that as the crystals get smaller the probability of hosting NV centre(s) decreases as $\sim R^3$ for hydrogen-terminated nanodiamond and as $\sim R^{2.72}$ for bucky-diamonds, R being the radius of the particle. This difference can be attributed to the fact that the defect is stable only in the core region of the particle and in that sense the bucky-diamonds have an “effective” reduced radius with respect to the total size of the particle due to the graphitisation of the outer layers (cf. s. 5.2.2).

Our study can also be regarded as complementary to that conducted by B. R. Smith and collaborators on the probability of diffusion of the vacancy of the NV complex towards the surface [299]. They addressed the problem in terms of the number of lattice steps, in the random walk, the vacancy requires to reach the surface, where this number goes as $\sim R^2$. Monte Carlo simulations show that as the surface becomes closer to the core of the nanoparticle, the probability of vacancies forming NV centres decreases with the square of the particle radius as expected. However, for relatively large crystals or diamonds with high concentrations of nitrogen, the probability saturates.

5.3 Conclusions: the role of size on carbon and NV centres stability

In this chapter I hope I have shown that at the nanoscale size is very important. It does affect carbon as a material and more specifically it affects the stability of colour centres in diamond nanoparticles.

For instance, I have shown that at the nanoscale, carbon gives rise to different and unique structures which are dictated by their size and could not exist at different scales (cf. s. 5.1.1). Experimental results and theoretical-computational analysis have revealed that even the phase stability of carbon is affected by size to the point that the dimension of the clusters is commonly accounted in the most recent studies as an additional parameter that effectively contributes in determining the thermodynamical equilibrium of carbon. Size in fact, defines regimes where certain carbon phases are more energetically stable than others, whether they are carbon rings, fullerenes, nanodiamond or nanographite (cf. ss. 5.1.2-3).

With more focus on colour centres in diamond nanocrystals, I have also shown that the size of the nanodiamonds affects the thermodynamical stability of hosted nitrogen-vacancy centres, which are the main interest of this work. Although not definitive, the extensive study we conducted in collaboration with Dr. A. S. Barnard strongly suggests that the NV centre is more stable within the core rather than at the surface of a nanodiamond (cf. s. 5.2.2). Moreover, the actual probability of observing an NV centre in diamond nanocrystals seems to be a function of their size and of the conditions under which the diamonds have been synthesised (cf. s. 5.2.3). These issues have been addressed systematically both via theoretical-computational modelling and via direct experimental measurements, showing good agreement also with respect to independent studies reported in the literature.

There is still one aspect though that needs to be addressed: whether the size of the nanodiamonds affects the *optical properties* of the hosted NV centre(s). I will analyse thoroughly this issue in the next chapter, considering not only the effects of the size, but also those of the nanodiamond surface. Possible alterations on the optical properties of the NV centres in fact have to be considered carefully if we want to be able to control the material and realise practical NV centre-based nanotechnologies.

6

Effects of size and surface on the optical properties of NV centres in nanodiamonds

In chapter 5, I analysed the role that the size of the clusters plays at the nanoscale (0-100 nm) in determining both the thermodynamical stability of the carbon phases and of the nitrogen-vacancy (NV) centres in nanodiamonds (NDs). I have shown that the size of the carbon cluster affects which phase is more energetically favourable (cf. c. 5, ss. 5.1.2-3). I have also shown that NV centres tend to be more stable in the core of the nanodiamonds rather than at the surface (cf. c. 5, s. 5.2.2) and that the probability of observing an NV centre depends on several factors including: the size of the nanoparticle, the conditions under which the nanodiamonds have been synthesised and the surface passivation (cf. c. 5, s. 5.2.3).

In this chapter, I expand this and analyse the effects that the reduced size of the nanodiamonds and the surface proximity have on the *optical properties* of the NV centres.

6.1 Making ultrasmall (size < 10 nm) fluorescent nanodiamonds

To synthesise and process diamond particles only a few nanometres in size and hosting active colour NV centres is a challenge due to the expected instability of the defect in such small nanodiamonds. Theoretical calculations show that in a diamond nanocluster with nitrogen inclusions, the minimisation of the crystal energy favours the nitrogen to be located at the surface rather than in the core of the particle (cf. c. 5, s. 5.2.2). Consequently, in very small nanodiamonds the NV centres tend to be unstable: either because the

vacancy of the nitrogen-vacancy complex is likely to diffuse and annihilate near the surface or because the NV centre undergoes a structural distortion which could render it optically inactive. This seems to justify the limited observation of fluorescent NV centres in chemical vapour deposition (CVD) [158] and high pressure high temperature (HPHT) [221] diamond grains less than 40 nm in size (cf. c. 5, s 5.2.3). In fact, not much longer before the latest discoveries in the field [222, 299, 301], several studies both theoretical [304] and experimental [311] manifested serious concerns about the possibility that nanodiamonds smaller than 10 nm in size could contain any optically active NV centre.

It was this concern and the call into question of the actual feasibility of NV centre-based technologies that boosted further research in the material science. As a result, several synthesis techniques and colour centre-forming processes have been designed with the intent to produce nanodiamonds as small as a few nanometres and hosting stable NV centres. I will present here some of these techniques and processes, and cite other works in the literature. I will also present some of the original solutions we have developed on our own for the same purpose.

6.1.1 Up-to-date studies on small fluorescent nanodiamonds

To date, several methods have been optimised for the synthesis of diamond nanoparticles. The majority of them are not different from those presented earlier in chapter 2 (cf. c. 2, ss. 2.3.1-5). What is new is specifically the focus on the fabrication of ultrasmall (only a few nanometres in size) diamond crystals hosting luminescent centres, since they are the key for several emerging nanotechnologies.

- Luminescent nanodiamonds (size ≤ 10 nm) have been synthesised by high pressure high temperature (HPHT) in combination with additional treatments [301, 312].
- Several works have been done on the synthesis of chemical vapour deposition (CVD) nanodiamonds, even though it has been argued that the incorporation of nitrogen in small CVD nanocrystals is inefficient [158, 313, 314].
- Diamond synthesis by detonation has recently gained renewed interest for the production of ultradispersed and ultrasmall (size ~ 4 -5 nm) nanodiamonds [299, 315-318].

- Dispersed nanodiamonds on average ~ 2-6 nm in diameter have been successfully synthesised using carbon black as a carbon source by a long-pulse-width laser irradiation in water at room temperature and normal pressure [319].
- Diamond nanocrystals ~ 25-50 nm in diameter have been produced via a microwave plasma torch technique with methane (CH₄) and argon (Ar) or molecular nitrogen (N₂) as catalysts [320].

Among these studies, two are particularly relevant for the purpose of this work which focuses on establishing whether NV centres can be thermodynamically and optically stable in ultrasmall (size < 10 nm) nanodiamonds. They are presented below.

In 2009, J. -P. Boudou and co-authors proposed a technique to fabricate fluorescent NV-rich nanodiamonds (size ≤ 10 nm) by irradiation and annealing in vacuum, of type Ib high pressure high temperature (HPHT) diamonds [312]. In this process, the fluorescent nanodiamonds are synthesised in a HPHT reactor where the nitrogen from the solvent metal, the carbon source material and the residual gas becomes incorporated in the crystals during growth (cf. c. 2, s. 2.3.1). Vacancies are formed subsequently by irradiation with photons, electrons, ions or neutrons. Annealing at 800 °C then favours the migration of the vacancies towards the immobile nitrogen atoms (nitrogen in diamond starts migrating at temperatures above ~ 1500 °C) and leads to the formation of NV centres (cf. c. 2, s. 2.3.5). The so-obtained diamonds are then reduced in size via a milling process which takes place in two steps: micronisation and nanomilling. The nanodiamonds are finally chemically decontaminated and neutralised before being desalted by ultra-filtration.

The authors reported that the nanodiamonds obtained with this process are isolated, have dimensions less than or equal to 10 nm and, most importantly, are hosting optically stable and non-bleachable NV centres.

This study has remarkable consequences. It provides a recipe for a high yield and industrially scalable method to fabricate isolated fluorescent nanodiamonds with dimensions less or equal to 10 nm. It also clearly proves that stable NV centres can actually be observed in nanodiamonds as small as only a few nanometres in size, clearing some of the doubts about this being physically possible.

As a follow-up, immediately after the publication of this study, J. Tisler and co-authors reported the observation of stable NV centres in 7-nm nanodiamonds [301].

In the last years, the synthesis of ultradispersed nanodiamonds by detonation has known a considerable upturn. This has been fuelled by the tangible possibility the method offers of producing ultrasmall diamond nanoparticles only ~ 4-5 nm in size [315-318]. Again, the question is raised whether such small crystals could host stable NV centres.

In 2009, B. R. Smith and collaborators partially provided a positive answer by reporting the observation of NV luminescence from aggregates of 5-nm nanodiamonds [299]. This was not trivial: they had to design a time-gated luminescence detection scheme to observe the NV centre fluorescence. The sample in fact, exhibited strong luminescence in the red spectral region, i.e. slightly blue-shifted with respect to the characteristic NV emission. The NV zero phonon lines, at 575 nm for the NV⁰ and 637 nm for the NV⁻, were not observable either. The explanation of such measured spectrum was that the signal was dominated by short-lived (lifetime < 0.5 ns) surface defects covering the emission of the NV centres [321, 322]. The detection was thus time-gated and the fluorescence acquired with a delay of 3.5 ns from the excitation pulse so that the long-lived component of the NV centre could be extracted. They reported a lifetime for this long-lived component of ~ 12 ns, which is shorter than the ~ 23 ns expected for a single 5-nm nanodiamond in air [250] and much closer to the ~ 11.6 ns value measured in bulk diamond [251] (cf. c. 4, s. 4.5.3). This was justified by observing that nanodiamonds tended to pack together into weakly bound clusters creating a bulk-like environment.

The study certainly showed that the stability of NV centres in nanodiamond as small as 5 nm is possible; however it did not resolve all the doubts since the bulk-like environment of the nanodiamond-aggregate left unsolved whether NV centres could be actually observed in strictly isolated 5-nm crystals.

6.1.2 Isolated 5-nm detonation nanodiamonds (DNDs)

The goal of investigating thoroughly the thermodynamical and optical stability of NV centres in nanodiamonds fuelled our own research on the material science. We first turned our attention to detonation nanodiamonds (DNDs) for a number of reasons. First, several studies have proven that nanodiamond can be synthesised in crystals as small as

4-5 nm in size [315-318], making them ideal for many applications. Second, NV luminescence has been observed in 5-nm detonation nanodiamonds, although only in crystal aggregates [299]. This motivated further investigation, together with the development of our own de-aggregation methodology, to attempt to observe single isolated crystals with NV centres. Finally, detonation nanodiamond crystals are routinely produced on an industrial scale nowadays and the material is easily accessible for research purposes.

The product of the synthesis of diamond by detonation of trinitrotoluene (TNT) and hexogen (RDX) is a heterogeneous material. The diamond soot in fact, often contains metals, metal oxides and impurities other than diamond. Moreover, the diamond nanoparticles are generally surrounded by non-diamond/graphitic (sp^2 -hybridised) carbon phases and are agglutinated in several orders of aggregation ranging from the ~ 4-5 nm of the non-aggregated primary diamond particles up to the ~ 30-50 μm of the more structured agglomerates [316]. The challenge is therefore to design a method to isolate the primary nanodiamonds.

To achieve that, we optimised a de-aggregation and dispersion process, which diminishes the crystal-crystal interaction and yields a quasi-isolated system of “free-space” crystals weakly coupled to the underlying substrate [222]. The method is described below; it has been developed from existing procedures [323, 324] and modified to achieve the maximum separation of the diamond nanoparticles.

DNDs: de-aggregation method.

- i) The nanodiamonds are mixed with sulphuric acid (H_2SO_4 , 98%, 9 ml) and nitric acid (HNO_3 , 70%, 1 ml) and then refluxed for three days at 70 °C.
- ii) The mixture is centrifuged, ultrasonicated (duty cycle 50%, output power 240 W, 1 h) and then refluxed again with a fresh acid mixture.
- iii) Nanodiamonds are washed with Milli-Q® then refluxed with sodium hydroxide (NaOH, 0.1 M, 8 ml, 1 h, 90 °C), washed, then refluxed with hydrochloric acid (HCl, 0.1 M, 8 ml).
- iv) The mixture of nanodiamonds-in-acid is washed with Milli-Q® and ultrasonicated (duty cycle 50%, output power 240 W, 1 h).
- v) The sample is diluted by addition of Milli-Q® (~ 20 ml) and ultracentrifuged (1 h, 100,000g, being $g = 9.81\text{m/s}^2$).
- vi) The whole procedure is repeated three times.

The heated (70 °C) sulphuric (H₂SO₄, 98%, 9 ml) and nitric (HNO₃, 70%, 1 ml) acids are used to oxidise the surface of the diamond particles. These are mainly carboxylic acid (R-COOH, R being some monovalent functional group), acid anhydride ((RC(O))₂O, being RC some acyl group), cyclic ether (COC) groups and lactone (-(CO)O-, closed ring molecule with two or more carbon atoms C and a single oxygen atom O, with a ketone group =O in one of the carbons adjacent to the other oxygen) [324-327].

The sodium hydroxide (NaOH, 0.1 M, 8 ml, 1 h, 90 °C) and the hydrochloric acid (HCl, 0.1 M, 8 ml) are used to react with these surface oxides (for instance NaOH reacts with the carboxylic acids to form their salts). The products of the reactions are then washed with water [323, 324].

The ultrasonication process breaks-up the aggregates, freeing the particles and exposing more of their surface to the chemical treatments.

The ultracentrifugation is used to separate and sort the nanodiamonds by size because of the dependence of sedimentation time on particle size. The force F on spherical particles under centrifugation with acceleration $R\omega^2$ can be expressed as:

$$F = (4/3)\pi r^3 (\sigma - \rho) R \omega^2 \quad (6.1)$$

where r is the radius of the (assumed) spherical particles, while σ and ρ are the densities of the particles and the solvent, respectively. According to equation (6.1), by changing acceleration and duration of the centrifugation, the particles can therefore be separated and sorted by size [323].

The whole process is repeated three times to enhance its effectiveness.

We tested the method on a sample of untreated detonation diamond nanocrystals from Diamond Technologies and Materials. According to the company specifications, the sample (TC 2-037-677-94) is constituted by detonation nanodiamonds 3-10 nm in size and with an average size of cluster formations of 1-4 μ m. Below are the results of the de-aggregation process.

Transmission electron microscopy (TEM). Figure 6.1 shows the transmission electron microscopy (TEM) images of the sample before and after the treatment. TEM-samples were prepared by floating a Pioloform (polyvinyl butyral) coated copper grid (ProSciTech) onto a drop of isolated DND suspension (10 μ L), for 2 min, followed by

drying and subsequent examination using a Philips CM10 TEM at an operating voltage of 100 kV.

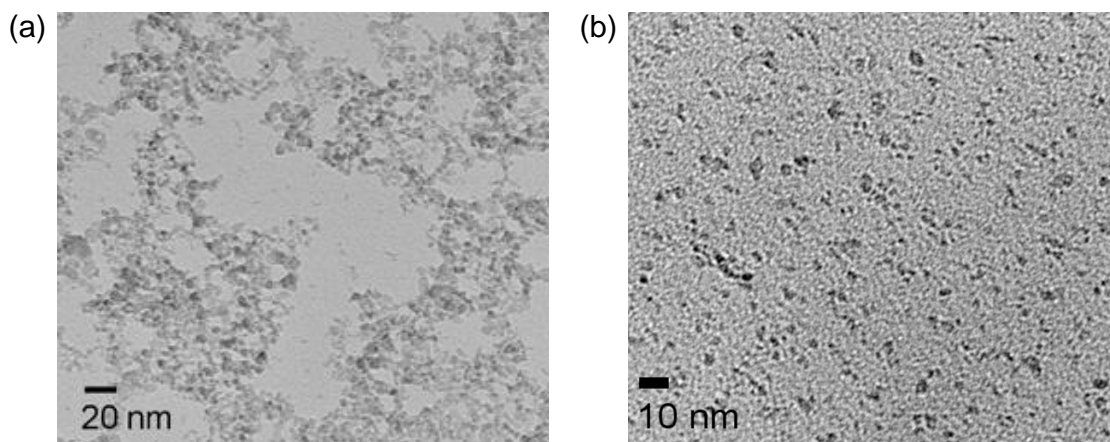


Figure 6.1. Transmission electron microscopy (TEM) of detonation nanodiamonds (sample from Diamond Technologies and Materials, TC 2-037-677-94). **a)** TEM micrograph of the as-received nanodiamonds; the high degree of particle aggregation is clearly noticeable. **b)** TEM magnified micrograph of the nanodiamonds after acid-treatment, ultrasonication and centrifugation, as described in the text; the treated particles are isolated and well separated, their size ranges from 2 to 7 nm. Note the different scale between (a) and (b).

There was a noticeable difference between the sample before and after the de-aggregation process (Fig. 6.1a and b, respectively). While the untreated sample is dominated by diamond aggregates, the processed material clearly shows well-isolated nanodiamonds with a size distribution of 2-7 nm.

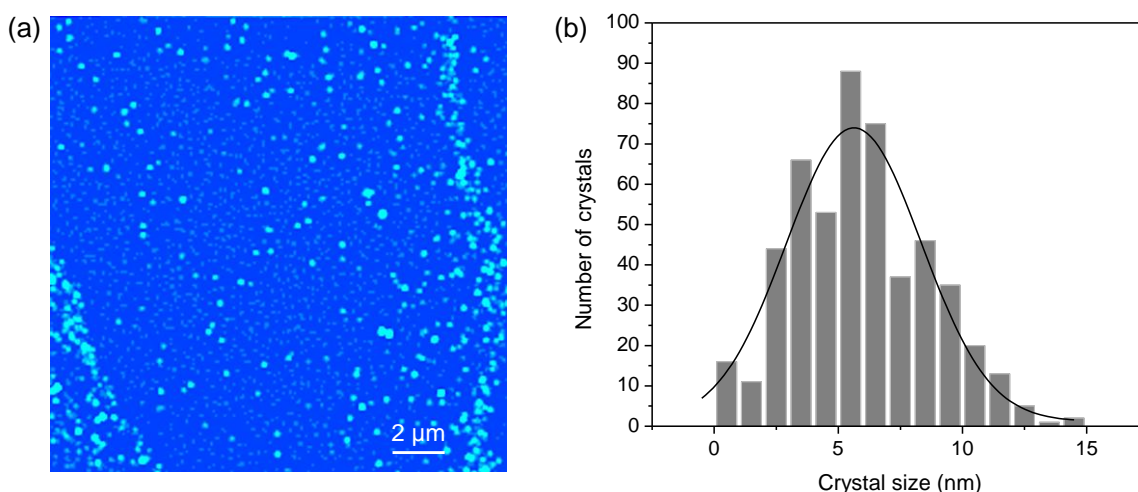


Figure 6.2. Topography and size distribution of processed detonation nanodiamonds. **a)** Atomic force microscope (AFM) scan showing the topography of the diamond particles dropped on a glass cover slip; areas with sparse, well isolated nanodiamonds are visible against other areas showing a certain degree of particle aggregation. **b)** Histogram of the size distribution of the diamond nanocrystals measured in an area of the sample free of aggregates (the solid line indicates fit with a Gaussian); the average size of the particles is (5.9 ± 2.7) nm.

Atomic force microscopy (AFM). We also measured the size of the treated diamond nanoparticles using an atomic force microscope. A few droplets of the processed water solution of detonation nanodiamonds were put onto a glass cover slip and either left to dry or spin coated. The topography of the sample and the size distribution of the diamond crystals are shown in figure 6.2.

The AFM scan (Fig. 6.2a) shows that while in some areas of the sample a certain degree of particle aggregation persists, there are other areas where the nanodiamonds are isolated and spatially separated. The histogram of the particle size distribution (Fig. 6.2b) shows that the average size of the isolated nanodiamonds is (5.9 ± 2.7) nm.

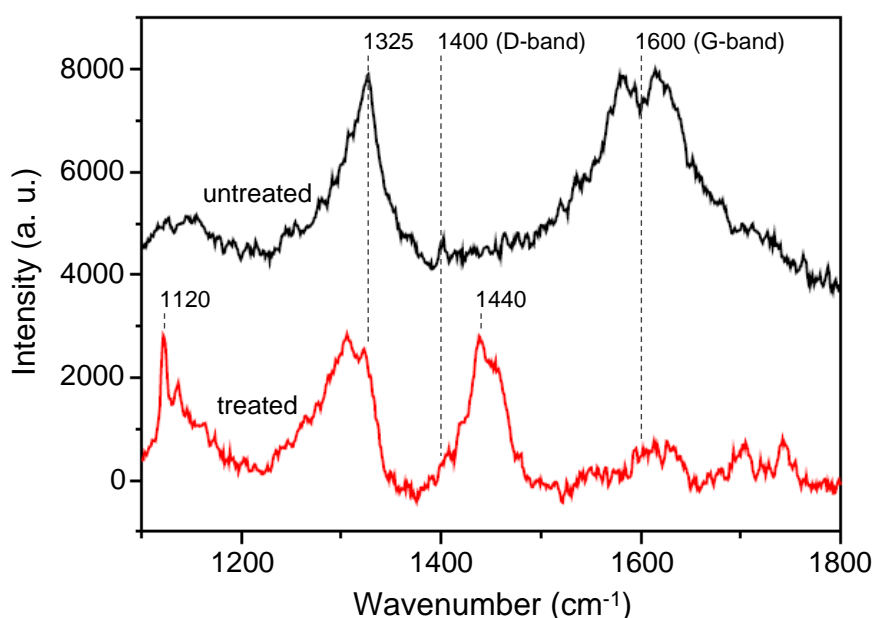


Figure 6.3. Raman spectroscopy of the detonation nanodiamond sample. The spectra are recorded from the as-received (top curve) and treated (bottom curve) nanodiamonds. The excitation laser was 514 nm.

Raman spectroscopy. As mentioned before, detonation nanodiamond often contains non-diamond/graphitic (sp^2 -hybridised) carbon phases. In order to assess the sp^3/sp^2 composition of the sample before and after the treatment, we also carried out Raman spectroscopy (Renishaw, InViva) on the as-received and treated samples. The excitation laser wavelength was 514 nm.

The results are shown in figure 6.3. The diamond peak centred at 1325 cm^{-1} is visible both in the as-received and processed material (the downward shift of the peak with respect to the value of 1332 cm^{-1} for bulk diamond is consistent with the shift expected from the

phonon confinement model for particles ~ 5 nm in size [328, 329]). After treatment, the G-band at 1600 cm^{-1} decreases dramatically (Fig. 6.3, bottom curve) in comparison with that of the as-received sample (Fig. 6.3, top curve). It is generally accepted that the G-band originates from the disordered phase of carbon (graphite); its near complete suppression suggests substantial removal of graphite from the processed diamond. There is also an increase in intensity of the peaks centred on 1120 cm^{-1} and 1440 cm^{-1} . These two peaks are attributed to the carbon-carbon (C=C) stretching and carbon-hydrogen (C-H) wagging modes of trans-poly-acetylene (trans-PA), which is a chain of sp^2 carbon atoms [330]. To explain these, we speculate that the removal of the amorphous carbon is likely to induce the formation of other carbon and hydrogen-related phases on the surface of the crystals.

This treatment effectively solves the two main problems which affect detonation synthesised nanodiamond: the aggregation of the particles and the presence of non-diamond, graphitic (sp^2 -hybridised) carbon phases.

Both transmission electron microscopy (TEM) and atomic force microscopy (AFM) show that the treated nanodiamond particles are sparse and isolated, while the Raman spectroscopy highlights the substantial suppression in the processed material of the disordered and graphitic phase of carbon.

6.1.3 Size reduction of nanodiamonds by air oxidation

With the focus on material, we pursued an alternative approach to process small diamond nanoparticles and control their size and properties: air oxidation. It is well known that thermal oxidation in air can modify the outer layers of diamond nanoparticles [331]. It can alter their surface chemistry and influence the charge state and the optical behaviour of hosted NV centres [308, 309]. We designed an experimental method which exploits air oxidation to control the final size of selected diamond nanoparticles and address the behaviour of the hosted colour centres [332].

Air oxidation is simple and inexpensive. It does not require the use of any toxic substance or specific catalysts and is safely conducted in a furnace in air and at ambient pressure. When diamond is oxidised in air, carbon (C) reacts with oxygen (O) to generate carbon monoxide (CO) and carbon dioxide (CO₂). During oxidation in air, several structures are

formed on the diamond surface, such as: keton (C=O), ether (C-O-C), lactone [C(O)-O-C] and carboxylic anhydride [C(O)-O-C(O)] [333]. More precisely, at temperatures ~ 300 - 380 °C the diamond surface is oxidised by the formation of keton and ether bridges, which develop into lactone and carboxylic anhydride structures at temperatures ~ 380 - 480 °C. Above ~ 480 °C, these latter complexes decompose leading to keton groups and carbon dioxide (CO₂). The continuous absorption of oxygen and desorption of CO₂ from the diamond surface results in the detachment of carbon atoms, i.e. in the “burning” of the diamond. The diamond etching rate increases for increasing values of temperatures until above ~ 900 °C where the dynamic of the process changes. In this temperature range, the thermochemical oxidation produces a nanocrystalline layer of graphite on the diamond surface which tends to lower the rate of material removal [334]. In general, the air oxidation of diamond occurs in two subsequent steps: first the formation of a graphitic layer at the surface and second its subsequent removal via the above mentioned CO₂ desorption. At temperatures below ~ 900 °C, the second step is faster and a clean diamond surface is formed. However, at temperatures above ~ 900 °C the speed of the first step increases and the removal of the graphitic layer becomes less efficient leading to a subsequent reduction of the overall diamond etching rate.

Diamond etching via thermochemical oxidation is in general a much more complicated mechanism with several factors involved. These include: the pressure as well as the temperature of oxygen [334-337], the crystallographic orientation of the diamond surface [334-337], the presence of traces of water vapour or fluorine [338] and the occurrence of twinning, graphitic and amorphous carbon inclusions in the crystals [336, 339]. Moreover, different carbon phases have different reaction energies: for instance, air molecules oxidise first the amorphous (sp^2) carbonaceous matter, while they react with the diamond (sp^3) phase only at higher temperatures [336, 338, 340, 341]. In confirmation of such a variety of influencing parameters, the study of first and second order diamond oxidation kinetics shows activation energies in quite a variable range: 149-293 kJ/mol, depending on the characteristics of the sample and on all the above mentioned factors [334-337, 342-344]. It is interesting to note that since the strength of a carbon-carbon (C-C) covalent bond is ~ 349 kJ/mol, the diamond oxidation process is likely to involve only one bond at a time [344].

By selecting the right combination of temperature and time we could potentially start with a nanodiamond of a certain size and by air oxidation remove all the surface impurities, the amorphous carbon phases and finally etch away, layer by layer, the diamond itself. We would obtain a purified diamond nanoparticle, tailored to the desired size. The idea is conceptually very simple however its practical realisation poses some technical challenges. That is why, even though air oxidation is a well-established technique for etching diamond, to date no direct analysis of the etch rate or of the effects of air oxidation on single isolated nanodiamonds has been carried out.

To determine the etch rate, we designed an experimental method on our own. We simply use an atomic force microscope (AFM), but the novelty resides in the arrangement of the sample: the diamond nanocrystals in fact, lay on a substrate where well-identifiable areas have been marked. This allows addressing easily and in a repeatable way the exact same nanodiamonds after each subsequent air oxidation step to see what changes, if any, have occurred.

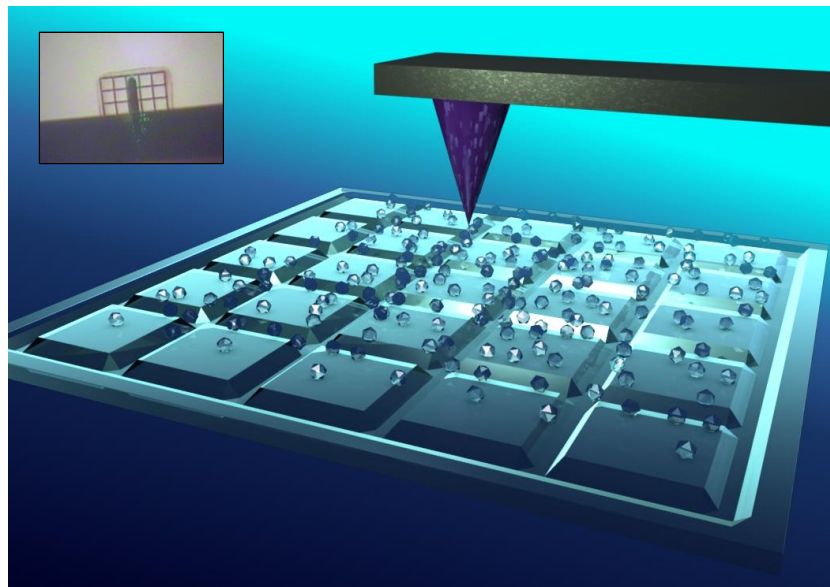


Figure 6.4. Illustration of the experimental arrangement of the sample. The diamond nanoparticles are prepared on a substrate where a grid has been laser-scribed as a reference. The AFM is used to measure the size of the crystals. The sample is repeatedly removed to be air-oxidised in a furnace and then put back on the AFM stage. The grid allows realigning the sample exactly in the same place after each oxidation step so that the size reduction of the very same crystals can be followed. The inset shows a real photograph (top view) of the actual setup: the 5×5 square grid (each square measuring $50 \times 50 \mu\text{m}^2$) is clearly visible under the AFM tip.

I present here the results we obtained for a sample of high pressure high temperature (HPHT) monocrystalline diamond powder (Microdiamant, MSY 0-0.1 μm).

The nanodiamonds were dropped on a glass cover slip (dimensions $22 \times 22 \text{ mm}^2$ and thickness $\sim 0.13\text{-}0.17 \text{ mm}$; Menzel-Glaser) on which a square 5×5 unit grid (each unit measuring $50 \times 50 \mu\text{m}^2$) has been previously laser-scribed (4th harmonic YAG (266 nm), μJ 10-ns pulses, spot size $\sim 6 \mu\text{m}$, 10 mW at 1 KHz). Figure 6.4 shows a representation of the experimental arrangement of the sample.

The nanodiamonds over the grid were scanned with the AFM and their size was measured. The sample was then removed and put in a tube furnace (Lenton Thermal Designs) where it was oxidised in air at ambient pressure (we performed the experiments with different temperatures and time durations). The temperature of the furnace was allowed to stabilise before inserting the sample into the heated region, and the oxidation time was measured from the instant the thermocouple, in contact with the metal sample holder, read the same temperature as the internal furnace sensor. After the oxidation step the sample was put back on the AFM stage. The grid allowed perfect realignment, so that the very same crystals could be remeasured and their size reduction could be tracked accurately over several oxidation steps. Note that we characterised the sample with the combined confocal-atomic force microscope (AFM) setup described in chapter 4, section 4.5. In the setup, the laser of the confocal microscope is aligned with the AFM tip from below the substrate. This means that contemporaneously to measuring the size reduction of the selected nanodiamonds we can study the evolution of the optical behaviour of the hosted NV centres. Here, I focus on the results for the size reduction of the nanodiamonds; I will present the results relevant to the luminescence of the NV centres later in this chapter (cf. ss. 6.3.1-4).

Figure 6.5 shows some of the results for the thermal oxidation in air of the HPHT nanodiamonds (MSY 0-0.1 μm) from Microdiamant. In this particular case the sample was put through four oxidation steps, each performed at $600 \text{ }^\circ\text{C}$ for 1 hour. The size of a few hundred diamond crystals was measured before any treatment, i.e. on the as-received material, and after each oxidation step.

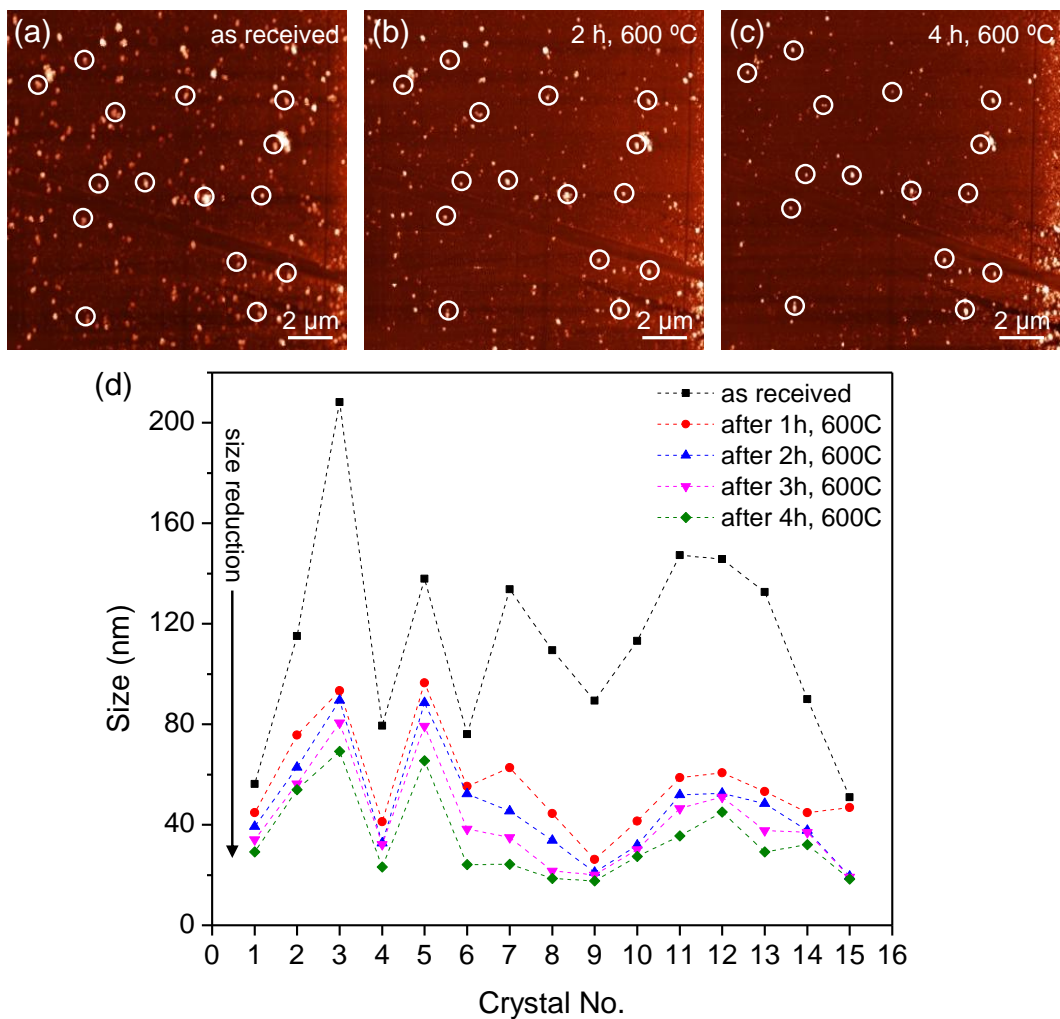


Figure 6.5. Analysis of the size reduction of oxidised nanodiamonds. **a, b, c** AFM scans of the same sample area taken at three different times: before any treatment (**a**), after a 2-hour oxidation at 600 °C (**b**) and after a 4-hour oxidation at 600 °C (**c**). As an example to show the principle, in these scans 15 crystals (circles) have been selected and their size measured over the subsequent thermal oxidation steps. The brightness of the spots is proportional to the size (height) of the crystals: from (**a**), through (**b**) and to (**c**) the relative brightness of the spots clearly decreases, meaning the size of the corresponding particles is being reduced. In some cases the nanodiamonds are completely etched away by the oxidation: note how scan (**a**) is denser of bright spots than (**c**). **d**) Size of the selected 15 crystals measured on the as-received sample and after consecutive oxidation treatments, each conducted for 1 hour at 600 °C. The size reduction is clearly visible. Note also how the first oxidation step seems to remove much more material than any subsequent step (see text).

Figure 6.5a, b and c are atomic force microscope scans of exactly the same area of the sample taken respectively for: a) the untreated nanodiamonds, b) after a 2-hour oxidation at 600 °C and c) after a 4-hour oxidation at 600 °C. In the scans, 15 crystals (circles) of the few hundred analysed have been highlighted just for demonstrative purposes. The brightness in the AFM images is proportional to the size (height) of the nanodiamonds. Already a rough qualitative observation reveals a decrease in the relative brightness (i.e.

size) of the corresponding spots from (a), through (b) and to (c). In some cases, the crystals have been completely etched away by the air oxidation process. Note in fact, how the scan of the untreated sample (a) has a much higher density of bright spots than that after the 4-hour oxidation at 600 °C (c).

Figure 6.5d shows the size of 15 reference diamond crystals measured for the as-received sample and after each one of the 1-hour oxidation steps at 600 °C. On the x -axis, every number identifies one specific crystal of the 15 considered. On the y -axis the size of each crystal is represented: before treatment (squares), after oxidation for 1 h at 600 °C (circles), after oxidation for 2 h at 600 °C (up triangles), after oxidation for 3 h at 600 °C (down triangles) and after oxidation for 4 h at 600 °C (rhombuses). The dashed lines have been drawn for clarity just to bundle the points that belong to the same dataset. The size reduction induced by the thermal oxidation in air is clearly visible: for each crystal the size measured at a certain step is reduced in comparison to that measured at the previous one.

Note that the first oxidation step performed on the as-received material causes, in almost all the cases, the most significant reduction in size. Quantitatively, we can define the average relative size reduction ($\Delta S_{i \rightarrow j}$) between two consecutive oxidation steps i and j as:

$$\Delta S_{i \rightarrow j} = \frac{\sum_{n=1}^N \frac{(S_i)_n - (S_j)_n}{(S_i)_n}}{N} \quad (6.2)$$

where S_j and S_i are the sizes of each n -crystal at the final (j) and initial (i) step respectively, while N is the total number of crystals analysed. Using equation (6.2) with $N = 200$ selected crystals, we found that the relative average size reduction measured after the very first oxidation step (1 h, at 600 °C), carried out on the untreated nanodiamonds, was $\sim 0.5 \pm 0.2$, which corresponds to a percentage size reduction of ~ 30 -70% (I will discuss the large variability of this value below). In contrast, we measured the size reduction between any other two subsequent oxidation steps to be only $\sim 0.07 \pm 0.02$, which corresponds to a percentage size reduction of ~ 5 -9%, i.e. almost one order of magnitude less. The difference in the rates is considerable. We attribute it to the fact that before any air oxidation step, the surface of the nanodiamonds may exhibit a high proportion of non-carbon impurities, sp^2 -bonded carbon phases and oxygen containing groups. They all

usually possess lower reaction energies than the sp^3 -bonded carbon of the nanodiamond core and tend therefore to oxidise much faster. This implies that in the very first oxidation step a higher proportion of (heterogeneous) material is removed from the nanodiamonds surface in comparison to any other subsequent oxidation steps during which only the strong sp^3 -bonded carbon is left to be etched away.

A Raman spectrum of the as-received nanodiamond sample confirms this hypothesis (Fig. 6.6a). The spectrum (excitation laser 514 nm) shows both the diamond peak at 1332 cm^{-1} and the G-band at 1600 cm^{-1} . The relatively high signal of the G-band suggests that as we concluded from the size reduction analysis, the as-received nanodiamond material contains a high fraction of the disordered phase of carbon (graphite, sp^2).

As an additional confirmation we also analysed a sample prepared in a slightly different way. Instead of using nanodiamond powder in “as-received” form, we processed it using the same acid treatment we optimised to separate the 5-nm detonation nanodiamonds (cf. s. 6.1.2). This process acts to de-aggregate the crystals and reduce the amount of graphitic carbon surrounding the diamond nanoparticles. We repeated the oxidation experiment on the acid treated nanodiamonds and we measured with equation (6.2) the average particle size reduction after the very first oxidation steps (1 h, at $600\text{ }^\circ\text{C}$). For consistency with the previous analysis we analysed again $N = 200$ crystals. We measured a relative size reduction of $\sim 0.3 \pm 0.2$, which corresponds to a percentage reduction of $\sim 10\text{-}50\%$, i.e. slightly lower than the one ($\sim 30\text{-}70\%$) measured for the untreated sample, but still higher than the reduction we measured after any other subsequent oxidation step ($\sim 5\text{-}9\%$). This can be explained by noticing that in the Raman spectrum of the acid-treated 5-nm nanodiamonds (cf. s. 6.1.2, Fig. 6.3), the G-band is strongly suppressed but still visible and there are vibrational modes possibly associated to chains of sp^2 carbon atoms surrounding the nanodiamonds. The fact that the acid treatment leaves traces of sp^2 -bonded carbon phases, although in smaller fractions compared to the as-received material, is consistent with the particle size reduction rates we measured.

Another proof is given by the optical investigation of NV centres in the nanodiamond material (Fig. 6.6b). I will analyse the optical properties of NV centres in small nanodiamonds later in the chapter (cf. ss. 6.3.1-4), here I only present some data to support the argument relevant to the different size reduction rates we observed. Figure 6.6b shows two emission spectra, collected with our combined confocal-AFM setup (cf. c.

4, s. 4.5), for the same NV centre hosted in a diamond nanocrystal. The black curve is the spectrum measured before oxidation, while the gray curve is the spectrum measured after carrying out an air oxidation step for 6 h at 600 °C. The spectrum of the defect taken after oxidation (grey curve) clearly shows all the features we expect to see for an NV centre at room temperature, including a zero phonon line (ZPL) which lies within the typical range for nanodiamonds. However, the spectrum of the same NV taken before oxidation (black curve) looks almost featureless and blue-shifted towards lower wavelengths. As discussed previously (cf. s. 6.1.1), this is attributable to short-lived surface defects and graphitic (sp^2) structures which cover the NV centre luminescence [299, 321, 322] and which are removed by the oxidation in air. This again seems to be consistent with the fact that the very first oxidation step shows a much higher etching rate than any subsequent step, since it involves the removal of heterogeneous material other than the carbon sp^3 -phase of the nanodiamonds core.

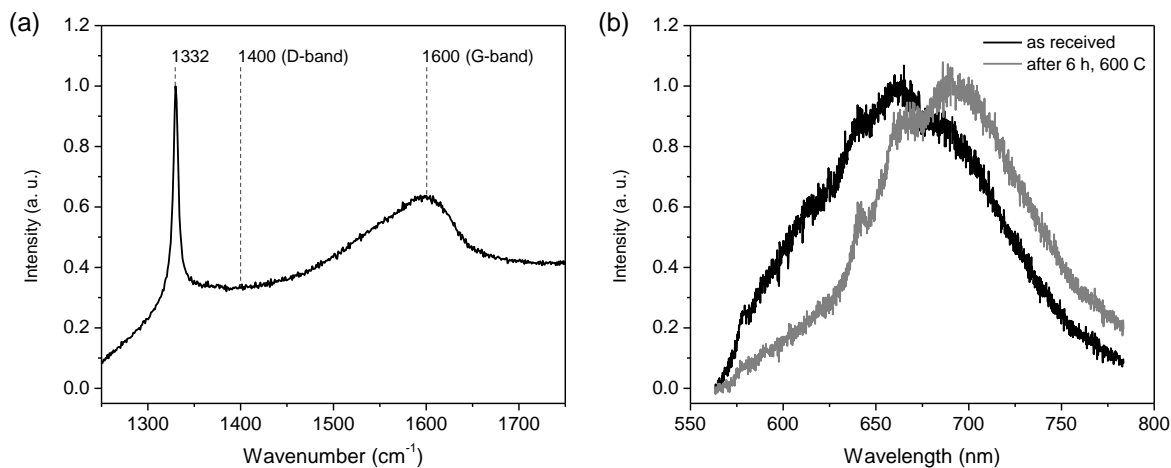


Figure 6.6. Raman spectrum of as-received HPHT nanodiamond (MSY 0-0.1 μm , Microdiamant) and fluorescence emission spectra of the same NV centre taken before and after oxidation. **a)** Raman spectrum (excitation laser wavelength 514 nm) of the as-received nanodiamond; both the diamond peak at 1332 cm^{-1} and the G-band at 1600 cm^{-1} are visible. The relatively high intensity signal of the G-band suggests the presence of graphitic (sp^2) carbon phases surrounding the sp^3 -bonded carbon of the nanodiamonds core. **b)** Emission spectra (excitation laser wavelength 532 nm) of the same NV centre in a diamond nanocrystal before (black curve) and after air oxidation for 6 h at 600 °C (gray curve). The luminescence before oxidation appears featureless and blue-shifted as a consequence of the fluorescence signal coming from surface defects and amorphous (sp^2) carbon phases.

From figure 6.5d we can deduce some other interesting results. The size reduction rate of the crystal No. 7 for instance, is quite different from that of No. 9. While centre No. 7 seems to etch with a fairly constant rate (excluding for the reasons I have just discussed

the first oxidation step), centre No. 9 seems to be barely affected by the oxidation process. In general: air oxidation etching rates differ amongst different individual diamond crystals. This is even more evident in Figure 6.7 which shows the evolution in size of the same three nanodiamonds over consecutive oxidation steps, each carried out for 2 h at 600 °C.

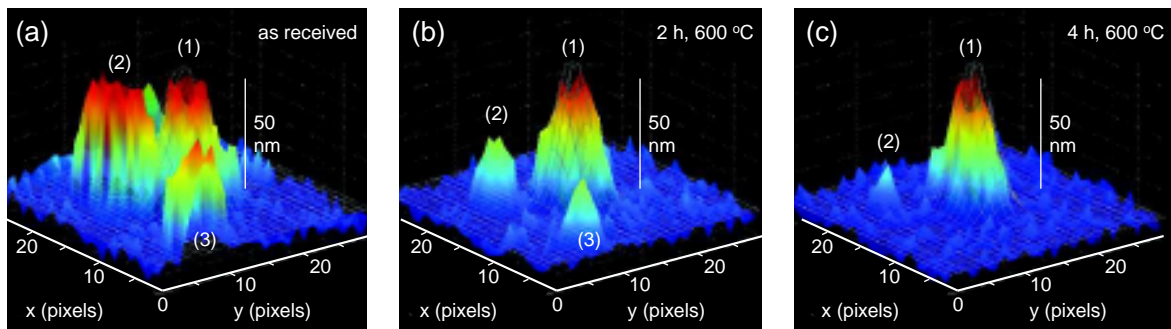


Figure 6.7. Size measurement of the same three nanodiamonds labelled (1), (2) and (3) tracked through subsequent oxidation steps. **a, b, c**) Size of the same three crystals measured for the as-received sample (a), after a 2-hour oxidation at 600 °C (b) and after a 4-hour oxidation at 600 °C (c). Over the oxidation steps, crystal (1) does not experience any reduction in height (z-axis), while crystals (2) and (3) do; crystal (3) eventually vanishes as oxidation completely etches it away. We attribute this difference in behaviour to the diamond anisotropy with its etching exhibiting strong surface orientation dependence. In support of this explanation, while the height of crystal (1) remains almost constant (~ 50 nm) through the consecutive oxidation steps, we measure a relative reduction of its x and y cross sections (i.e. of its width), from 130 nm, to 120 nm and eventually to 100 nm.

The height of the nanodiamonds is obtained from the AFM scan topographies by fitting each crystal with 2-dimensional Gaussians after the subtraction of the background height offset. The height of crystal (1) remains constant at ~ 50 nm after every step. Conversely, the height of crystals (2) and (3) continues to decrease as the diamond layers are etched away by air oxidation, with crystal (3) ultimately vanishing completely. Our explanation of such a behaviour is the anisotropy in the etch rate for the different diamond crystallographic planes and directions. As I have mentioned before, the etching rates of diamond show strong orientation dependence. In general the (111) surface exhibits the highest oxidation rate, followed by the (110) and the (100) exhibiting the lowest rate [334, 338, 344]. It is undeniably quite hard though to address and investigate the anisotropy of the etching rate in diamond nanocrystals. The reason is that we cannot control the surface crystallographic orientation of the nanodiamonds dispersed on the substrate. However, it seems reasonable to explain the difference in behaviour we observed for crystal (1) and

for crystals (2) and (3) by resorting to the etching anisotropy. In fact, although the height (z-axis) of crystal (1) remained constant through the following oxidations, the relatively “crude” measure of its x and y cross sections (i.e. the width of the nanocrystal) did show a reduction going from 130 nm, to 120 nm and eventually to 100 nm. Note that these values for the crystal widths are meaningful in a relative sense, i.e. as an indication of the relative size reduction through the subsequent oxidation steps, rather than as absolute measurements since the lateral resolution of the AFM is much lower than the vertical one (cf. c. 4, s. 4.3).

The parameters of temperature and time offer excellent control over the air oxidation process. We therefore measured the size reduction and etching rates as a function of temperature and time.

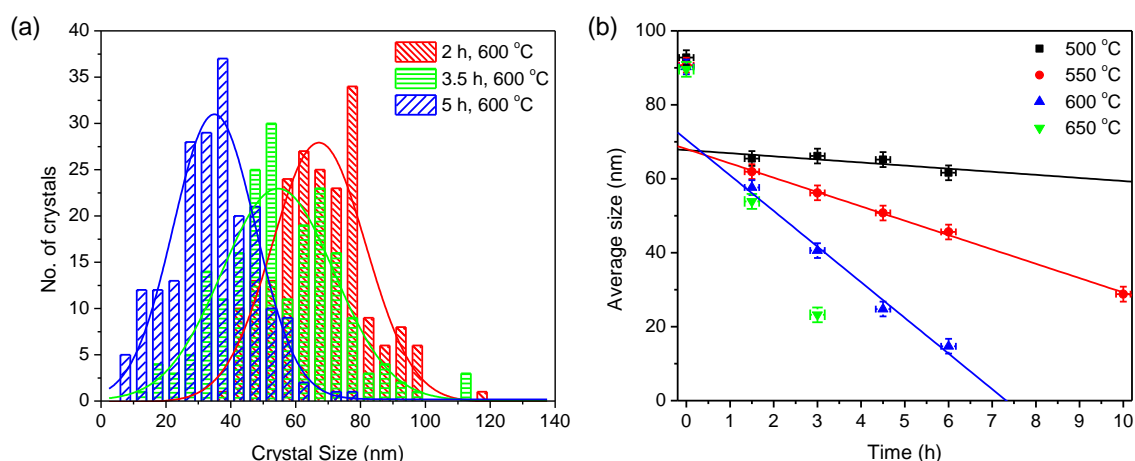


Figure 6.8. Average size reduction of nanodiamonds due to oxidation in air. **a)** Histograms of the nanodiamond size (height) distribution with their Gaussian fits (solid lines) after consecutive oxidation steps (showing only the 2-h, 3.5-h and 5-h oxidation steps at 600 °C). Overall we performed the analysis over several oxidation steps of 30 minutes each and at four different temperatures: 500 °C, 550 °C, 600 °C and 650 °C. **b)** Evolution of the average crystal size as a function of oxidation time at 500 °C (squares), 550 °C (circles), 600 °C (up triangles) and 650 °C (down triangles). The solid lines are linear fits of the average etching rates of the nanodiamonds. They are: < 1 nm/h at 500 °C, (4 ± 1) nm/h at 550 °C and (10 ± 1) nm/h at 600 °C.

We selected a specific area of the sample and measured the height of individual nanodiamonds after every oxidation step. We then built the corresponding histograms of the height distribution and fitted them with Gaussians to extract the average crystal size at each step. Figure 6.8a shows such height distribution histograms for the oxidation at 600 °C. Only the histograms for the 2-h, 3.5-h and 5-h oxidations are shown, however the full analysis included oxidation steps of 30 minutes each and at four different

temperatures: 500 °C, 550 °C, 600 °C and 650 °C. The results are summarised in figure 6.8b, where the average crystal sizes are plotted as a function of the oxidation time and fitted with lines that give the average etching rates. The dramatic reduction after the first oxidation step is due to the initial high fraction of non-carbon and non-diamond carbon materials which surround the nanodiamond surface and have a faster etch rate than the diamond (sp^3) carbon phases of the particle core. Based on this observation, we excluded the first point from the linear fit. The average etch rate of the nanodiamond was found to be: < 1 nm/h at 500 °C, (4 ± 1) nm/h at 550 °C and (10 ± 1) nm/h at 600 °C. We measured the average size reduction also for the oxidation at 650 °C; in this case though the fit is not shown since we could acquire only two data points.

The activation energy determined from an Arrhenius plot is 126 kJ/mol.

As I mentioned at the beginning of this section, the thermal oxidation of diamond in air is quite a complicated mechanism. Although the chemistry and, to some extent, the dynamic of the reactions involved are well understood, air oxidation of diamond shows a lot of variability due to the specific characteristic of the material examined and to all the different factors that influence the process (e.g. pressure and temperature of oxygen, crystallographic orientation of the diamond surface, presence of water vapour or fluorine, occurrence of twinning, graphitic and amorphous carbon inclusions in the crystals and carbon phases composition of the nanodiamond surface).

In the case of nanodiamonds, the results I have presented above show that, apart from temperature, the composition of the particle surface with its content of non-carbon impurities, amorphous (sp^2) and diamond (sp^3) phases, and also the diamond anisotropy are all factors which significantly participate in the thermal oxidation process. They are responsible, for instance, for the large variability (\sim tens of percentage points) we measured using equation (6.2) for the relative particle size reduction between subsequent air oxidation steps. On some of these factors we do not have full control. For instance, we cannot choose the carbon phase composition of the nanodiamond surface or the orientation of their crystalline planes with respect to the substrate. This makes exploiting air oxidation to process nanodiamonds a very challenging task. However, I hope I have convincingly shown that the method we developed allows a substantial degree of control.

We can in fact control the size and, as I will show in the next sections (cf. ss. 6.3.1-4), even the optical properties of targeted nanodiamonds. We could select a diamond nanoparticle, purify its surface with a first oxidation step and determine its etch rate after several further minutes of oxidation at a selected temperature. Then, just by controlling the time, we could tailor its size at the exact desired value for the specific designed purpose. This is ideal for many applications including, for instance, single-spin magnetometry (cf. c. 3, s. 3.3) where the nanodiamond to be attached at the apex of the AFM tip for sensing has to contain a single NV centre and has to be as small as possible to increase the detecting resolution ($\sim 1/r^3$, being r the distance between the single spin to detect and the probing NV centre; cf. c. 3, s 3.3.4, equation (3.8)).

6.1.4 Final remarks on the fabrication of ultrasmall nanodiamonds

Most diamond-based nanotechnologies are currently pushing the limits towards the fabrication of the smallest possible nanodiamonds and the control of their physical and optical properties (cf. c. 2, s. 2.4). I do believe that this is crucial for the practical implementation of such technologies and it is also the reason why we have invested such a great effort in the material science aspect of our research. The methods I have presented both for the de-aggregation of 5-nm detonation nanodiamonds (cf. s. 6.1.2) and the size reduction of nanodiamonds by air oxidation (cf. s. 6.1.3) are our own original contributions to the large set of techniques recently developed (cf. s. 6.1.1) to respond to the challenges identified in nanodiamond technologies.

6.2 Optical properties of NV centres in ultrasmall nanodiamonds

Our recent capability of fabricating smaller and smaller nanodiamonds raises new questions. The focus has shifted to understanding the effect of a reduced diamond crystal size and surface proximity of nitrogen-vacancy centres on their optical properties.

In the following sections, I will address this problem and present some original results regarding newly observed phenomena such as the NV luminescence intermittency or “blinking”.

6.2.1 Luminescent NV centres in isolated 5-nm nanodiamonds

We initially investigated the effects that size and surface proximity have on the optical properties of NV centres in 5-nm detonation nanodiamonds [222]. We used the detonation nanodiamond sample (TC 2-037-677-94) from Diamond Technologies and Materials on which we performed the acid treatment described in section 6.1.2 to de-aggregate the particles and remove the surrounding amorphous/graphitic (sp^2) carbon phases.

The treated diamond nanocrystals were dispersed on a glass cover slip, where we could then easily identify areas with well-isolated nanodiamonds (Fig. 6.2a) of only 3-9 nm average size (Fig 6.2b). The sample was characterised with the combined confocal-atomic force microscope (AFM) setup described in chapter 4, section 4.5 to simultaneously correlate the optical behaviour of the centres with the size of the hosting crystals. Figure 6.9 shows an example of the corresponding confocal and AFM images taken from an area of the examined sample.

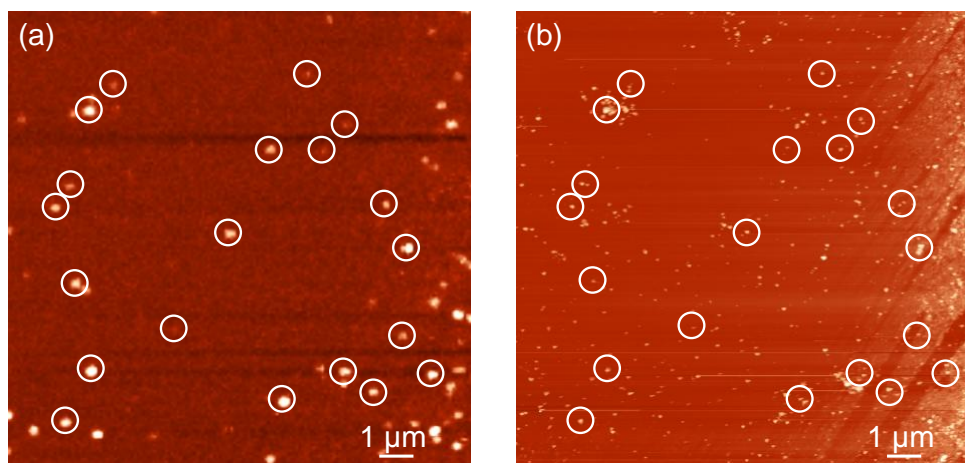


Figure 6.9. Confocal and AFM images of acid-treated, isolated 5-nm detonation nanodiamonds (sample TC 2-037-677-94; Diamond Technologies and Materials). **a)** Confocal image: bright fluorescing spots indicate emission from NV centre(s). **b)** Corresponding AFM image: the brightness of the spots is directly proportional to the height of the crystals. Note how the crystals are highly isolated on the substrate.

The characterisation of the sample revealed that $\sim 1\%$ of the total diamond nanocrystals were fluorescent, showing emission from hosted NV centres. Note that the nanodiamond material had *not* been irradiated or annealed to enhance the presence of colour centres. Although NV centres had been previously detected in ~ 5 -nm nanodiamond agglomerates [299], we observed for the very *first* time the emission from single NV centres in fully *isolated* 5-nm nanodiamonds (Fig. 6.10).

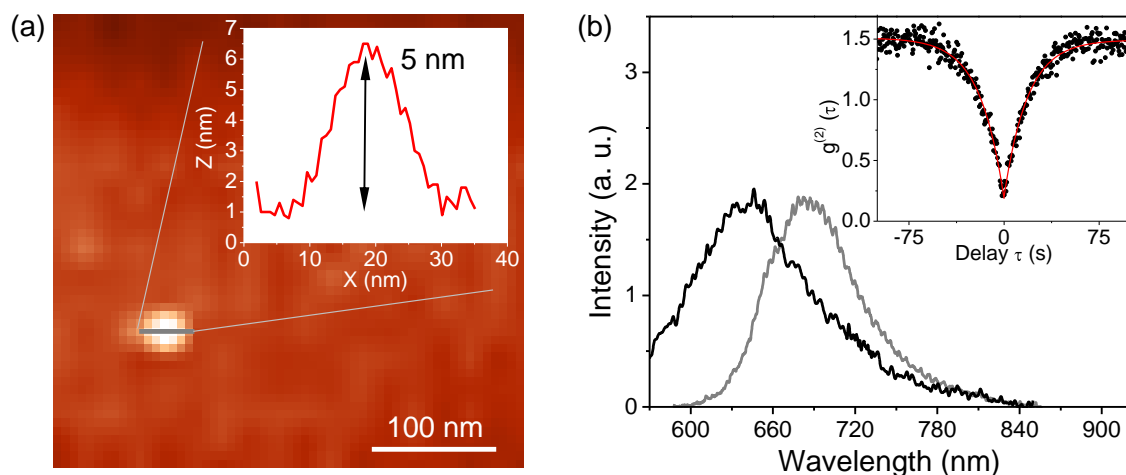


Figure 6.10. Analysis of a 5-nm diamond nanocrystal hosting a single NV centre (data refers to the acid-treated and ultrasonicated detonation nanodiamond sample). **a)** Magnified AFM image and corresponding height profile (inset) of a 5-nm nanodiamond. **b)** Emission spectrum (grey curve) and corresponding second-order correlation function $g^{(2)}$ (inset) of a single NV centre hosted in the 5-nm crystal. For comparison, the emission spectrum (black curve) acquired from the as-received, untreated nanodiamond material is shown. This spectrum is centred at 650 nm, likely as a consequence of the fluorescence signal coming from surface defects and amorphous (sp^2) carbon phases as discussed previously (cf. s. 6.1.3, Fig. 6.6).

Such an observation is important because it resolves some of the concerns regarding whether nanodiamonds smaller than 10 nm in size could host any optically active NV centre [304, 311]. As extensively discussed previously (cf. c. 5, s. 5.2), the minimisation of the crystal energy favours the nitrogen atoms to be located at the surface rather than in the core of the nanoparticles. This was thought to lead, possibly, to the instability of the nitrogen-vacancy centre in very small nanodiamonds; either because the vacancy would likely diffuse and annihilate at the near surface or because the NV centre would undergo structural distortions which could make it no longer optically active (cf. c. 5, s. 5.2.2). Although these considerations still hold true, our observation of optically active NV centres in isolated 5-nm nanodiamonds established that the stability of the defect is possible even in ultrasmall nanodiamonds.

6.2.2 Blinking NV centres in isolated 5-nm nanodiamonds

The second interesting result of our study on isolated 5-nm detonation nanodiamonds, was a *newly* observed property of NV centres: the luminescence intermittency or blinking [222].

The NV centre is a single photon source. Upon excitation and on a time scale comparable to the lifetime of its excited state (\sim ns), it emits antibunched/one-by-one photons (cf. c. 4, s. 4.5.3). On larger time scales (\sim ms), the photons emitted by a stable NV centre appear as a continuous stream (Fig. 6.11a). However, in a blinking NV centre such continuity is disrupted (Fig. 6.11c).

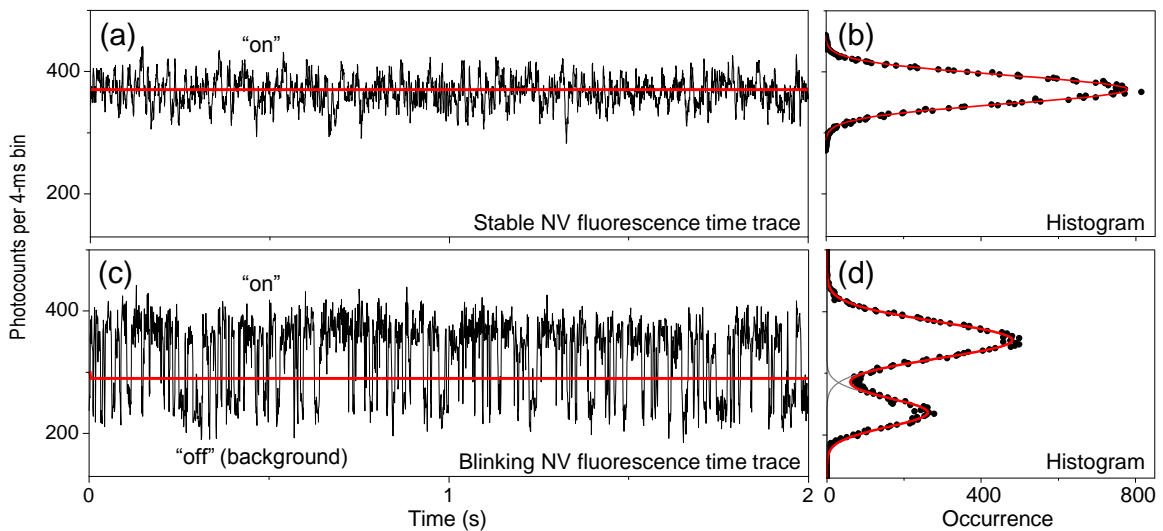


Figure 6.11. Comparison between stable and blinking NV fluorescence time traces. **a, b)** Fluorescence time trace of a stable NV centre (a) and corresponding histogram of the “on” state occurrence fitted with a single Gaussian (b). **c, d)** Fluorescence time trace of a blinking NV centre (c) and corresponding histogram of the “on” and “off” states occurrence fitted with two Gaussians (d). The NV fluorescence time traces in (a) and (c) have been sampled into 4-ms bins. The Gaussian in (d) are fitted to the “on” and “off” state photon distributions with respect to the on/off threshold indicated by the horizontal line in (c). The analysis clearly shows the striking contrast between the photoemission of a stable NV centre and that of a blinking one.

The simplest and earliest model which was proposed to explain the blinking mechanism in quantum systems assumed that the fluorophore would undergo a non-radiative transition from the excited state to a non-fluorescent level having a lifetime far beyond the fluorescence lifetime [345]. This would mean that in a blinking NV centre the continuous stream that we should observe at large time scales is interrupted by so called “off” or “dark” intervals, the duration of which coincides with the lifetime of the non fluorescent level. Therefore, a blinking NV centre randomly switches between dark (off) and bright (on) states.

At the nanoscale, almost all known fluorophores exhibit emission intermittency or blinking. For instance, in single-molecules a common cause for blinking is the intersystem

crossing from the excited to a triplet state from which the transition to the ground state is symmetry-forbidden and occurs non-radiatively [346-349]. The triplet lifetime generally falls in the microsecond regime, much longer than the nanosecond singlet excited state lifetime, and the resulting fluorescence shows the characteristic on/off blinking behaviour on large time scales. Blinking has also been observed in other systems including: organic molecules [348-353], fluorescent proteins [354], multichromophore conjugated polymers [355], quantum dots [356], individual porous silicon nanoparticles [357], nanorods [358] and nanowires [359-361]. However, it has never been observed before in NV centres. As a matter of fact, to date, NV centres in diamond have always been acclaimed to be photostable single photon sources, immune to blinking and bleaching [167]. In our study of all the fluorescent nanocrystals ($\sim 1\%$ of the total number of nanocrystals) measured in the de-aggregated 5-nm detonation nanodiamond sample, $\sim 1/4$ showed blinking.

The observation of blinking NV centres in 5-nm nanodiamonds is remarkable. It suggests that at the nanoscale, while the defect can still be thermodynamically stable, its electronic structure may undergo changes or be subject to effects that are not observable for instance in bulk diamond NV centres.

Despite the almost thirty years of studying the blinking phenomenon in several quantum systems, a deep understanding of the mechanism is still missing. If we look in the literature, the simplest model for blinking was developed by N. Bohr and later (1985) refined by R. J. Cook and H. J. Kimble [345]. As introduced previously, this simple model is based on the idea that the system undergoes fast fluorescence cycling between ground and excited states, followed by infrequent “jumps” to a non-fluorescent triplet or metastable shelf state which subsequently recovers to the ground state. A more elaborate model explaining blinking in quantum dots (QD), was subsequently (1997) developed by A. L. Efros and M. Rosen [362]. According to it, the system is thought to undergo Auger ionisation events upon excitation. Electrons can be ejected from the QD and get trapped by surrounding acceptor-like states. The electron-hole ($e-h$) pairs experience Auger-like, non-radiative relaxation to the ground state, quenching (“off” period) any emission associated to the “normal” $e-h$ pair radiative recombination (“on” period). In more detail, upon photoexcitation a few $e-h$ pairs are created in the nanocrystal. The excitation of

multiple $e-h$ pairs is possible due to the high density of excited states. However, after the first pair has been created, the system is in a charged state and the energy resulting from the recombination of any second $e-h$ pair is more efficiently transferred to the charge carrier already present in the nanocrystal, preventing its radiative recombination and therefore the photon emission. The nanocrystal regains its ability to emit photons only upon recovery of the charge neutrality. This non-radiative decay is known as Auger recombination and its rate is several orders of magnitude bigger than that of the radiative recombination, turning out to be therefore highly efficient and probable. The Coulomb interaction between the charge carriers mediates the Auger recombination and it has been proposed [363] that it might play a crucial role in determining the blinking mechanism. In fact, the observation of long on-times indicates that the ionisation of the nanocrystal core towards “distant” traps is prevented. A possible explanation is that the Coulomb interaction works as an ionisation-stopping mechanism since in a small-enough nanocrystal, once one electron has been transferred to a distant trap, another ionisation would cost more electrostatic energy than the exciting photon can provide. As a confirmation of that, electrostatic force microscopy (EFM) measurements (on CdSe nanocrystals) [364] have shown that blinking is indeed related to charge rearrangements via electron transfer and that individual nanocrystals accommodate at most one or two positive charges (holes). It could be speculated that since the Coulomb interaction is enhanced in small nanocrystals due to their reduced dimensionality, the reduced dimensionality itself is one of the reasons why blinking is ubiquitously observed across so many nanoscale systems, NV centres in ultrasmall nanodiamonds included.

The Efros-Rosen model has been extremely successful in providing an intuitive picture of blinking and despite few limitations it is still considered a benchmark in the understanding of the phenomenon. However, one of the key aspects that still limit the full comprehension is the *trapping* mechanism. A certain degree of information about the trapping mechanism can be extracted from the analysis of the statistics of the intermittency, i.e. from the probability distributions $P(t_{on})$ and $P(t_{off})$ of finding the system respectively in the “on” or “off” state. The characterisation of the on/off dynamics, is achieved by compiling histograms of the duration of the “on” and “off” events with respect to a threshold that serves to discriminate between the events (similarly to what is shown in Fig. 6.11c). In their analysis, Efros and Rosen [362] propose that the probability

densities, i.e. the histograms of the lengths, of the “on” and “off” periods follow exponential laws in contrast to other findings [365-367] which suggest that they rather follow power laws. This is crucial. In fact, an exponential decay in time of the off-time probability density $P(t_{off})$ would imply the existence of a single non-radiative decay channel, due to a single trap, with associated blinking recovery kinetics governed by a single rate constant characteristic for that channel [362, 365]. If we extend this concept, a multi-exponential probability density $P(t_{off})$ would imply the existence of multiple traps for the system with an associate finite number of decay rates per each acceptor-like state. Finally as a further extension, power law decays could be interpreted as the result of an existing distribution of acceptor-like states with an associated distribution of trapping and de-trapping rates. A sufficiently dense combination of decaying exponentials with appropriate weighting coefficients in fact, can accurately reproduce the power law behaviour in the probability density $P(t_{off})$ [366].

In the literature, most authors describe the on- and off-time probability densities $P(t)$ by power law, i.e. $P(t) \sim t^{-\alpha}$ with values for the exponent α varying between 1.1 and 2.2 and peaking at about 1.5 [368, 369].

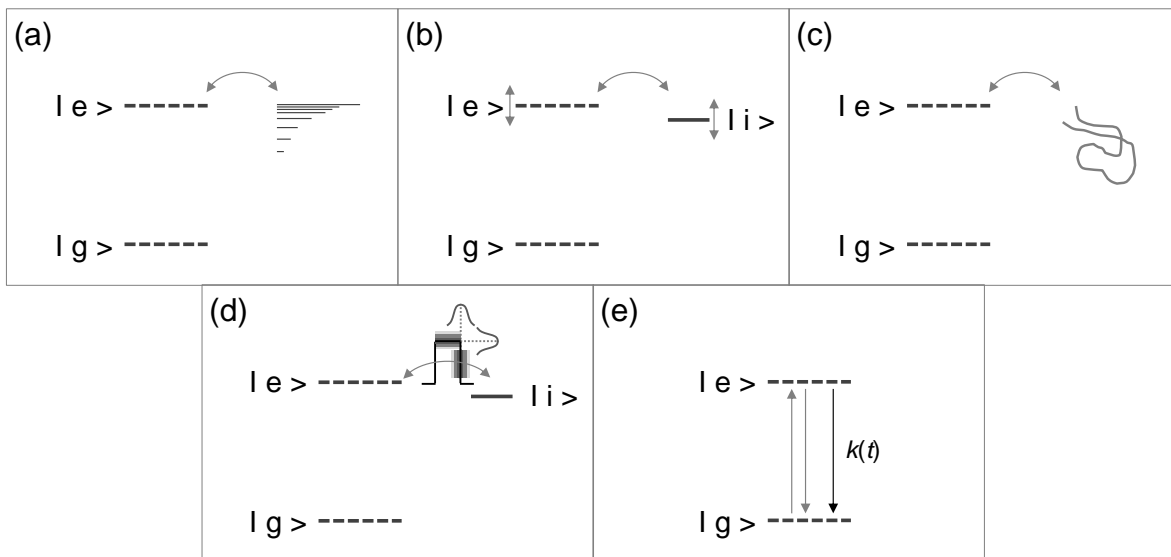


Figure 6.12. Schematic diagram of some of the proposed models explaining blinking (adapted from [370]). **a)** Blinking occurs via the electron jumping between the excited state and a uniform distribution of traps in the matrix around the nanocrystal [363]. **b)** Blinking occurs via the electron jumping between resonant excited and trap states [367]. **c)** Blinking occurs upon the electron undergoing a three-dimensional spatial diffusion before returning [371]. **d)** Blinking occurs via the electron tunnelling between the excited and the trap states through a barrier fluctuating in height and width [366]. **e)** Blinking occurs without considering long-lived trap states, the system comes back to the ground state after photoexcitation via a non-radiative channel (dark arrow) with a fluctuating decay rate $k(t)$ over long time intervals [372].

I summarise here some of the models that have been proposed to explain the power law behaviour of the probability densities $P(t)$ in blinking systems (Fig. 6.12).

R. Verberk and collaborators [363] extended the Efros-Rosen model by postulating the existence of a uniform distribution of traps in the matrix around the nanocrystal instead of a single one (Fig. 6.12a). This is associated with a distribution of trapping and de-trapping rates varying with the distance and the characteristic of the acceptor-like states, leading ultimately to a power-law off-time probability density $P(t_{off})$.

K. T. Shimizu and co-authors [367] explained blinking resorting to tunnelling of the electron when the excited state of the system and the trap energy level are resonant (Fig. 6.12b). By observing that the off-time statistics are temperature and excitation-intensity independent, they inferred that the coupling of a dark to a bright state occurs via a tunnelling process and is not photoassisted. The power-law distribution of the blinking statistics would derive from the (spectral) diffusion of the environment acceptor energy level.

J. Tang and R. A. Marcus [373], developed a similar model in which the electron transfer is as well diffusion-controlled with both the quantum dot and acceptor state energies undergoing spectral diffusion.

G. Margolin and collaborators [371] suggested a spatial diffusion mechanism to explain blinking (Fig. 16.2c). The excited electron would experience a three-dimensional diffusion in space (with a corresponding off-time) and would then come back to the quantum dot. The model predicts the power law behaviour for the off-time probability density $P(t_{off}) \sim t^{-\alpha}$ with $\alpha = 1.5$, which is generally observed experimentally in blinking QDs. The authors also suggest that blinking nanocrystals could exhibit a non-ergodic behaviour deriving from the possibility that the electron could escape indefinitely, leaving the quantum dot permanently dark.

M. Kuno and colleagues [366] analysed the possibility that blinking could involve the tunnelling of the electron from the quantum dot to a trap state through a barrier whose height and width can fluctuate (Fig. 16.2d). Such barrier fluctuations occur on a faster

timescale than that of the on/off events. This is concluded by observing that the durations of adjacent “on” (and “off”) events are uncorrelated. The model is particularly elegant. First, the mechanism based on the electron tunnelling through a fast fluctuating barrier naturally produces the power law kinetics for the blinking (note that if the fluctuations were much slower than the timescale between “on” and “off” episodes a memory effect would be expected and the blinking would show statistics with exponential rates). Second, between each off-to-on and on-to-off event the tunnelling barrier is likely to fluctuate rapidly, giving rise to a continuous distribution of trapping and de-trapping rates. This means that the model does not require the large densities of trap states that are implicitly assumed in other static models to account for the power law statistics.

P. Frantsuzov and R. A. Marcus [372] proposed an alternative model which does not assume any long-lived trap state. The system would always return back to the ground (neutral) state after photoexcitation. The on/off switching is caused by large variations of the non-radiative relaxation rate (Fig. 16.2e). Recombinations occur through the Auger-assisted excitation of surface states. Via the Auger mechanism the already photoexcited system reaches a second excited quantum dot state from which it decays non-radiatively towards the ground state. The trapping rate is governed by the spectral diffusion of such second excited state which modulates the eventual non-radiative recovery. The mechanism predicts a continuous distribution of relaxation time with subsequent power law blinking statistics.

Before our investigation on isolated 5-nm nanodiamonds, blinking has never been observed in NV centres. Therefore, even though the majority of the models presented above refer specifically to quantum dots, we used them as background premises to try addressing the same phenomenon of blinking for NV centres hosted in ultrasmall nanodiamonds.

Emission trajectories. One of the first issues we faced was the analysis of the emission trajectory, i.e. the emission intensity of the centres as a function of time. In fact, the emission trajectories of different blinking centres can be substantially dissimilar from one another. Sometimes we could clearly identify two states for the centre: “on” and “off” or

“bright” and “dark” (Fig 6.11c). But, other times the centre showed few, discrete emission “jumps” (Fig 6.13a) or even a continuous-looking distribution of them (Fig. 6.13b), indicating the possible existence of several accessible states. This is somehow consistent with what I have discussed about the blinking mechanism in other systems, where the validity of the two-state on/off model is being debated due to the observation of emission trajectories showing for instance three states [369] or a continuous distribution of states [374].

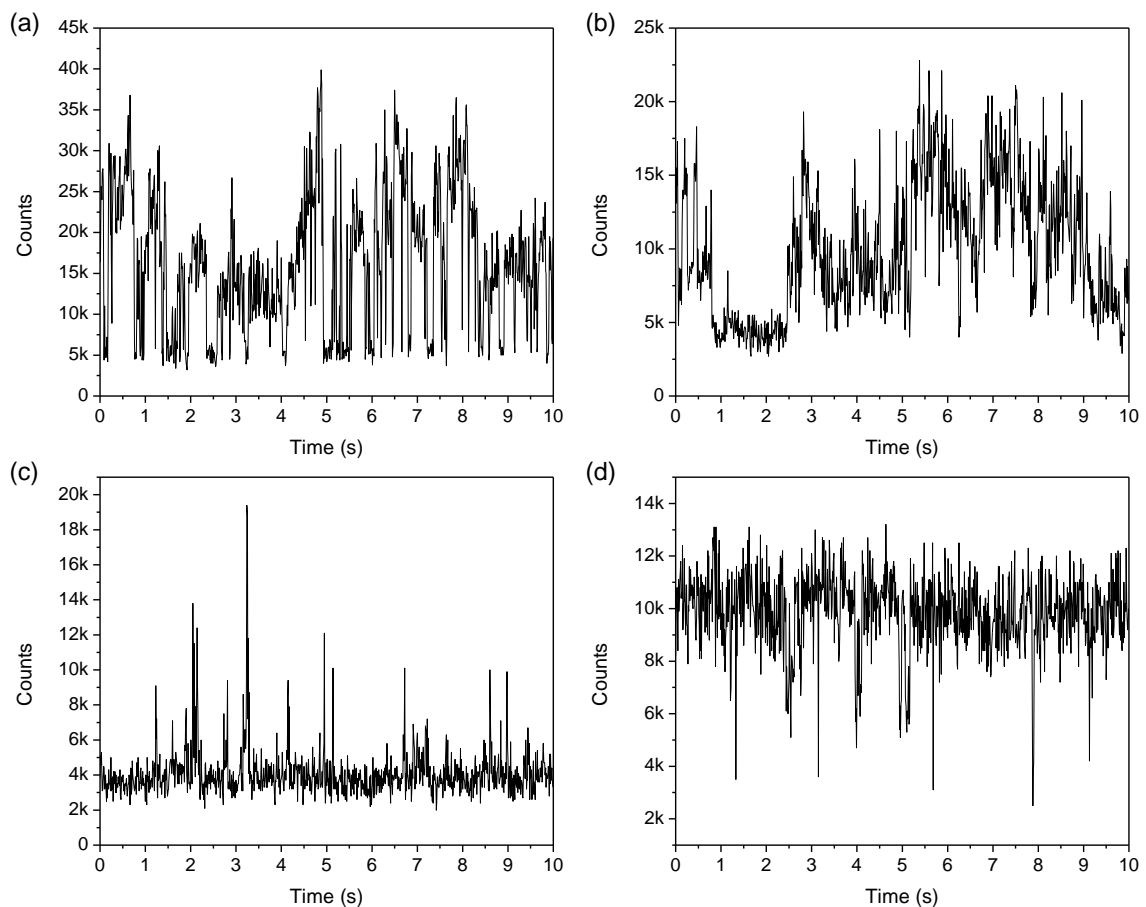


Figure 6.13. A few examples of blinking emission trajectories measured for different NV centres. **a, b, c, d)** The traces display different characteristics. In (a), the centre seems to “jump” amongst a discrete number of possible states, while in (b) it seems there is rather a continuous distribution of them; (c) and (d) highlight two opposite behaviours, respectively of a centre which is mostly “off” and only rarely switches “on” and vice versa of a centre which mostly “on” and only rarely switches “off”.

Photobleaching. We observed cases of photobleaching NV centres, i.e. the transition from a blinking behaviour to permanent darkness. In the vast majority of the cases, such photobleaching occurred within ~ 10 -200 s from the initial laser excitation (wavelength

532 nm). However, many NV centres maintained their blinking luminescence over several hours of illumination, suggesting once again that despite the “optical instability” the thermodynamic stability of the centre in ultrasmall nanodiamonds is possible. The centres resistant from photobleaching were the ones we considered in our analysis.

Photochromism. Because the “off” state of the centres was at the level of the background signal, we ruled out the possibility that blinking could be caused by photochromism, since the luminescence signature (cf. c. 2, s. 2.2.3, Fig. 2.7b) of the neutral charge state of the centre (NV^0) was never observed in the spectra. The photochromism of the NV centre consists in the conversion of the centre from the negatively (NV^-) to the neutral (NV^0) charged state and it can be induced by intense irradiation of the defect [84]. However, if photochromism was the cause of the blinking behaviour, we would expect to see in the spectrum of the blinking centres a superposition of the spectral features from both the negatively and the neutral charged state of the defect, which we did not.

Blinking statistics. Having ruled out photochromism as the mechanism for blinking, a different explanation is needed. As per any other study of blinking systems the determination of the blinking kinetics is fundamental. We studied thus the on/off statistics of a few blinking NV centres. We analysed only centres which showed blinking luminescence for several hours and in which we were clearly able to distinguish “on” and “off” states with regard to a fixed threshold. Figure 6.11c shows an example of a typical NV time trajectory we analysed. In all the centres we considered, the threshold was determined assuming the validity for blinking NV centres of a two-state, on/off model in which the photon distribution in “on” and “off” states is based on the Gaussian distribution:

$$P(N) = \frac{p_{on}}{\sqrt{2\pi}\sigma_{on}} \exp\left[-\frac{(N - \bar{N}_{on})^2}{2\sigma_{on}^2}\right] + \frac{p_{off}}{\sqrt{2\pi}\sigma_{off}} \exp\left[-\frac{(N - \bar{N}_{off})^2}{2\sigma_{off}^2}\right] \quad (6.3)$$

where \bar{N} represents the mean value of the number of photon in each on/off state, p is the population of the states, N the total number of photons and σ^2 the variance of the distribution (for a stable photoemission the variance equals the mean value). For each specific NV time trajectory, we set the threshold at the intersection of the two Gaussians in

equation (6.3), where the probabilities for N to be at the “on” and “off” levels were equal (similarly to what is shown in Fig. 6.11c, d).

In the analysis of the blinking statistics, the choice of binning time was crucial. In the NV time trace of figure 6.11c for instance, we sampled the luminescence trajectory at 4-ms time bins. The 4-ms bin width provided in this case the deepest minimum between the histograms of the “on” and “off” states occurrence fitted with the two Gaussians (Fig. 6.11d), emphasising the two-state luminescence intermittency. A 2-ms time bin sampling did not change the result, while a 1-ms bin sampling showed too much statistical noise to extract meaningful information. The choice of the binning time must be considered carefully. In the case presented, the 4-ms binning time is relatively long and, if on one hand it highlights the two-state blinking of the NV centres, on the other it ignores possible rapid events occurring at a faster timescale associated with complex dynamics. The effects of the integration time become significant when the blinking follows power law statistics. This is elegantly shown by M. Kuno and collaborators [366]. They demonstrated that experimental quantities, such as the average $\langle t_{on} \rangle$ or $\langle t_{off} \rangle$, remain explicitly dependent on the measurement time window for densities $P(t_{on})$ and $P(t_{off})$ following power law kinetics. For example, an experimentally defined average time would be given by:

$$\langle t \rangle = \frac{\int_{t_{min}}^{t_{max}} \tau P(\tau) d\tau}{\int_{t_{min}}^{t_{max}} P(\tau) d\tau} \quad (6.4)$$

where t_{min} is the minimum integration window in which “on” and “off” events are distinguishable, while t_{max} is the maximum integration window set arbitrarily or limited by experimental factors (e.g. drift of the piezo stage on which the sample is mounted). If we solve equation (6.4) with an exponential density distribution $P(t) \sim e^{-kt}$ governed by a single rate process k , k being $t_{min} < k < t_{max}$, we obtain $\langle t \rangle \approx 1/k$ independent of (t_{min}, t_{max}) . However, if we solve equation (6.4) with a power law density distribution of the type $P(t) \sim t^{-\alpha}$, we obtain $\langle t \rangle = [(\alpha-1)/(2-\alpha)]t_{max}(2-\alpha)t_{min}^{(\alpha-1)}$, which is clearly dependent on the integration windows t_{min} and t_{max} . The physical reason for this is that the number of occurrences observed for each successive ten-fold sampling time increase (decrease), goes down (up) as $\sim 10^{-(\alpha-1)}$, i.e. algebraically rather than exponentially. In other words, in power law statistics there will always be events which are too fast or too slow to be observed for any given time window.

Figure 6.14 shows the distribution of the “on” and “off” times for a representative blinking NV centre. The semi-logarithmic scale of the graph, with the curves fitting the data, highlights the exponential trends in both the “on” and “off” cases. In the blinking NV centres we studied experimentally then, the analysis of the on/off statistics seems to suggest a single relaxation path associated to the transition of the system to a single trap state.

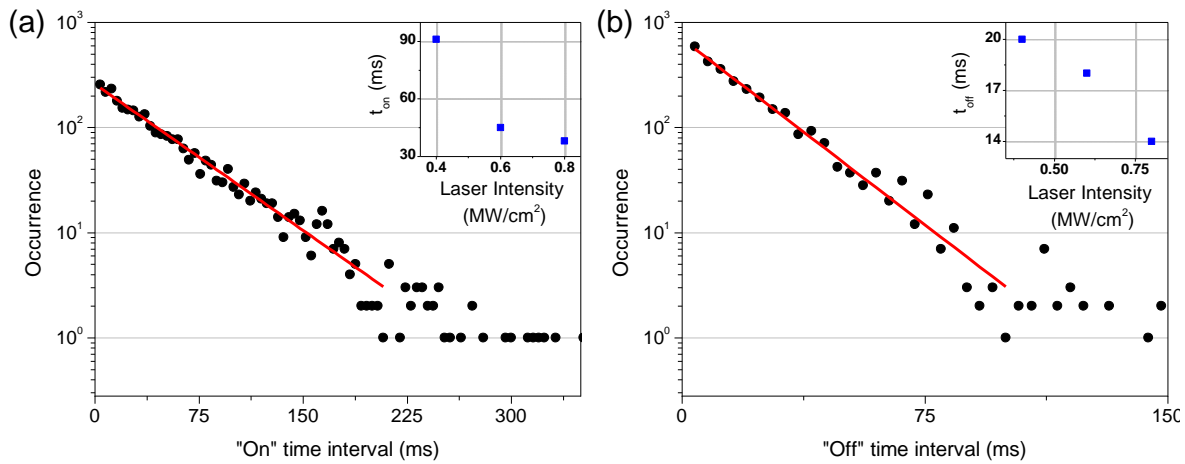


Figure 6.14. Analysis of the luminescence intermittency statistics of a typical blinking NV centre. **a)** Blinking statistics (symbols) of the “on” state on a semi-logarithmic scale, fitted by a single exponential (solid line) with time constant 45 ms. **b)** Blinking statistics (symbols) of the “off” state on a semi-logarithmic scale, fitted by a single exponential (line) with time constant 18 ms. The insets in (a) and (b) show the blinking time constant versus the excitation laser intensity (wavelength 532 nm) for the “on” and “off” states, respectively.

Excitation intensity. We also characterised the blinking phenomena as a function of the excitation intensity varying, in our confocal setup (cf. c. 4, s. 4.5), the intensity I of the excitation laser (wavelength 532 nm, spot diameter \sim 250 nm) between 0.15 MW/cm² and 0.8 MW/cm². In general, we observed that at low intensities, the NV centres we investigated tended to stay in the “on” and “off” states for longer periods of time in comparison to higher intensities where they tended to “jump” more frequently between the two states. For instance, the data of a typical blinking NV centre (Fig. 6.14a, b insets) shows that its “on” time constant t_{on} varied from 91 ms at $I = 0.8$ MW/cm² to 38 ms at $I = 0.4$ MW/cm². Similarly, but to a much lesser extent, t_{off} increased from 14 ms at $I = 0.8$ MW/cm² to 20 ms $I = 0.4$ MW/cm². This suggests that the on/off state switching in the analysed NV centres is a photoinduced process (otherwise $t_{on/off}$ would be intensity independent). Such a result is consistent with similar observations made in different

systems where an inverse proportionality dependence of t_{on} versus I has also been reported [356, 371]. In the case of t_{off} instead, the dependence on the intensity I we have found is too weak to be conclusive.

Lifetime. We also measured the emission lifetime (cf. c. 4, s. 4.5.3) of both stable and blinking NV centres in 5-nm nanodiamonds. The lifetime varied from 2 ns to 14 ns, with a mean value of ~ 5.5 ns. There was no difference in the distribution of lifetimes for stable and blinking centres.

The observation of luminescence intermittency of NV centres in ultras-small nanodiamonds is very interesting. It reinvigorates the idea that blinking is a ubiquitous phenomenon in quantum systems, regardless of their “nature”. It is encountered across a wide variety of quantum systems all sharing, as a common feature, the fact of being at the nanoscale, as the dimensionality was perhaps the key for such luminescence intermittency to happen. Our analysis revealed that for the NV centres we studied, the blinking kinetics seem to follow a single exponential decay, meaning that the electron trapping mechanism involves a single acceptor-like state with a single definite relaxation rate. In other systems, like quantum dots, the vast majority of the studies report instead power law blinking statistics. This discrepancy is still the subject of investigation and stimulates the debate about two-state versus multi-state blinking models [370]. For the sake of completeness, it must be said that the number of blinking NV centres we analysed was too small to allow firm conclusions. In fact, in the 5-nm nanodiamond sample, only $\sim 1\%$ of the total crystals were fluorescent and of these only $\sim \frac{1}{4}$ were blinking. Moreover of these blinking centres many photobleached or showed emission trajectories for which it was impossible to determine on/off thresholds for meaningful results (e.g. 6.13a, b). It could be then speculated that what we analysed was actually a subset of several other possible NV blinking kinetics. Further investigations are necessary. We still do not have a clear picture of what causes blinking in NV centres, which is not surprising considering that almost thirty years of studies on other systems have not been able to fully unravel the luminescence intermittency mechanism. This motivated further experiments on NV centres with the idea of determining which parameters are directly involved in the mechanism and which are not. In the next sections I will analyse that and I will also

present a possible model we propose to explain the blinking of NV centres in nanodiamonds.

6.3 Parameters which influence blinking in NV centres

To pinpoint the blinking mechanism in NV centres we designed and performed experiments to rule out, one by one, any parameter which did not directly contribute to blinking. The intent was to reduce the number of variables amongst which we should look to understand the origin of luminescence intermittency in NV centres.

6.3.1 Effects of the nanodiamond size on NV centres

One of the possible candidates involved in causing NV blinking is the size of the nanocrystals. We investigated this effect by using air oxidation to gradually reduce the size of nanodiamonds and monitor how the fluorescence of the hosted NV centres would change, if at all.

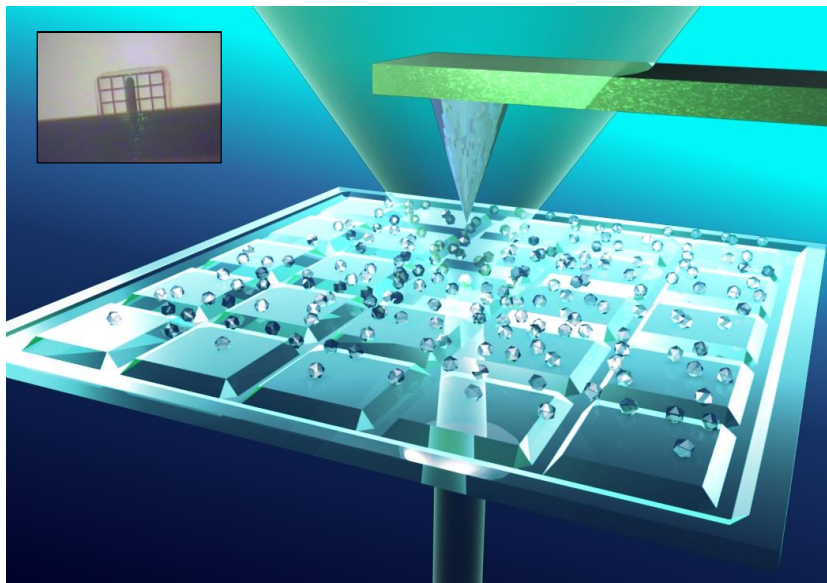


Figure 6.15. Illustration of the experimental arrangement of the sample (cf. s. 6.1.3, Fig. 6.4). The diamond nanoparticles are prepared on a substrate where a grid has been laser-scribed as a reference. The atomic force microscope (AFM) measures the size of the crystals from above and is aligned with the laser of the confocal setup from below which optically probes the NV centres. The sample is repeatedly removed to be air oxidised and perfectly realigned, using the grid, on the AFM stage. The inset shows a real photograph (top view) of the setup with the AFM tip visible above the 5×5 square grid (each square measuring $50 \times 50 \mu\text{m}^2$).

The experiment we conducted is the one I have described above in section 6.1.3, but in this case, the measurement of the size of the crystals is integrated with their optical

characterisation. Briefly, the nanodiamonds were dispersed on a cover slip where a reference grid had been previously laser-scribed; the size and fluorescence of a number of selected crystals were measured with the combined confocal-AFM setup (cf. c. 4, s. 4.5); the sample was then oxidised in air in consecutive steps, under controlled temperature and time. After each of these steps, the size and fluorescence of the same selected diamonds were remeasured to identify possible changes. Figure 6.15 shows the experimental arrangement of the sample, which is the same depicted in figure 6.4. Here, the laser of the confocal system exciting the target nanocrystals is shown from below to address the change of their fluorescence behaviour as a function of the gradual nanodiamond size reduction.

We carried out the experiment on a sample of high pressure high temperature (HPHT) monocrystalline diamond powder (Microdiamant, MSY 0-0.1 μm). The use of HPHT, as opposed to detonation nanodiamonds, helped to rule out whether the process used to synthesise nanodiamonds is involved in determining the fluorescence intermittency.

We analysed the material in consecutive steps as described below.

Step 0. The as-received nanodiamond material, consisting of unprocessed nanodiamonds from the supplier.

Step 1. The nanodiamond material, from step 0, purified via the acid-treatment process described above (cf. s. 6.1.2) to remove the lax amorphous, graphitic (sp^2) carbon phases.

Step 2. The nanodiamond material, from step 1, oxidised in air for 2.5 h at 600 °C. This first oxidation step removes from the nanocrystals mainly water, physisorbed organic and non-carbon impurities, tight amorphous carbon phases (sp^2) and potentially the most outer layers of the nanoparticles diamond core (sp^3).

Step 3 et seq. The nanodiamond material from, step 2, further oxidised in air via consecutive steps each of 30 min at 600 °C. At this stage, the diamond core (sp^3) of the nanocrystals is exposed and any thermal oxidation step after the 3rd removes more and more of the outer diamond layers, etching the crystals and reducing their size (cf. s. 6.1.3). This is probably the most interesting part of the characterisation since we can determine whether or not the optical behaviour of the NV centres change as the diamond material surrounding the centres is etched away.

Before giving the results of the step-treatment characterisation, I introduce the following definitions:

$$\begin{cases} \eta_{em} = N_{NV} / N_{ND} \\ \eta_{blink} = N_{blink} / N_{NV} \end{cases} \quad (6.5)$$

where N_{ND} is the total number of nanodiamonds, N_{NV} is the number of fluorescing nanodiamonds hosting (negatively charged) NV centres and N_{blink} is the number of nanodiamonds hosting blinking NV centres.

For the as-received step 0-material, on the areas scanned with the combined confocal-AFM system, we identified over 20400 diamond nanocrystals of which 428 (i.e. $\eta_{em} \sim 2\%$) were fluorescing. Out of these 428 fluorescing NDs, 3 centres (i.e. $\eta_{blink} \sim 0.7\%$) were blinking.

For the acid-treated step 1-material, we analysed ~ 7000 diamond nanocrystals of which 561 (i.e. $\eta_{em} \sim 8\%$) were fluorescing. Out of these 561 fluorescing NDs, 5 centres (i.e. $\eta_{blink} \sim 1\%$) were blinking.

From these measurements we can already draw two interesting conclusions. First, the removal from the as-received nanodiamonds of the lax amorphous graphitic (sp^2) carbon phase (see Raman spectrum, cf. s. 6.1.3, Fig. 6.6a) via the acid-treatment seems to activate somehow NV centres which are quiescent in the raw material. In fact from the step 0- to the step 1-material η_{em} increases significantly from $\sim 2\%$ to $\sim 8\%$. Second, blinking NV centres are observable in HPHT nanodiamonds (therefore independently of the process utilised to synthesise the diamond material) and, even more interestingly, independently of the size of the hosting nanodiamonds. In fact, between the step 0- and step 1-materials, we identified overall 8 blinking NV centres and these were hosted in nanocrystals whose size, measured with the AFM, varied on a relatively large range from 18 nm for the smallest crystal to 86 nm for the largest.

For the step 2-, and 3 and seq.-materials we studied different sets of samples identifying overall more than 44000 crystals of which over 3500 ($\eta_{em} \sim 8\%$) were fluorescing. Clearly, from step 1 to step 2, the removal of the tight amorphous (sp^2) carbon phase due to air oxidation did not change the ratio η_{em} of fluorescent nanodiamond to the total number of nanocrystals ($\eta_{em} \sim 8\%$ both for the step 1- and step 2-material). However, we observed a significant change in η_{blink} . We analysed in detail more than 400 fluorescing nanodiamonds over several samples and oxidation steps and found consistently that the ratio η_{blink} of

blinking NV centres to the number of fluorescing nanodiamonds varied on average between 6% and 15%, which is much greater than $\eta_{blink} \sim 1\%$ measured for the step 1-material. Again, we found blinking NV centres hosted in relatively large nanodiamonds, up to 100 nm in size. Figure 6.16 shows the histograms of the size distribution of nanodiamonds hosting stable and blinking NV centres (the data is a collection gathered over several samples and different step-materials, all shown together in the same graph).

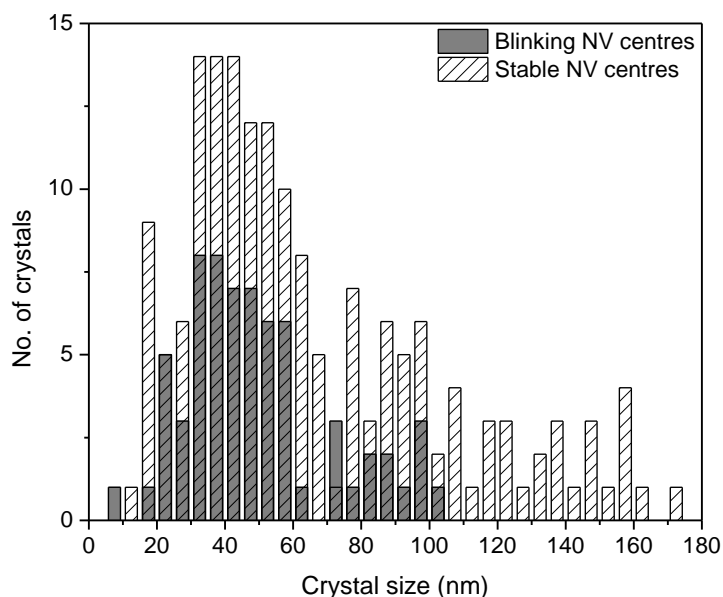


Figure 6.16. Histograms of the size distribution of nanodiamonds containing stable (hatched) and blinking (grey) NV centres. The histograms collect data from several samples and different step-materials, all represented together in the same graph. Note how blinking NV centres can be observed in relatively large nanocrystals, even up to 100 nm in size.

A complete summary of the nanodiamond size and corresponding NV optical properties through the progressive step-treatment is shown in table 6.1.

The observation of blinking NV centres in relatively large nanodiamonds, up to 100 nm in size is notable because it suggests that the nanocrystal size itself is not the key factor in the fluorescence intermittency mechanism. We thus focused our attention on other possibilities.

Although this is the first report of blinking in NV centres, the almost thirty years of study of the fluorescence intermittency in other system such as quantum dots (cf. s. 6.2.2) provides us a useful guideline. Full understanding of the blinking phenomenon is still forthcoming, but what we know for certain is that for the blinking to occur there must be

a trapping mechanism that “subtracts” one (or more) electron(s) from the NV centre making it “dark” on a time scale of ~ ms-s. It could be speculated that what causes NV centres to blink might be the proximity of the NV centre to the surface rather than the actual size of the nanodiamond. At the surface, a few factors could affect the NV photoluminescence. For instance at the surface, the nanodiamond is more prone to structural rearrangements driven by the minimisation of the crystal energy (cf. c. 5, s. 5.2) and this can lead to an increased probability of formation of traps and acceptor-like states. Also, the chemistry of the surface with the presence of chemicals that are electron acceptors or donors can affect the NV centre if this is close enough to the boundary to experience such effects. Finally, the interaction at the interface between the nanodiamonds and the substrate could be another factor to take into account (note that other than the substrate it could even be the interface between the diamond and the air or any substance surrounding the nanodiamond). For instance, the relative position of the diamond energy bands to those of the interface substance could produce band shifts with respect to which the electron transfer towards acceptor-like states is favoured (or disfavoured). All these scenarios seem reasonable, but more evidence is needed.

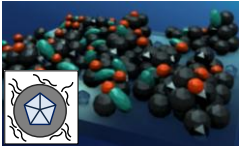
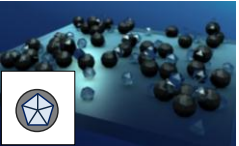
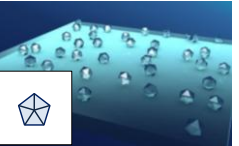
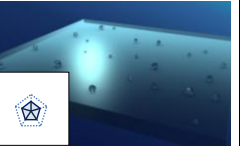
Table 6.1 – NV-ND fluorescence-size analysis through step-treatment				
Progressive treatment	Step 0: as-received	Step 1: acid-cleaning	Step 2: air oxidation	Step 3 et seq.: air oxidation
Sample composition	water, physisorbed impurities, lax & tight amorphous carbon (sp^2), ND-core (sp^3)	traces of tight amorphous carbon and graphitic (sp^2) shell, ND-core (sp^3)	ND-core (sp^3)	reduced ND-core (sp^3)
Sample schematic view				
η_{em}	~ 2%	~ 8%	~ 8%	~ 8%
η_{blink}	< 1%	~ 1%	~ 10%	~ 10%

Table 6.1. Analysis of the NV centres fluorescence after progressive step-treatment of the hosting nanodiamonds. The sample composition and the fluorescence of the NV centres are different at each progressive step. The quantity $\eta_{em} = N_{NV}/N_{ND}$ is the ratio between the number of fluorescent nanodiamonds due to NV emitters (N_{NV}) and the total number of nanocrystals (N_{ND}). The quantity $\eta_{blink} = N_{blink}/N_{NV}$ is the ratio between the number of blinking centre (N_{blink}) and the number of fluorescent nanodiamonds (N_{NV}).

6.3.2 Effects of the nanodiamond surface on NV centres

Having ruled out the direct involvement of the nanodiamond size, we focused on surface proximity.

We investigated that by performing size-reduction of nanodiamonds via thermal oxidation in air (cf. s. 6.1.3). As the oxidative etching of diamond progressed, we monitored carefully the size and the optical behaviour of selected nanocrystals to address their evolution. The starting material was the step 2-material, consisting of HPHT nanodiamonds acid-cleaned, dispersed on a cover slip (having the laser-scribed grid for reference) and then subjected to a first air oxidation step for 2.5 h at 600 °C. This was done to assure that both the lax and tight amorphous, graphitic (sp^2) carbon phase had been removed from the nanodiamonds. We kept track of the optical and size evolution of the target nanodiamonds over seven consecutive air oxidation steps each for 30 min at 600 °C.

Table 6.2 – ND/NV-size/fluorescence evolution through progressive oxidative etching					
Centre No.	Size (nm) after 2.5 h, 600 °C	Size (nm) after 3 h, 600 °C	Size (nm) after 3.5 h, 600 °C	Size (nm) after 4 h, 600 °C	Size (nm) after 4.5 h, 600 °C
1	74.9	64.0	44.4	44.1	43.3
2	39.3	35.9	35.8	33.5	30.5
3	115.2	103.3	98.7	71.4	67.8
4	39.0	27.0	21.9	19.4	14.1
5	78.0	70.5	61.4	57.4	57.1
6	63.1	59.3	56.1	48.5	43.2
7	78.7	60.2	56.0	52.4	48.6
8	38.8	32.3	31.6	27.2	21.7
9	24.3	17.0	8.3	-	-
10	50.2	49.3	45.9	38.7	34.1

Table 6.2. Evolution of the nanodiamonds (NDs) size and NV fluorescence through progressive oxidative etching. The size (nm) of the very same NDs, measured with the AFM after every air-oxidation step, is reported in the columns as numbers. The colour coding conveys instead the information about the photoluminescence of the hosted NV centres: green stands for stable emitting NV, yellow for blinking and red for annihilated NV. Analysing the table by lines clearly shows that consistently, as each nanodiamond gets gradually etched, the hosting single NV centre passes from being stable (green) to blink (yellow) and eventually to annihilate (red) at the surface, while the hosting nanodiamond is still detectable by AFM. For demonstrative purposes, the data shown in the table refers to only 10 of the total 32 centres analysed and over 5 of the 7 oxidation steps actually performed.

What we observed during the progressive oxidative etching of the same nanodiamonds was that, *consistently*, the stable emitting NV centres after a certain number of oxidation

steps started blinking and after another certain number of oxidation steps eventually disappeared, while their respective hosting nanodiamonds remained detectable by atomic force microscopy (AFM). This evolution was observed over 30 single NV centres. Some of the results are summarised in table 6.2 and figure 6.17.

As the oxidative etching of the nanodiamonds progressed, the evolution of the hosted NV centres fluorescence from “stable”, through “blinking”, to “annihilated” was systematic. Our interpretation is that as the outer diamond layers of the crystal etch, the NV centre, initially stable within the core of the nanodiamond, becomes exposed to the surface and becomes susceptible to electron(s)-trapping mechanisms thus giving rise to blinking. Eventually, as the diamond size decreases, the NV centre becomes too close to the surface to be energetically stable and the vacancy annihilates; the defect ceases to exist, but the hosting nanocrystal is still there and can be measured with the atomic force microscope (Fig. 6.17).

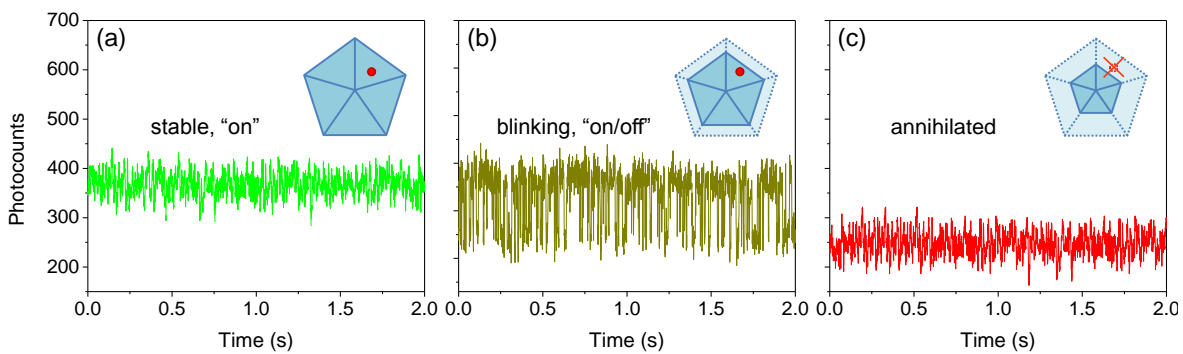


Figure 6.17. Evolution of emission trajectories for a representative NV centre through progressive oxidative etching. **a)** The NV centre, within the nanodiamond core, shows a stable luminescence. **b)** After the etching of outer diamond layers due to air oxidation the same NV starts blinking. **c)** Further etching of the nanodiamond leads to the annihilation of the NV centre, while the hosting nanocrystal is still detectable by AFM. The cartoon shows our interpretation of the location of the NV centre (red dot) with respect to the hosting nanodiamond during the progressive air oxidation steps.

To verify this hypothesis we estimated quantitatively the physical location of the blinking NV centres with respect to the surface of the hosting nanodiamonds. During the progressive oxidative treatment, we monitored each NV centre from stable, through blinking to annihilated, recording the size of the nanodiamonds. At each oxidation step, we also measured how many and which NV centres remained blinking and which went instead from blinking to annihilated. We then built a histogram of the statistic (Fig. 6.18).

The histogram clearly shows that already after the second oxidative step more than 50% of the blinking centres (17 out of 32) were annihilated and after the third step 75% (24 out of 32) have disappeared. Based on this statistical analysis we estimate that the blinking NV centres are located within ~ 5-8 nm from the surface, as explained below.

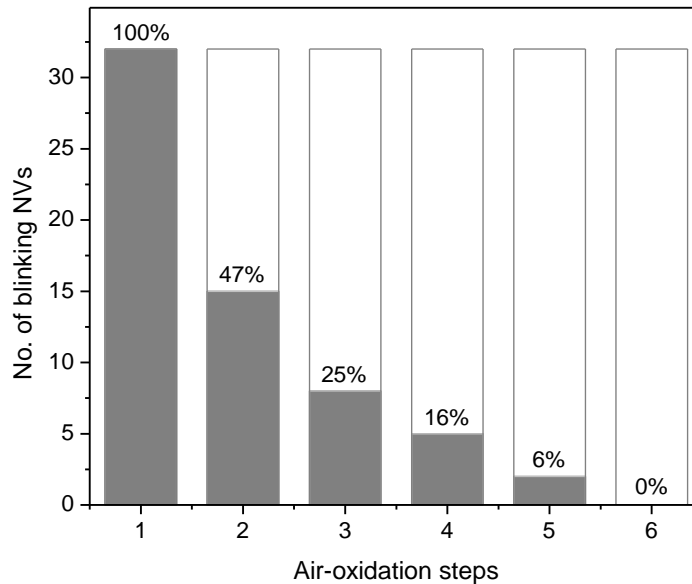


Figure 6.18. Histogram of the number of blinking centres at each air oxidation step. The histogram shows that already after the second oxidative step more than 50% of the blinking NV centres (17 out of 32) have annihilated and after the third step 75% (24 out of 32) have disappeared. This locates the blinking NV centres within ~ 5-8 nm from the surface (see text).

Our estimation of the proximity of blinking NV centres to the surface is based on a few assumptions and simplifications which are made necessary by intrinsic and experimental limitations in the measurement. Due to the anisotropy of diamond, the oxidative etching of the nanocrystals is orientation dependent with different rates for different diamond crystallographic planes and directions (cf. s. 6.1.3). This is an intrinsic limitation since we have no control over the orientation of the nanocrystals relative to the substrate and the NV could be placed anywhere along any of the crystallographic directions. Experimentally, we are also limited by the fact that the AFM is able to measure with high resolution (± 0.7 nm) only the height of the nanodiamonds along the z-axis: this is the only quantity we can determine precisely. Based on these considerations, in our model we assume for simplicity that the nanodiamonds are spherical and have an isotropic etching rate uniform in every direction. With reference to figure 6.19, the nanodiamond is etched progressively, step-wise from i , through j , through k and to a terminal NV centre

annihilation state l . After each air oxidation step, a diamond layer of thickness $\Delta h/2$ is etched from the nanocrystal, being Δh the difference between the heights h_{index} (e.g. h_i-h_j) measured by AFM before and after the oxidation, respectively. In our experimental conditions (air oxidation for 30 min at 600 °C), the measured average value of Δh is (5 ± 0.5) nm per step (cf. s. 6.1.3), which means that the distance d between the NV centre and the nearest surface is reduced by $\Delta d \sim 2.5$ nm after each oxidation treatment. The statistical analysis (Fig. 6.18) shows that the majority of blinking NV centres annihilated after 2-3 consecutive oxidation steps, which locates them within $\sim 5-7.5$ nm (i.e. $2\Delta d, 3\Delta d$) from the nearest surface, on the basis of the measured etching rate. The uncertainty on this value is given, as mentioned before, by the possible anisotropy in the etching rates of the diamond. Quantitatively, the size reduction measured with the AFM can vary significantly from crystal to crystal. However, the etching rate of (10 ± 1) nm/h (cf. s. 6.1.3) has been measured on a large population of 200 nanodiamonds and gives a relative error of $\sim 10\%$. We can therefore reasonably assume that the same relative error applies to the estimation of the blinking NV centres distance from the nanodiamond surface (see also next section 6.3.3, for the estimated NV-to-substrate distance).

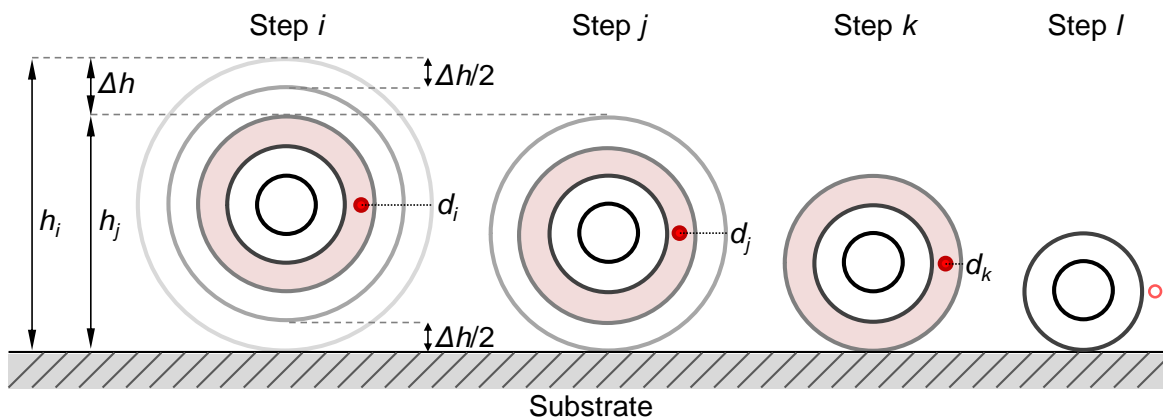


Fig. 6.19. Model for estimating the distance of blinking NV centres from the nanodiamond surface. For simplicity the nanodiamonds are assumed spherical with isotropic etching rate in all directions. After a single oxidation step, progressing $i \rightarrow j \rightarrow k \rightarrow l$, a diamond layer of thickness $\Delta h/2$ is removed from the nanocrystal, Δh being the difference between the heights h_{index} (e.g. h_i-h_j) measured by AFM before and after the oxidation. For air oxidation steps of 30 min at 600 °C, the measured average value of Δh is (5 ± 0.5) nm per step; therefore the distance d between the NV centre (red dot) and the nearest surface is reduced by $\Delta d \sim 2.5$ nm after each oxidation treatment.

The estimation of the blinking NV centres proximity to the surface in the range $\sim 5-8$ nm is consistent with the blinking model for quantum dots (QDs) proposed by M. Kuno and

collaborators [375]. According to this model, the blinking mechanism would be dominated by direct electron tunnelling towards and from trap states, where such traps have to be at distances at least of the order of $\sim 1\text{-}2$ nm, located for instance in the surrounding substrate. In fact, acceptor-like states physically positioned much closer to the emitter would have tunnelling rates $\sim 10^{-7}\text{-}10^{-8}$ s, which are almost of the same order of the emitter lifetime $\sim 10^{-9}$ s and would therefore influence its emission quantum yield rather than causing fluorescence intermittency at the $\sim 10^{-3}\text{-}10^{-4}$ s time scale. Our experiment gives an even deeper insight. In a QD in fact the origin and position of the traps could be the subject of debate. A QD is a complex structure, imagine for instance a QD consisting of a CdSe core within a Zn shell with surface passivated by organic ligands such as tri-*n*-octylphosphine oxide (TOPO) and placed on a fused silica substrate. Potentially, traps causing blinking could originate anywhere: at each one of these interfaces or, as M. Kuno and colleagues suggested [375], even outside the QD, in the substrate. Such a numerous variety of possibilities makes the understanding of the phenomenon quite complicated. However, the experiment we conducted suggests that in the specific case of the NV centre the origin of the trapping mechanism causing blinking has to be *external*. The fact that the very same NV centres turn from being *not* blinking when surrounded by a thicker diamond layer to blinking when close to the surface, proves that it is at the surface of the nanodiamond that trap states are provided. What still needs to be understood however, is the nature of these traps; whether they “belong” to the nanodiamond as a consequence, for instance, of surface crystallographic rearrangements, whether they originate because of the chemistry at the interface or whether they are located externally, for example in the substrate on which the nanodiamonds are dispersed. I will address this problem in the next section.

6.3.3. Effects of the nanodiamond surrounding environment on NV centres

The dependence of blinking on the proximity of the NV centre to the surface of the nanodiamond suggests an interpretation of the mechanism in terms of charge separation and recombination occurring at the surface itself. More specifically, upon photoexcitation of the NV centre, an electron-hole (*e-h*) pair is formed and in addition to the “normal” radiative recombination accompanied by the emission of a photon (and in addition to the non-radiative phonon-mediated processes), the system would gain an alternative path of

“decaying”. This would involve the capture of the electron (or the hole) by an external trap located at the nanodiamond surface or in the adjacent medium. The emission would be interrupted (blinking off-time) until the release of the electron from the trap back to the NV centre, or its replacement with a donor electron from somewhere else (e.g. a neighbour nitrogen atom), which would restore the luminescence (blinking on-time) until the next capture occurs. In this scheme though, what is unclear is the actual *nature* of the trap reservoir. We tried to address this issue by setting other experiments involving changing the substrate, the media surrounding the nanodiamonds and the surface groups.

Substrate. Step 2-nanodiamonds were analysed in three different scenarios: i) dispersed on a substrate of borosilicate glass (BK7), ii) dispersed on a substrate of silica and iii) aggregated with other nanodiamonds in clusters, over a borosilicate glass (BK7) substrate. The result was immediately evident. While the BK7 substrate promoted blinking ($\eta^{blink} \sim 6-15\%$), the silica one inhibited it ($\eta^{blink} < 1\%$). Plus, the blinking of NV centres was also inhibited in nanodiamond clusters ($\eta^{blink} < 1\%$) regardless of the substrate.

This observation about the influence of the substrate, together with the previously established requirement for the NV to be close to the ND surface to exhibit blinking, led us to the following model to explain the luminescence intermittency of NV centres in nanodiamonds. As briefly anticipated at the end of the previous section (cf. s. 6.3.2), the photoexcited electron of an NV would tunnel to an electron acceptor trap located in the adjacent substrate. For the tunnelling to take place two conditions have to be satisfied.

- 1) The physical distance between the acceptor-like state and the NV centre has to be only a few nm, as it has also been reported for blinking quantum dots [368, 375].
- 2) The energy levels of the participating quantum systems (the NV and the medium) must be close [375].

The first requirement is justified by our observation that NV centres, initially stable within the core of the nanodiamonds, start blinking when the outer layers of the particles get etched away and leave the centre exposed to the surface (within $\sim 5-8$ nm from it, as per our estimation).

The second requirement is deduced by examining the energy level structure of the NV in surface-oxidised (C-O) NDs in relation to that of the two substrates utilised (Fig. 6.20).

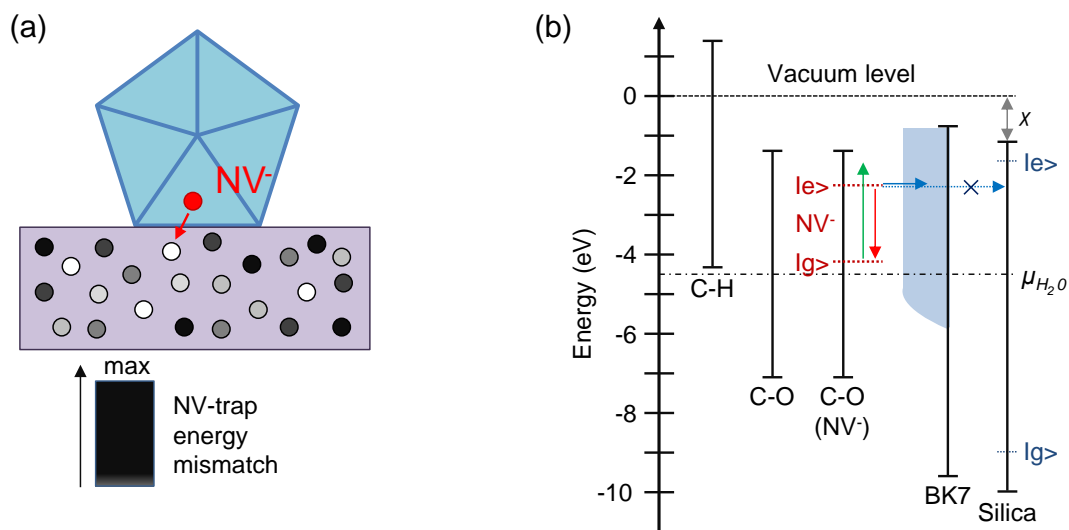


Figure 6.20. Representation of the conditions required for the NV centre to blink, upon tunnelling of the photoexcited electron. **a)** Schematic view: the photoexcited electron from an NV (red dot) can tunnel (red arrow) to an acceptor-like state (greyscale dots) only if the requirements of physical proximity and small energy mismatch (in the scale, white = equal match) are satisfied. **b)** Energy levels of the quantum systems with respect to the vacuum energy level as inferred from the electron affinity (χ) data for silica, BK7 [376] and nanodiamond [310, 377]. The bandgap and the defect centre ground ($|g\rangle$) and excited ($|e\rangle$) states for silica and (NV)-diamond are adapted from [378] and [377], respectively. The shaded area plot at BK7 represents the defect-populated absorption band we measured. The electrochemical potential ($\mu_{\text{H}_2\text{O}}$) of pure water is shown. The oxygen- and hydrogen-ND surface moieties are indicated as C-O and C-H respectively.

The borosilicate glass (BK7) is a heavy-doped derivative of the silica (vitreous SiO_2). The pure silica has a wide band gap of ~ 9 eV and it is scarcely populated by defects whose typical ground and excited states ($|g\rangle$ and $|e\rangle$, respectively in Fig. 6.20) yield an absorption peak at 7.4 eV [378]. Oppositely, the BK7 bandgap is heavily populated by defects which leave an unoccupied band that we measured being ~ 4 eV (shaded area at BK7 in Fig. 6.20). Therefore, the BK7 substrate provides acceptor-like energy levels for the tunnelling of the NV photoexcited electron, while the silica substrate does not. This is consistent with our experimental observation about the substrates promoting (BK7) or inhibiting (silica) the blinking of NV centres in nanodiamonds.

In this perspective, we can also interpret the fact that we could not observe blinking ($\eta_{\text{blink}} < 1\%$) for aggregates of nanodiamonds, despite them being on a BK7 substrate. The nanodiamond aggregates received the same step 2-treatment as the isolated nanocrystals. There is thus no reason to believe there were differences in the material other than the

clustered appearance. The crystals were simply dispersed on the substrate from a solution of NDs in water higher in concentration, which led to crystal aggregation; the diamonds were then oxidised (2.5 h, 600 °C) as per the usual treatment. Nevertheless, a lower percentage of NV blinkers was observed in ND aggregates. The most reasonable conclusion is that in ND clusters, those crystals for which air oxidation made the NV centres close enough to the nanocrystal surface to potentially experience blinking, are also the ones which do not have access to the adjacent substrate (were the electron traps, necessary for the fluorescence intermittency, are). In fact, for the etching of diamond by air oxidation to be effective, the nanocrystals have to be exposed to the oxygen so that the carbon from the nanodiamond can bind with the oxygen in the air, form carbon monoxide/dioxide (CO/CO₂) and etch away from the surface (cf. s. 6.1.3). However, the NDs which are more likely to be exposed to the oxygen and subsequently have the hosted NVs closer to the surface are located further away from the substrate, on the outer regions of the aggregates, unable to access the substrate traps. These considerations have two main implications. First, the trap states have to be of *external* origin: in fact, if they were “diamond” traps formed for instance, as a consequence of the relaxation-reconstruction of the nanodiamond surface, we should not measure any difference in the number of blinking NV centres between the isolated and the clustered diamond crystals on the same BK7 substrate. Second, it seems indeed the interaction with the substrate, which provides the acceptor-like state for the NV photoexcited electron, to be fundamental for the centres to blink.

With this new insight, we need to reconsider the estimate we made regarding the distance the NV centres have to be from the surface to experience blinking (cf. s. 6.3.2). In fact, rather than generically considering the distance of the NV from the nearest surface, we need to specifically consider its distance from the substrate. The arguments we made in the previous section still hold, but the value of the NV surface/substrate proximity of ~ 5-8 nm is likely to be affected by a larger uncertainty. We refer again to figure 6.19. From the way our measurement is done, we can determine precisely the distance of the NV centre from the nearest surface, but not how far it actually is from the substrate. The NV can in fact, be located anywhere in the ~ 2.5-nm layer indicated by the shaded area in figure 6.19. To put an upper limit to the distance an NV centre could be from the substrate to experience blinking, we concentrated on the smallest nanodiamonds. The smaller volume

naturally reduces the number of possible positions the NV centre can occupy within the particle and consequently reduces the uncertainty on the NV-substrate distance we want to estimate. In the progressive oxidative analysis, the smallest blinking nanocrystal we measured by AFM was 13 nm in height when the hosted NV centre annihilated. If we refer to figure 6.19, this means that in the worst case scenario when the NV was still active and blinking it was, at maximum, ~ 13 nm away from the substrate (assuming it was in the top region of the nanodiamond, the farthest away from the substrate). At the previous oxidation step, when the centre was active and blinking the height of the hosting nanodiamond we measured by AFM was 18 nm, which locates the NV centre, again at maximum, ~ 15.5 nm [= $(13 + \Delta h/2)$ nm, being $\Delta h = (18-13)$ nm] from the substrate. In the oxidation step previous to that, the NV centre was optically stable; the measured height of the crystal was 19 nm which locates the NV ~ 18.5 nm [= $(18 + \Delta h/2)$ nm, being $\Delta h = (19-18)$ nm] from the substrate. This means that the NV centre had to be, at most, somewhere between 15.5 nm and 18.5 nm from the substrate when it started exhibiting the blinking behaviour. Repeating this very same analysis for another six centres with measured heights within 13-19 nm (when the hosted NV centre annihilated), set the average upper limit of the NV-to-substrate distance to $\sim (22 \pm 3)$ nm. We take this value as the maximum upper limit. Any distance larger than that would most probably block the tunnelling of the photoexcited electron from the NV towards the acceptor states in the substrate, preventing the centre from exhibiting fluorescence intermittency.

Surrounding media. To further investigate the origin of the blinking mechanism we set up additional experiments. We considered several samples of isolated, step 2-nanodiamonds on BK7 substrate with measured values for $\eta^{blink} \sim 6-15\%$. We then dropped on top of the nanodiamonds: water, oil and a 0.25% solution of polyvinyl alcohol (PVA) in de-ionised water. No apparent changes in η^{blink} were measured. These experimental results further pointed to the proximity of the NV centre to an electron acceptor reservoir provided by the substrate as the key factor for the blinking phenomenon to occur. The blinking instead appears insensitive to a chemically inert environment like the one provided by the tested water, oil and PVA films. However, the result was completely different when the nanodiamond surface was functionalised with chemically-active moieties, as explained below.

Surface groups. As an additional test, we investigated the effects of chemically-active moieties at the nanodiamond surface on the NV fluorescence. We prepared a sample of step 2-nanodiamond on a BK7 substrate which had been previously laser-scribed with a reference grid. On a square of $50 \times 50 \mu\text{m}^2$, we identified ~ 3600 crystals of which 224 showed NV centre fluorescence ($\eta_{em} \sim 6\%$); of these 224, 15 were blinking ($\eta_{blink} \sim 7\%$). The nanodiamonds were then hydrogen-terminated in a plasma reactor for 5 min, at 25 mbar and $450 \text{ }^\circ\text{C}$; the very same $50 \times 50 \mu\text{m}^2$ square area of the sample was imaged again. The effect of the hydrogenation was evident. The number of emitters in the hydrogen-terminated sample diminished almost ten-fold in comparison with the original oxygen-terminated as shown in the confocal scans of figure 6.21 (overall, after H-termination only 33 centres out of the starting 224 were still fluorescing). An atomic force microscope (AFM) scan of the sample before and after the plasma treatment confirmed that the diamond crystals were left unmodified in position and size: the hydrogenation simply “switched off” the optical activity of the NV centres.

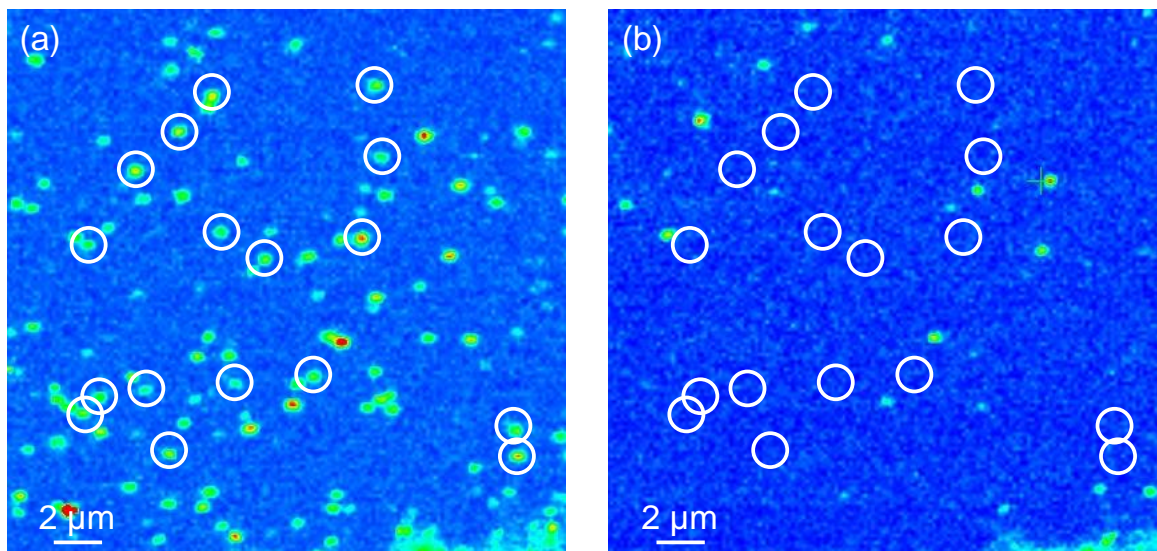


Figure 6.21. Effects of surface hydrogenation on fluorescent nanodiamonds. **a)** Confocal image of step 2-NDs on a BK7 substrate; the spots indicate fluorescence from NV centres. **b)** Confocal image of the same sample area in (a) after the NDs were hydrogen-terminated in a plasma reactor for 5 min, at 25 mbar and $450 \text{ }^\circ\text{C}$. The number of emitters after the hydrogen termination decreased almost ten-fold.

The striking reduction in the NV emission is explained in terms of charge transfer. The hydrogenation mediated by a layer of adsorbed water from the air would remove electrons from the NV centres which would no longer emit. It is known that the hydrogen

termination of the diamond surface results in the accumulation of holes [379]. The C-H bonds induce an effective surface dipole moment, which shifts the conduction and valence bands upward and leads to a negative electron affinity [380] (Fig. 6.20b). In contact with air, adsorbates form at the diamond surface and provide energy levels which serve as acceptor states for electrons from the diamond valence band and from defects, such as the NV centre, in the band gap. The energy increase of the valence band edge in comparison to the electrochemical potential $\mu_{\text{H}_2\text{O}}$ of water, drives electrons from several nm of the ND surface to the adsorbate layer, until the Fermi level E_F in the diamond equilibrates the electrochemical potential [377]. This leads to a band bending at the diamond surface with subsequent accumulation of holes and electron-depletion of NV centres. The NVs are brought thus to an “unknown” (positively charged) and no longer fluorescing state. This was beautifully demonstrated by M. V. Hauf and collaborators [310] and is confirmed in our experiment where the hydrogenation of the nanodiamond surface “switches off” a significant number of NV⁻ centres. After H-termination neither NV⁻ nor NV⁰ were observed suggesting that the NV centres went to the above mentioned “unknown” dark state.

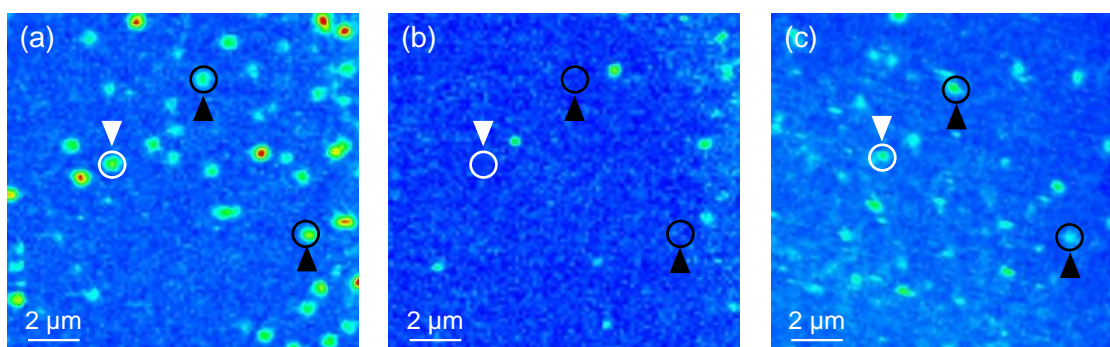


Figure 6.22. Effects of surface hydrogenation and subsequent air oxidation on fluorescent nanodiamonds. **a)** Confocal image of step 2-nanodiamonds on a BK7 substrate, showing emission from NV⁻ centres; the black upward arrowheads show two stable emitters for reference, while the white downward arrowhead highlights a blinking NV⁻ centre. **b)** Confocal image of the same sample area in (a) after hydrogen termination of the nanodiamonds in a plasma reactor for 5 min, at 25 mbar and 450 °C; ~ 85% of the centres (191 out of 224) went into an “unknown” dark state and stopped fluorescing. **c)** Confocal image of the same sample area in (a) and (b) after a subsequent air oxidation step at lower temperature (1 h, 500 °C); the majority of the NV centres (195 out of 224, ~ 87%) including blinking emitters were restored.

A further corroboration of this idea comes from the fact that, in our experiment, a subsequent air oxidation treatment at a lower temperature (1 h, at 500 °C), to not etch the

diamond, resulted in an impressive recovery of the NV centres emission ($\sim 87\%$) including the recovery of blinking NV centres, with a total of 195 fluorescing centres restored out of the original 224 (Fig. 6.22). In other words, the removal of hydrogen from the surface re-established the charge state and fluorescence of the NV⁻ centres.

These results about the change of the NV charge state upon hydrogenation of the diamond nanocrystals indicate a strong dependence on surface.

Figure 6.23 summarises the blinking behaviour of NV centres on different substrates, surrounding media and surface groups.

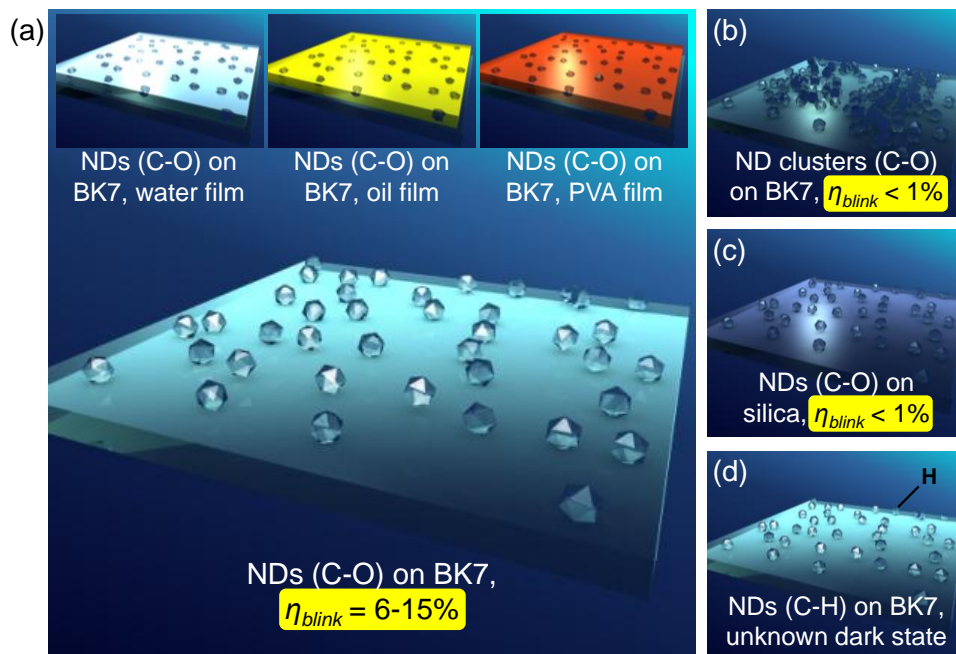


Figure 6.23. Summary of optical behaviour of NV centres in nanodiamonds on different substrates, surrounding media and surface groups. **a)** Oxygen-terminated (C-O) isolated nanodiamonds (NDs) on a BK7 substrate. The measured value for η_{blink} was $\sim 6-15\%$, suggesting that the BK7 substrate promotes blinking. The blinking behaviour was insensitive to the chemical inert environment provided by water, oil or PVA films, for which η_{blink} did not change. **b)** Oxygen-terminated (C-O) clustered NDs on a BK7 substrate. The measured value for η_{blink} was $< 1\%$, suggesting that the ND agglomeration inhibits blinking, possibly because it prevents potential blinking NV centres from accessing the substrate traps. **c)** Oxygen-terminated (C-O) isolated NDs on a silica substrate. The measured value for η_{blink} was $< 1\%$, suggesting that the silica substrate inhibits blinking. The silica substrate does not provide acceptor energy levels for the tunnelling of the NV photoexcited electrons. **d)** Hydrogen-terminated (C-H) isolated nanodiamonds (NDs) on a BK7 substrate. The hydrogenation mediated by a layer of adsorbed water from the air subtracts electrons from the NV centres and brings them to an “unknown” (positively charged) state no longer optically active.

6.3.4. Final remarks on the blinking mechanism in NV centres

Recently, several studies have been conducted aiming to address the effects that the size of the nanodiamonds [322] and the chemistry of the surface [308-310] have on the fluorescence properties and charge state of NV centres. These studies and the experimental results I have shown in the previous sections prove that the surrounding environment affects the properties of the NV centre. In the specific case of blinking, the experimental evidence seems to point to the proximity of the NV centre to the surface and the availability of traps as the key conditions for the fluorescence intermittency to occur. The size of the nanodiamonds instead, is only indirectly involved. Although our first consistent observation of blinking NV centres was in extremely small (~ 5 nm) nanocrystals, this seemed to be just an indirect consequence of the fact that the small size made the NVs more likely to be close to the surface of the nanodiamonds and therefore more likely to access the acceptor-like states in the adjacent substrate.

The model we suggested to explain the blinking of NV centres via the tunnelling of the photoexcited electrons to the adjacent substrate is only a proposal, although reasonable. Perhaps, the key message is that phenomena such as the blinking and the change of charge state of the NV upon surface hydrogenation show, again, that the interaction of the NV centre with the surrounding environment is possible. This certainly pushes towards a change of attitude with respect to the assumption that the NV centre in nanodiamond is an "imperturbable" entity. It may even force us to rethink the feasibility of some of the proposed NV centre-based applications, but at the same time it may open up a new range of possibilities which would potentially exploit this newly acquired control variable.

7

Conclusions and future work

NV colour centres in diamond have captured considerable attention in the recent past. Several potential NV centre-based technologies have been identified exploiting the unique optical and spin properties of the defect. As shown, the possible applications span over an impressive interdisciplinary range of research fields including quantum information technology, high-resolution magnetometry, biotechnology and nanomedicine.

To date, the majority of the NV-related studies have shown optimistic results with regard to the actual feasibility of these applications. However, some of them have specific material requirements. For instance, diamond must be of ultra high purity for quantum technologies where the spin coherence is critical, while for high-resolution magnetometry and biomedical imaging the small size of the diamond nanocrystals and the optical stability of the hosted NV centres are crucial. These requirements have always been carefully taken into account, but often they could have not been directly put under test due to the limitation on the capability to appropriately process the diamond material. It is only recently for example, that ultrasmall (size < 10 nm) nanodiamonds containing NV centres have been practically synthesised; prior to that, we could only speculate about the behaviour of the defects in such small nanoparticles. The diamond material science is finally and incredibly fast becoming mature for some of these requirements to be experimentally tested.

7.1 Conclusions

In this thesis I focused on the properties of NV centres in nanodiamonds (NDs). The goals were to investigate whether certain parameters such as size, surface termination and synthesis conditions affect the properties of the NV centre when it is hosted in a diamond crystal in the nanometre size range (0-100 nm). This is important for certain NV centre-based applications such as single spin detection in high-resolution magnetometry and biomedical imaging, tracking and drug-delivery.

One of the main factors that have to be taken into account is *size*. It is well established that the size of the cluster determines the thermodynamical stability of the carbon phases and at the nanoscale it even dictates whether certain structures can or cannot exist (cf. c. 5, ss. 5.1.2-3). The direct effects of the size of the nanodiamonds on the properties of the hosted NV centres are unclear and experimentally unverified. Recent theoretical and experimental studies manifested serious concerns about the possibility that nanodiamonds smaller than 10 nm in size could contain any optically active NV centre (cf. c. 6, s. 6.1). We specifically investigated this problem. The concerns were justified as we found that there was a correlation between the size of the nanodiamonds and the probability of observing hosted NV centres. In agreement with theoretical predictions, our experimental analysis showed that as the size of the nanodiamond decreases, the probability of observing NV centres decreases exponentially (cf. c. 5, s. 5.2.3). Nevertheless, we also demonstrated that optically active NV centres do exist in isolated 5-nm detonation nanodiamonds, proving that the thermodynamical stability of the centre in such small particles is possible (cf. c. 6, s. 6.2.1).

At the same time, despite preserving the thermodynamical stability of the NV centre, the reduced size of the hosting nanocrystals seems to affect its optical stability. In the 5-nm NDs in fact, we observed for the first time a completely new optical property of the NV centre: the fluorescence intermittency or blinking (cf. c. 6, s. 6.2.2). The centre undergoes optical “jumps” between dark off-states and bright on-states in the millisecond to second time scale. Although the blinking is a commonly observed phenomenon in almost all-known nanoscale fluorophores, it has never been reported before in NV centres. This result is remarkable. It is interesting from the perspective of fundamental physics,

especially considering the fact that the blinking phenomenon seems to be ubiquitous across diverse quantum systems, regardless of their “nature”. It also forces us to positively question some of the popular assumptions with regard for instance to its photostability.

The observation of NV blinking centres in small nanodiamonds fuelled further research, especially considering the general lack of understanding of the mechanism even in systems where it has been observed and studied for a few decades (cf. c. 6, s. 6.2.2). We perfected our own method (cf. c. 6, s. 6.1.3), based on the well-known technique of oxidation in air, to reduce the size of selected nanodiamonds and monitor the evolution of the optical behaviour of the NV centres as the size of the hosting particles decreases (cf. c. 6, s. 6.3.1). Our systematic experimental analysis showed that the size of the nanodiamonds was only incidentally involved in triggering the blinking mechanism for the NV. The data suggests that is rather the proximity of the centre to the *surface*, to be responsible for the fluorescence intermittency, possibly promoting a tunnelling mechanism of photoexcited electrons from the NV centres to trap states located in the adjacent *substrate*, whose characteristics are hence crucial themselves (cf. c. 6, s. 6.3.3).

In addition, we observed that terminating the nanodiamond surface with active *functional groups*, such as hydrogen, resulted in the optical extinction of the NV centres, which can be reactivated upon the removal of such groups. Hydrogen-termination and formation of a layer of adsorbed water from the air would in fact subtract electrons from the NV centres bringing them to an “unknown” (positively) charged state in which they are no longer emitting (cf. c. 6, s. 6.3.3).

Based on these observations, this work leads to the conclusion that the *size* of the crystals, the *surface* proximity of the NVs, the characteristic of the *substrate* and those of the *surrounding media*, are all key factors that influence the properties of NV centres in nanodiamonds. Within ultrasmall nanodiamonds the physics of NV centres obeys to specific rules that do not necessarily hold in larger diamond crystals or in the bulk. Although “encaged”, in small nanodiamonds the interaction of the NV centres with the surrounding environment is possible and the NV is not an “imperturbable” entity. This

may shake some of our convictions and even force a reassessment of the feasibility of some of the proposed NV centre-based technologies, but at the same time it may lead to a novel range of possibilities which could potentially exploit this newly acquired control variable.

7.2 Future work

The relevance of this research resides in having investigated and established some fundamental properties of the NV centre in nanodiamond. We demonstrated that the nanodiamond host and the surrounding environment do affect characteristically the thermodynamical and optical stability of the NV centres. However, along with these new acquired certainties, new questions arise. Figure 7.1 shows a schematic roadmap for future studies.

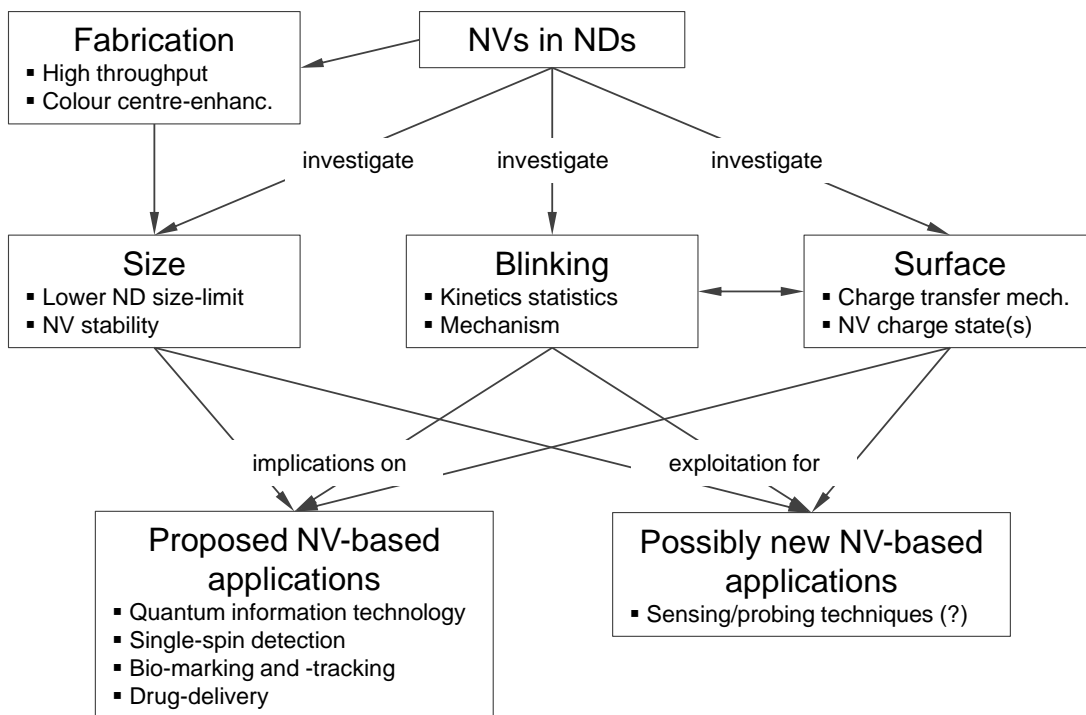


Figure 7.1. Schematic roadmap for future studies regarding NV centres in nanodiamonds and the development of relative technologies.

We have demonstrated the stability of NV centre in isolated 5-nm nanodiamonds, but this is probably not the lower limit. Further efforts should be pursued with the aim of fabricating, ideally on large scales, even smaller fluorescent diamond and determine the minimum particle size which could guarantee the stability of the hosted NV centre. This is

necessary to establish the intrinsic limitations we will have to deal with for certain NV centre-based applications such as high-resolution magnetometry or biomedical imaging, which critically rely on the reduced size of the hosting nanocrystals.

We observed for the first time the fluorescence intermittency or blinking of NV centres. This is an extremely intriguing phenomenon that requires further investigation. In fact, we could not be conclusive about the blinking kinetics, following rather exponential or power-law statistics. Plus, the model we suggested to explain the blinking of NV centres, via the tunnelling of the photoexcited electrons to the adjacent substrate, is a proposal open to discussion rather than a definitive explanation. Future studies should be focused on better understanding and ultimately controlling the fluorescence intermittency of the NV centre. We need to determine whether the blinking is a restraining effect we have to account for in realising certain NV centre-based technologies or whether we could even try to exploit it in specific applications.

Finally, we reported on the effects of terminating the nanodiamonds surface with active functional groups, such as hydrogen. Our results, in line with those of the most recent literature, show that we can interact with the NV centre by modifying the environment around the nanodiamond host. This potentially opens a whole new field of research. Further studies should be directed towards a better understanding of the mechanism in order, again, to cope with it in the proposed NV centre-based technologies or to possibly develop a whole new range of specific applications based on the exploitation of this extra control variable.

Appendix **A**

Publications arising from this thesis

A.1 Publications in peer-reviewed journals

1. Gaebel T., **Bradac C.**, Chan J., Say J. M., Brown L. J., Hemmer P. and Rabeau J. R., "Size-reduction of nanodiamonds via air oxidation", *Diamond and Related Materials*, 2011, 21(0): p. 28-32.
2. Inam F. A., Gaebel T., **Bradac C.**, Stewart L., Withford M. J., Dawes J. M., Rabeau J. R. and Steel M. J., "Modification of spontaneous emission from nanodiamond colour centres on a structured surface", *New Journal of Physics*, 2011, 13(7), p. 073012.
3. **Bradac C.**, Gaebel T., Naidoo N., Sellars M. J., Twamley J., Brown L. J., Barnard A. S., Plakhotnik T., Zvyagin A. V. and Rabeau J. R., "Observation and control of blinking nitrogen-vacancy centres in discrete nanodiamonds", *Nature Nanotechnology*, 2010, 5(5), p. 345-349.
4. **Bradac C.**, Gaebel T., Naidoo N., Rabeau J. R. and Barnard A. S., "Prediction and measurement of the size-dependent stability of fluorescence in diamond over the entire nanoscale", *Nano Letters*, 2009, 9 (10), p. 3555-3564.

A.2 Conference papers and proceedings

1. **Bradac C.**, Gaebel T. and Rabeau J. R., "The effects of size and surface on nitrogen-vacancy centres in nanodiamond", *22nd European Conference on Diamond, Diamond-like*

The properties of nitrogen-vacancy centres in nanodiamond

materials, Carbon Nanotubes and Nitrides (Diamond), Garmisch-Partenkirchen, Bavaria Germany, Sep. 4th – 8th, 2011. **Winner** of the: **Young Scholar Award**.

2. **Bradac C.**, Gaebel T., Zvyagin A. V. and Rabeau J. R., "Nitrogen-vacancy centres in nanodiamond: effects of size, surface and surrounding environment on luminescence", *IQEC/CLEO Pacific Rim*, Sydney (AU), Aug. 28th – Sep. 1st, 2011.
3. **Bradac C.**, Gaebel T. and Rabeau J. R., "Tailoring nanodiamonds containing nitrogen-vacancy (NV) centres", *Conference on Optics And Laser Application (KOALA)*, Dunedin (NZ), Nov. 28th – Dec. 4th, 2010.
4. **Bradac C.**, Gaebel T., Naidoo N., Sellars M. J., Twamley J., Brown L. J., Barnard A. S., Plakhotnik T., Zvyagin A. V. and Rabeau J. R., "Processing 5-nm nanodiamonds containing nitrogen-vacancy centres", *International conference on Quantum Communication, Measurement and Computation (QCMC)*, Brisbane, July 19th – 23rd, 2010.
5. **Bradac C.**, Gaebel T., Naidoo N., Sellars M. J., Twamley J., Brown L. J., Barnard A. S., Plakhotnik T., Zvyagin A. V. and Rabeau J. R., "Nitrogen-vacancy centres in 5-nm nanodiamonds", *International conference on Quantum Optics and Quantum Information (ICQOQI)*, Kyiv, May 28th – Jun. 1st, 2010. **Invited talk**.
6. **Bradac C.**, Gaebel T., Naidoo N., Rabeau J. R. and Barnard A. S., "Prediction and measurement of the size-dependent stability of fluorescence in nano-scale diamonds", *International Conference On Nanoscience and Nanotechnology (ICONN)*, Sydney (AU), Feb. 22nd – 26th, 2010.
7. **Bradac C.**, Gaebel T., Naidoo N., Sellars M. J., and Rabeau J. R., "NV centres in nanodiamonds: towards a magnetometer based on single spins", *Asher Peres International Physics School*, Sydney (AU), Nov 30th – Dec. 4th, 2009.

8. **Bradac C.**, Gaebel T., Naidoo N., Sellars M. J., and Rabeau J. R., "NV centres in nanodiamonds: towards a magnetometer based on single spins", *Conference on Optics And Laser Application (KOALA)*, Sydney (AU), Nov 23rd – Nov. 27th, 2009.
9. **Bradac C.**, Gaebel T., Sellars M. J., and Rabeau J. R., "A magnetometer based on single spins in nanodiamond", *Hole Burning Single Molecule(HBSM)*, Palm Cove Cairns (AU), Jun. 22nd – 27th 2009.
10. **Bradac C.**, Gaebel T., Sellars M. J., and Rabeau J. R., "A magnetometer based on single spins in nanodiamond", *Australian Research Council Nanotechnology Network (ARCNN)*, Canberra (AU), Feb. 19th -20th 2009.
11. **Bradac C.**, Gaebel T., Sellars M. J., and Rabeau J. R., "A magnetometer based on single spins in nanodiamond", *Australian Institute of Physics (AIP)*, Adelaide (AU), Dec. 1st – 5th, 2008.

A.3 Other publications

1. **Bradac C.**, Gaebel T., Rabeau J. R. and Barnard A. S., "Nitrogen-vacancy colour centres in diamond: theory, characterisation and applications", in *Nanotechnology in Australia. Showcase of early career research*, 2011, Pan Stanford Publishing, p. 113-149.

References

1. Kittel, C., *Introduction to Solid State Physics*. Third ed. 1968, New York: John Wiley and Sons.
2. Mohs, F., *Treatise on Mineralogy*. 1825, Edimburgh: Caledonian Mercury Press. 458.
3. Knoop, F., Peters, C.G., Emerson, W.B., *A Sensitive Pyramidal-Diamond Tool for Indentation Measurements* Journal of Research of the National Bureau of Standards 1939. **23**(1): p. 39-61, Research Paper RP1220.
4. Brookes, C.A., *Plastic Deformation and Anisotropy in the Hardness of Diamond*. Nature, 1970. **228**(5272): p. 660-661.
5. Bowden, F.P. and A.E. Hanwell, *The Friction of Clean Crystal Surfaces*. Proceedings of the Royal Society of London. Series A. Mathematical and Physical Sciences, 1966. **295**(1442): p. 233-243.
6. Telling, R.H., et al., *Theoretical Strength and Cleavage of Diamond*. Physical Review Letters, 2000. **84**(22): p. 5160.
7. Roundy, D. and M.L. Cohen, *Ideal strength of diamond, Si, and Ge*. Physical Review B, 2001. **64**(21): p. 212103.
8. Tyson, W.R., *Theoretical strength of perfect crystals*. Philosophical Magazine, 1966. **14**(131): p. 925 - 936.
9. Luo, X., et al., *Compressive Strength of Diamond from First-Principles Calculation*. The Journal of Physical Chemistry C. **114**(41): p. 17851-17853.
10. Field, J.E. and C.S.J. Pickles, *Strength, fracture and friction properties of diamond*. Diamond and Related Materials, 1996. **5**(6-8): p. 625-634.
11. Zhang, Y., H. Sun, and C. Chen, *Strain dependent bonding in solid C₃N₄ : High elastic moduli but low strength*. Physical Review B, 2006. **73**(6): p. 064109.
12. Field, J.E., *The Properties of Diamond* 1979, London: Academic press.
13. Ma, F., K.W. Xu, and D.W. Fan, *Strain energy anisotropy in germanium and other diamond-cubic polycrystalline films*. Thin Solid Films, 2006. **500**(1-2): p. 164-168.
14. Colm, M.F. and et al., *Acoustic wave properties of CVD diamond*. Semiconductor Science and Technology, 2003. **18**(3): p. S86.
15. Evans, T. and R.K. Wild, *Plastic deformation of diamond at temperatures below 1800 °C*. Philosophical Magazine, 1966. **13**(121): p. 209 - 210.
16. Achard, J., et al., *Thick boron doped diamond single crystals for high power electronics*. Diamond and Related Materials. **20**(2): p. 145-152.

17. Wort, C.J.H. and R.S. Balmer, *Diamond as an electronic material*. Materials Today. **11**(1-2): p. 22-28.
18. Kidalov, S. and F. Shakhov, *Thermal Conductivity of Diamond Composites*. Materials, 2009. **2**(4): p. 2467-2495.
19. Anthony, T.R., et al., *Thermal diffusivity of isotopically enriched¹²C diamond*. Physical Review B, 1990. **42**(2): p. 1104.
20. Burgemeister, E.A. and C.A.J. Ammerlaan, *High-temperature thermal conductivity of electron-irradiated diamond*. Physical Review B, 1980. **21**(6): p. 2499.
21. Slack, G.A. and S.F. Bartram, *Thermal expansion of some diamondlike crystals*. Journal of Applied Physics, 1975. **46**(1): p. 89-98.
22. Slack, G.A., *Effect of Isotopes on Low-Temperature Thermal Conductivity*. Physical Review, 1957. **105**(3): p. 829.
23. K. E. Spear, J.P.D., J. I. Pankove, C. Qui, *Synthetic Diamond: Engineering CVD Science and Technology*. 1994, New York: Wiley.
24. Bundy, F.P., *Pressure-temperature phase diagram of elemental carbon*. Physica A: Statistical Mechanics and its Applications, 1989. **156**(1): p. 169-178.
25. Ashcroft, N.V., Mermin N.D., *Solid State Physics*. 1976: Brooks/Cole.
26. Isberg, J., et al., *High Carrier Mobility in Single-Crystal Plasma-Deposited Diamond*. Science, 2002. **297**(5587): p. 1670-1672.
27. Kemmey, P.J., Wedepohl, P.T., *Physical Properties of Diamond*. 1965, Oxford: Clarendon Press.
28. Pierson, H.O., *Handbook of Carbon, Graphite, Diamond and Fullerenes - Properties, Processing and Applications*. 2004: William Andrew Publishing/Noyes.
29. Ekimov, E.A., et al., *Superconductivity in diamond*. Nature, 2004. **428**(6982): p. 542-545.
30. Sze, S.M., Kwok, K.Ng, *Physics of Semiconductor Devices*. Third ed. 2007: John Wiley and Sons.
31. Nava, F., et al., *Transport Properties of Natural Diamond Used as Nuclear Particle Detector for a Wide Temperature Range*. Nuclear Science, IEEE Transactions on, 1979. **26**(1): p. 308-315.
32. Fox, B.A., et al., *Diamond devices and electrical properties*. Diamond and Related Materials, 1995. **4**(5-6): p. 622-627.
33. Zaitsev, A.M., *Optical Properties of Diamond: A Data Handbook*. 2001: Springer-Verlag.
34. Pan, L.S., Kania, D.R., *Diamond: electronic properties and applications*. 1994: Springer.
35. Wrachtrup, J., Jelezko, F., *Processing quantum information in diamond*. Journal of Physics: Condensed Matter, 2006(21): p. S807.
36. Dutt, M.V.G., et al., *Quantum Register Based on Individual Electronic and Nuclear Spin Qubits in Diamond*. Science, 2007. **316**(5829): p. 1312-1316.
37. Balasubramanian, G., et al., *Nanoscale imaging magnetometry with diamond spins under ambient conditions*. Nature, 2008. **455**(7213): p. 648-651.
38. Maze, J.R., et al., *Nanoscale magnetic sensing with an individual electronic spin in diamond*. Nature, 2008. **455**(7213): p. 644-647.
39. Chao, J.-I., et al., *Nanometer-Sized Diamond Particle as a Probe for Biolabeling*. Biophysical Journal, 2007. **93**(6): p. 2199-2208.

40. Yu, S.-J., et al., *Bright Fluorescent Nanodiamonds: No Photobleaching and Low Cytotoxicity*. Journal of the American Chemical Society, 2005. **127**(50): p. 17604-17605.
41. Edwards, D.F. and E. Ochoa, *Infrared refractive index of diamond*. J. Opt. Soc. Am., 1981. **71**(5): p. 607-608.
42. Harlow, G.E., *The Nature of Diamonds*. 1998: Cambridge University Press.
43. Tolansky, S., *Birefringence of Diamond*. Nature, 1966. **211**(5045): p. 158-160.
44. Lang, A.R., *Causes of Birefringence in Diamond*. Nature, 1967. **213**(5073): p. 248-251.
45. Poindexter, E., *Piezobirefringence in Diamond*. American Mineralogist, 1955. **40**: p. 1135-1139.
46. Seal, M., *Thermal and Optical Applications of Thin Film Diamond*. Philosophical Transactions: Physical Sciences and Engineering, 1993. **342**(1664): p. 313-322.
47. Hounscome, L.S., et al., *Origin of brown coloration in diamond*. Physical Review B, 2006. **73**(12): p. 125203.
48. Koizumi, S., et al., *Growth and characterization of phosphorous doped {111} homoepitaxial diamond thin films*. Applied Physics Letters, 1997. **71**(8): p. 1065-1067.
49. Jelezko, F. and J. Wrachtrup, *Single defect centres in diamond: a review*. Physica Status Solidi A, 2006. **203**(13): p. 3207-3225.
50. Jelezko, F. and J. Wrachtrup, *Read-out of single spins by optical spectroscopy*. Journal of Physics: Condensed Matter, 2004. **16**(30): p. R1089-R1104.
51. Hunt, D.C., et al., *Identification of the neutral carbon <100>-split interstitial in diamond*. Physical Review B, 2000. **61**(6): p. 3863.
52. Smith, H.E., et al., *Structure of the self-interstitial in diamond*. Physical Review B, 2004. **69**(4): p. 045203.
53. Iakoubovskii, K., S. Dannefaer, and A. Stesmans, *Evidence for vacancy-interstitial pairs in Ib-type diamond*. Physical Review B, 2005. **71**(23): p. 233201.
54. Kiflawi, I. and et al., *Electron irradiation and the formation of vacancy-interstitial pairs in diamond*. Journal of Physics: Condensed Matter, 2007. **19**(4): p. 046216.
55. Iakoubovskii, K., et al., *Annealing of vacancies and interstitials in diamond*. Physica B: Condensed Matter, 2003. **340-342**: p. 67-75.
56. Dannefaer, S. and K. Iakoubovskii, *Defects in electron irradiated boron-doped diamonds investigated by positron annihilation and optical absorption*. Journal of Physics: Condensed Matter, 2008. **20**(23): p. 235225.
57. Twitchen, D.J., et al., *Electron-paramagnetic-resonance measurements on the divacancy defect center R4/W6 in diamond*. Physical Review B, 1999. **59**(20): p. 12900.
58. Iakoubovskii, K. and A. Stesmans, *Dominant paramagnetic centers in ¹⁷O-implanted diamond*. Physical Review B, 2002. **66**(4): p. 045406.
59. Hanley, P.L., I. Kiflawi, and A.R. Lang, *On Topographically Identifiable Sources of Cathodoluminescence in Natural Diamonds*. Philosophical Transactions of the Royal Society of London. Series A, Mathematical and Physical Sciences, 1977. **284**(1324): p. 329-368.
60. Kiflawi, I., et al., *'Natural' and 'man-made' platelets in type-Ia diamonds*. Philosophical Magazine Part B, 1998. **78**(3): p. 299 - 314.
61. Goss, J.P., et al., *Extended defects in diamond: The interstitial platelet*. Physical Review B, 2003. **67**(16): p. 165208.
62. Iakoubovskii, K. and G.J. Adriaenssens, *Characterization of platelet-related infrared luminescence in diamond*. Philosophical Magazine Letters, 2000. **80**(6): p. 441-444.

63. Chen, J.H., et al., *Voidites in polycrystalline natural diamond*. Philosophical Magazine Letters, 1998. **77**(3): p. 135-140.
64. Kiflawi, I. and J. Bruley, *The nitrogen aggregation sequence and the formation of voidites in diamond*. Diamond and Related Materials, 2000. **9**(1): p. 87-93.
65. Walker, J., *Optical absorption and luminescence in diamond*. Reports on Progress in Physics, 1979(10): p. 1605.
66. Collins, A.T., *The detection of colour-enhanced and synthetic gem diamonds by optical spectroscopy*. Diamond and Related Materials, 2003. **12**(10-11): p. 1976-1983.
67. Kaiser, W. and W.L. Bond, *Nitrogen, A Major Impurity in Common Type I Diamond*. Physical Review, 1959. **115**(4): p. 857.
68. Robertson, R., J.J. Fox, and A.E. Martin, *Two types of diamond*. Philosophical Transactions of the Royal Society of London, 1934. **232**: p. 463-535.
69. Kajihara, S.A., et al., *Nitrogen and potential n-type dopants in diamond*. Physical Review Letters, 1991. **66**(15): p. 2010.
70. Titus, E., et al., *Nitrogen and hydrogen related infrared absorption in CVD diamond films*. Thin Solid Films, 2006. **515**(1): p. 201-206.
71. Loubser, J.H.N. and J.A. van Wyk, *Electron spin resonance in the study of diamond*. Reports on Progress in Physics, 1978. **41**(8): p. 1201-1248.
72. Davies, G., *Properties and growth of diamond* Data Review. 1994, London: IET. 427.
73. Jones, R., P.R. Briddon, and S. Oberg, *First-principles theory of nitrogen aggregates in diamond*. Philosophical Magazine Letters, 1992. **66**(2): p. 67-74.
74. Read, P.G., *Gemmology*. 2005: Butterworth-Heinemann.
75. Lang, A.R., *A proposed structure for nitrogen impurity platelets in diamond*. Proceedings of the Physical Society, 1964. **84**(6): p. 871.
76. Woods, G.S., *Platelets and the infrared Absorption of Type Ia Diamonds*. Proceedings of the Royal Society of London. Series A, Mathematical and Physical Sciences, 1986. **407**(1832): p. 219-238.
77. Davies, G., et al., *Vacancy-related centers in diamond*. Physical Review B, 1992. **46**(20): p. 13157.
78. Mainwood, A., *Nitrogen and nitrogen-vacancy complexes and their formation in diamond*. Physical Review B (Condensed Matter), 1994. **49**(12): p. 7934-7940.
79. Jones, R., et al., *Theory of nitrogen aggregates in diamond: the H3 and H4 defects*. Materials Science Forum, 1994. **143-147**: p. 45-49.
80. Gali, A., M. Fyta, and E. Kaxiras, *Ab initio supercell calculations on nitrogen-vacancy center in diamond: Electronic structure and hyperfine tensors*. Physical Review B, 2008. **77**(15): p. 155206.
81. He, X.-F., N.B. Manson, and P.T.H. Fisk, *Paramagnetic resonance of photoexcited N-V defects in diamond. II. Hyperfine interaction with the ¹⁴N nucleus*. Physical Review B, 1993. **47**(14): p. 8816.
82. Mita, Y., *Change of absorption spectra in type-Ib diamond with heavy neutron irradiation*. Physical Review B (Condensed Matter), 1996. **53**(17): p. 11360-11364.
83. Collins, A.T., *The Fermi level in diamond*. Journal of Physics: Condensed Matter, 2002. **14**(14): p. 3743.
84. Gaebel, T., et al., *Photochromism in single nitrogen-vacancy defect in diamond*. Applied Physics B: Lasers and Optics, 2006. **82**(2): p. 243-246.
85. Manson, N.B. and J.P. Harrison, *Photo-ionization of the nitrogen-vacancy center in diamond*. Diamond and Related Materials, 2005. **14**(10): p. 1705-1710.

86. Davies, G. and M.F. Hamer, *Optical Studies of the 1.945 eV Vibronic Band in Diamond*. Proceedings of the Royal Society of London. Series A, Mathematical and Physical Sciences (1934-1990), 1976. **348**(1653): p. 285-298.
87. Redman, D.A., et al., *Spin dynamics and electronic states of N-V centers in diamond by EPR and four-wave-mixing spectroscopy*. Physical Review Letters, 1991. **67**(24): p. 3420.
88. Fu, K.-M.C., et al., *Observation of the Dynamic Jahn-Teller Effect in the Excited States of Nitrogen-Vacancy Centers in Diamond*. Physical Review Letters, 2009. **103**(25): p. 256404.
89. Jahn, H.A. and E. Teller, *Stability of Polyatomic Molecules in Degenerate Electronic States. I. Orbital Degeneracy*. Proceedings of the Royal Society of London. Series A - Mathematical and Physical Sciences, 1937. **161**(905): p. 220-235.
90. Gali, A. and et al., *An ab initio study of local vibration modes of the nitrogen-vacancy center in diamond*. New Journal of Physics, 2011. **13**(2): p. 025016.
91. Davies, G., *Dynamic Jahn-Teller distortions at trigonal optical centres in diamond*. Journal of Physics C: Solid State Physics, 1979. **12**(13): p. 2551.
92. Felton, S., et al., *Electron paramagnetic resonance studies of the neutral nitrogen vacancy in diamond*. Physical Review B, 2008. **77**(8): p. 081201.
93. Manson, N.B., J.P. Harrison, and M.J. Sellars, *Nitrogen-vacancy center in diamond: Model of the electronic structure and associated dynamics*. Physical Review B (Condensed Matter and Materials Physics), 2006. **74**(10): p. 104303-11.
94. Manson, N.B. and R.L. McMurtrie, *Issues concerning the nitrogen-vacancy center in diamond*. Journal of Luminescence, 2007. **127**(1): p. 98-103.
95. Tamarat, P., Manson, N.B., Harrison, J.P., McMurtrie, R.L., Nizovtsev, A., Santori, C., Deausoleil, R.G., Neumann, P., Gaebel, T., Jelezko, F., Hemmer, P., Wrachtrup, J., *Spin-flip and spin-conserving optical transitions of the nitrogen-vacancy centre in diamond*. New Journal of Physics, 2008. **10**(4): p. 045004.
96. Redman, D., S. Brown, and S.C. Rand, *Origin of persistent hole burning of N-V centers in diamond*. J. Opt. Soc. Am. B, 1992. **9**(5): p. 768-774.
97. Harley, R.T., M.J. Henderson, and R.M. Macfarlane, *Persistent spectral hole burning of colour centres in diamond*. Journal of Physics C: Solid State Physics, 1984(8): p. L233.
98. Reddy, N.R.S., N.B. Manson, and E.R. Krausz, *Two-laser spectral hole burning in a colour centre in diamond*. Journal of Luminescence, 1987. **38**(1-6): p. 46-47.
99. Holliday, K., et al., *Optical hole-bleaching by level anti-crossing and cross relaxation in the N-V centre in diamond*. Journal of Physics: Condensed Matter, 1989(39): p. 7093.
100. van Oort, E., P. Stroomeer, and M. Glasbeek, *Low-field optically detected magnetic resonance of a coupled triplet-doublet defect pair in diamond*. Physical Review B, 1990. **42**(13): p. 8605.
101. van Oort, E., et al., *Microwave-induced line-narrowing of the N-V defect absorption in diamond*. Journal of Luminescence, 1991. **48-49**(PART 2): p. 803-806.
102. Hiromitsu, I., J. Westra, and M. Glasbeek, *Cross-relaxation dynamics of the N-V center in diamond as studied via optically detected microwave recovery transients*. Physical Review B, 1992. **46**(17): p. 10600.
103. He, X.-F., N.B. Manson, and P.T.H. Fisk, *Paramagnetic resonance of photoexcited N-V defects in diamond. I. Level anticrossing in the 3A ground state*. Physical Review B, 1993. **47**(14): p. 8809.

104. Oort, E.v. and et al., *Optically detected spin coherence of the diamond N-V centre in its triplet ground state*. Journal of Physics C: Solid State Physics, 1988. **21**(23): p. 4385.
105. Holliday, K., et al., *Raman heterodyne detection of electron paramagnetic resonance*. Opt. Lett., 1990. **15**(17): p. 983-985.
106. Manson, N.B., X.-F. He, and P.T.H. Fisk, *Raman heterodyne detected electron-nuclear-double-resonance measurements of the nitrogen-vacancy center in diamond*. Opt. Lett., 1990. **15**(19): p. 1094-1096.
107. Neumann, P., et al., *Excited-state spectroscopy of single NV defects in diamond using optically detected magnetic resonance*. New Journal of Physics, 2009. **11**(1): p. 013017.
108. Acosta, V.M., et al., *Optical properties of the nitrogen-vacancy singlet levels in diamond*. Physical Review B, 2011. **82**(20): p. 201202.
109. Goss, J.P., et al., *The Twelve-Line 1.682 eV Luminescence Center in Diamond and the Vacancy-Silicon Complex*. Physical Review Letters, 1996. **77**(14): p. 3041.
110. Delaney, P., J.C. Greer, and J.A. Larsson, *Spin-Polarization Mechanisms of the Nitrogen-Vacancy Center in Diamond*. Nano Letters, 2010. **10**(2): p. 610-614.
111. Harrison, J., M.J. Sellars, and N.B. Manson, *Optical spin polarisation of the N-V centre in diamond*. Journal of Luminescence, 2004. **107**(1-4): p. 245-248.
112. Harrison, J., M.J. Sellars, and N.B. Manson, *Measurement of the optically induced spin polarisation of N-V centres in diamond*. Diamond and Related Materials, 2006. **15**(4-8): p. 586-588.
113. Manson, N.B. and C. Wei, *Transient hole burning in N-V centre in diamond*. Journal of Luminescence, 1994. **58**(1-6): p. 158-160.
114. Santori, C., et al., *Coherent population trapping in diamond N-V centers at zero magnetic field*. Opt. Express, 2006. **14**(17): p. 7986-7993.
115. Martin, J.P.D., *Fine structure of excited 3E state in nitrogen-vacancy centre of diamond*. Journal of Luminescence, 1999. **81**(4): p. 237-247.
116. Nizovtsev, A.P., et al., *NV centers in diamond: spin-selective photokinetics, optical ground-state spin alignment and hole burning*. Physica B: Condensed Matter, 2003. **340-342**: p. 106-110.
117. Wells, H.G., *The Diamond Maker. The Door in the Wall and Other Stories*. 1911, New York: Mitchell Kennerley.
118. Tennant, S., *On the Nature of the Diamond*. By Smithson Tennant, Esq. F. R. S. Philosophical Transactions of the Royal Society of London, 1797. **87**: p. 123-127.
119. Hannay, J.B., *On the Artificial Formation of the Diamond*. Proceedings of the Royal Society of London, 1879. **30**(200-205): p. 450-461.
120. Moissan, H., *Nouvelles experiences sur la reproduction du diamant*. C. R. Acad. Sci., Paris, 1894. **118**: p. 320-326.
121. Story-Maskelyne, N., The Times, Feb. 20, 1880.
122. Rossini, F.D., Jessup, R.S., Nat. Bur. Stand. J. Research, 1938. **21**: p. 491-514.
123. Berman, R., Simon, F.E., *On The Graphite-Diamond Equilibrium*. Zeitschr. Electroch., 1955. **59**: p. 333.
124. Bridgman, P.W., *An Experimental Contribution to the Problem of Diamond Synthesis*. The Journal of Chemical Physics, 1947. **15**(2): p. 92-98.
125. Bundy, F.P., et al., *Man-Made Diamonds*. Nature, 1955. **176**(4471): p. 51-55.
126. Hazen, R.M., *The Diamond Makers*. 1999, Cambridge, UK: Cambridge University Press.

127. Ito, E. and S. Gerald, *Theory and Practice - Multianvil Cells and High-Pressure Experimental Methods*, in *Treatise on Geophysics*. 2007, Elsevier: Amsterdam. p. 197-230.
128. Hall, H.T., *Some High-Pressure, High-Temperature Apparatus Design Considerations: Equipment for Use at 100 000 Atmospheres and 3000 °C*. *Review of Scientific Instruments*, 1958. **29**(4): p. 267-275.
129. Pal'yanov, N., et al., *Fluid-bearing alkaline carbonate melts as the medium for the formation of diamonds in the Earth's mantle: an experimental study*. *Lithos*, 2002. **60**(3-4): p. 145-159.
130. Linares, R.C., Doering, P.J., *System and method for producing synthetic diamond* 2011: U.S. Patent No. 7879148.
131. Eversole, W.G., *Synthesis of Diamond*. 1962: US Patents No. 3030187, 3030188.
132. Derjaguin, B.V., et al., *Filamentary diamond crystals*. *Journal of Crystal Growth*, 1968. **2**(6): p. 380-384.
133. Matsumoto, S., Sato, Y., Kamo, M., Setaka, N. , *Vapour deposition of Diamond Particles from Methane*. *Jpn J. Appl. Phys*, 1982. **21**: p. L183-L185.
134. Matsumoto, S., Sato, Y., Tsutsumi, M., Setaka, N., *Growth of Diamond Particles from Methane-Hydrogen Gas*. *J Mater. Sci.*, 1982. **17**: p. 3106-3112.
135. Kamo, M., et al., *Diamond synthesis from gas phase in microwave plasma*. *Journal of Crystal Growth*, 1983. **62**(3): p. 642-644.
136. Matsumoto, S. and Y. Matsui, *Electron microscopic observation of diamond particles grown from the vapour phase*. *Journal of Materials Science*, 1983. **18**(6): p. 1785-1793.
137. Boser, U., *Diamonds on Demand*. *Smithsonian Magazine*, 2008(June).
138. DeCarli, P.S. and J.C. Jamieson, *Formation of Diamond by Explosive Shock*. *Science*, 1961. **134**(3472): p. 92.
139. Danilenko, V.V., Trefilov, V.I., Danilenko, V.N. 1991: USSR Patent No. SU 181, 329 AZ.
140. Greiner, N.R., et al., *Diamonds in detonation soot*. *Nature*, 1988. **333**(6172): p. 440-442.
141. Danilenko, V.V., *On the history of the discovery of nanodiamond synthesis*. *Physics of the Solid State*, 2004. **46**: p. 595-599.
142. Ho, D., *Nanodiamonds: Applications in Biology and Nanoscale Medicine*. *Technology and Engineering*. 2009: Springer.
143. Dolmatov, V., et al., *Currently available methods of industrial nanodiamond synthesis*. *Physics of the Solid State*, 2004. **46**(4): p. 611-615.
144. Dolmatov, V., *Development of a rational technology for synthesis of high-quality detonation nanodiamonds*. *Russian Journal of Applied Chemistry*, 2006. **79**(12): p. 1913-1918.
145. Galimov, E.M., *Possibility of Natural Diamond Synthesis under Conditions of Cavitation, occurring in a Fast-moving Magmatic Melt*. *Nature*, 1973. **243**(5407): p. 389-391.
146. Frank, F.C., A.R. Lang, and M. Moore, *Cavitation as a Mechanism for the Synthesis of Natural Diamonds*. *Nature*, 1973. **246**(5429): p. 143-144.
147. Galimov, É., et al., *Experimental corroboration of the synthesis of diamond in the cavitation process*. *Doklady Physics*, 2004. **49**(3): p. 150-153.
148. Flynn, H.G., *Method and means for converting graphite to diamond*. 1986: US Patent No. 4563341.

149. Yang, G.W. and J.B. Wang, *Pulsed-laser-induced transformation path of graphite to diamond via an intermediate rhombohedral graphite*. Applied Physics A: Materials Science and Processing, 2001. **72**(4): p. 475-479.
150. Pearce, S.R.J., et al., *Production of nanocrystalline diamond by laser ablation at the solid/liquid interface*. Diamond and Related Materials, 2004. **13**(4-8): p. 661-665.
151. Khachatryan, A.K., et al., *Graphite-to-diamond transformation induced by ultrasound cavitation*. Diamond and Related Materials, 2008. **17**(6): p. 931-936.
152. Meijer, J., et al., *Concept of deterministic single ion doping with sub-nm spatial resolution*. Applied Physics A (Materials Science Processing), 2006. **A83**(2): p. 321-327.
153. Martin, J., et al., *Generation and detection of fluorescent color centers in diamond with submicron resolution*. Applied Physics Letters, 1999. **75**(20): p. 3096-3098.
154. Kalish, R., et al., *Nitrogen doping of diamond by ion implantation*. Diamond and Related Materials, 1997. **6**(2-4): p. 516-520.
155. Meijer, J., et al., *Generation of single color centers by focused nitrogen implantation*. Applied Physics Letters, 2005. **87**(26): p. 1-3.
156. Rabeau, J.R., et al., *Implantation of labelled single nitrogen vacancy centers in diamond using ¹⁵N*. Applied Physics Letters, 2006. **88**(2): p. 023113-3.
157. Pezzagna, S., et al., *Creation efficiency of nitrogen-vacancy centres in diamond*. New Journal of Physics, 2010. **12**(6): p. 065017.
158. Rabeau, J.R., et al., *Single Nitrogen Vacancy Centers in Chemical Vapor Deposited Diamond Nanocrystals*. Nano Letters, 2007. **7**(11): p. 3433-3437.
159. DiVincenzo, D.P., *Quantum Computation*. Science, 1995. **270**(5234): p. 255-261.
160. Gaebel, T., et al., *Room-temperature coherent coupling of single spins in diamond*. Nat Phys, 2006. **2**(6): p. 408-413.
161. Jelezko, F., et al., *Observation of Coherent Oscillations in a Single Electron Spin*. Physical Review Letters, 2004. **92**(7): p. 076401.
162. Jelezko, F., et al., *Observation of Coherent Oscillation of a Single Nuclear Spin and Realization of a Two-Qubit Conditional Quantum Gate*. Physical Review Letters, 2004. **93**(13): p. 130501.
163. Childress, L., et al., *Coherent Dynamics of Coupled Electron and Nuclear Spin Qubits in Diamond*. Science, 2006. **314**(5797): p. 281-285.
164. Hanson, R., et al., *Polarization and Readout of Coupled Single Spins in Diamond*. Physical Review Letters, 2006. **97**(8): p. 087601.
165. Neumann, P., et al., *Quantum register based on coupled electron spins in a room-temperature solid*. Nat Phys, 2010. **6**(4): p. 249-253.
166. Gisin, N., et al., *Quantum cryptography*. Reviews of Modern Physics, 2002. **74**(1): p. 145.
167. Kurtsiefer, C., et al., *Stable solid-state source of single photons*. Physical Review Letters, 2000. **85**(2): p. 290-293.
168. Park, Y.-S., A.K. Cook, and H. Wang, *Cavity QED with Diamond Nanocrystals and Silica Microspheres*. Nano Letters, 2006. **6**(9): p. 2075-2079.
169. Schietinger, S. and O. Benson, *Coupling single NV-centres to high-Q whispering gallery modes of a preselected frequency-matched microresonator*. Journal of Physics B: Atomic, Molecular and Optical Physics, 2009. **42**(11): p. 114001.
170. Santori, C., et al., *Nanophotonics for quantum optics using nitrogen-vacancy centers in diamond*. Nanotechnology, 2010. **21**(27): p. 274008.

171. Stewart, L.A., et al., *Single Photon Emission from Diamond nanocrystals in an Opal Photonic Crystal*. Opt. Express, 2009. **17**(20): p. 18044-18053.
172. Wolters, J., et al., *Enhancement of the zero phonon line emission from a single nitrogen vacancy center in a nanodiamond via coupling to a photonic crystal cavity*. Applied Physics Letters, 2010. **97**(14): p. 141108.
173. Van der Sar, T., et al., *Deterministic nanoassembly of a coupled quantum emitter-photonic crystal cavity system*. Applied Physics Letters, 2011. **98**(19): p. 193103.
174. Englund, D., et al., *Deterministic Coupling of a Single Nitrogen Vacancy Center to a Photonic Crystal Cavity*. Nano Letters, 2010. **10**(10): p. 3922-3926.
175. Schroder, T., et al., *Ultrabright and efficient single-photon generation based on nitrogen-vacancy centres in nanodiamonds on a solid immersion lens*. New Journal of Physics, 2011. **13**(5): p. 055017.
176. Castelletto, S., et al., *Diamond-based structures to collect and guide light*. New Journal of Physics, 2011. **13**(2): p. 025020.
177. Schietinger, S., et al., *Plasmon-Enhanced Single Photon Emission from a Nanoassembled Metal-Diamond Hybrid Structure at Room Temperature*. Nano Letters, 2009. **9**(4): p. 1694-1698.
178. Kolesov, R., et al., *Wave-particle duality of single surface plasmon polaritons*. Nat Phys, 2009. **5**(7): p. 470-474.
179. Fu, C.-C., et al., *Characterization and application of single fluorescent nanodiamonds as cellular biomarkers*. Proceedings of the National Academy of Sciences, 2007. **104**(3): p. 727-732.
180. Huang, L.C.L. and H.-C. Chang, *Adsorption and Immobilization of Cytochrome c on Nanodiamonds*. Langmuir, 2004. **20**(14): p. 5879-5884.
181. Schrand, A.M., et al., *Differential biocompatibility of carbon nanotubes and nanodiamonds*. Diamond and Related Materials, 2007. **16**(12): p. 2118-2123.
182. Schrand, A.M., et al., *Are Diamond Nanoparticles Cytotoxic?* The Journal of Physical Chemistry B, 2006. **111**(1): p. 2-7.
183. Treussart, F., et al., *Photoluminescence of single colour defects in 50 nm diamond nanocrystals*. Physica B: Condensed Matter, 2006. **376-377**: p. 926-929.
184. Barnard, A.S., *Diamond standard in diagnostics: nanodiamond biolabels make their mark*. The Analyst, 2009. **134**(9): p. 1751-1764.
185. Chang, Y.-R., et al., *Mass production and dynamic imaging of fluorescent nanodiamonds*. Nat Nano, 2008. **3**(5): p. 284-288.
186. Abbe, E., *Beitraege zur Theorie des Mikroskops und der mikroskopischen Wahrnehmung*. Archiv für Mikroskopische Anatomie, 1873. **9**: p. 413-420.
187. Rayleigh, L., *On the theory of optical images, with special reference to the microscope*. Philos. Mag., 1896. **42**: p. 167-195.
188. Schermelleh, L., R. Heintzmann, and H. Leonhardt, *A guide to super-resolution fluorescence microscopy*. The Journal of Cell Biology, 2010. **190**(2): p. 165-175.
189. Rabi, I.I., et al., *A New Method of Measuring Nuclear Magnetic Moment*. Physical Review, 1938. **53**(4): p. 318.
190. Rabi, I.I., et al., *Molecular beam resonance method for measuring nuclear magnetic moments*. Physical Review, 1939. **55**: p. 526-535.
191. Lauterbur, P.C., *Image formation by induced local interactions: examples employing nuclear magnetic resonance*. Nature, 1973. **242**(5394): p. 190-191.

192. Aguayo, J.B., et al., *Nuclear magnetic resonance imaging of a single cell*. *Nature*, 1986. **322**(6075): p. 190-191.
193. Cho, Z.H., et al., *Nuclear magnetic resonance microscopy with 4-um resolution: Theoretical study and experimental results*. *Medical Physics*, 1988. **15**(6): p. 815-824.
194. Cho, Z.H., et al., *Recent Progress in NMR Microscopy towards Cellular Imaging*. *Philosophical Transactions: Physical Sciences and Engineering*, 1990. **333**(1632): p. 469-475.
195. Lee, S.C., et al., *One micrometer resolution NMR microscopy*. *Journal of Magnetic Resonance*, 2001. **150**(2): p. 207-213.
196. Ciobanu, L., D.A. Seeber, and C.H. Pennington, *3D MR microscopy with resolution 3.7 um by 3.3 um by 3.3 um*. *Journal of Magnetic Resonance*, 2002. **158**(1-2): p. 178-182.
197. Sidles, J.A., *Noninductive detection of single-proton magnetic resonance*. *Applied Physics Letters*, 1991. **58**(24): p. 2854-2856.
198. Zuger, O. and D. Rugar, *First images from a magnetic resonance force microscope*. *Applied Physics Letters*, 1993. **63**(18): p. 2496-2498.
199. Rugar, D., et al., *Single spin detection by magnetic resonance force microscopy*. *Nature*, 2004. **430**(6997): p. 329-332.
200. Mamin, H.J., et al., *Nuclear magnetic resonance imaging with 90-nm resolution*. *Nat Nano*, 2007. **2**(5): p. 301-306.
201. Zuger, O., et al., *Three-dimensional imaging with a nuclear magnetic resonance force microscope*. *Journal of Applied Physics*, 1996. **79**(4): p. 1881-1884.
202. Glover, P. and P. Mansfield, *Limits to magnetic resonance microscopy*. *Reports on Progress in Physics*, 2002. **65**(10): p. 1489-1511.
203. Breiland, W.G., H.C. Brenner, and C.B. Harris, *Coherence in multilevel systems. I. Coherence in excited states and its application to optically detected magnetic resonance in phosphorescent triplet states*. *The Journal of Chemical Physics*, 1975. **62**(9): p. 3458-3475.
204. Balasubramanian, G., et al., *Ultralong spin coherence time in isotopically engineered diamond*. *Nat Mater*, 2009. **8**(5): p. 383-387.
205. Pake, G.E., *Paramagnetic Resonance, An Introductory Monograph*. 1962, New York: W. A. Benjamin.
206. Orbach, R., *Spin-Lattice Relaxation in Rare-Earth Salts*. *Proceedings of the Royal Society of London. Series A. Mathematical and Physical Sciences*, 1961. **264**(1319): p. 458-484.
207. Takahashi, S., et al., *Quenching Spin Decoherence in Diamond through Spin Bath Polarization*. *Physical Review Letters*, 2008. **101**(4): p. 047601.
208. Zurek, W.H., *Decoherence, einselection, and the quantum origins of the classical*. *Reviews of Modern Physics*, 2003. **75**(3): p. 715-775.
209. Hanson, R., O. Gywat, and D.D. Awschalom, *Room-temperature manipulation and decoherence of a single spin in diamond*. *Physical Review B*, 2006. **74**(16): p. 161203.
210. Maze, J.R., J.M. Taylor, and M.D. Lukin, *Electron spin decoherence of single nitrogen-vacancy defects in diamond*. *Physical Review B*, 2008. **78**(9): p. 094303.
211. Schweiger, A., Jeschke, G., *Principles of Pulse Electron Paramagnetic Resonance*. 2001: Oxford University Press.
212. Petta, J.R., et al., *Coherent Manipulation of Coupled Electron Spins in Semiconductor Quantum Dots*. *Science*, 2005. **309**(5744): p. 2180-2184.

213. Hill, S., et al., *Quantum Coherence in an Exchange-Coupled Dimer of Single-Molecule Magnets*. Science, 2003. **302**(5647): p. 1015-1018.
214. Loubens, G.d., et al., *High frequency EPR on dilute solutions of the single molecule magnet Ni₄*. Journal of Applied Physics, 2008. **103**(7): p. 07B910.
215. Gruber, A., et al., *Scanning confocal optical microscopy and magnetic resonance on single defect centers*. Science, 1997. **276**(5321): p. 2012-2014.
216. Wei, C., N.B. Manson, and J.P.D. Martin, *Experimental investigations of absorption and dispersion profiles of a strongly driven transition: ssV-shaped three-level system with a strong probe*. Physical Review A, 1995. **51**(2): p. 1438.
217. Howard, M., et al., *Quantum process tomography and Linblad estimation of a solid-state qubit*. New Journal of Physics, 2006(3): p. 33.
218. Kohler, J., et al., *Magnetic resonance of a single molecular spin*. Nature, 1993. **363**(6426): p. 242-244.
219. Wrachtrup, J., et al., *Optical detection of magnetic resonance in a single molecule*. Nature, 1993. **363**(6426): p. 244-245.
220. Chernobrod, B.M. and G.P. Berman, *Spin microscope based on optically detected magnetic resonance*. Journal of Applied Physics, 2005. **97**(1): p. 014903-3.
221. Bradac, C., et al., *Prediction and Measurement of the Size-Dependent Stability of Fluorescence in Diamond over the Entire Nanoscale*. Nano Letters, 2009. **9**(10): p. 3555-3564.
222. Bradac, C., et al., *Observation and control of blinking nitrogen-vacancy centres in discrete nanodiamonds*. Nat Nano, 2010. **5**(5): p. 345-349.
223. Ong, Q.K. and I. Sokolov, *Attachment of nanoparticles to the AFM tips for direct measurements of interaction between a single nanoparticle and surfaces*. Journal of Colloid and Interface Science, 2007. **310**(2): p. 385-390.
224. Ducker, W.A., T.J. Senden, and R.M. Pashley, *Direct measurement of colloidal forces using an atomic force microscope*. Nature, 1991. **353**(6341): p. 239-241.
225. Schietinger, S., T. Schröder, and O. Benson, *One-by-One Coupling of Single Defect Centers in Nanodiamonds to High-Q Modes of an Optical Microresonator*. Nano Letters, 2008. **8**(11): p. 3911-3915.
226. Barth, M., et al., *Controlled coupling of a single-diamond nanocrystal to a photonic crystal cavity*. Opt. Lett., 2009. **34**(7): p. 1108-1110.
227. Givargizov, E.I., et al., *Ultrasharp diamond-coated silicon tips for scanning-probe devices*. Microelectronic Engineering, 1998. **41-42**: p. 499-502.
228. Kulisch, W., et al., *Fabrication of integrated diamond cantilevers with tips for SPM applications*. Diamond and Related Materials, 1997. **6**(5-7): p. 906-911.
229. Oesterschulze, E., et al., *Diamond cantilever with integrated tip for nanomachining*. Diamond and Related Materials, 2002. **11**(3-6): p. 667-671.
230. Álvarez, D., et al., *Fabrication and characterization of full diamond tips for scanning spreading-resistance microscopy*. Microelectronic Engineering, 2004. **73-74**: p. 910-915.
231. Taylor, J.M., et al., *High-sensitivity diamond magnetometer with nanoscale resolution*. Nat Phys, 2008. **4**(10): p. 810-816.
232. Naydenov, B., et al., *Dynamical decoupling of a single-electron spin at room temperature*. Physical Review B, 2011. **83**(8): p. 081201.
233. de Lange, G., et al., *Single-Spin Magnetometry with Multipulse Sensing Sequences*. Physical Review Letters, 2011. **106**(8): p. 080802.
234. Minsky, M., *Memoir on inventing the confocal microscopy*. Scanning. Vol. 10. 1988.

235. Minsky, M., *Microscopy Apparatus*. Filed in 1957 and granted in 1961, US3013467 (A).
236. Lukosz, W., *Optical Systems with Resolving Powers Exceeding the Classical Limit*. J. Opt. Soc. Am., 1966. **56**(11): p. 1463-1471.
237. Wilson, T. and A.R. Carlini, *Three dimensional imaging in confocal imaging systems with finite-sized detectors*. Journal of Microscopy, 1988. **141**: p. 51-66.
238. Sheppard, C.J.R. and D.M. Shotton, *Image formation in the confocal laser scanning microscope*. 1997 ed. Confocal Laser Scanning Microscopy. 1997, New York: Springer-Verlag, New York Inc.
239. Webb, R., H., *Confocal Optical Microscopy*. Reports on Progress in Physics, 1996. **59**(3): p. 427.
240. Binnig, G., C.F. Quate, and C. Gerber, *Atomic Force Microscope*. Physical Review Letters, 1986. **56**(9): p. 930.
241. Binnig, G. and H. Rohrer, *Scanning tunneling microscopy*. Surface Science, 1983. **126**(1-3): p. 236-244.
242. Jalili, N., Laxminarayana, K., *A Review of Atomic Force Microscopy Imaging Systems: Application to Molecular Metrology and Biological Sciences*. Mechatronics, 2004. **14**(8): p. 907-945.
243. Brown, R.H. and R.Q. Twiss, *A new type of interferometer for use in radio astronomy*. Philosophical Magazine, 1954. **45**: p. 663-682.
244. Brown, R.H. and R.Q. Twiss, *Correlation between Photons in two Coherent Beams of Light*. Nature, 1956. **177**(4497): p. 27-29.
245. Brown, R.H. and R.Q. Twiss, *Interferometry of the Intensity Fluctuations in Light. I. Basic Theory: The Correlation between Photons in Coherent Beams of Radiation*. Proceedings of the Royal Society of London. Series A, Mathematical and Physical Sciences (1934-1990), 1957. **242**(1230): p. 300-324.
246. Brown, R.H. and R.Q. Twiss, *Interferometry of the Intensity Fluctuations in Light II. An Experimental Test of the Theory for Partially Coherent Light*. Proceedings of the Royal Society of London. Series A, Mathematical and Physical Sciences (1934-1990), 1958. **243**(1234): p. 291-319.
247. Michelson, A.A., *The Relative Motion of the Earth and the Luminiferous Ether* Am. J. Sci., 1881. **22**: p. 120-129.
248. Michelson, A.A., Morley, E., *On the Relative Motion of the Earth and the Luminiferous Ether*. Am. J. Sci., 1887. **34**: p. 333-345.
249. Brouri, R., et al., *Photon antibunching in the fluorescence of individual color centers in diamond*. Opt. Lett., 2000. **25**(17): p. 1294-1296.
250. Beveratos, A., et al., *Nonclassical radiation from diamond nanocrystals*. Physical Review A, 2001. **64**(6): p. 061802.
251. Collins, A.T. and et al., *Luminescence decay time of the 1.945 eV centre in type Ib diamond*. Journal of Physics C: Solid State Physics, 1983. **16**(11): p. 2177.
252. Lukosz, W. and R.E. Kunz, *Light emission by magnetic and electric dipoles close to a plane interface. I. Total radiated power*. J. Opt. Soc. Am., 1977. **67**(12): p. 1607-1615.
253. Inam, F.A., et al., *Modification of spontaneous emission from nanodiamond colour centres on a structured surface*. New Journal of Physics, 2011. **13**(7): p. 073012.
254. Inagaki, M., *New Carbons - Control of Structure and Functions*. 2000: Elsevier.
255. Timp, G., *Nanotechnology*. 1999, New York: Springer.

256. Osawa, E., Yoshida, M., Fujita, M., *Shape and Fantasy of Fullerenes*. MRS Bulletin, 1994. **19**(11): p. 33-36.
257. Heinmann, R.B., Evsyukov, S.E., Koga, Y., *Carbon Allotropes: a Suggested Classification Scheme Based on Valence Orbital Hybridization Carbon*, 1997. **35**: p. 1654-1658.
258. Shenderova, O.A., V.V. Zhirnov, and D.W. Brenner, *Carbon Nanostructures*. Critical Reviews in Solid State and Materials Sciences, 2002. **27**(3-4): p. 227-356.
259. Bundy, F.P., et al., *The pressure-temperature phase and transformation diagram for carbon; updated through 1994*. Carbon, 1996. **34**(2): p. 141-153.
260. Ree, F.H., et al., *Kinetics and thermodynamic behavior of carbon clusters under high pressure and high temperature*. Physica B: Condensed Matter, 1999. **265**(1-4): p. 223-229.
261. Charlet, F., et al., *Evaluation of various theoretical equations of state used in calculation of detonation properties*. Vol. 84. 1998: AIP. 4227-4238.
262. Vicelli, J.A. and F.H. Ree, *Carbon particle phase transformation kinetics in detonation waves*. Vol. 88. 2000: AIP. 683-690.
263. Shaw, M.S. and J.D. Johnson, *Carbon clustering in detonations*. Journal of Applied Physics, 1987. **62**(5): p. 2080.
264. Vicelli, J.A., et al., *Phase transformations of nanometer size carbon particles in shocked hydrocarbons and explosives*. Vol. 115. 2001: AIP. 2730-2736.
265. Vereshchagin, A.L., *Phase Diagram of Ultrafine Carbon*. Combustion, Explosion, and Shock Waves, 2002. **38**(3): p. 358-359.
266. Kuznetsov, V.L., Chuvilin, A.L., Butenko, Yu.V., Mal'kov, I.Yu., Gutakovsii, A.K., Stankus, S.V., Khairulin, S.R., *Science and Technology of Fullerene Materials* Vol. 359. 1995, Pittsburgh: MRS Proceedings.
267. Sundqvist, B., *Buckyballs under Pressure*. physica status solidi (b), 2001. **223**(2): p. 469-477.
268. Korobov, M.V., et al., *Phase Transformations in Pressure Polymerized C60*. Chemical Physics Letters, 2003. **381**(3-4): p. 410-415.
269. Schöll-Paschinger, E. and G. Kahl, *Accurate Determination of the Phase Diagram of Model Fullerenes*. EPL (Europhysics Letters), 2003. **63**(4): p. 538.
270. Barnard, A.S., *Theory and modeling of nanocarbon phase stability*. Diamond and Related Materials, 2006. **15**(2-3): p. 285-291.
271. Amlöf, J., Lüthi, H.P., *Supercomputer Research in Chemistry and Chemical Engineering* Am. Chem. Soc. Symposium Series. 1987, Washington DC.
272. Weast, R.C., *Handbook of Chemistry and Physics*. 65th ed. 1984-85, Boca Raton, FL: CRC Press.
273. Winter, N. and F. Ree, *Carbon particle phase stability as a function of size*. Journal of Computer-Aided Materials Design, 1998. **5**(2): p. 279-294.
274. Badziag, P., et al., *Nanometre-sized diamonds are more stable than graphite*. Nature, 1990. **343**(6255): p. 244-245.
275. Brenner, D.W., Shenderova, O.A., Areshkin, D.A., Schall, J.D., Frankland, S.J.V., *Atomic Modeling of Carbon-based Nanostructures as a Tool for Developing New Materials and Technologies*. CMES-Computer Modeling in Engineering and Sciences 2002. **3**: p. 643.
276. Gamarnik, M.Y., *Size-related stabilization of diamond nanoparticles*. Nanostructured Materials, 1996. **7**(6): p. 651-658.

277. Hwang, N.M. and D.Y. Yoon, *Thermodynamic approach to the paradox of diamond formation with simultaneous graphite etching in the low pressure synthesis of diamond*. Journal of Crystal Growth, 1996. **160**(1-2): p. 98-103.
278. Hwang, N.M., J.H. Hahn, and D.Y. Yoon, *Charged cluster model in the low pressure synthesis of diamond*. Journal of Crystal Growth, 1996. **162**(1-2): p. 55-68.
279. Jang, H.M. and N.M. Hwang, *Theory of the charged cluster formation in the low pressure synthesis of diamond: Part I. Charge-induced nucleation*. Journal of Materials Research, 1998. **13**(12): p. 3527-3535.
280. Jiang, Q. and et al., *The size dependence of the diamond-graphite transition*. Journal of Physics: Condensed Matter, 2000. **12**(26): p. 5623.
281. Zhao, D.S., M. Zhao, and Q. Jiang, *Size and temperature dependence of nanodiamond-nanographite transition related with surface stress*. Diamond and Related Materials, 2002. **11**(2): p. 234-236.
282. Barnard, A.S., S.P. Russo, and I.K. Snook, *Size dependent phase stability of carbon nanoparticles: Nanodiamond versus fullerenes*. The Journal of Chemical Physics, 2003. **118**(11): p. 5094-5097.
283. Tománek, D. and M.A. Schluter, *Growth regimes of carbon clusters*. Physical Review Letters, 1991. **67**(17): p. 2331.
284. Jones, R.O., *Density functional study of carbon clusters C_{2n} ($2 \leq n \leq 16$). I. Structure and bonding in the neutral clusters*. The Journal of Chemical Physics, 1999. **110**(11): p. 5189-5200.
285. Martins, J.L., F.A. Reuse, and S.N. Khanna, *Growth and Formation of Fullerene Clusters*. Journal of Cluster Science, 2001. **12**(3): p. 513-525.
286. Kent, P.R.C., et al., *Carbon clusters near the crossover to fullerene stability*. Physical Review B, 2000. **62**(23): p. 15394.
287. Park, N., et al., *Energetics of large carbon clusters: Crossover from fullerenes to nanotubes*. Physical Review B, 2002. **65**(12): p. 121405.
288. Barnard, A.S., S.P. Russo, and I.K. Snook, *Coexistence of bucky diamond with nanodiamond and fullerene carbon phases*. Physical Review B, 2003. **68**(7): p. 073406.
289. Barnard, A.S., S.P. Russo, and I.K. Snook, *Structural relaxation and relative stability of nanodiamond morphologies*. Diamond and Related Materials, 2003. **12**(10-11): p. 1867-1872.
290. Churilov, G.N., et al., *On the mechanism of fullerene formation in a carbon plasma*. Carbon, 2002. **40**(6): p. 891-896.
291. Zaiser, M. and F. Banhart, *Radiation-Induced Transformation of Graphite to Diamond*. Physical Review Letters, 1997. **79**(19): p. 3680.
292. Sinnott, S.B., et al., *Model of carbon nanotube growth through chemical vapor deposition*. Chemical Physics Letters, 1999. **315**(1-2): p. 25-30.
293. Butenko, Y.V., et al., *Kinetics of the graphitization of dispersed diamonds at "low" temperatures*. Vol. 88. 2000: AIP. 4380-4388.
294. Shenderova, O.A., Hu, Z., Brenner, D. , *Carbon family at the nanoscale*. Synthesis, Properties And Applications of Ultrananocrystalline Diamond, ed. D.M. Gruen, Shenderova, O.A., Vul Ya. A. . 2005: Springer.
295. Raty, J.-Y., et al., *Quantum Confinement and Fullerenelike Surface Reconstructions in Nanodiamonds*. Physical Review Letters, 2003. **90**(3): p. 037401.
296. Matsumoto, S., *Chemical vapour deposition of diamond in RF glow discharge*. Journal of Materials Science Letters, 1985. **4**(5): p. 600-602.

297. Kim, J.S., et al., *The morphology changes in diamond synthesized by hot-filament chemical vapor deposition*. Vol. 67. 1990: AIP. 3354-3357.
298. Dilawar, N., et al., *Structure of diamond and diamond like carbon thin films grown by hot-filament chemical vapour deposition technique*. Bulletin of Materials Science, 1996. **19**(3): p. 467-473.
299. Smith, B.R., et al., *Five-Nanometer Diamond with Luminescent Nitrogen-Vacancy Defect Centers*. Small, 2009. **5**(14): p. 1649-1653.
300. Barnard, A.S. and M. Sternberg, *Mapping the location and configuration of nitrogen in diamond nanoparticles*. Nanotechnology, 2007. **18**(2): p. 025702.
301. Tisler, J., et al., *Fluorescence and Spin Properties of Defects in Single Digit Nanodiamonds*. ACS Nano, 2009. **3**(7): p. 1959-1965.
302. Porezag, D., et al., *Construction of tight-binding-like potentials on the basis of density-functional theory: Application to carbon*. Physical Review B, 1995. **51**(19): p. 12947.
303. Thomas, F., et al., *Atomistic simulations of complex materials: ground-state and excited-state properties*. Journal of Physics: Condensed Matter, 2002(11): p. 3015.
304. Barnard, A.S. and M. Sternberg, *Substitutional Nitrogen in Nanodiamond and Bucky-Diamond Particles*. The Journal of Physical Chemistry B, 2005. **109**(36): p. 17107-17112.
305. Turner, S., et al., *Determination of Size, Morphology, and Nitrogen Impurity Location in Treated Detonation Nanodiamond by Transmission Electron Microscopy*. Advanced Functional Materials, 2009. **19**(13): p. 2116-2124.
306. Barnard, A.S., *Private communication*. 2012.
307. Smith, A., A. Mainwood, and M. Watkins, *The kinetics of the capture of nitrogen by nickel defects in diamond*. Diamond and Related Materials. **11**(3-6): p. 312-315.
308. Fu, K.M.C., et al., *Conversion of neutral nitrogen-vacancy centers to negatively charged nitrogen-vacancy centers through selective oxidation*. Applied Physics Letters, 2010. **96**(12): p. 121907.
309. Rondin, L., et al., *Surface-induced charge state conversion of nitrogen-vacancy defects in nanodiamonds*. Physical Review B, 2010. **82**(11): p. 115449.
310. Hauf, M.V., et al., *Chemical control of the charge state of nitrogen-vacancy centers in diamond*. Physical Review B, 2011. **83**(8): p. 081304.
311. Vlasov, I.I., et al., *Nitrogen and Luminescent Nitrogen-Vacancy Defects in Detonation Nanodiamond*. Small, 2010. **6**(5): p. 687-694.
312. Boudou, J.-P. and et al., *High yield fabrication of fluorescent nanodiamonds*. Nanotechnology, 2009. **20**(23): p. 235602.
313. Stacey, A., et al., *Controlled synthesis of high quality micro/nano-diamonds by microwave plasma chemical vapor deposition*. Diamond and Related Materials, 2009. **18**(1): p. 51-55.
314. Kennedy, T.A., et al., *Long coherence times at 300 K for nitrogen-vacancy center spins in diamond grown by chemical vapor deposition*. Vol. 83. 2003: AIP. 4190-4192.
315. Krüger, A., et al., *Unusually tight aggregation in detonation nanodiamond: Identification and disintegration*. Carbon, 2005. **43**(8): p. 1722-1730.
316. Osawa, E., *Monodisperse single nanodiamond particulates*. Pure Appl. Chem., 2008. **80**(7): p. 1365-1379.
317. Osswald, S., et al., *Increase of nanodiamond crystal size by selective oxidation*. Diamond and Related Materials, 2008. **17**(7-10): p. 1122-1126.

318. Iakoubovskii, K. and et al., *High-resolution electron microscopy of detonation nanodiamond*. *Nanotechnology*, 2008. **19**(15): p. 155705.
319. Hu, S., et al., *Synthesis and luminescence of nanodiamonds from carbon black*. *Materials Science and Engineering: B*, 2009. **157**(1-3): p. 11-14.
320. Ting, C.-C., T.-F. Young, and C.-S. Jwo, *Fabrication of diamond nanopowder using microwave plasma torch technique*. *The International Journal of Advanced Manufacturing Technology*, 2007. **34**(3): p. 316-322.
321. Zhao, F.L., et al., *Ultrafast optical emission of nanodiamond induced by laser excitation*. Vol. 85. 2004: AIP. 914-916.
322. Chung, P.H., E. Perevedentseva, and C.L. Cheng, *The particle size-dependent photoluminescence of nanodiamonds*. *Surface Science*, 2007. **601**(18): p. 3866-3870.
323. Morita, Y., et al., *A Facile and Scalable Process for Size-Controllable Separation of Nanodiamond Particles as Small as 4 nm*. *Small*, 2008. **4**(12): p. 2154-2157.
324. Ushizawa, K., et al., *Covalent immobilization of DNA on diamond and its verification by diffuse reflectance infrared spectroscopy*. *Chemical Physics Letters*, 2002. **351**(1-2): p. 105-108.
325. Ando, T., et al., *Thermal hydrogenation of diamond surfaces studied by diffuse reflectance Fourier-transform infrared, temperature-programmed desorption and laser Raman spectroscopy*. *Journal of the Chemical Society, Faraday Transactions*, 1993. **89**(11): p. 1783-1789.
326. Evans, S., *The Properties of Natural and Synthetic Diamond*, ed. J.E. Field. 1992, London: Academic Press.
327. Evans, S. and C.E. Riley, *Angular dependence of X-ray-excited valence-band photoelectron spectra of diamond*. *Journal of the Chemical Society, Faraday Transactions 2: Molecular and Chemical Physics*, 1986. **82**(4): p. 541-550.
328. Praver, S., et al., *The Raman spectrum of nanocrystalline diamond*. *Chemical Physics Letters*, 2000. **332**(1-2): p. 93-97.
329. Ager, J.W., D.K. Veirs, and G.M. Rosenblatt, *Spatially resolved Raman studies of diamond films grown by chemical vapor deposition*. *Physical Review B*, 1991. **43**(8): p. 6491-6499.
330. Ferrari, A.C. and J. Robertson, *Origin of the 1150-cm⁻¹ Raman mode in nanocrystalline diamond*. *Physical Review B*, 2001. **63**(12): p. 121405.
331. Osswald, S., et al., *Control of sp²/sp³ Carbon Ratio and Surface Chemistry of Nanodiamond Powders by Selective Oxidation in Air*. *Journal of the American Chemical Society*, 2006. **128**(35): p. 11635-11642.
332. Gaebel, T., et al., *Size-reduction of nanodiamonds via air oxidation*. *Diamond and Related Materials*, 2011. **21**(0): p. 28-32.
333. Ando, T., et al., *Vapour-phase oxidation of diamond surfaces in O₂ studied by diffuse reflectance Fourier-transform infrared and temperature-programmed desorption spectroscopy*. *Journal of the Chemical Society, Faraday Transactions*, 1993. **89**(19): p. 3635-3640.
334. Evans, T., *The Properties of Diamond*, ed. J.E. Field. 1979, London: Academic Press.
335. Alam, M., Sun, Q., *Relative Oxidation Behavior of Chemical Vapor Deposited and Type IIa Natural Diamonds*. *Journal of The Electrochemical Society*, 1992. **139**(3): p. 933-936.

336. Joshi, A., R. Nimmagadda, and J. Herrington, *Oxidation kinetics of diamond, graphite, and chemical vapor deposited diamond films by thermal gravimetry*. Vol. 8. 1990: AVS. 2137-2142.
337. Nimmagadda, R.R., A. Joshi, and W.L. Hsu, *Role of microstructure on the oxidation behavior of microwave plasma synthesized diamond and diamond-like carbon films*. *Journal of Materials Research*, 1990. 5(11): p. 2445-2450.
338. Chu, C.J., et al., *F₂, H₂O, and O₂ etching rates of diamond and the effects of F₂, HF and H₂O on the molecular O₂ etching of (110) diamond*. *Diamond and Related Materials*, 1995. 4(12): p. 1317-1324.
339. Uchida, N., et al., *Thermochemical etching effect on CVD diamond film in an oxygen atmosphere*. *Journal of Materials Science Letters*, 1990. 9(3): p. 249-250.
340. Pang, L.S.K., J.D. Saxby, and S.P. Chatfield, *Thermogravimetric analysis of carbon nanotubes and nanoparticles*. *The Journal of Physical Chemistry*, 1993. 97(27): p. 6941-6942.
341. Bom, D., et al., *Thermogravimetric Analysis of the Oxidation of Multiwalled Carbon Nanotubes: Evidence for the Role of Defect Sites in Carbon Nanotube Chemistry*. *Nano Letters*, 2002. 2(6): p. 615-619.
342. Thomas, R.E., R.A. Rudder, and R.J. Markunas, *Thermal desorption from hydrogenated and oxygenated diamond (100) surfaces*. Vol. 10. 1992: AVS. 2451-2457.
343. de Theije, F.K., et al., *A surface topographic investigation of {001} diamond surfaces etched in oxygen*. *Philosophical Magazine A*, 2000. 80(3): p. 725-745.
344. de Theije, F.K., et al., *Oxidative etching of diamond*. *Diamond and Related Materials*, 2000. 9(3-6): p. 929-934.
345. Cook, R.J. and H.J. Kimble, *Possibility of Direct Observation of Quantum Jumps*. *Physical Review Letters*, 1985. 54(10): p. 1023-1026.
346. Veerman, J.A., et al., *Time-Varying Triplet State Lifetimes of Single Molecules*. *Physical Review Letters*, 1999. 83(11): p. 2155-2158.
347. Kohn, F., et al., *Parameters Influencing the On- and Off-Times in the Fluorescence Intensity Traces of Single Cyanine Dye Molecules*. *The Journal of Physical Chemistry A*, 2002. 106(19): p. 4808-4814.
348. Tinnefeld, P., et al., *Higher-Excited-State Photophysical Pathways in Multichromophoric Systems Revealed by Single-Molecule Fluorescence Spectroscopy*. *ChemPhysChem*, 2004. 5(11): p. 1786-1790.
349. Haase, M., et al., *Exponential and Power-Law Kinetics in Single-Molecule Fluorescence Intermittency* *The Journal of Physical Chemistry B*, 2004. 108(29): p. 10445-10450.
350. Christ, T., et al., *Watching the Photo-Oxidation of a Single Aromatic Hydrocarbon Molecule*. *Angewandte Chemie International Edition*, 2001. 40(22): p. 4192-4195.
351. Hernando, J., et al., *Excitonic Behavior of Rhodamine Dimers: A Single-Molecule Study*. *The Journal of Physical Chemistry A*, 2002. 107(1): p. 43-52.
352. Liu, R., et al., *Single-Molecule Spectroscopy of Intramolecular Electron Transfer in Donor-Bridge-Acceptor Systems*. *The Journal of Physical Chemistry A*, 2003. 107(34): p. 6522-6526.
353. Schuster, J., F. Cichos, and C.v. Borczykowski, *Influence of self-trapped states on the fluorescence intermittency of single molecules*. Vol. 87. 2005: AIP. 051915.
354. Dickson, R.M., et al., *On/off blinking and switching behaviour of single molecules of green fluorescent protein*. *Nature*, 1997. 388(6640): p. 355-358.

355. Bout, D.A.V., et al., *Discrete Intensity Jumps and Intramolecular Electronic Energy Transfer in the Spectroscopy of Single Conjugated Polymer Molecules*. *Science*, 1997. **277**(5329): p. 1074-1077.
356. Nirmal, M., et al., *Fluorescence intermittency in single cadmium selenide nanocrystals*. *Nature*, 1996. **383**(6603): p. 802-804.
357. Mason, M.D., et al., *Luminescence of Individual Porous Si Chromophores*. *Physical Review Letters*, 1998. **80**(24): p. 5405-5408.
358. Wang, S., et al., *Fluorescence Blinking Statistics from CdSe Core and Core/Shell Nanorods*. *The Journal of Physical Chemistry B*, 2006. **110**(46): p. 23221-23227.
359. Protasenko, V.V., K.L. Hull, and M. Kuno, *Disorder-Induced Optical Heterogeneity in Single CdSe Nanowires*. *Advanced Materials*, 2005. **17**(24): p. 2942-2949.
360. Protasenko, V., S. Gordeyev, and M. Kuno, *Spatial and Intensity Modulation of Nanowire Emission Induced by Mobile Charges*. *Journal of the American Chemical Society*, 2007. **129**(43): p. 13160-13171.
361. Glennon, J.J., et al., *Synchronous Photoluminescence Intermittency (Blinking) along Whole Semiconductor Quantum Wires*. *Nano Letters*, 2007. **7**(11): p. 3290-3295.
362. Efros, A.L. and M. Rosen, *Random Telegraph Signal in the Photoluminescence Intensity of a Single Quantum Dot*. *Physical Review Letters*, 1997. **78**(6): p. 1110-1113.
363. Verberk, R., A.M. van Oijen, and M. Orrit, *Simple model for the power-law blinking of single semiconductor nanocrystals*. *Physical Review B*, 2002. **66**(23): p. 233202.
364. Krauss, T.D., S. O'Brien, and L.E. Brus, *Charge and Photoionization Properties of Single Semiconductor Nanocrystals*. *The Journal of Physical Chemistry B*, 2001. **105**(9): p. 1725-1733.
365. Kuno, M., et al., *Nonexponential "blinking" kinetics of single CdSe quantum dots: A universal power law behavior*. *The Journal of Chemical Physics*, 2000. **112**(7): p. 3117-3120.
366. Kuno, M., et al., *"On"/"off" fluorescence intermittency of single semiconductor quantum dots*. *The Journal of Chemical Physics*, 2001. **115**(2): p. 1028-1040.
367. Shimizu, K.T., et al., *Blinking statistics in single semiconductor nanocrystal quantum dots*. *Physical Review B*, 2001. **63**(20): p. 205316.
368. Cichos, F., C. von Borczyskowski, and M. Orrit, *Power-law intermittency of single emitters*. *Current Opinion in Colloid & Interface Science*, 2007. **12**(6): p. 272-284.
369. Gomez, D.E., et al., *Exciton-Trion Transitions in Single CdSe-CdS Core-Shell Nanocrystals*. *ACS Nano*, 2009. **3**(8): p. 2281-2287.
370. Frantsuzov, P., et al., *Universal emission intermittency in quantum dots, nanorods and nanowires*. *Nat Phys*, 2008. **4**(5): p. 519-522.
371. Margolin, G., Protasenko, V., Kuno, M., Barkai, E., *Power law blinking quantum dots: Stochastic and physical models*. *Adv. Chem. Phys.*, 2006. **133**: p. 327-356.
372. Frantsuzov, P.A. and R.A. Marcus, *Explanation of quantum dot blinking without the long-lived trap hypothesis*. *Physical Review B*, 2005. **72**(15): p. 155321.
373. Tang, J. and R.A. Marcus, *Diffusion-Controlled Electron Transfer Processes and Power-Law Statistics of Fluorescence Intermittency of Nanoparticles*. *Physical Review Letters*, 2005. **95**(10): p. 107401.
374. Zhang, K., et al., *Continuous Distribution of Emission States from Single CdSe/ZnS Quantum Dots*. *Nano Letters*, 2006. **6**(4): p. 843-847.

375. Kuno, M., et al., *Modeling distributed kinetics in isolated semiconductor quantum dots*. Physical Review B, 2003. **67**(12): p. 125304.
376. Uchiike, H., Miura, K., Nakayama, N., Shinoda, T., Fukushima, Y., *Secondary Electron Emission Characteristics of Dielectric Materials in AC-Operated Plasma Display Panels* IEEE Transactions of Electron Devices 1976. **23**(11): p. 1211-1217.
377. Maier, F., et al., *Origin of Surface Conductivity in Diamond*. Physical Review Letters, 2000. **85**(16): p. 3472-3475.
378. Griscom, D., *Defect structure of glasses: Some outstanding questions in regard to vitreous silica*. Journal of Non-Crystalline Solids, 1985. **73**(1-3): p. 51-77.
379. Landstrass, M.I. and K.V. Ravi, *Resistivity of chemical vapor deposited diamond films*. Applied Physics Letters, 1989. **55**(10): p. 975-977.
380. Garrido, J.A., et al., *The Diamond/Aqueous Electrolyte Interface: an Impedance Investigation*. Langmuir, 2008. **24**(8): p. 3897-3904.